

ÉCOLE DOCTORALE _____ 222 _____
ISIS - UMR7006

THÈSE présentée par:
Alberto Giuseppe CATALANO
sotenu le: 02 septembre 2024

pour obtenir le grade de: **Docteur de l'Université de Strasbourg**
Discipline / Spécialité: Physique

**Understanding and exploiting non-local
effects in quantum spin chains**

THÈSE dirigée par:
Dr. Fabio Franchini
Prof. Guido Pupillo

Directeur de recherches, Institut Ruder BOškovic
Professeur, Université de Strasbourg

RAPPORTEURS:
Prof. Maria Luisa Chiofalo
Prof. Marcello Dalmonte

Professeur, University of Pisa
Directeur de recherches, ICTP

AUTRES MEMBRES DU JURY:
Prof. Nicoló Defenu

Professeur, ETH Zurich

List of Publications

- [1] A. G. Catalano, D. Brtan, F. Franchini and S. M. Giampaolo, *Simulating continuous symmetry models with discrete ones*, Phys. Rev. B, 106, 125145 (2022).
- [2] A. G. Catalano, F. Mattiotti, J. Dubail, D. Hagenmüller, T. Prosen, F. Franchini, G. Pupillo, *Anomalous diffusion in the Long-Range Haken-Strobl-Reineker model*, Phys. Rev. Lett. 131, 053401 (2023).
- [3] A. G. Catalano, S. M. Giampaolo, Oliver Morsch, V. Giovannetti, F. Franchini, *Frustrating quantum batteries*, PRX Quantum 5, 030319 (2024).
- [4] D. Sacco Shaikh, A. G. Catalano, F. Cavaliere, F. Franchini, M. Sassetti, N. Traverso Ziani, *Towards a phase diagram of the topologically frustrated XY chain*, (2024).
- [5] A. G. Catalano, *Numerically efficient unitary evolution for Hamiltonians beyond nearest-neighbors*, arXiv:2402.05198 (2024).
- [6] G. Torre, A. G. Catalano, S. B. Kožić, F. Franchini, S. M. Giampaolo, *Interplay between local and non-local frustration in the 1D ANNNI chain I – The even case*, arXiv:2406.19449 (2024)
- [7] A. G. Catalano, J. Odavić, G. Torre, A. Hamma, F. Franchini, S. M. Giampaolo, *Magic phase transition and non-local complexity in generalized W State*, arXiv:2406.19457 (2024).

Acknowledgements

As this important chapter of my professional and personal life comes to an end, I am very grateful for the opportunity I had to cross paths with many outstanding individuals, who I will always value for their advice, friendship, and for serving as an inspiration in a special way.

I would like to begin by thanking my advisor Fabio Franchini, for contributing to my thesis as well as introducing me to the world of scientific research. I will always cherish his encouragement, guidance and advices, which helped me grow in many ways. This whole thesis would not exist without him.

I am also deeply thankful to Guido Pupillo, my advisor at the University of Strasbourg, for the invaluable collaboration and, most of all, for his efforts in the scientific management of the MSCA ITN *MOlecular Quantum Simulations* (MOQS), of which I had the pleasure to be a part. This experience enriched my PhD journey beyond measure.

I gratefully acknowledge Salvatore Marco Giampaolo, for the constant collaboration on the research presented in the thesis, the advices and the discussions. His contribution was invaluable.

I would like to thank also the whole team at the Ruđer Bošković Institute, and in particular Gianpaolo, Daria, Riccarda, Jovan, Karlo and Sven, both for the scientific collaboration and for creating a very comfortable and enjoyable work environment. At the same time, I acknowledge all the researchers, also from other institutes and countries, that have contributed to the works presented in this thesis.

A special thank you to my sister, Anastasia. Your love and encouragement was an

indispensable presence. And to my parents, Giovanni and Daniela. You are the reason I am here today. I owe you everything and will continue to make you proud.

Hvala od srca, Kristina, for standing by my side during these important years, supporting and encouraging me to pursue my dreams. I deeply treasure the time we spent together, exploring Croatia and traveling the world. Your love, patience, and joy gave me the strength to push through moments of doubt and insecurity. You were like a light guiding me through the storm during my most difficult moments. *‘Sei la piccola stella che porto, nei momenti in cui non ho luce.’* I can’t wait to discover together what the future has in store for us.

Résumé

À l'aube de la seconde révolution quantique, comprendre et exploiter les phénomènes résultant de l'interaction entre la non-localité intrinsèque de la mécanique quantique et les interactions purement non-locales est d'une importance cruciale pour le développement de nouvelles technologies quantiques. Dans cette thèse, nous nous concentrerons principalement sur les effets non-locaux introduits par la frustration topologique (FT), une forme de frustration faible qui a été introduite pour la première fois dans le contexte des chaînes de spins quantiques antiferromagnétiques en appliquant les conditions aux limites frustrées, réalisées comme une combinaison de conditions aux limites périodiques et d'un nombre impair de spins. Notre objectif est double. D'une part, nous améliorerons la compréhension théorique des phases topologiquement frustrées. Au-delà de ces implications théoriques, ce travail démontrera que les chaînes de spins FT présentent un potentiel technologique convaincant, les proposant comme des candidats compétitifs pour le développement de batteries quantiques robustes et efficaces.

Résumé en anglais

At the verge of the second quantum revolution, understanding and exploiting the phenomena resulting from the interplay between the intrinsic non-locality of quantum mechanics and purely non-local interactions is of crucial importance for the development of novel quantum technologies. In this thesis, we will mostly focus on the non-local effects introduced by topological frustration (TF), a form of weak frustration that was first introduced in the context of antiferromagnetic quantum spin chains by applying the so called frustrated boundary conditions, realized as a combination of periodic boundary conditions and odd number of spins. Our goal is double. From one side, we will further improve the theoretical understanding of topologically frustrated phases. Beyond these theoretical implications, this work will demonstrate that TF spin chains exhibit compelling technological potential, proposing them as competitive candidates for the development of robust and efficient quantum batteries.

RESUME

1) Introduction

Le domaine des systèmes complexes quantiques a émergé comme l'extension naturelle de la physique statistique classique. Il n'est donc pas surprenant que les premières études aient été centrées sur l'analyse de quantités telles que les fonctions de corrélation et les paramètres d'ordre locaux qui, en accord avec la théorie de Landau [1], caractérisent les différentes phases d'un système physique. Cette approche a obtenu des succès remarquables, mais la non-localité inhérente de la mécanique quantique a donné lieu à une phénoménologie bien plus large que celle des systèmes classiques, qu'il était impossible d'englober entièrement dans ce cadre.

Un exemple notable de ce fait est représenté par les phases ordonnées topologiquement qui se caractérisent par des dégénérescences robustes de l'état fondamental [2] et peuvent être révélées par des invariants topologiques qui restent inchangés par des déformations continues des paramètres hamiltoniens [3,4]. Dans ces phases, les structures globales des états fondamentaux sont liées à des corrélations non locales dont la présence peut être mise en évidence par les propriétés d'intrication [5-7]. Cependant, cet ordre représente seulement un exemple, même s'il est le plus connu, des différentes phénoménologies échappant à la théorie de Landau qui sont continuellement dévoilées.

Un autre exemple, qui est à la base des résultats présentés dans cette thèse, est la soi-disant frustration topologique (FT). Un système classique à plusieurs corps est dit frustré lorsqu'il est impossible de minimiser simultanément l'énergie de toutes les interactions entre ses constituants. En mécanique quantique, ce concept doit être manipulé avec précaution. En effet, en raison de la nature non commutative de la mécanique quantique, à quelques exceptions près, comme les modèles libres frustrés [8] et les systèmes au point de factorisation [9], selon la définition classique presque tous les systèmes quantiques incluent une certaine quantité de frustration [10,11]. Cependant, en accord avec l'usage récent dans la communauté scientifique, ce travail restreint le concept de frustration aux effets induits par des interactions concurrentes, des propriétés de réseau ou des conditions aux limites, en l'étendant directement des systèmes classiques [12,13].

Le cas introduit par les conditions aux limites est celui de la FT, une forme de frustration faible qui a été d'abord introduite dans le contexte des chaînes de spins quantiques antiferromagnétiques (AFM) en appliquant les soi-disant conditions aux limites frustrées (FBCs) [14], qui sont réalisées comme une combinaison de conditions aux limites périodiques et d'un nombre impair de spins. La physique de la FT a récemment suscité un intérêt significatif. D'un point de vue théorique, comme anticipé, ces systèmes semblent défier les prédictions de la théorie de Landau : bien qu'introduite par un choix approprié de conditions aux limites, la FT peut profondément modifier le diagramme de phase des chaînes de spins quantiques, par exemple en induisant de nouvelles transitions de phase ou en affectant les paramètres d'ordre locaux [15-17]. De plus, puisque dans la limite classique ces systèmes développent une dégénérescence étendue de l'état fondamental qui est levée dès que des

interactions quantiques sont ajoutées [18,19], une structure de bande sans gap remplace la phase avec gap présentée par les mêmes systèmes dans la même région des espaces de paramètres mais avec des conditions aux limites différentes. Ce fait est associé à l'émergence d'une phénoménologie particulière impliquant l'augmentation de la complexité de l'état fondamental, comme en témoignent des ressources quantiques telles que l'entropie d'intrication et la non-stabilisation quantique, ainsi qu'une énorme sensibilité des propriétés dynamiques aux petites perturbations locales [20]. Fait intéressant, la plupart de ces résultats peuvent être décrits dans le cadre d'une image de particule unique, correspondant à une excitation délocalisée induite par la FT dans l'état fondamental des chaînes de spins 1D.

L'objectif de cette thèse est double. D'un côté, elle vise à approfondir la compréhension des phases topologiquement frustrées, en se concentrant sur les phases chirales particulières émergeant dans le diagramme de phase de certaines chaînes de spins TF et en étendant le modèle de quasi-particule à des systèmes avec des sources multiples et étendues de frustration. Au-delà de ces implications théoriques, ce travail démontre également que les chaînes de spins TF présentent un potentiel technologique remarquable, les proposant comme des candidats compétitifs pour le développement de dispositifs de stockage d'énergie quantique robustes et efficaces [21].

2) Résultats et discussions

2.1) Phases chirales dans les chaînes de spins topologiquement frustrées

L'un des exemples les plus généraux d'une chaîne de spins à courte portée et topologiquement frustrée est donné par la chaîne de Heisenberg entièrement anisotrope avec un champ magnétique global le long de l'axe z, dont le Hamiltonien s'écrit :

$$H_{XYZ} = \sum_{l=1}^L \sum_{\alpha=x,y,z} J_{\alpha} \sigma_l^{\alpha} \sigma_{l+1}^{\alpha} + h \sum_{l=1}^L \sigma_l^z, \quad (1)$$

où les J_{α} déterminent la force et la nature des interactions selon chaque direction spatiale. En raison des conditions aux limites frustrées (FBCs), le nombre total de spins est impair (c'est-à-dire $L = 2n - 1$ pour $n \in \mathbb{N}$) et des conditions aux limites périodiques sont supposées (c'est-à-dire $\sigma_l^{\alpha} = \sigma_{l+L}^{\alpha}, \forall l$). En utilisant des techniques de diagonalisation exacte numérique, nous avons montré qu'en fixant $J_x = 1$ et en supposant $J_x > |J_y|, |J_z|$, il existe une valeur critique du champ magnétique externe $h_c > 0$ telle que pour $|h| < h_c$, l'état fondamental possède un moment cinétique fini $p \neq 0$ et est au moins deux fois dégénéré, la dégénérescence étant réalisée par des états propres de moment avec des moments opposés $|\pm p\rangle$ (voir Figure 1). Malheureusement, comme l'Hamiltonien H_{XYZ} est non intégrable, il est impossible de déterminer une expression analytique pour le champ critique $h_c(J_x, J_y, J_z)$.

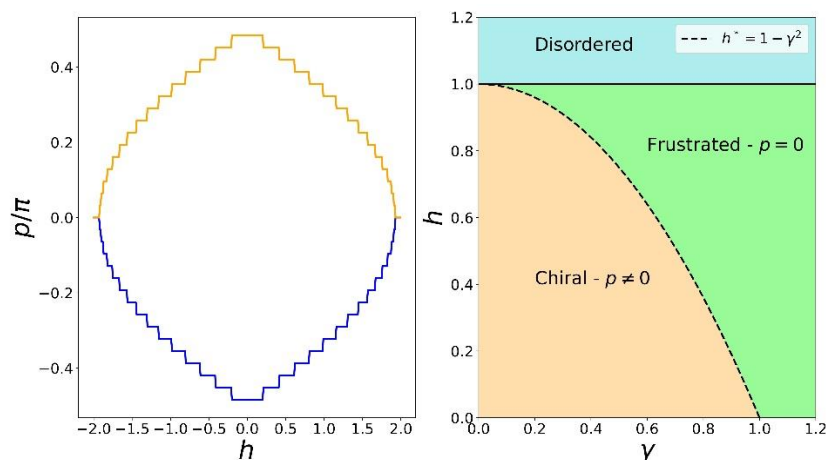


Figure 1 : Gauche : moments de l'état fondamental pour la chaîne XYZ en fonction du champ magnétique externe h , pour $J_x = 1, J_y = 0.6, J_z = 0.2$ et $L = 31$. Droite : diagramme de phase de la chaîne XY topologiquement frustrée pour $J = 1$.

Cependant, en présence de FBCs, cette transition vers une phase chirale se produit également dans une version simplifiée de la chaîne XYZ obtenue en fixant $J_z = 0$, c'est-à-dire la chaîne XY dans un champ transverse:

$$H_{XY} = J \sum_{l=1}^L \left(\frac{1+\gamma}{2} \sigma_l^x \sigma_{l+1}^x + \frac{1-\gamma}{2} \sigma_l^y \sigma_{l+1}^y \right) + h \sum_{l=1}^L \sigma_l^z, \quad (2)$$

où $0 < \gamma < 1$ paramètre l'anisotropie de l'interaction spin-spin dans le plan xy. Ce modèle peut être résolu analytiquement grâce au fait qu'une transformation de Jordan-Wigner le mappe sur un système de fermions libres sans spin. Par conséquent, dans ce cas, il est possible de déterminer analytiquement la frontière de la région chirale, qui pour $J = 1$ est donnée par la parabole $h_c = 1 - \gamma^2$ (voir Figure 1) [17,21]. En utilisant des méthodes analytiques, nous avons montré qu'à l'intérieur de la phase chirale, l'état fondamental du système présente plusieurs propriétés qui sont typiquement observées dans les états fondamentaux des modèles décrits par des Hamiltoniens possédant des symétries continues, alors que H_{XYZ} et H_{XY} ne possèdent que des symétries discrètes. Des exemples de telles propriétés sont l'émergence d'un momentum de Fermi effectif fini autour duquel des excitations de basse énergie peuvent émerger, un spectre pseudo-gapless (le gap énergétique se ferme comme L^{-2}) et des transitions continues, dans la limite thermodynamique, entre des états fondamentaux décrits par différents nombres quantiques [21].

2.2) Une transition de phase « magique »

Motivés par ces propriétés intéressantes et inattendues de l'état fondamental, nous avons essayé de caractériser la nature de la transition vers la phase chirale. Les approches bien établies impliquent l'étude du comportement non analytique de quantités telles que l'entropie d'intrication, les fonctions

de corrélation, la fidélité de l'état fondamental ou l'énergie libre à travers la parabole critique. Cependant, notre analyse a montré que toutes ces quantités deviennent analytiques dans la limite thermodynamique, puisque tout saut dans leurs dérivées disparaît typiquement au moins comme L^{-1} , échouant ainsi à signaler la présence d'une transition de phase quantique à la frontière de la région chirale [21]. En fin de compte, la seule quantité montrant une discontinuité finie dans la limite thermodynamique à la frontière de la région chirale est l'entropie de Renyi du stabilisateur (SRE) [22], également connue sous le nom de magie quantique. Pour un état quantique de L qubits $|\psi\rangle$, cela est défini comme

$$M_2(|\psi\rangle) = -\log_2 \frac{1}{2^L} \sum_P |\langle \psi | P | \psi \rangle|^4, \quad (3)$$

où P est une chaîne de Pauli de L qubits et mesure le nombre de portes non-Clifford nécessaires pour produire $|\psi\rangle$ en utilisant un circuit quantique. Récemment, il a été montré que cette quantité peut être calculée efficacement pour les états produits par matrices (MPSs). Ainsi, en réalisant une analyse d'échelle de taille finie en utilisant des algorithmes basés sur les réseaux de tenseurs [23], nous avons pu établir que dans la limite thermodynamique, la magie présente un saut fini d'amplitude $\Delta M_2 = \log_2(7/6)$, comme montré dans la Figure 2.

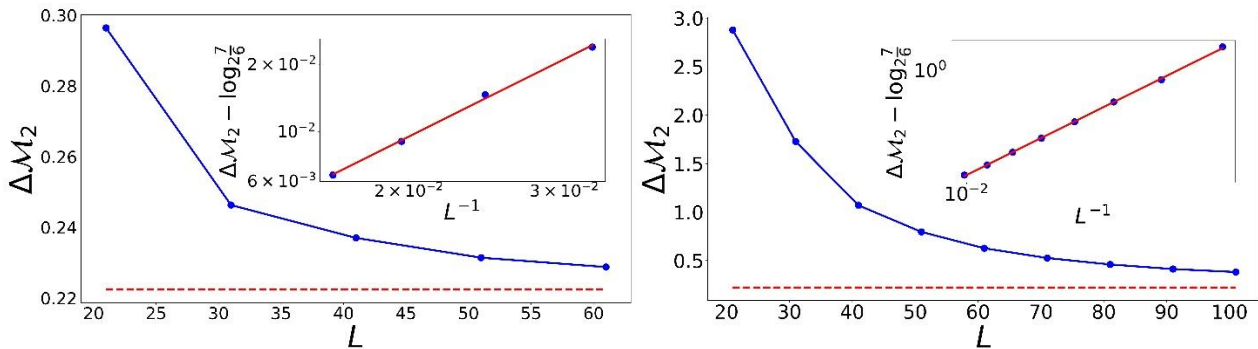


Figure 2: Analyse de mise à l'échelle en fonction de la taille finie du saut dans l'entropie de Renyi du stabilisateur (SRE) pour la chaîne XY (gauche) et la chaîne XYZ (droite). Les encarts, utilisant une échelle logarithmique-logarithmique, montrent une convergence en loi de puissance de ΔM_2 vers la valeur constante $\log_2(7/6)$.

Ce résultat numérique peut également être compris analytiquement en considérant que, en négligeant les contributions locales qui sont égales des deux côtés de la frontière de la phase chirale, l'état fondamental frustré pour $h > h_c$ possède la même magie qu'un état W:

$$W = \frac{1}{\sqrt{L}} \sum_{l=1}^L \sigma_l^z | \leftarrow \rangle^{\otimes L} \quad (4)$$

alors que l'état fondamental frustré pour $h < h_c$ possède la même magie qu'un état W généralisé avec un moment cinétique fini p :

$$W_p = \frac{1}{\sqrt{L}} \sum_{l=1}^L e^{ipl} \sigma_l^z | \leftarrow \rangle^{\otimes L} \quad (5)$$

et, dans la limite thermodynamique, il peut être démontré analytiquement que

$$\lim_{L \rightarrow \infty} M_2(W_p) - M_2(W) = \log_2(7/6). \quad (6)$$

Alors que les transitions de phase quantique induites par la mesure, signalées par la magie mais non par l'intrication, ont déjà été rapportées dans des circuits quantiques aléatoires, notre résultat représente la première instance d'une transition de phase quantique qui est attestée exclusivement par la magie quantique dans un système hamiltonien déterministe.

2.3) Interaction entre frustration locale et non locale

Les propriétés particulières des états fondamentaux des systèmes TF que nous avons décrites jusqu'à présent peuvent toutes s'expliquer dans le cadre d'une image de quasi-particules. Typiquement, cela est considéré comme possible grâce au fait que TF n'introduit qu'une quantité non extensive de frustration dans les chaînes de spins quantiques AFM voisines. D'autre part, il existe également des modèles unidimensionnels dans lesquels la quantité de frustration est extensive. C'est le cas des chaînes de spins quantiques avec des interactions locales concurrentes, entraînant un nombre étendu de liaisons frustrées. Le modèle prototypique de frustration locale sans désordre est sûrement la chaîne d'Ising axiale à voisins les plus proches, également appelée chaîne ANNNI [24], dont l'hamiltonien s'écrit :

$$H_{ANNNI} = J_1 \sum_{l=1}^L \sigma_l^x \sigma_{l+1}^x + J_2 \sum_{l=1}^L \sigma_l^x \sigma_{l+2}^x + h \sum_{l=1}^L \sigma_l^z, \quad (7)$$

où $J_{1,2}$ sont respectivement les interactions entre les voisins les plus proches et les voisins les plus proches suivants, et h est un champ magnétique transverse. Lorsque $J_2 > 0$, le système est localement frustré, car l'ordre promu par l'interaction entre les voisins les plus proches suivants entre en conflit avec celui promu par J_1 . Au point classique (c'est-à-dire $h = 0$), cette compétition résulte en

une transition de phase entre une phase ordonnée et une phase frustrée appelée antiphase pour $\kappa = J_2/|J_1| > 1/2$. Lorsque le champ transverse est activé, les fluctuations quantiques enrichissent davantage le diagramme de phase du modèle, ce qui résulte en quatre phases différentes qui ont été largement étudiées dans la littérature.

Cependant, tous les résultats connus sur ce modèle sont généralement limités à une situation où la taille totale du système est un multiple entier de 4, c'est-à-dire $L = 4n$ pour certains $n \in \mathbb{N}$. Dans ce cas, l'antiphase est une phase à gap, dans laquelle la bande de l'état fondamental contient quatre états exponentiellement proches, séparés de la bande d'états excités par un gap fini important. Afin d'étudier l'interaction entre la frustration locale et topologique, nous avons décidé de considérer des systèmes dans lesquels le nombre de spins est pair mais non un multiple de 4, c'est-à-dire $L = 4n + 2$ pour $n \in \mathbb{N}$. Dans ce cas, le système peut être considéré comme constitué de deux chaînes d'Ising TF interagissantes avec $L/2$ spins chacune, correspondant respectivement aux sous-réseaux contenant les sites pairs et impairs. Dans cette représentation, J_2 est l'interaction effective entre les voisins les plus proches AFM le long de chacun des deux anneaux TF, et J_1 règle l'interaction entre les deux anneaux et est responsable de la frustration locale extensive.

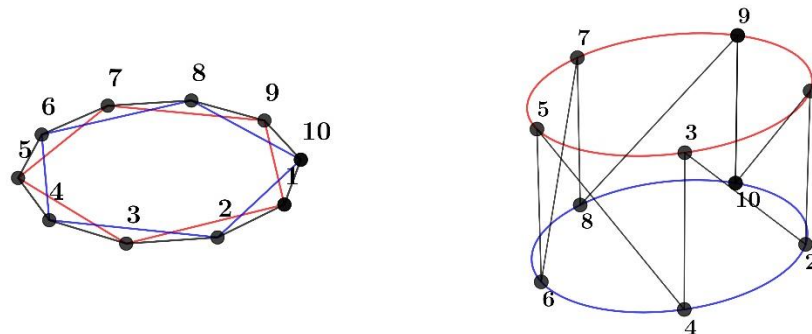


Figure 3: La chaîne ANNNI de longueur $L = 10$ vue comme deux chaînes d'Ising TF interagissantes de longueur $L/2$.

Les effets de la TF dans les deux sous-chaînes peuvent déjà être observés au point classique, résultant en une dégénérescence d'état fondamental super-extensive avec $L^2/2$ configurations dégénérées. En présence de fluctuations quantiques ($\hbar > 0$), les effets de la TF peuvent être observés en examinant l'entropie d'intrication bipartite (EE) du système, qui pour une bipartition en deux sous-systèmes A et B est calculée comme :

$$S_A = Tr[\rho_A \log \rho_A] \tag{8}$$

où ρ_A est la matrice de densité réduite de A obtenue en traçant les degrés de liberté de B à partir du projecteur sur l'état fondamental du système. En effet, il est connu que les états fondamentaux des Hamiltoniens TF en 1D violent une loi stricte de l'aire pour l'EE et possèdent un excès d'intrication dû

à l'excitation de quasi-particules induite par la TF [25]. Comme l'Hamiltonien ANNNI n'est pas intégrable, nous avons calculé l'EE en utilisant des algorithmes basés sur les réseaux de tenseurs, et les résultats montrent effectivement la présence d'un excès d'intrication dans l'antiphase du modèle ANNNI avec TF.

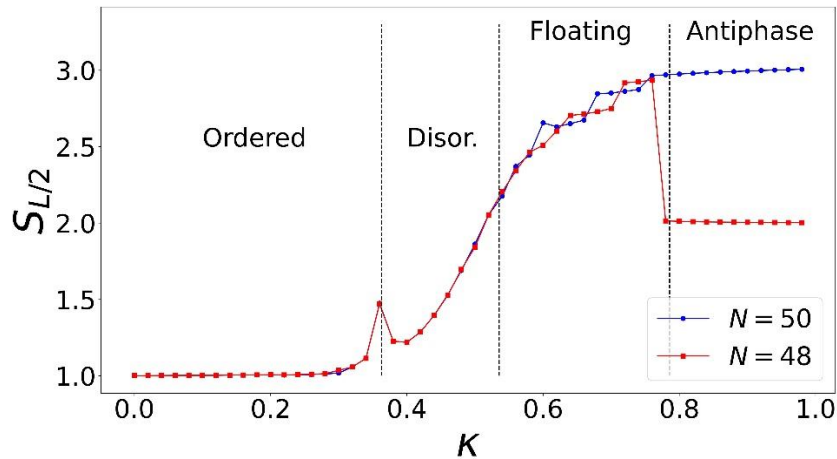


Figure 4: Entropie d'intrication bipartite pour la moitié de la chaîne en fonction de κ pour $h/J_1 = 0.3$, pour le modèle ANNNI avec frustration topologique (points bleus) et localement (carrés rouges).

Cependant, cet excès d'intrication ne correspond ni à la contribution d'une seule excitation de quasi-particule, ni à celle de deux quasi-particules indépendantes. Pour obtenir un aperçu analytique du comportement de l'EE, nous avons utilisé la théorie de perturbation dégénérée en \hbar proche de $\hbar = 0$ afin de calculer analytiquement la matrice de densité réduite du modèle. En particulier, nous avons trouvé que l'EE du modèle ANNNI avec TF peut être écrite comme

$$S(x) = \text{const} - z \log z - (1 - z) \log(1 - z) - y \log y - (1 - y) \log(1 - y), \quad (9)$$

où $z = x + \sin(x/\pi i)$, $y = x - \sin(x/\pi i)$ et $x = M/L$, avec M correspondant à la longueur de la sous-partition choisie du système. Cette structure de l'EE signale l'existence de deux excitations séparées dans les chaînes, qui affectent néanmoins l'une l'autre. Ainsi, même en présence d'une quantité extensive de frustration provenant d'interactions locales concurrentes, la TF permet toujours une description en quasi-particules de l'EE du système et l'effet de l'interaction, dans ce cas, est de moduler la probabilité de trouver la quasi-particule dans la sous-partition choisie. De manière intéressante, notre résultat ressemble à l'EE de deux fermions en interaction occupant les deux plus bas états propres de moment cinétique autorisés.

2.4) Batteries quantiques frustrées

Enfin, nous avons exploré la possibilité d'exploiter les propriétés spectrales et de corrélation des chaînes de spins avec TF afin de réaliser des dispositifs quantiques efficaces. En particulier, nous nous sommes concentrés sur les dispositifs de stockage d'énergie, notamment les batteries quantiques (QBs) [26], et avons conçu un protocole complet pour une QB basée sur une chaîne d'Ising TF [21] :

$$H_{Ising} = J \sum_{l=1}^L \sigma_l^x \sigma_{l+1}^x + h \sum_{l=1}^L \sigma_l^z. \quad (10)$$

Nous proposons un nouveau protocole pour stocker de l'énergie dans une chaîne de spins quantiques, basé sur un effondrement quantique global dans le champ magnétique externe (voir Figure 5) : après avoir initialisé le système dans l'état fondamental de H_{Ising} pour une valeur h_0 du champ magnétique externe, nous effondrons le champ magnétique à une nouvelle valeur h_1 et laissons le système évoluer unitairement sous le nouveau Hamiltonien ; après un certain temps τ , nous ramenons le champ magnétique à sa valeur initiale, fermant le cycle de chargement.

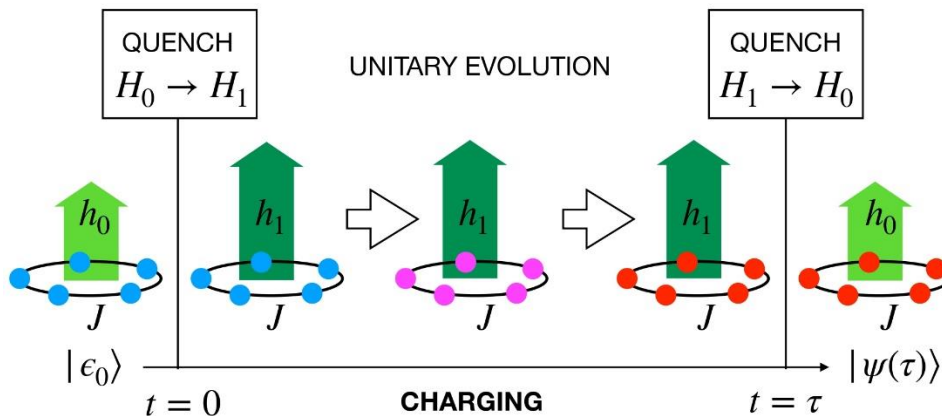


Figure 5

Grâce aux corrélations et aux caractéristiques spectrales induites par la frustration topologique, ces systèmes sont extrêmement robustes contre certains types de décohérences intrinsèques, qui sinon détérioreraient rapidement l'énergie stockée en eux. En termes quantitatifs, nous avons montré qu'une batterie TF conserve jusqu'à 90% de sa charge initiale après que la décohérence ait eu lieu, tandis que le niveau de charge d'une batterie similaire non frustrée tombe en dessous de 20% de la valeur initiale. De plus, nous avons également conçu un protocole de décharge pour transférer de l'énergie de la chaîne de spins quantiques chargée à un spin auxiliaire, montrant que seulement dans le cas d'un dispositif topologiquement frustré il est possible de transférer de l'énergie utile (sous forme d'ergotropie) et pas seulement de la chaleur. Nous soulignons également comment notre protocole complet, de la charge à la décharge, pourrait être réalisé en utilisant des anneaux d'atomes de Rydberg TF sur les plates-formes actuelles d'atomes froids.

2.5) Autres travaux

La thèse contient également deux travaux supplémentaires, qui ne sont pas directement liés à la frustration topologique.

Le premier travail contient une étude du saut d'excitons en loi de puissance dans des systèmes à deux niveaux en présence de déphasage pur [27]. En utilisant des techniques analytiques, nous avons dérivé une expression asymptotique pour le profil de transport, montrant l'existence d'un exposant critique du taux de saut en loi de puissance en dessous duquel le système présente une diffusion anormale, tout en étant diffusif avec une constante de diffusion accrue au-dessus de l'exposant critique. Ces résultats peuvent être utilisés pour expliquer, par exemple, pourquoi la longueur de diffusion mesurée expérimentalement dans les points quantiques de nanocristal est considérablement plus élevée que celle prédite par les modèles de diffusion standard à courte portée.

Le deuxième concerne une nouvelle approche de la simulation numérique de l'évolution temporelle de systèmes avec des interactions non locales et en cluster en utilisant la technique de décomposition de bloc d'évolution temporelle (TEBD). En particulier, nous fournissons une manière efficace et naturelle de construire des MPO compacts pour l'exponentielle des portes N-qubits non locales, qui peuvent ensuite être utilisées pour construire des opérateurs d'évolution temporelle trotterisés et évoluer dans le temps des MPS [28].

3) Conclusion générale

Notre exploration de la frustration topologique dans les systèmes de chaînes de spins a révélé des phénomènes intrigants et des applications potentielles dans la technologie quantique. Grâce à des investigations numériques et analytiques, nous avons découvert une phase chirale, caractérisée par des propriétés uniques de l'état fondamental. Remarquablement, la transition vers cette phase ne peut être détectée que par la magie quantique, ce qui indique son importance pour capturer les propriétés insaisissables des nouvelles phases quantiques et potentiellement ouvrir une nouvelle classe de transitions de phase quantique pour les systèmes hamiltoniens.

Notre étude a également inclus l'interaction de la frustration locale et topologique dans le modèle ANNNI, montrant comment même sans appliquer de conditions aux limites frustrées, la frustration topologique peut toujours être présente dans une chaîne de spins quantiques. La théorie de perturbation dégénérée a fourni une description en quasi-particules de l'entropie d'intrication dans ces systèmes, prouvant que les propriétés de la frustration topologique sont résilientes également en présence de différentes sources de frustration.

Des applications aux technologies quantiques ont également émergé de nos recherches, avec la conception de batteries quantiques basées sur des chaînes de spins topologiquement frustrées. Ces dispositifs présentent une robustesse remarquable à certains types de décohérences, conservant jusqu'à 90% de leur charge initiale, et permettent un transfert d'énergie efficace, les distinguant de leurs homologues non frustrés.

Bien que la frustration topologique ait été le principal sujet de recherche, comme cela arrive souvent, la curiosité nous a poussés à considérer également d'autres problèmes, tels que les propriétés de transport sous l'effet simultané d'interactions à longue portée et de dissipation locale, ou une mise en œuvre plus efficace de l'évolution unitaire dans l'approche TEBD appliquée à une représentation de réseau de tenseurs.

En conclusion, nos découvertes approfondissent non seulement notre compréhension de la frustration topologique dans les systèmes quantiques d'un point de vue fondamental, avec ses défis pour la classification standard des phases, mais elles montrent également le potentiel pour des technologies quantiques innovantes avec des mises en œuvre proches et des implications pratiques, nous positionnant à l'avant-garde de la recherche et des applications quantiques.

4) Références

- [1] L. D. Landau, *On the Theory of Phase Transitions*, Zh. Eksp. Teor. Fiz. 7: 19-32 (1937).
- [2] X.-G. Wen, Q. Niu, *Ground state degeneracy of the FQH states in presence of random potential and on high genus Riemann surfaces*, Phys. Rev. B. 41, 9377 (1990).
- [3] X.-G. Wen, *Topological Orders in Rigid States*, Int. J. Mod. Phys. B. 4, 239 (1990).
- [4] B. Zeng, X. Chen, D.-L. Zhou, X.-G. Wen, *Quantum Information Meets Quantum Matter: From Quantum Entanglement to Topological Phases of Many-Body Systems*, (Springer, 2019).
- [5] X.-G. Wen, *Quantum order: a quantum entanglement of many particles*, Physics Letters A 300, 175–181 (2002).
- [6] X.-G. Wen, *Colloquium: Zoo of quantum-topological phases of matter*, Rev. Mod. Phys. 89, 041004 (2017).
- [7] X.-G. Wen, *Choreographed entanglement dances: Topological states of quantum matter*, Science 363, eaal3099 (2019).
- [8] R. Movassagh, P. W. Shor, *Supercritical entanglement in local systems: counterexample to the area law for quantum matter*, Proc. Natl Acad. Sci. USA 113, 13278 (2016).
- [9] S. M. Giampaolo, G. Adesso, and F. Illuminati, *Probing Quantum Frustrated Systems via Factorization of the Ground State*, Physical Review Letters 104, 207202 (2010).
- [10] M. M. Wolf, F. Verstraete, J. I. Cirac, *Entanglement and Frustration in Ordered Systems*, Int. Journal of Quantum Information 1, 465 (2003).
- [11] S. M. Giampaolo, G. Gualdi, A. Monras, F. Illuminati, *Characterizing and quantifying frustration in quantum many-body systems*, Phys. Rev. Lett. 107, 260602 (2011).
- [12] G. Toulouse, *Theory of the frustration effect in spin glasses: I*, Commun. Phys. 2, 115 (1977).
- [13] J. Vannimenus, G. Toulouse, *Theory of the frustration effect. II. Ising spins on a square lattice*, J. Phys. C 10, L537 (1977).
- [14] J.-J. Dong, P. Li, Q. -H. Chen, *The A-Cycle Problem for Transverse Ising Ring*, J. Stat. Mech. P113102 (2016).
- [15] V. Marić, S. M. Giampaolo, F. Franchini, *Quantum phase transition induced by topological frustration*, Communications Physics 3, 220 (2020).

- [16] V. Marić, S. M. Giampaolo, F. Franchini, *The frustration of being odd: how boundary conditions can destroy local order*, New Journal of Physics, 22, 083024 (2020).
- [17] D. Sacco Shaikh, A. G. Catalano, F. Cavaliere, F. Franchini, M. Sassetti, N. Traverso Ziani, *Towards a phase diagram of the topologically frustrated XY chain*, arXiv:2312.06291 (2023).
- [18] V. Marić, S. M. Giampaolo, and Fabio Franchini, *Fate of local order in topologically frustrated spin chains*, Physical Review B 105, 064408 (2022).
- [19] A. G. Catalano, D. Brtan, F. Franchini and S. M. Giampaolo, *Simulating continuous symmetry models with discrete ones*, Phys. Rev. B, 106, 125145 (2022).
- [20] G. Torre, V. Marić, D. Kuić, F. Franchini, and S. M. Giampaolo, *Odd thermodynamic limit for the Loschmidt echo*, Physical Review B, 105, 184424 (2022).
- [21] A. G. Catalano, S. M. Giampaolo, O. Morsch, V. Giovannetti, F. Franchini, *Frustrating quantum batteries*, arXiv:2307.02529 (2023).
- [22] L. Leone, S. F. E. Oliviero, A. Hamma, *Stabilizer Rényi Entropy*, Phys. Rev. Lett. 128, 050402 (2022).
- [23] P. S. Tarabunga, E. Tirrito, M. C. Bañuls, M. Dalmonte, *Quantum Nonstabilizerness via matrix product states in the Pauli basis*, ArXiv:2401.16498 (2024).
- [24] S. Suzuki, J. Inoue, B. K. Chakrabarti, *Quantum Ising Phases and Transitions in Transverse Ising Models*, Lecture Notes in Physics 862, Springer (2013).
- [25] S. M. Giampaolo, F. B. Ramos, F. Franchini, *The Frustration of being Odd: Universal area law violation in local systems*, Journal of Physics Communication 3, 081001 (2019).
- [26] R. Alicki and M. Fannes, *Entanglement boost for extractable work from ensembles of quantum batteries*, Phys. Rev. E 87, 042123 (2013).
- [27] A. G. Catalano, F. Mattiotti, J. Dubail, D. Hagenmüller, T. Prosen, F. Franchini, G. Pupillo, *Anomalous diffusion in the Long-Range Haken-Strobl-Reineker model*, Phys. Rev. Lett. 131, 053401 (2023).
- [28] A. G. Catalano, *Numerically efficient unitary evolution for Hamiltonians beyond nearest-neighbors*, arXiv:2402.05198 (2024).

Contents

1	Introduction	1
1.1	Non-locality in quantum spin chains	1
1.2	Applications to quantum technologies	3
1.2.1	Quantum computing	4
1.2.2	Quantum simulators	4
1.2.3	Quantum teleportation	5
1.2.4	Quantum cryptography	5
1.2.5	Quantum sensors and metrology	5
1.2.6	Quantum thermal machines	6
1.3	Topological frustration	7
1.4	Organization of the thesis and main results	12
2	Simulating continuous symmetry models with discrete ones	17
2.1	Introduction	18
2.2	Anisotropic XYZ chain	21
2.3	Ground state fidelity	24
2.4	Characterization of the critical line	31
2.5	Conclusions	34
3	W-states, chiral phases and a <i>magic</i> phase transition	37
3.1	Introduction	37
3.2	Generalized W-states and the complexity of TF ground states	42

3.2.1	Non-stabilizerness of generalized W-states	42
3.2.2	Entanglement of TF ground states	44
3.2.3	Non-stabilizerness of TF ground states	46
3.3	The magic transition	48
3.4	Conclusion	48
4	Interplay between local and non-local frustration	51
4.1	Introduction	52
4.2	The Phase Diagram of the ANNNI Model	53
4.3	Analytical results close to the classical point	54
4.3.1	GSM degeneracy for $J_1 = 0$	55
4.3.2	GSM degeneracy for $J_1 > 0$	56
4.3.3	Ground state near the classical point	56
4.3.4	EE near the classical point	57
4.4	Numerical analysis	61
4.5	Conclusion	64
5	Frustrating quantum batteries	67
5.1	Introduction	67
5.2	The theoretical framework	70
5.2.1	The model	70
5.2.2	The charging protocol	71
5.2.3	The role of decoherence	72
5.3	The fast-charging regime	76
5.4	The slow-charging regime	81
5.5	Discharging the device	84
5.6	Conclusion and discussion of results	88
6	Exciton transport in two levels systems with long-range interaction	91
6.1	Introduction.	92

6.2	The single-exciton case	94
6.2.1	Strong dephasing: mapping to classical Markov process.	96
6.2.2	Anomalous diffusion of single exciton.	97
6.3	Many excitons: speedup of relaxation.	99
6.4	Conclusion	102
7	Numerically efficient unitary evolution for Hamiltonians beyond nearest-neighbors	103
7.1	Introduction	104
7.2	Standard TEBD and its problems for long-range systems	106
7.3	Compact MPOs for the exponential of Pauli strings	110
7.4	Some applications	111
7.4.1	Anisotropic XYZ ring	113
7.4.2	Ising chain with third neighbors interactions	114
7.4.3	A non-integrable cluster model	115
7.4.4	Other approximation schemes	116
7.5	Conclusions	117
8	Conclusion	119
A	Analytical results for the TF XY chain	123
A.1	Solution of the topologically frustrated XY chain	123
A.2	Global state fidelity and fidelity susceptibility	130
A.3	Majorana Correlation functions	132
B	Analytical results for the magic and entanglement of TF spin chains	135
B.1	Entanglement Entropies of TF ground states close to the classical point	135
B.2	Analytic derivations of Stabilizer Rényi entropy for generalized W states	137
C	Analytical results for the ground state of the ANNNI model	139
C.1	Perturbation theory close to the classical line	139

C.1.1	Determination of the ground state	139
C.1.2	Asymptotic expression of the bipartite Entanglement Entropy close to the classical line.	145
C.2	Numerical analysis	150
D	Analytical results on the Ising chain quantum battery	153
D.1	Projection coefficients after a global quench	153
D.2	Formal integration of Eq. (5.5)	155
D.3	The choice of the charging time	157
D.4	Analysis of the discharging protocol	158
E	Analytical results for long-range exciton transport in presence of dephas- ing	163
E.1	The single-particle problem	164
E.1.1	From the quantum master equation (QME) to the classical master equation (CME): alternative derivation	164
E.1.2	Moments of the distribution	166
E.1.3	The critical exponent	167
E.1.4	Analytical properties of $\mathcal{A}_{2\alpha,d}(\mathbf{q})$	168
E.1.5	Asymptotic properties of $\mathbf{n}_j(\mathbf{t})$: $d = 1$	171
E.1.6	Asymptotic properties of $\mathbf{n}_j(\mathbf{t})$: $d > 1$	173
E.1.7	Length scale for the crossover between the Gaussian and the power-law profiles	174
E.1.8	Diffusion-enhancement in the case of Förster energy transfer . . .	175
E.2	The many-particle problem	177
E.2.1	Derivation of the effective Liouvillian	177
E.2.2	Occupation probability for the 1D symmetric exclusion process with long-jumps	178
E.3	The quantum case: weak-dephasing regime	181

E.3.1	Small dephasing: perturbation theory	183
E.3.2	Exact diagonalization	184

Chapter 1

Introduction

1.1 Non-locality in quantum spin chains

Over the past century, the study of complex many-body systems has yielded groundbreaking results, profoundly transforming our understanding of collective phenomena in nature [8, 9]. Within this context, mathematical spin models held a special role in statistical mechanics, serving as quintessential frameworks for understanding phase transitions. Celebrated models including the Ising model [10, 11], Heisenberg model [12] and Potts model [13] have provided simplified yet powerful abstractions of magnetic materials and other systems where constituent particles exhibit discrete states. By capturing essential interactions among spins, these models facilitate the exploration of critical phenomena, such as spontaneous magnetization and the emergence of long-range order. Moreover, together with the advent of mathematical techniques such as the renormalization group [14–16], they allowed to explain how physical systems exhibit self-similarity and scale invariance near critical points, leading to the modern concept of universality. Following these admirable successes, it is thus not surprising that the field of quantum complex systems initially emerged as the natural extension of classical statistical physics. Accordingly, the first studies were focused on the analysis of quantities such as correlation functions and local order parameters that, in agreement with Landau's

theory [17], characterize the different phases of a physical system. However, quantum mechanics can feature several non-local aspects, which give rise to a much broader phenomenology than that of classical systems, and which is impossible to fully encompass purely within Landau's framework.

From one side, quantum mechanics is endowed with an inherent non-locality, a phenomenon wherein particles that are entangled remain interconnected, such that the state of one particle instantaneously affects the state of the other, irrespective of the distance between them. This concept was famously challenged by the Einstein-Podolsky-Rosen (EPR) paradox [18], which questioned the completeness of quantum mechanics. John Bell's theorem later provided a tangible way to test the non-local nature of quantum mechanics through Bell inequalities [19]. Experiments, including and following those conducted by Alain Aspect in the 1980s [20, 21], have consistently demonstrated violations of Bell inequalities, affirming that entangled particles exhibit correlations that cannot be explained by any local hidden variable theory. The intrinsic non-locality of quantum mechanics thus represents a fundamental departure from classical intuitions about the separability and independence of distant objects, highlighting the profoundly interconnected nature of the quantum world.

Non-local properties can also result from the presence of non-local interactions between the constituents of a physical system, i.e. interactions extending beyond nearest neighbors. Such systems provide a fertile ground for the investigation of exotic quantum phenomena [22], resulting from the interplay between quantum entanglement and non-local interactions [23]. For example, it has been observed that non-local interactions can induce a higher degree of quantum correlation spread over the chain, which is witnessed by an enhancement in the entanglement entropy. By itself, this is not surprising. It is indeed known that the entanglement entropy in critical spin chains, where the system undergoes a quantum phase transition, often develops logarithmic corrections in the size of the subsystem [24], reflecting the presence of long-range correlations. However, in systems with non-local interactions the enhancement of entanglement entropy

does not need to be associated with the emergence of long-range order. A notable example is the one of the Haldane-Shastry spin 1/2 chain [25, 26], in which the long-range spin interactions decay as the square of the inverse of the distance. The ground-state of this model, which is exactly solvable by Bethe ansatz, possesses the features of a spin liquid [27], characterized by a critical scaling of the entanglement entropy without possessing long-range magnetic order. Similar phases are observed also in other spin models like the J_1 - J_2 model, where J_1 and J_2 represent the interaction strengths between nearest and next-nearest neighbors. The competition between these interactions produces a variety of different phases, including spin-liquid states and valence bond solids [28, 29].

Another notable example of systems that escape the Landau's framework because of their non-local features is represented by topologically ordered phases, characterized by robust ground state degeneracies [30] and can be unveiled by topological invariants that remain unaffected by continuous deformations of the Hamiltonian parameters [31–33]. In these phases, the global structures of the ground states are connected to non-local correlations whose presence can be highlighted, once again, by the entanglement properties [34–39].

1.2 Applications to quantum technologies

In recent years, there has been a global surge of interest in harnessing quantum phenomena at the microscopic level, driven by the rapid advancement of new quantum technologies [40, 41]. In this context, it was soon realized that non-local interactions in quantum spin chains are not just a theoretical curiosity, but they have strong implications in several quantum technologies which are at the forefront of scientific and technological innovation, promising transformative advances in various fields.

1.2.1 Quantum computing

Quantum computers are computers that exploit quantum phenomena to perform complex computations. The computational units are represented by qubits, i.e. two-level quantum systems which can exist in multiple states simultaneously thanks to superposition and entanglement. Unlike classical bits that are strictly binary, qubits can therefore perform complex calculations with unprecedented algorithmic efficiency. Quantum algorithms, such as Shor's algorithm [42, 43] for factoring large numbers and Grover's algorithm [44] for searching unsorted databases, demonstrate exponential speed-ups over their classical counterparts. While superconducting qubits based on Josephson junctions are still the most diffused technology [45], in the past few years neutral atoms-based qubits are becoming a competitive alternative [46].

1.2.2 Quantum simulators

An alternative approach to algorithmic quantum computing is the possibility to simulate complex quantum systems starting from other systems that can be experimentally realized in laboratories. Accordingly, the expanding capabilities in controlling and manipulating atomic, molecular, and optical systems (AMO) has allowed to explore engineered spin chains with tunable non-local interactions for their use in quantum simulators. Diverse platforms such as Rydberg atoms, dipolar quantum gases, polar molecules, quantum gases within optical cavities, and trapped ions exhibit inherent two-body long-range interactions characterized by algebraic decay with distance [47–51]. These simulators can model complex quantum systems that are otherwise intractable with classical computers. By precisely controlling interactions in synthetic spin chains, researchers can simulate and study phenomena such as quantum magnetism [48–50, 52], topological phases [53], superfluid-Mott insulator transition [54], time crystals [55], and other exotic quantum phases of matter.

1.2.3 Quantum teleportation

Quantum teleportation exploits entanglement to transmit the state of a particle to another particle at a distant location without physically transferring the particle itself [56, 57]. The simplest protocol that one can think of involves three qubits, and can be schematized into three main steps. First, we need to entangle two particles, one belonging to the sender and one belonging to the receiver: this step creates the quantum channel for teleportation. Next, we need to perform a joint measurement on one of the two entangled particles (the sender's one) and the third qubit, which represents the quantum state to be teleported. Finally, the receiver can apply corresponding operation on the second entangled particle based on the measurement result and recreate the state of the third qubit. Quantum teleportation is fundamental for quantum networks and quantum computing, allowing the transfer of quantum information across quantum nodes. Recent experiments have achieved quantum teleportation over increasingly long distances, paving the way for robust quantum communication infrastructures [58–60].

1.2.4 Quantum cryptography

Quantum key distribution (QKD) is a method that uses the principles of quantum mechanics to secure communication. Due to wave-function collapse, any attempt at eavesdropping on the key distribution could be detected, thereby guaranteeing the security of the key exchange [61]. The most famous QKD protocol, BB84 [62], relies on the polarization states of photons to encode information.

1.2.5 Quantum sensors and metrology

Quantum sensors leverage entanglement and superposition to achieve unprecedented sensitivity and precision in measurements [63]. Applications include atomic clocks [64, 65], which are the most accurate timekeeping devices and rely on quantum superposition states, and magnetometers [66] that can detect minute changes in magnetic fields

using entangled particles. These sensors have wide-ranging applications in navigation, medical imaging, and fundamental physics research [67].

1.2.6 Quantum thermal machines

Another fundamental question that has been addressed is that of energy storage and transfer at the quantum level, keeping in mind possible adversary effects that can interfere. To answer this question, quantum thermal machines [68] have been proposed as devices that exploit quantum effects like superposition, entanglement, and coherence to extract and transfer energy between quantum systems. Typical examples are quantum thermal engines [69] and refrigerators [70], which are typically realized within the paradigm of the quantum Otto cycle [71–73]. Recently, it has also been shown that long-range interactions can improve the performances of these thermal machines, by reducing the non-adiabatic energy losses suppressing the detrimental effects of dynamically generated excitations [74].

In this work, we will pay special attention to the problem of quantum energy storage. Within this context, an intriguing area of exploration that has attracted a considerable attention recently is the study of "quantum batteries" [75–83] (QBs). Such devices utilize quantum effects to achieve more efficient and rapid charging processes compared to classical systems, by circumventing the need to physically move the energy carriers through driven diffusion. This burgeoning field of research encompasses numerous intriguing questions, ranging from the stabilization of stored energy [84, 85] to the investigation of optimal charging protocols [86–93]. One of the first practical implementations of this type of device is the quantum Dicke battery in Ref. [78], where the energy from a photonic cavity mode (acting as a charger) is transferred to a battery comprising N quantum units, each described by a two-level system. Such a model exhibits a collective speed-up [94] in the charging process. The Dicke battery has garnered significant interest due to its versatility in various implementation platforms (e.g., superconducting qubits [95], quantum dots [96, 97], coupled with a microwave resonator, Rydberg

atoms in a cavity [98], etc.), leading to the exploration of numerous variations of this model [99–108].

To have a practical application, QBs must however not only rapidly store energy but also be able to provide useful energy (i.e. work) once charged [80, 109–111]. A crucial aspect of the problem is to assess the stability of these models in realistic scenarios where they are subject to environmental noise. Preliminary studies in this direction have been obtained in Refs. [84, 112–125] where various schemes have been proposed to stabilize QBs in the presence of specific types of perturbations. In Refs. [86–89] a general theory of work extraction for noisy QB models composed by large collections of non-interacting subsystems (quantum cells) have been presented. The fundamental theoretical tool for this type of study is provided by the *ergotropy* [126, 127], a non-linear functional that gauges the maximum amount of energy that can be extracted from an assigned input state of a quantum system under reversible, i.e. unitary operations that do not alter the system entropy.

1.3 Topological frustration

The sources of non-local quantum effects presented in Section 1.1 represent only a few examples, even if the most widely known, of the different phenomenologies lying outside Landau’s theory that are continually unveiled. Another example, which lies at the basis of the results presented in the bulk of this thesis, is the so-called *topological frustration* (TF).

A classical many-body system is said to be frustrated when it is impossible to simultaneously minimize all the constraints imposed by its Hamiltonian. In magnetic systems, this means that the spins cannot be oriented in such a way that the interactions with the other spins are all simultaneously satisfied. Two main factors are responsible for the introduction of classical frustration in a system, namely its geometry or topology, and the competition between different kinds of interactions between its constituents.

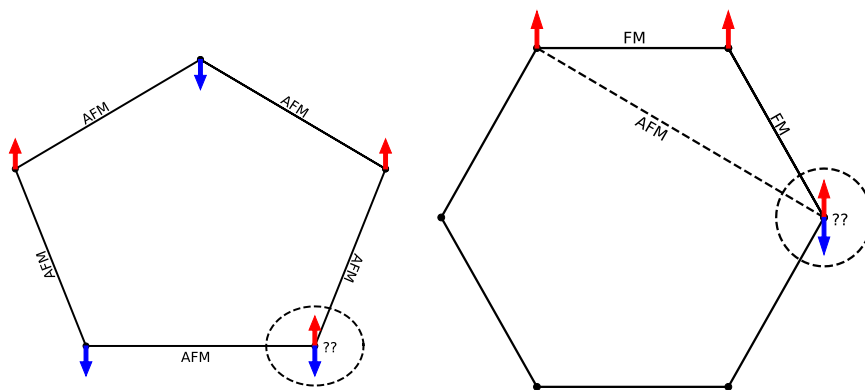


Figure 1.1: Two examples of classically frustrated systems. In one case, frustration is introduced by tuning the geometry or topology of the system (left) in an antiferromagnetic nearest-neighbor spin chain. In the second case (right) frustration is introduced by the competition between local ferromagnetic interactions and non-local antiferromagnetic ones.

The prototypical case in which frustration is introduced by the geometry of the system is that of nearest-neighbors antiferromagnets. Indeed, if we consider a ring geometry with an odd number of spins, it is easy to realize that it is impossible to find a configuration where all the antiferromagnetic (AFM) interactions between neighboring spins are satisfied (see Fig. 1.1). If instead of a ring we consider an open chain, then it is clear that all the interactions can be simultaneously satisfied.

In systems possessing also different non-local interactions, i.e. interactions going beyond nearest neighbors, frustration can instead arise from the competition of interactions at different ranges, see Fig. 1.1.

Among the most important effects introduced by frustration we must recall massive ground-state degeneracies, often associated with an excess entropy at zero temperature. However, frustration is also associated to the emergence of spin liquid phases in which, despite strong interactions between spins, the system does not exhibit conventional long-range magnetic order even at very low temperatures. Typical examples of such phenomenology can be found in spin models defined on the triangular [128, 129], Kagome [130] or pyrochlore lattices [131–133].

Another interesting concept related to frustration is that of "order by disorder" [134, 135].

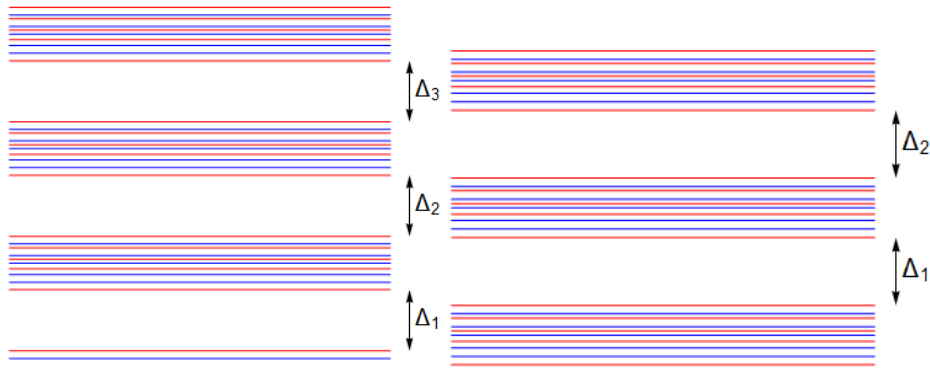


Figure 1.2: Structure of the energy spectrum for a non-frustrated (left) and a topologically frustrated (right) quantum Ising chain. In presence of TF the ground state of the system belongs to a pseudo-gapless band.

At zero temperature, the high ground state degeneracy induced by frustration often determines vanishing order parameters, even if some of the ground-states in the degenerate manifold might possess some ordered structure. In general, since all these ground-states are associated with different free energy fluctuations, the introduction of thermal fluctuations might select one of these particularly ordered states as the ground-state. This counterintuitive phenomenon contrasts with the typical expectation that fluctuations destroy order; instead, in frustrated systems, they can stabilize a more ordered state.

In quantum mechanics, the concept of frustration must be handled with care. Indeed, due to the non-commuting nature of quantum mechanics, with few exceptions as the frustration free models [136, 137] and systems at the factorization point [138–140], according to the classical definition almost every quantum system includes some amount of frustration [141–144]. But, in line with recent usage in the scientific community, this work restricts the concept of frustration to effects induced by competing interactions, lattice properties or boundary conditions, extending it directly from classical systems [145, 146].

The one introduced by boundary conditions is the case of TF, a form of weak frustration that was first introduced in the context of local AFM quantum spin chains by applying the so called frustrated boundary conditions (FBCs) [147], which are realized as a combination of periodic boundary conditions and odd number of spins. Since in the classical

limit these systems develop an extensive degeneracy of the ground state which is lifted as soon as quantum interactions are added [1, 148, 149], a gapless band structure replaces the gapped phase featured by the same systems in the same region of parameter space but with different boundary conditions. This produces several surprising and interesting consequences in the low-energy physics of these systems which, interestingly, can mostly be described within a single particle picture, corresponding to a delocalized excitation induced by TF in the ground-state of 1D spin chains. Below, we present the most important among these features.

- **Modification of the phase diagram and of order parameters:** as anticipated, TF models seem to defy the predictions of Landau's theory: while being introduced by a suitable choice of boundary conditions, TF can deeply modify the phase diagram of quantum spin chains even in their gapped phases, where a finite correlation length should prevent boundary conditions from affecting large distance behaviors. For example, it has been shown that if from one side TF can destroy order parameters [150], from the other it is also able to induce phase transitions to phases which are characterized by incommensurate antiferromagnetic order [151]. Moreover, in the context of exactly solvable 2-Cluster Ising models, it was shown that TF can destroy order parameters (replacing them with new string orders) on both sides of a phase transition, consequently changing its nature [152].
- **Strong dynamical response to local perturbations:** the fact that the ground-state of TF systems belongs to a gapless band with an extensive number of states has deep consequences in the dynamics of these systems. Indeed, because of this band structure, small perturbations can hybridize several low energy states, producing tangible effects on dynamical observables. This was shown studying the evolution of the Loschmidt echo (LE) after a local quantum quench in the external magnetic field in an Ising chain [153]. Comparing the oscillations of the Loschmidt echo for AFM rings with an even and odd number of particles, it was shown that while in the first case the fluctuations of the LE are very small, in the second case

(i.e. the TF frustrated one) the amplitude of the oscillations of the LE is much larger and increases with the system's size, signaling the hybridization of states within the gapless band. Interestingly, these results point towards the counterintuitive conclusion that, thanks to TF, it would be possible to distinguish a system with a number of Avogadro N_A of particles, and a system with $N_A + 1$ particles. While these results were shown in the contexts of the Ising chain, their validity can be easily extended to other TF models, since the result depends only on this peculiar spectral structure common to every TF Hamiltonian.

- **Enhanced quantum resources:** TF is associated with the rise of a peculiar phenomenology involving the increment in complexity of the ground state, as witnessed by quantum resources such as the entanglement entropy and the quantum non-stabilizerness [154, 155]. It was indeed shown that these quantum resources possess a non-zero contribution coming from the presence of a delocalized excitation in the ground-state of TF systems. More in general, the results obtained so far within this context point towards the validity of the following conjecture:

any quantum resource Q of a TF ground-state can be written as the sum of the quantum resource of the corresponding non-frustrated ground-state, and the value of the quantum resource associated to the topological excitation, i.e.

$$Q^{TF} = Q^{NF} + Q^e. \quad (1.1)$$

The value of the quantum resource associated with the topological excitation Q^e can typically be evaluated perturbatively close to the classical point of these models. This was done analytically in a TF transverse field Ising chain both for the bipartite entanglement entropy S [154], measured by the Von Neumann entropy, and for the quantum magic \mathcal{M} [155], measured by the stabilizer 2-Rényi entropy, yielding (we will return to these quantities and their precise definitions later on in

this thesis)

$$S^e(x) = -x \log x - (1 - x) \log(1 - x), \quad (1.2)$$

and

$$\mathcal{M}^e = 3 \log_2(L) - \log_2(7L - 6), \quad (1.3)$$

where L is the length of the chain and $x = M/L$ is the relative length of the subpartition chosen to compute the entanglement entropy. Notably, S^e corresponds to the entanglement entropy associated to the presence of a fermionic quasi-particle on top of a vacuum state, with x representing the probability of finding the quasi-particle inside the chosen subpartition. The presence of this extra term in the entanglement entropy represents a violation of a strict area law, since a finite, non-diverging dependence on the subpartition length is acquired by S . In the case of the quantum magic, the effects of TF manifest instead as a logarithmic correction to the typically linear scaling of \mathcal{M} in non-frustrated systems.

- **Long-range entanglement and topological order:** in [156] the presence of long-range entanglement in the ground-state of TF spin chains was shown by studying the disconnected entanglement entropy, a quantity that was originally introduced to detect (symmetry-protected) topological phases [157, 158]. In this way, in addition to showing that this quantity is able to respond beyond its original scope and reveal also the presence of the long-range entanglement generated by a single, delocalized and fractionalized topological excitation, it suggests that TF phases possess topological features despite not being a typical topological order or symmetry-protected one.

1.4 Organization of the thesis and main results

This thesis presents the work the author has done during his PhD with his collaborators, mainly (but not limited to) from the Ruđer Bošković Institute in Zagreb and University of

Strasbourg. The thesis is based on the publications, and papers still under evaluation, related to this work. One chapter of the thesis is devoted to each paper. While this introductory chapter has presented a general motivation for studying topological frustration and, more in general, non-local effects in quantum spin chains, each chapter will have separated introductions and conclusions. We end the main part of the thesis by a general conclusion. After the conclusion there are different appendices, referenced in different chapters, that give the details of the calculations done in the thesis. The main results, chapter by chapter, are the following.

- In Chapter 2 we study the TF fully anisotropic Heisenberg chain, aka the XYZ chain. We provide numerical evidence for the existence of a chiral region in the phase diagram, in which the ground-state of the systems is doubly degenerate. This degeneracy is realized by two states with opposite, intensive momentum. To provide an analytical analysis of this phase transition we restrict ourselves to an XY chain, which is integrable. We demonstrated that, despite the Hamiltonian of the system is characterized by a discrete \mathbb{Z}_2 symmetry, in the chiral region the TF displays several features that would typically be associated with the presence of continuous symmetries in the Hamiltonian. Finally, we show that quantities like the free energy derivatives, local correlators and the ground-state fidelity are not able to characterize the phase transition to the chiral region. This chapter is based on [1].
- In Chapter 3 we study the connection between the ground-state of TF spin chains to the so called W states, which held relevance in the field of quantum information and complexity. Exploiting this connection we show that, while also the entanglement entropy fails in detecting the chiral phase transition introduced in the previous chapter, the non-stabilizerness or quantum magic can capture it, showing a finite discontinuity in the thermodynamic limit. This represent the first instance of a magic transition in Hamiltonian systems. This chapter is based on [7].

- In Chapter 4 we explore the interplay between local and non-local frustration in the anisotropic next to nearest neighbor Ising (ANNNI) chain. After showing that TF can be introduced in this model even without applying FBCs, we use a combination of numerical and analytical techniques to study the entanglement entropy of the ground-state. Thanks to this analysis, we are able to extend the quasi-particle picture introduced in nearest neighbors spin chains to more complex systems with different sources of frustration, where the existence of such a picture was not expected. This chapter is based on [6].
- In Chapter 5 we propose the design of a complete protocol for the realization of a quantum energy storage device, namely a quantum battery, based on a TF Ising chain. We show that the spectral properties and the inherently non-local correlations introduced by TF can enhance the storage efficiency of the battery making it resilient to some type of intrinsic decoherence, and allow for efficient work transfer to an ancillary qubit. This chapter is based on [3].
- In Chapter 6 we depart from the context of TF and study exciton transport in a quantum spin chain with long-range interactions, characterized by a power-law decay with the distance between particles $r^{-\alpha}$, in presence of pure dephasing. We show the existence of a critical value of the hopping range α_{cr} below which the transport is purely long-range and non-diffusive. For $\alpha > \alpha_{cr}$ we observe diffusive transport with enhanced diffusion constant. Our findings are relevant to long-range exciton diffusion in light-harvesting systems such as nanocrystal quantum dots, where discrepancies between experimental observations and theory have been reported. This chapter is based on [2].
- In Chapter 7 we discuss an new approach for the construction of matrix product operators (MPOs) for the exponential of Pauli strings. This can be used for the simulation of the time evolution of spin chains with non-local interactions, periodic boundary conditions or more complex cluster interactions using the time evolution

block decimation algorithm (TEBD). This chapter is based on [5].

Chapter 2

Simulating continuous symmetry models with discrete ones

Especially in one dimension, models with discrete and continuous symmetries display different physical properties, starting from the existence of long-range order. In this chapter we will show that, by adding topological frustration, an antiferromagnetic XYZ spin chain, characterized by a discrete global symmetry, develops a region in parameter space which mimics the features of models with continuous symmetries. For instance, frustration closes the mass gap and we describe a continuous crossover between ground states with different quantum numbers, a finite (Fermi) momentum for low energy states, and the disappearance of the finite order parameter. Moreover, we observe non-trivial ground state degeneracies, non-vanishing chirality and a singular foliation of the ground state fidelity. Across the boundary between this chiral region and the rest of the phase diagram any discontinuity in the energy derivatives vanishes in the thermodynamic limit.

2.1 Introduction

Assuming invariance under spatial translation and limiting to systems with finite range interactions, in agreement with Goldstone's theorem [159, 160], one-dimensional spin-1/2 systems they are usually classified into two large families. The first includes models in which Hamiltonians show global continuous symmetries. In these cases, the systems admit sets of quantum numbers, i.e. sets of distinct eigenvalues of operators commuting with the Hamiltonian, whose size scales with the chain length. In these models, properly ordered phases are absent [161] even at zero temperature, due to quantum fluctuations. Another remarkable property of these system is that, at criticality (that is, when the mass gap vanishes) a parameter change can trigger continuous cross-overs between non-degenerate ground states with different quantum numbers. To fix the ideas let us consider the example of the XXZ spin-1/2 chain. Such a model holds a continuous $U(1)$ rotational symmetry along the z -axis and, due to such symmetry, the eigenstates of the Hamiltonian can be classified by their total magnetization in the z direction. In a region of small interaction along z (in modulus) without local fields, the ground state has a vanishing total magnetization, and the energy spectrum is gapless in the thermodynamic limit [162]. Turning on a magnetic field along z induces a finite magnetization in the ground state preserving the criticality of the system up to a critical value. Moreover, together with the nonvanishing magnetization, the ground state also acquires a non-zero momentum, although not a macroscopic one. Usually, the ground state is static, in order to minimize the kinetic energy, but here we show that, in presence of topological frustration, the lowest energy state of a system can be just stationary. Moreover, since low energy excitations are also characterized by momenta close to that of the ground state, this constitutes a *Fermi momentum*. Note that, contrary to what happens in higher-dimensions, 1D models with continuous symmetry possess a Fermi momentum independently from the statistics of the microscopical degrees of freedom [27]. Thus, by changing the external field, the system undergoes a series of

ground state cross-overs between non-degenerate states with different values of the total magnetization, i.e. different quantum numbers, that are clearly mutually orthogonal. Hence, in the thermodynamic limit, systems like the XXZ chain in this regime show an extreme case of orthogonality catastrophe [163, 164]: ground states of arbitrarily similar Hamiltonian are not only orthogonal in the thermodynamic limit, but at any finite size any change in the Hamiltonian parameters continuously moves between states with zero overlap [165].

On the opposite side, the second family of one-dimensional models is made by systems whose Hamiltonians display only discrete global symmetries, so that its eigenstates are characterized just by finite sets of quantum numbers. The physical properties of this second family are different from those above. In their gapless regimes, that is when the mass gap closes algebraically with the system size, one cannot define a Fermi momentum for low energy excitations, and in the gapped case, these systems can develop a finite order parameter as a reflection of a spontaneously broken (discrete) symmetry. In fact, few nearly degenerate low-energy states, possessing different quantum numbers, are separated by a finite energy gap from the rest of the spectrum. The gap between these states closes exponentially with the system size [27, 162] and in the thermodynamic limit the system can select a superposition of them as a ground state that violates a Hamiltonian's symmetry. Such state is thus characterized by a non-zero order parameter, i.e. a non-vanishing expectation value for an operator that should otherwise vanish due to symmetry.

In this chapter, we will show that it is possible to simulate the physics of models with continuous symmetries using models whose Hamiltonians possess only discrete symmetries. The key ingredient will be the introduction of a frustration [141–143, 146, 166–168] of topological origin in the latter models. As mentioned in Chapter 1, topological frustration can be induced in a system with short-range antiferromagnetic interactions through a special set of boundary conditions, the so-called frustrated boundary conditions (FBC) [147, 150, 151, 154, 169, 170], which are realized assuming periodic

boundary conditions in a system made of an odd number of spins. In this setting, as described in detail in the rest of this work, the ground-state is described by an excitation delocalized along the whole chain. As a consequence, the length of the chain becomes a relevant scale for the system and, despite being just boundary conditions, FBCs can actually affect the thermodynamic limit and thus the physics of the system.

We will show that moving in a region of phase space, these systems undergo repeated crossovers between exactly orthogonal states. Since the discrete global symmetries of these models separate states only into finite sets (of quantum numbers), frustration further uses the representation of spatial translation to differentiate between the different ground states. Namely, depending on the Hamiltonian parameters, the ground states acquire finite momenta. As discussed in a series of recent works, unless higher symmetries are considered which constrain the ground state momenta to specific values, FBC prevent the formation of a finite order parameter in the thermodynamic limit [149–151], again mimicking the behavior of continuous symmetry systems.

We will illustrate this phenomenology in the framework of the topologically frustrated short-range anisotropic XYZ chain, a prototypical model featuring a \mathbb{Z}_2 symmetry, realized by the parity of the magnetization. With the help of both numerical diagonalization and analytical evaluations, we will prove that it presents a region of parameter space, which we name *chiral region*, in which even at finite sizes several two-fold degenerate manifolds play, alternatively, the role of ground states. Such manifolds, whose elements belong to the same parity, are completely identified by two eigenstates with opposite quantum numbers for the momentum operator. Increasing the size of the system, the number of possible eigenvalues of the momentum grows, hence increasing also the number of crossovers in the chiral region. Thereby, in the thermodynamic limit, this system will show a behavior mimicking the critical phase of models with global continuous symmetry. Moreover, these ground state momenta act as Fermi points, and low energy excitations lie close to them. The chiral region is separated from the rest of the parameter space by a line at which the degeneracy of the ground state changes. However,

none of the derivatives of the energy show non-analytic behavior. On the other hand, consistently with the fact that this transition is induced by the particular choice of boundary conditions, all the parameters we have analyzed in the attempt to classify the chiral region vanish algebraically with the chain length. The latter two properties support the idea that we are looking at a boundary-BKT-like phase transition, but we are not aware of such occurrence in the literature, in any model.

To highlight this peculiar picture, in the beginning, we will focus on different observables, such as chirality and the ground-state momentum. Such observables are known, in some cases, to be different from zero in systems with continuous symmetry such as the Heisenberg chain [171–173], but have never previously been observed in systems with discrete symmetries. Moreover, to have a more direct characterization of the ground states in this region, we focus our attention on the ground-state fidelity. This is a quantity directly borrowed from quantum information theory and it allows to appreciate how a system reacts to a small change of the Hamiltonian parameters [174–180].

2.2 Anisotropic XYZ chain

Let us start by introducing the model that we use in this chapter as an example of the phenomenology we are presenting. The model is a very general short-range anisotropic Heisenberg chain with a local field that, without losing generality, we assume to align with the z axis. To induce topological frustration, we consider only the cases made of an odd number of sites with periodic boundary conditions in which the dominant interaction is antiferromagnetic. The Hamiltonian of such a system reads

$$H = \sum_{j=1}^N \sum_{\alpha=x,y,z} J_{\alpha} \sigma_j^{\alpha} \sigma_{j+1}^{\alpha} - h \sum_{j=1}^N \sigma_j^z, \quad (2.1)$$

where σ_j^{α} , for $\alpha = x, y, z$, are Pauli matrices and periodic boundary conditions require $\sigma_j^{\alpha} = \sigma_{j+N}^{\alpha}$. Moreover, we assume that $J_x \neq J_y$ to avoid that, the system acquires a con-

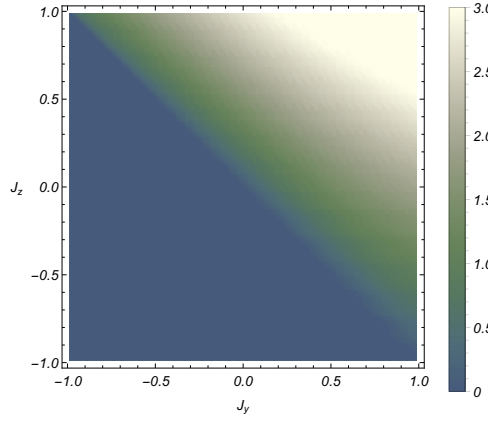


Figure 2.1: Dependence of the threshold value h^* as a function of $J_y \in (-1, 1)$ and $J_z \in (-1, 1)$ for $N = 15$ and $J_x = 1$. For $|h| < h^*$ (the *chiral region*) the ground state manifold is at least two-fold degenerate and spanned by states with finite and opposite momentum.

tinuous rotational symmetry around the z axis, like the XXZ chains shortly described in the introduction. As a consequence, the system holds only the discrete parity symmetry along z ($\Pi^z = \prod_{i=1}^N \sigma_i^z$, $[\Pi^z, H] = 0$) that, independently of the system size, admits only two quantum numbers (± 1). Despite its apparent simplicity, the model in (2.1) does not admit any analytical solution. Therefore, all our analyses are based on a numerical approach based on the Lanczos algorithm [181, 182] for the exact diagonalization of the Hamiltonian. Keeping $J_x = 1$ and assuming $J_x > |J_y|, |J_z|$, we obtain that, for several odd N , in the region $J_z > -J_y$ there is a threshold value of the local field $h^* > 0$, which delimits the chiral region, such that for each $h \in (-h^*, h^*)$ the ground-state manifold is at least two-fold degenerate (see Fig. 2.1). Such a manifold can be completely described in terms of the eigenstates of the momentum operator P that is the generator of the translation operator T , i.e. $T = e^{iP}$, whose action shifts all the spins by one site in the lattice. For a one-dimensional system with periodic boundary condition, the operator T can be written in terms of the Pauli ones as [162, 183]

$$T = \bigotimes_{i=1}^{N-1} \frac{1}{2} \left(\mathbb{I} + \sum_{\alpha=x,y,z} \sigma_i^\alpha \sigma_{i+1}^\alpha \right), \quad (2.2)$$

From the numerical analysis, we have that the ground state manifold admits a basis made by the two eigenstates of the momentum $|\pm p\rangle$ with opposite quantum number

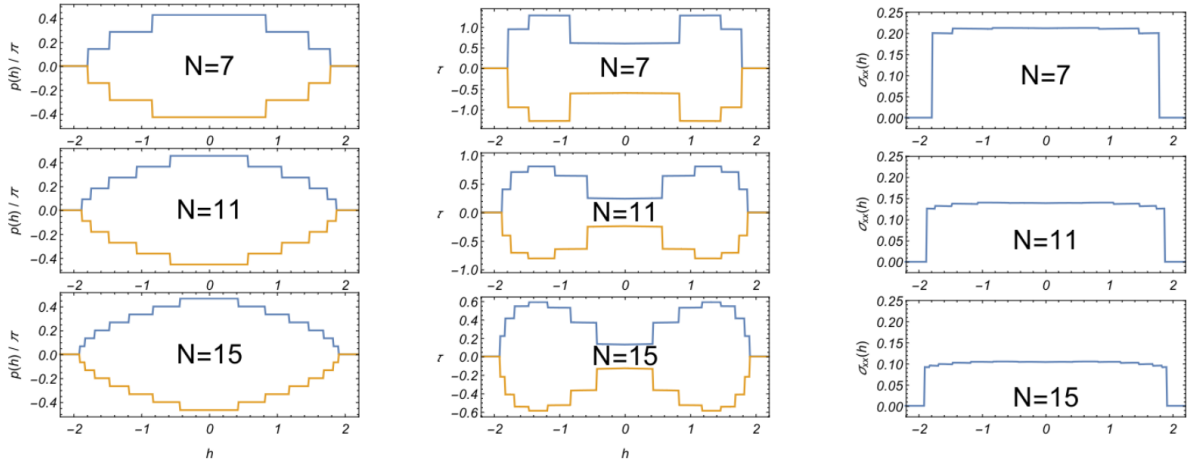


Figure 2.2: Ground-state momenta $p(h)$ (left), chirality τ (center) and variance $\sigma_{xx}(h)$ of expectation values of $\sigma_i^x \sigma_{i+1}^x$ (right) as a function of the local field amplitude h for different sizes of the chain at fixed values of the anisotropies $J_x = 1.0$, $J_y = 0.6$ and $J_z = 0.2$. The momenta are expressed in units of π and are compactified between $-\pi/2$ and $\pi/2$. Except in the cases of a zero ground state momentum, the ground state manifold is always twofold degenerate with the two ground states carrying opposite momenta. Moving in phase space, the ground state vectors acquire all momenta allowed by the quantization rule. A finite chirality reflects the finite momentum carried by the ground state vector, indicating that, in its lowest energy state, the system moves in a stationary way. Note that, while the values of the momenta and of the chirality are evaluated for ground-states which are also momentum eigenstates, the variance of the correlation functions is measured using the ground state vector $\frac{1}{\sqrt{2}}(|p\rangle + |-p\rangle)$.

$\pm p(h)$, as it can be seen in Fig. 2.2. Moreover, the momentum $p(h)$ acts as a Fermi point, in a system whose discrete symmetry should not allow for its existence, as low energy excitations lie nearby. Moving h throughout the region $(-h^*, h^*)$, the system visits all possible values of the momentum quantum number. Since states with different quantum numbers are exactly orthogonal to each other and the size of the set of the momentum quantum numbers scales with the chain length, the number of different crossovers occurring in the region $(-h^*, h^*)$ increases with N .

The presence of degeneracy in the ground state manifold of systems with only global discrete symmetries is not rare and it is at the basis of the mechanism of the symmetry violation. However, in the present case, we have two relevant peculiarities. First, the exact degeneracy is present even for finite sizes, while it usually appears only in the thermodynamic limit. Second, the degeneracy involves states of the same parity, hence not allowing the system to violate the parity symmetry, as it happens in the ordered

phase of unfrustrated systems. On the contrary, such degeneracy stems from the mirror symmetry (that is, a reflection with respect to any site), which implies that each eigenstate has to be at least two-fold degenerate, with the only exception of zero momentum states [151, 184].

This structure of the ground-state manifold has some interesting implications. Since in the chiral region $(-h^*, h^*)$ the ground-states typically have a non-vanishing momentum, they are expected to be characterized by a non-zero expectation value of the chiral operator $\hat{\tau} \equiv \vec{\sigma}_{i-1} \cdot \vec{\sigma}_i \times \vec{\sigma}_{i+1}$ [171, 185]. In Fig. 2.2 we plot the behavior of the site independent expectation value $\tau \equiv \langle \pm p | \hat{\tau} | \pm p \rangle$. On the other side, a ground state that is a linear superposition of $|\pm p\rangle$, violates the invariance under the spatial translation of the Hamiltonian. This fact is not expected, at the ground-state level, in models possessing only discrete symmetries, and can be highlighted by analyzing the variance of the spatial distribution of the two-body next-neighbor spin correlation function along x , i.e. the expectation values of $\sigma_i^x \sigma_{i+1}^x$, on the state $\frac{1}{\sqrt{2}}(|p\rangle + |-p\rangle)$. Fixing $J_x = 1$, $J_y = 0.6$ and $J_z = 0.2$ the variances as a function of the local field obtained with the exact diagonalization approach are depicted in Fig. 2.2.

All these behaviors have already been previously observed in systems with continuous global symmetries, such as the Isotropic Heisenberg model [171–173], but they turn out to be completely new for systems with only global discrete symmetries.

2.3 Ground state fidelity

The analysis of the different quantities we have shown so far provides indirect information on the behavior of the ground state. To access more directly the crossovers between the ground states of the topologically frustrated XYZ chain, in this section, we will analyze a quantity derived from the quantum information theory, namely the ground state fidelity, which will give us a clearer picture of how the system responds to small changes in its parameters.

For a parameters-dependent Hamiltonian $H(\vec{\lambda})$, the ground-state fidelity is defined as the square modulus of the overlap between two ground-states associated with slightly different sets of parameters, i.e.

$$\mathcal{F}(\vec{\lambda}) = \left| \langle G(\vec{\lambda}) | G(\vec{\lambda} + d\vec{\lambda}) \rangle \right|. \quad (2.3)$$

The ground state fidelity has already been widely used to analyze in detail the properties of the ground state of different one-dimensional systems [174–180]. Since, in the thermodynamic limit, two neighboring ground state are always orthogonal, as a consequence of what is commonly referred to as the Anderson’s Orthogonality Catastrophe [163, 164], the most interesting quantity to consider is the finite size rate of change, the so called *Fidelity Susceptibility*. In systems with only discrete global symmetries, this quantity is continuous and diverges only approaching a quantum phase transition. It has thus been argued that it is a good quantity to use to detect criticality. On the contrary, in systems with continuous symmetry, certain change in the system parameters trigger crossovers between states with different quantum numbers and the ground state fidelity presents as many points of discontinuity as the number of sites in the chain. For the XXZ chain discussed above, these discontinuities are induced by changes in the external magnetic field and it represent an extreme case of orthogonality catastrophe because two neighboring ground states are exactly orthogonal even for small system sizes because they carry different quantum numbers. In our case, the ground state fidelity behaves exactly like this: moving in almost every direction in the parameter space, the system changes the ground-state momentum, making the fidelity drop to zero. But there exists a particular direction along which the momentum stays constant and the fidelity shows a more regular behavior.

To study how these properties scale with the system size, we need to consider much longer chains than those treatable within an exact diagonalization approach. Even advanced numerical methods, such as existing DMRG routines, are not easily applicable

to models showing topological frustration: from one side, some problems are created by the implementation of the periodic boundary conditions imposed by the FBCs; from the other, especially in the region of interest of the present work, issues arise due to the simultaneous presence of both a degeneracy between ground-states in the same parity sector and the closing of the energy gap between the ground-states and the immediately overlying excited states. Therefore, to push our study towards larger sizes we now focus on the case $J_z = 0$ which can be mapped into a free-fermionic model, thus disclosing the possibility for an analytical solution. Introducing the anisotropic parameter γ and defining $J_x = \frac{1+\gamma}{2}$ and $J_y = \frac{1-\gamma}{2}$, the Hamiltonian of the model in (2.1) reduces to the one of the XY chain in a transverse field

$$H = \sum_{j=1}^N \left[\frac{1+\gamma}{2} \sigma_j^x \sigma_{j+1}^x + \frac{1-\gamma}{2} \sigma_j^y \sigma_{j+1}^y - h \sigma_j^z \right]. \quad (2.4)$$

This is a prototypical exactly solvable model which, through a series of exact, although non-local, transformations can be brought into a free fermionic form. Its method of solution is known since the famous 1961 paper by Lieb, Schultz, and Mattis [186] and since then many interesting observables have been calculated for it, including the fundamental correlation functions [187], establishing it as a corner stone in many-body, strongly correlated quantum systems. However, virtually all these works have been interested in bulk properties deemed independent from the boundary conditions and have thus been quite cavalier in this respect (notice that, without a proper account of boundary conditions it is not possible even to establish the asymptotic ground state degeneracy of this model in its ordered phase [162, 188]). As a matter of fact, as it has been only recently appreciated, FBC induce several subtle differences in the solution of the XY chain which yield surprising outcomes [147, 150, 151, 154], such as those that we discuss in this work. The exact analytical solution of this model is presented in Appendix A, while here we focus on the physical results. In complete agreement with the previous numerical results, we find that it exists a chiral region, defined for $|h| < h^* = 1 - \gamma^2$, were

the ground-state possesses a non-zero momentum \tilde{q} which depends on the driving parameters as

$$\tilde{q} = \arccos\left(\frac{h}{\gamma^2 - 1}\right). \quad (2.5)$$

In this situation, we have two different possibilities for ground-state fidelity: the states $|G(\vec{\lambda})\rangle$ and $|G(\vec{\lambda} + d\vec{\lambda})\rangle$ can either be exactly orthogonal, or not. The first happens either because they live in different parity sectors and hence are characterized by a different number of fermions, or because the fermions occupy different fermionic modes.

Instead, if we move the parameter along one of the parabolas $h = c(1 - \gamma^2)$, the two ground states have the same parity and their fidelity can be written as (see Appendix A.2 for details)

$$\mathcal{F} = \prod_{q \in \Gamma_2^+ / \{\tilde{q}^+\}} \cos(\tilde{\theta}_q - \theta_q), \quad (2.6)$$

for the even parity and

$$\mathcal{F} = \prod_{q \in \Gamma_2^- / \{\tilde{q}^-\}} \cos(\tilde{\theta}_q - \theta_q), \quad (2.7)$$

for the odd one. These expressions are very similar to the ones characterizing the ground-state fidelity of both the unfrustrated systems and the region with $|h| > h^*$.

Along these parabolas it is also possible to evaluate the fidelity susceptibility χ that, by definition, is equal to the leading order of the expansion of the ground-state fidelity in the parameter change:

$$\mathcal{F} \approx 1 - \frac{1}{2}\chi d\gamma^2, \quad (2.8)$$

Such quantity has been widely studied in the context of the unfrustrated XY chain [175, 176], proving to be able to correctly predict the phase transition at $h = \pm 1$ and $\gamma = 0$ [179]. In agreement with the Anderson orthogonality catastrophe [163, 164], the fidelity susceptibility always tends to diverge in the thermodynamic limit. However, while at a regular point, this divergence is only extensive, it becomes super-extensive close to a quantum phase transition [176]. Therefore, to study the behavior of the fidelity susceptibility in the thermodynamic limit let us introduce the re-normalized fidelity susceptibility

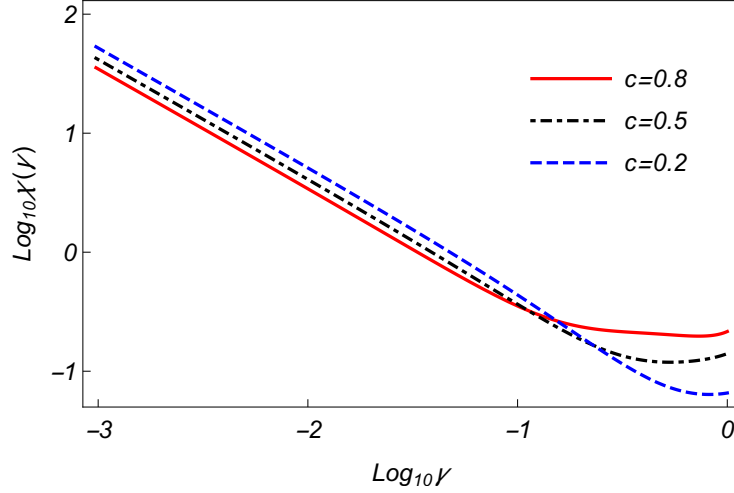


Figure 2.3: Thermodynamic limit of the global state fidelity susceptibility $\tilde{\chi}$ along manifolds of constant momentum \tilde{q} obtained moving along the parabola $h = c(1 - \gamma^2)$ as a function of γ . Going towards $\gamma = 0$ the fidelity susceptibility diverges signaling the presence of the quantum phase transition between the anisotropic XY chain and the isotropic XX one.

$\tilde{\chi}$ obtained by dividing χ by the system volume. After a long but straightforward evaluation it is possible to prove (see Appendix for details) that, independently from the parity sector, the normalized fidelity susceptibility is

$$\tilde{\chi} = \frac{1}{16} \frac{1 + c^2(1 + \gamma)^3(3\gamma - 1)}{\gamma(1 + \gamma)^2(1 - c^2(1 - \gamma^2)^2)}. \quad (2.9)$$

One can check, and Fig. 2.3 confirms, that the re-normalized fidelity susceptibility diverges at $\gamma \rightarrow 0$, hence signaling the presence of the critical phase of the quantum XX chain, i.e. the continuous symmetry model emerging by setting $\gamma = 0$.

However, as noted above, if we do not assume that $\vec{\lambda}$ and $\vec{\lambda} + d\vec{\lambda}$ are on the same parabola, the ground state fidelity vanishes identically as it occurs within the gapless phases of systems with continuous symmetries. In the latter case, to avoid the problem associated with the scaling analysis of such a ground-state fidelity, it is normal to resort to the reduced fidelity [165, 178, 189, 190]. The reduced fidelity can be seen as a generalization of the ground state fidelity, and it represents the overlap between the reduced density matrices for a fixed subsystem, obtained from the ground states corresponding

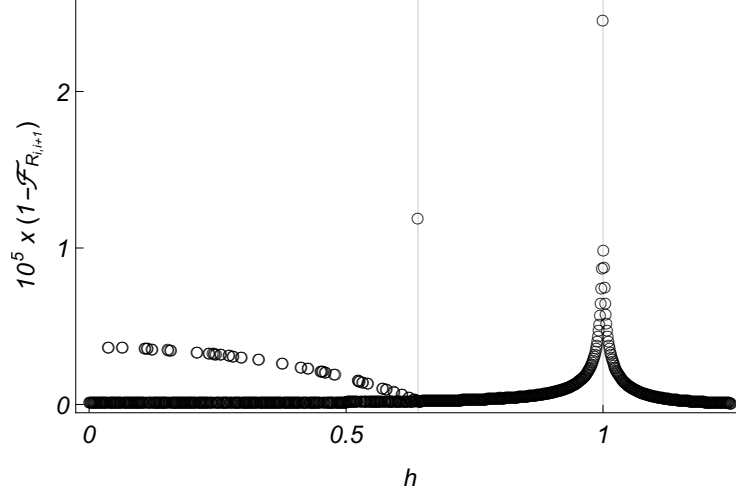


Figure 2.4: Reduced fidelity obtained projecting a ground state eigenstate of the momentum operators into the Hilbert space defined by two nearest neighbor spins. The data are obtained considering an XY spin chain made of 1001 spins, fixing $\gamma = 0.6$ and moving h from 0 to 1.25. For $h < h^*$ the lower points refer to movement along a parabola $h = c(1 - \gamma^2)$, while the higher values represent a generic flow in which neighboring ground states are characterized by different occupied modes.

to different parameters, i.e.

$$\mathcal{F}_{R_A} = \text{Tr} \sqrt{\rho_A(\vec{\lambda})^{1/2} \rho_A(\vec{\lambda} + \vec{d}\vec{\lambda}) \rho_A(\vec{\lambda})^{1/2}}. \quad (2.10)$$

Here $\rho_A(\vec{\lambda})$ ($\rho_A(\vec{\lambda} + \vec{d}\vec{\lambda})$) denotes the reduced density matrix of the ground state $|G(\vec{\lambda})\rangle$ ($|G(\vec{\lambda} + \vec{d}\vec{\lambda})\rangle$), obtained by tracing out all the degrees of freedom associated to sites outside the chosen subset A : $\rho_A(\vec{\lambda}) \equiv \text{tr}_B |G(\vec{\lambda})\rangle \langle G(\vec{\lambda})|$ ($\rho_A(\vec{\lambda} + \vec{d}\vec{\lambda}) \equiv \text{tr}_B |G(\vec{\lambda} + \vec{d}\vec{\lambda})\rangle \langle G(\vec{\lambda} + \vec{d}\vec{\lambda})|$). Among all the possibilities we decided to focus on the reduced matrix obtained by projecting the ground state on two nearest-neighbor spins, but we checked that other choices lead to similar results. The reduced density matrix on two nearest-neighbor sites can be written in terms of the spin correlation functions [191] as

$$\rho_{ij} = \frac{1}{4} \sum_{\alpha, \beta=0,x,y,z} \langle \sigma_i^\alpha \sigma_j^\beta \rangle \sigma_i^\alpha \otimes \sigma_j^\beta, \quad (2.11)$$

where σ^0 denotes the identity and the analytic expressions for the correlation functions appearing in (2.11) are presented in the Appendix A.3.

The results obtained for the reduced fidelity, in a system composed of 1001 sites, by keeping the value of γ fixed and changing h with uniform steps equal to 10^{-4} are shown in Figure 2.4.

In the chiral region $h < h^*$ we plot two sets of points: the lowest ones refer to the reduced fidelity while moving along one of the parabolas which keep the occupied modes in the ground state fixed, while the higher ones represent a generic change for which neighboring ground states have vanishing overlaps and even the reduced fidelity gets significantly dampened. Note that a clear discontinuity is observable at the boundary of the chiral region for $h = h^*$, where an isolated point develops, which reflects the fact that outside the chiral region the ground state is a vacuum and thus has different correlation functions compared to those for $h < h^*$. However, in Fig. 2.5 we can observe that the value of this discontinuity decreases proportionally to $1/N^2$ and therefore disappears in the thermodynamic limit. Similar analysis can be performed for all other points in which the reduced fidelity shows a discontinuity, always yielding discontinuities which vanish algebraically with the chain length and hence, in the thermodynamic limit, the behavior of the reduced fidelity for the topologically frustrated spin models is indistinguishable from the one of the unfrustrated models. We should remark, here, that in systems with continuous symmetry, although the discontinuities in the reduced fidelity susceptibility between neighboring state also vanish in the thermodynamic limit, the region of crossovers between different ground states is a true quantum phase and thus the discontinuity at the boundary survives the thermodynamic limit [165].

Clearly, since on one side the whole ground state fidelity is singular and produces a foliation of the parameters space, while the two sites reduced fidelity becomes continuous in the thermodynamic limit, a crossover is expected between two behaviors if more sites are included in the subset A , ideally scaling with the total chain length. However, such analysis cannot be carried out analytically and requires too heavy of a numerical study, which is beyond the scope of the current work.

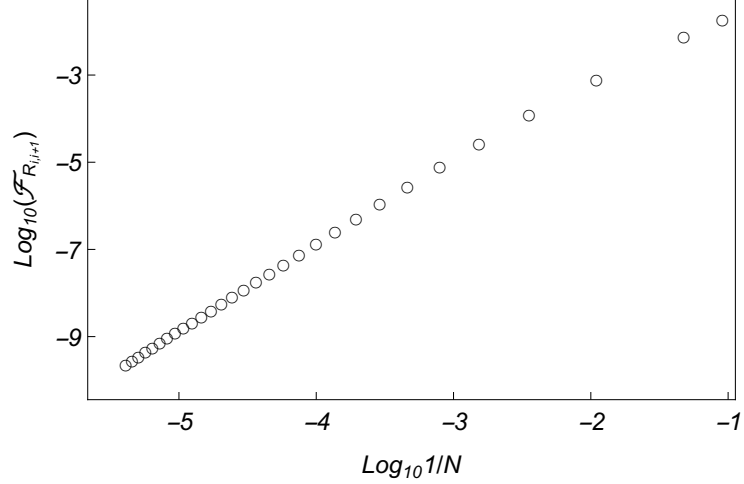


Figure 2.5: Reduced fidelity at the line $h = h^*$ obtained projecting a ground state eigenstate of the momentum operators into the Hilbert space defined by two next neighbor spins as function of the size of the system. The data are obtained considering $\gamma = 0.6$. Although at finite sizes a discontinuity is evident, in the thermodynamic limit it vanishes algebraically.

2.4 Characterization of the critical line

Thanks to the analytical solution of the XY chain it is possible to study how all the other features of the chiral region scale in the thermodynamic limit, namely the chirality and the breaking of translational invariance. Hence, we can address the question of whether this represents a different thermodynamic phase or not.

For $h^* < h < 1$ one can show that the ground state is always represented by the fermionic vacuum state, while in the chiral region the ground state manifold keeps changing its parity and momenta. Even increasing the chain length without moving h and γ can switch the ground state parity, because of the shift in the momenta quantization. Moreover, the gap between the alternating ground-states in different parity sectors closes exponentially with the chain length, which means that in the thermodynamic limit the two manifolds become effectively degenerate: crossing the line $h = h^*$ the ground state degeneracy thus grows from 1 to 4, which could indicate a first-order quantum phase transition. However, analyzing the free energy derivatives (which at zero temperature coincide with the ground state energy) we cannot detect any discontinuity that remains finite in the thermodynamic limit, as shown in Fig. 2.6. This fact implies that in

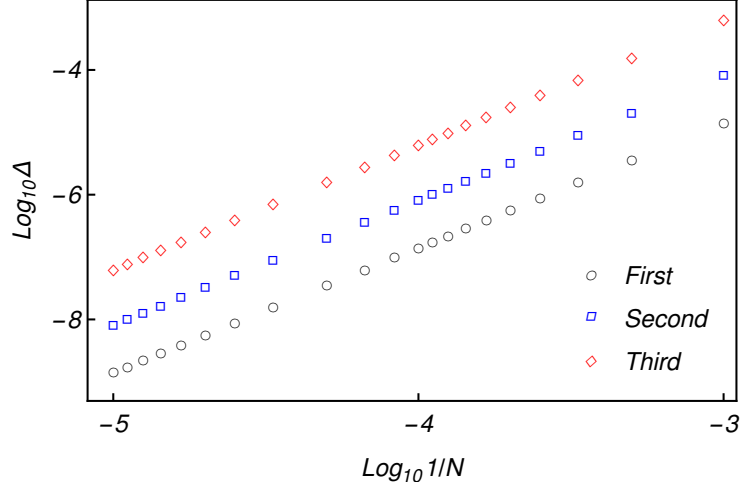


Figure 2.6: Behavior of the jump in the energy derivatives $\Delta(n)$, for $n = 1, 2, 3$ as a function of the inverse chain length, in logarithmic scale, obtained crossing the threshold $h = h^*$ along a line with constant γ . The data are obtained setting $\gamma = 0.6$. All derivatives display a vanishing discontinuity in the thermodynamic limit.

the thermodynamic limit all derivatives are analytical and hence that if $h = h^*$ represents a quantum phase transition, it has to be one akin to a BKT transition [192–194]. This result is in stark contrast with the other phase transition induced by topological frustration discovered in models without external field [151]. In fact, in that transition, the first derivative of the ground-state energy shows a discontinuity that stays finite even in the thermodynamic limit. The reason behind this different behavior is that the transition point in Ref. [151] possesses a higher symmetry that produces a massive (thermodynamically large) ground state degeneracy. In this way, crossing this point, there is a true discontinuity and, for instance, the mode occupied in the odd parity sector of the ground state has momentum close to $\pm \frac{\pi}{2}$, instead of $\pm \pi$ as we have here.

On the other hand, phase transitions are associated with a macroscopic reordering of the system properties that can be detected by opportunely chosen quantities. From what we have seen in the previous section, among others, two possible quantities can be considered: the chirality parameter that detects the existence of ground-states with a non-vanishing momentum and the spatial variance of local observables that highlights the violation of the invariance under spatial translation. Both quantities, and in general each spin correlation function on a ground-state with a fixed parity, can be obtained

analytically in the framework of the analytical approach that we are using. The key point is the introduction of two sets of Majorana operators so that each spin correlation function can be mapped to a string of Majoranas [162]. By exploiting Wick's theorem, the expectation value of these correlation functions can be reduced to the evaluation of Pfaffians whose elements are the expectation values of two Majorana operators. As we show in the appendix, for $h > h^*$ these expectation values can be classified into two different families: a) when the two Majorana operators come from the same set, the expectation value vanishes unless the two operators coincide; b) when the two Majorana operators come from different sets, the expectation value assumes values in the range $[-1, 1]$ and are invariant under spatial translation. Entering the region $h < h^*$ both these properties are changed. Indeed, the expectation values of Majorana operators coming from the same set but defined on different fermionic sites assume values proportional to $1/N$ that hold the property to be invariant under spatial translation. On the other hand, the expectation values for Majorana in different sets acquire corrections proportional to $1/N$ that explicitly violate the invariance under spatial translation.

These two corrections and their proportionality to $1/N$ explain why both the chirality and the variance of the distribution of local quantities are different from zero in a finite frustrated system but disappear when the thermodynamic limit is taken into account. Indeed, using Wick's theorem, the expectation value of the chirality operator τ can be reduced to a sum of products of expectations of pairs of Majorana fermions, with the peculiarity that each term in the sum contains at least an expectation on pairs of Majorana belonging to the same set, thus providing an algebraic decay with the system size to the whole expression. On the other hand, since all the site-dependent contributions to a local quantity scale with $1/N$, the variance is also vanishing in the thermodynamic limit. Both these behaviors should be compared to other observables calculated in presence of topological frustration in [150, 151]: there the $1/N$ corrections coming from frustration appeared in combination with finite terms present also in absence of frustration and when an expectation value involved a sufficiently high number of corrections (also scal-

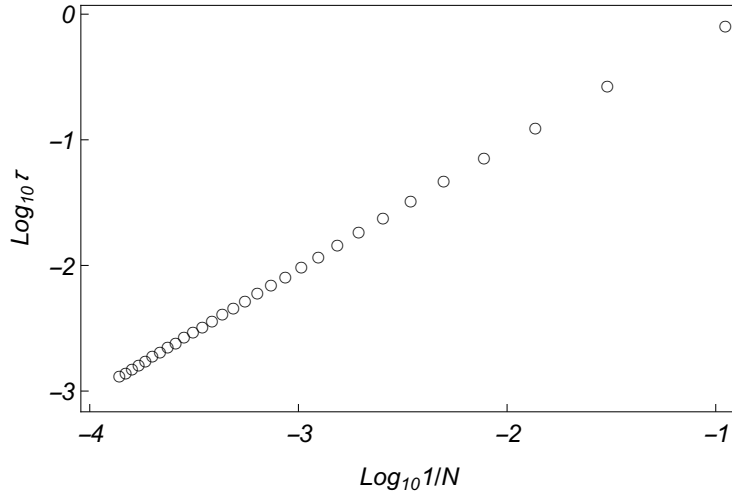


Figure 2.7: Behavior of the chirality τ for ground states that are eigenvalues of the momentum operator as a function of the length of the chain N . The data are obtained for the XY chain setting $\gamma = 0.6$ and $h = 0.4$

ing with N), the resulting expression brought finite contributions. The analytic derivation of both quantities can be found in the Appendix A.3 while in Fig. 2.7 and Fig. 2.8 their dependence on the chain length is depicted for some relevant ground-states choice. The disappearance in the thermodynamic limit of both properties that characterize this region of the parameter space, associated with the absence of any local discontinuity in the energy derivatives on the line $h = h^*$ support the idea that we are looking at a boundary transition whose effects disappear when the size of the system diverges.

2.5 Conclusions

In conclusion, we have seen how, in presence of topological frustration, an anisotropic Heisenberg chain, which presents only discrete rotational symmetries associated with finite sets of quantum numbers, is characterized by a region of parameter space (*chiral region*) in which the system mimics that of a system with continuous symmetries. In fact, in analogy with the latter, the system not only presents a gapless energy spectrum with a finite Fermi momentum but shows, in the thermodynamic limit, a ground-state characterized by a continuous cross-over between two-dimensional mutually orthogo-

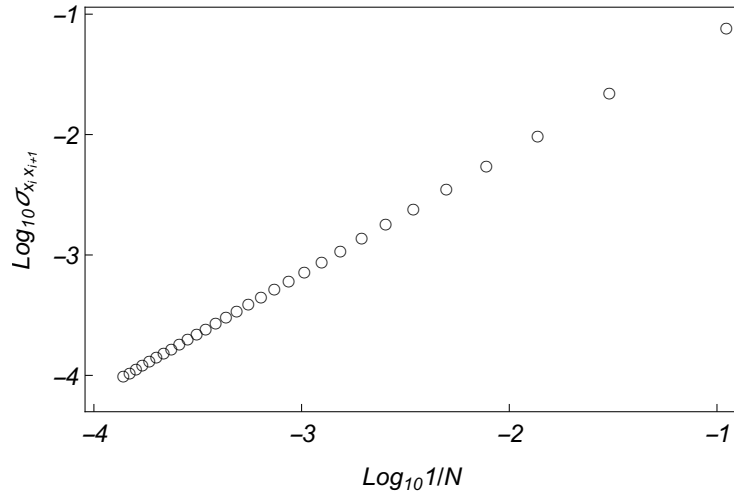


Figure 2.8: Variance of the spatial distribution for the two-point spin correlation functions $\langle \sigma_i^x \sigma_{i+1}^x \rangle$ for ground states obtained as a real symmetric combination of the two ground states with a definite momentum, as a function of the length of the chain N . The data are obtained for the XY chain setting $\gamma = 0.6$ and $h = 0.4$

nal manifolds. Each one of these manifolds is spanned by eigenstates of the lattice momentum with the same eigenvalues but opposite signs. This fact has several interesting consequences. At first, since these states are characterized by a non-zero momentum when the system is made of a finite number of spins, they show a non-zero chirality that vanishes in the thermodynamic limit. At the same time, any non-trivial linear combination of such states produces a new ground-state violating the invariance under spatial translation, which, in the case of finite systems, can be observed through the variance associated with the spatial distribution of local observables, but which are zeroed when the dimension of the system diverges. This chiral region is separated from the rest by a threshold line that separates it from a region in which the system is still gap-less but the ground state is unique and characterized by zero momentum. Our analysis clearly shows that such change in the ground state degeneracy is not mirrored in the behavior of the energy. Indeed, in the thermodynamic limit, all energy derivatives are analytical, and hence the transition has to be akin to a BKT transition. However, the disappearance in the thermodynamic limit of both properties that characterize this region of parameter space supports the idea that we are looking at a boundary transition whose effects disappear when the size of the system diverges. Indeed, to the best of our knowledge,

boundary BKT transitions have not been observed before. Consistently with this picture, the ground state fidelity obtained by continuously varying the parameters of the system, in the thermodynamic limit, is identically zero in almost all directions. The only exception is obtained when the change of the Hamiltonian parameters is carried out in such a way as to keep the momenta characterizing the ground state manifold constant, which, in the particular case of the XY chain for which it is possible to carry out an analytical treatment, occurs when the ratio $h/(1 - \gamma^2)$ is kept constant.

Chapter 3

W -states, chiral phases and a *magic* phase transition

In Chapter 1 we discussed the existence of a chiral phase in the phase diagram of the topologically frustrated XYZ spin-1/2 chain, and showed that the phase transition to this region cannot be detected with standard techniques.

In this chapter, we employ the Stabilizer Rényi Entropy (SRE) to characterize the quantum phase transition to the chiral region, demonstrating that it can be explained in terms of the interplay between its non-stabilizer properties and entanglement. We show that SRE has a jump at the crossing points, while the entanglement entropy remains continuous. Moreover, by leveraging on a Clifford circuit mapping, we connect the observed jump in SRE to that occurring between standard and generalized W -states with finite, quantized momenta. This mapping allows us to quantify the SRE discontinuity analytically.

3.1 Introduction

Entanglement has played an important role in impetuously developing our understanding of quantum many-body systems [195, 196]. However, over the years it has become

increasingly clear that entanglement alone is not able to capture every feature that differentiate quantum from classical systems [197, 198]. The most relevant example of this is the fact that entanglement alone does not guarantee the so-called *Quantum Supremacy* [199]. Indeed, some classes of highly entangled quantum states can be simulated efficiently using only classical resources. Among others, this is the case of the so-called stabilizer states, which can be obtained from a fully factorized state by circuits made of Clifford gates [200, 201], i.e. a series of operations that, according to the celebrated Gottesman-Knill theorem [200], can be efficiently simulated on a classical computer. While the concept of stabilizer state is a completely general concept in group theory, here we focus on the stabilizer states of the n -qubit Pauli group \mathcal{G}_n because of their relevance to quantum information. For a single qubit, the Pauli group is generated by the Pauli matrices with possible phase factors ± 1 and $\pm i$:

$$\mathcal{G}_1 = \{\pm \mathbb{I}, \pm i\mathbb{I}, \pm \sigma^x, \pm i\sigma^x, \pm \sigma^y, \pm i\sigma^y, \pm \sigma^z, \pm i\sigma^z\}. \quad (3.1)$$

In turns, the n -qubit Pauli group contains all the 4^{n+1} n -fold tensor products of elements of \mathcal{G}_1

$$\mathcal{G}_n = \{g_1 \otimes \cdots \otimes g_n \mid g_1, \dots, g_n \in \mathcal{G}_1\}. \quad (3.2)$$

A notable subset of \mathcal{G}_n is the one obtained without considering the possible phase factors, which corresponds to the set of all the possible n -qubit Pauli strings $\mathcal{P} = \bigotimes_{i=1}^n P_i$, with $P_i \in \{\mathbb{I}, \sigma_i^x, \sigma_i^y, \sigma_i^z\}$. Going back to the notion of stabilizer states, we say that a state $|\psi\rangle$ is a stabilizer state of \mathcal{G}_n if a subset $G \subset \mathcal{G}_n$ exists such that $|G| = 2^n$ and $g|\psi\rangle = |\psi\rangle \forall g \in G$. In other words, $|\psi\rangle$ is a stabilizer state of \mathcal{G}_n if it is an eigenstate of 2^n elements of \mathcal{G}_n with eigenvalue 1. The simplest example is that of a two-qubit GHZ state $|\psi\rangle = \frac{|\downarrow\downarrow\rangle + |\uparrow\uparrow\rangle}{2}$, which is an eigenstate of the 4 operators $\mathbb{I} \otimes \mathbb{I}$, $\sigma^x \otimes \sigma^x$, $-\sigma^y \otimes \sigma^y$ and $\sigma^z \otimes \sigma^z$ with eigenvalue 1. The reason why the stabilizer states of the n -qubit Pauli group can be simulated efficiently using only classical resources is that the n -qubit Clifford group \mathcal{C}_n is the normalizer group of the Pauli group, i.e. it is the set of all the unitary operators

that map elements of \mathcal{G}_n into themselves

$$\mathcal{C}_n = \{c : cgc^\dagger = g' \mid g' \in \mathcal{G}_n\}. \quad (3.3)$$

It is thus straightforward to understand that any state obtained by acting on a stabilizer state $|\psi\rangle$ with an element of \mathcal{C}_n will still be a stabilizer state. Now, since the generators of \mathcal{C}_n are the so-called Clifford gates (i.e. the Hadamard, $\pi/4$ phase and CNOT gates), it follows that any state obtained applying a Clifford circuit to a fully factorized state is a stabilizer state itself, and can be simulated efficiently on a classical computer because of the Gottesman-Knill theorem.

It hence becomes clear that quantum advantage must be attained at the price of non Clifford resources and exponential increment in the difficulty of simulating a quantum circuit on classical computers [199, 202]. The resource beyond Clifford operations is colloquially known as *magic* [203, 204] and the definition of a resource theory for this quantity has been a formidable challenge for quantum information science [203]. Within this context, one of the central questions has been that of quantifying the distance between a given quantum state and a stabilizer state, defining a measure which at the same time is stable under operations that send stabilizer states into stabilizer states, and faithful, that is, stabilizer states (and only those) must return zero. Notable examples are the minimum and maximum relative entropies of magic, robustness of magic, Bell magic, stabilizer nullity and the so-called *Stabilizer Rényi Entropies* (SREs) [204–208]. For a generic state, all of these quantities are in principle computationally hard to compute, either requiring the evaluation of extremes over all the possible stabilizer decompositions of a state or the computation of an exponential number of correlation functions. However, recently, the family of SREs, which are defined as a function of the index α by

$$\mathcal{M}_\alpha(|\psi\rangle) = (1 - \alpha)^{-1} \log_2 \left(\frac{1}{2^L} \sum_{\mathcal{P}} \langle \psi | \mathcal{P} | \psi \rangle^{2\alpha} \right), \quad (3.4)$$

has raised a lot of interest in the community. Indeed, it was proven that SREs with Rényi

index greater or equal to 2 are monotones of magic for pure states [208] and, among the others, the one with Rényi index equal to 2 has acquired a prominent role since in some cases is experimentally achievable [209–211]. Moreover, this family of stabilizer entropies has provided a way for analyzing the complexity of quantum states in quantum many-body systems [155, 212, 213]. In gapped local systems, it was found that the SRE of ground states follows a volume law in which the slope can be determined using single-spin expectation values [213]. On the contrary, this local behavior of the SRE disappears in the presence of long-range correlations that can be induced either by placing the system near a phase transition or, as emphasized in recent years, by introducing topological frustration in the system [150, 153, 154, 156]. SRE, and more generally, other magic measures, have thus proved to be useful in the analysis of quantum many-body phases[204].

Here, we show that one can employ SRE to characterize the mirror symmetry breaking transition in the anisotropic Heisenberg model that has been introduced in Chapter 2. As argued in Section 2.4, this transition has so far been particularly elusive and hard to detect since, up to today, there are no known non-vanishing order parameters in the thermodynamic limit and even the analysis of entanglement properties has not been helpful.

For reading convenience, we propose again the expression of the Hamiltonian of the 1D fully anisotropic Heisenberg chain (also known as the XYZ chain) with a global magnetic field along the z -axis, which was already given in Eq. (2.1)

$$H_{XYZ} = \sum_{n=1}^L \sum_{\alpha} J_{\alpha} \sigma_n^{\alpha} \sigma_{n+1}^{\alpha} + h \sum_{n=1}^L \sigma_n^z. \quad (3.5)$$

Here and in the following we will always assume that $J_x = 1$ and $|J_y|, |J_z| < J_x$. For certain values of the Hamiltonian parameter this model is exactly solvable, but we will consider it in generality and thus approach it numerically. Within Frustrated Boundary Conditions (FBCs) [147, 150, 151, 154, 169, 170], the number of sites is taken to be odd

($L = 2M + 1$ for $M \in \mathbb{N}$) and periodic boundary conditions are assumed ($\sigma_n^\alpha = \sigma_{n+L}^\alpha, \forall n$).

As described in detail in Appendix A, the frustrated phase of the XYZ model divides into two regions. In the first, which includes the Ising chain, the ground state is unique and has zero momentum. In the second one, the ground-state is exactly doubly degenerate, with the degeneracy being realized by eigenstates of the momentum operator with opposite non-zero values. In [2] it was argued that the line dividing the two regions is a second order boundary QPT, but that analysis did not account for the lattice momentum quantization. In fact, the analysis performed in [1] and described in Section 2.4 showed no discontinuities in the free energy and did not find any observable that survive the thermodynamic limit. In this chapter, we analyze such a transition, considering it as an example of a general kind of phase transitions that can be characterized in terms of a discontinuity in the SRE. To the best of our knowledge, this is the first instance of a “pure magic transition” in a deterministic quantum system, even if, a shift between local and non-local magic has been recently observed in random quantum circuits [211, 214–216].

The generality of this result comes from the unique behavior of SRE in a family of generalized W -states in which each element is defined by its phase. Unlike bipartite entanglement, in the thermodynamic limit, the value of magic remains a function of the phase. As we will show in the following, these states can be mapped into the elements of the lower energy band of the topologically frustrated XYZ model close to the classical point, i.e. when the Hamiltonian is close to the one of classical Ising. Therefore, a crossover in the elements of the lowest energy band is associated to a change for the SRE of the ground state. To extend this result outside the perturbative regime, we generalize the results in [155]. We provide numerical evidence that, in the thermodynamic limit, it is possible to write the SRE of the ground states of a topologically frustrated spin chain as the sum of the SRE of the ground state of the corresponding non-frustrated model plus the SRE of the associated generalized W -states. Since without frustration the SRE is continuous within a given phase, the SRE of the topologically frustrated chain shows the same signature of phase transition inherited from the generalized W -states

even outside the perturbative regime.

3.2 Generalized W -states and the complexity of TF ground states

We start our analysis by calling to mind the W -states [217] that play a pivotal role in quantum information [218–220] finding applications in various quantum protocols, such as anonymous transmission in quantum networks [221], quantum communication [222], and error detection [223]. The family of generalized W -states (gWs) that we consider reads

$$|W_p\rangle = \frac{1}{\sqrt{L}} \sum_{j=1}^L e^{ipj} \sigma_j^z |-\rangle^{\otimes L}. \quad (3.6)$$

Here L is the number of qubits in our system, $p = \frac{2\pi}{L}l$, for $l = 0, \dots, L-1$, is a quantized lattice momentum, and $|\pm\rangle$ are the eigenstates of the Pauli operator σ^x corresponding to eigenvalues ± 1 . The original W -states are recovered by setting $p = 0$. Being a generalization, some properties of the W -states extend to the whole family, while others will depend on p . Among the properties of the W -states that extend to every gWs there is the entanglement, which is independent of p . Indeed, for any bipartition, there are only two non-vanishing eigenvalues of the reduced density matrix and are equal to $(1 \pm x)/2$, where x is the difference between the dimension of the two subsystems normalized by L .

3.2.1 Non-stabilizerness of generalized W -states

For a pure state $|\psi\rangle$ defined in a system of L qubits, the SRE (of index 2) is defined as

$$\mathcal{M}_2(|\psi\rangle) = -\log_2 \left(\frac{1}{2^L} \sum_{\mathcal{P}} \langle \psi | \mathcal{P} | \psi \rangle^4 \right). \quad (3.7)$$

Although eq. (3.7) implies a summation of 4^L expectation values, it allows for an efficient treatment with tensor networks [224–229].

The expression of the SRE for gWs, Eq.3.6 is a function on L and p and we evaluated it analytically to be (see Appendix B.2)

$$\mathcal{M}_2(p, L) = -\log_2 \left(-\frac{11 - 12L + \frac{\sin((2-4L)p)}{\sin(2p)}}{2L^3} \right). \quad (3.8)$$

In the limit $p \rightarrow 0$ we reach the minimum of eq. (3.8) and recover the SRE for the W state:

$$\mathcal{M}_2(0, L) = 3 \log_2(L) - \log_2(7L - 6). \quad (3.9)$$

Moreover, taking into account the quantization of the momenta, which ensures that the states in (3.6) must be also eigenstates of the translation operator [230], we have that eq. (3.8) reduces to

$$\mathcal{M}_2 \left(\frac{2\pi}{L} \ell, L \right) \Big|_{\ell \neq 0} = \mathcal{M}_2(0, L) + \log_2 \left(\frac{7L - 6}{6L - 6} \right). \quad (3.10)$$

Note that this expression is independent from ℓ , as long as it is finite: the difference $\Delta \mathcal{M}_2(L) = \mathcal{M}_2 \left(\frac{2\pi}{L} \ell, L \right) - \mathcal{M}_2(0, L)$ represents the gap in the SRE, which is associated with the state acquiring non-zero momentum that reduces to $\log_2(7/6)$ in the thermodynamic limit.

The family of states in (3.6) plays a central role in the study of topologically frustrated 1D systems. Indeed, applying on them the (magic preserving) Clifford circuit

$$\hat{S} = \prod_{j=1}^{L-1} C(L, L-j) \left(\prod_{j=1}^M \sigma_{2j-1}^z \right) \mathbf{H}(L) \sigma_L^z \prod_{j=1}^{L-1} C(j, j+1) \Pi^z \quad (3.11)$$

introduced in Ref. [155] it is possible to obtain the elements of the low energy band of the 1D topologically frustrated XYZ model close to the classical point. Here $\mathbf{H}(j) \equiv \frac{1}{\sqrt{2}}(\sigma_j^x +$

σ_j^z) is the *Hadamard gate* on the j -th qubit, while $C(j, l) \equiv \exp \left[\frac{\pi}{4} (1 - \sigma_j^x)(1 - \sigma_l^z) \right]$ is the *CNOT gate* on the l -th qubit controlled by the value of the j -th one and $\Pi^z = \bigotimes_{j=1}^L \sigma_j^z$ is the parity operator along z .

3.2.2 Entanglement of TF ground states

The non-trivial response of AFM spin chains to FBC is also witnessed by an excess of bipartite entanglement beyond the area-law contribution [154, 156, 231]. While these properties characterize the whole frustrated phase, accordingly with [1] and as presented in Chapter 2, assuming $J_z \geq -J_y$ there exists a critical value of the external magnetic field $h^* > 0$ (see Fig. 3.1) such that for $|h| < h^*$ the ground state manifold becomes twofold degenerate and spanned by states with finite, opposite momenta $p \neq 0$. Interestingly, the physics of the whole frustrated phase can be described in a quasi-particle picture through a single delocalized excitation in the ground state of frustrated chains. While in most cases this excitation carries zero momentum, below h^* , where the ground-state manifold is at least two-fold degenerate, it owns a non-vanishing one.

In the spirit of adiabatic continuation, let us analyze a particularly simple case where the calculations can be carried out analytically, and subsequently, we will show how the results thus obtained generalize to the entire phase. Therefore, let us focus on the case in which the system is close to the classical point. We define as classical point the case in which J_x is the only non-vanishing Hamiltonian parameter. Indeed, in this case, eq. (3.5) reduces to a sum of mutually commuting terms, i.e. to a classical Hamiltonian. In this region, exploiting perturbation theory, we obtain that the elements of the lowest energy band can be written as *kink states*

$$|\omega_p\rangle = \frac{1}{\sqrt{2L}} \sum_{k=1}^L e^{ipk} (|k\rangle + |k'\rangle), \quad (3.12)$$

where p is the quantized momentum, i.e. $p = 2\pi\ell/L$, with $\ell = 0, \dots, L-1$. The kinks are embedded in Néel order states and are made of the union of two extensive sets of

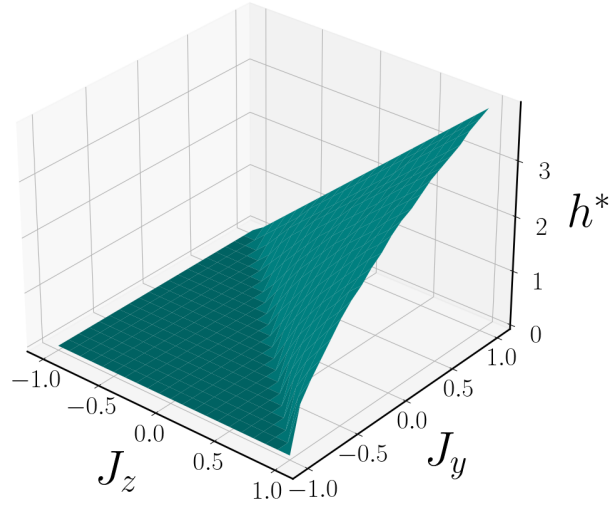


Figure 3.1: Value of h^* as function of J_y and J_z (J_x is assumed to be equal to 1) for the Hamiltonian in eq. (3.5). The data is obtained numerically looking at the momentum of the ground state for a system made of $L = 15$ spins. For $h^* > 0$, choosing $|h| < h^*$ the ground state manifold has dimension equal to 2 and is spanned by states with finite, opposite momenta $p \neq 0$.

states defined as $|k\rangle = \mathcal{T}^k \otimes_{j=1}^M \sigma_{2j}^z |-\rangle^{\otimes L}$ and $|k'\rangle = \mathcal{T}^k \otimes_{j=1}^M \sigma_{2j}^z |+\rangle^{\otimes L}$ with k and k' running from 1 to L . Turning on J_y J_z and/or h in the proximity of the classical point we can have either a unique or a two-fold degenerate ground state. In the first case, the lowest energy is obtained by setting $p = 0$, while in the other case, the two ground states display equal but opposite momenta p , dependent on the Hamiltonian parameters.

Therefore, it becomes crucial to have a physical quantity able to discriminate between states that yield results dependent on p , or at least whether, p is zero or not. In Chapter 2 we showed how chirality, generally sensitive to the momentum, cannot be used in this case since, even if different from 0 for finite L , it vanishes in the thermodynamic limit. A natural second candidate is represented by the entanglement, which has often been used to reveal the presence of non-local correlations. Summarizing the results reported in Appendix B.1, we have that, limiting ourselves to partitions $(A|B)$ composed of connected subsets, regardless of their dimensions, the reduced density

matrix $\rho_A(p) = \text{Tr}_B(|\omega_p\rangle\langle\omega_p|)$ admits only 4 non-zero eigenvalues:

$$\begin{aligned} \lambda_{1,\dots,4} &= \frac{1}{4L} \left(L + 2\gamma \cos(p\chi) \pm \right. \\ &\quad \left. \pm \sqrt{(L - 2a)^2 + 4L(1 + \gamma \cos(p\chi)) - 4 \sin^2(p\chi)} \right), \end{aligned} \quad (3.13)$$

where $a = \dim(A)$, $\chi = L - a$ and $\gamma = \pm 1$. From eq. (3.13) it is evident that the momentum dependent contributions scale at most with the inverse square-root of L and thus vanish in the thermodynamic limit. Therefore, for large L the entanglement does not depend on p . To provide an example, setting $a = (L - 1)/2$ and evaluating the 2-Rényi entropy of $|\omega_p\rangle$ we obtain

$$S_2(\omega_p) = -\log_2 \left[\frac{1 + L(4 + L) + 4 \cos(p)}{4L^2} \right] \quad (3.14)$$

that becomes independent on p when L diverges.

3.2.3 Non-stabilizerness of TF ground states

Contrary to entanglement, magic works perfectly to detect the finite momentum. Since the states $|\omega_p\rangle$ can be obtained from the $|W_p\rangle$ via a Clifford circuit, they share the same value of magic. When the ground state is unique and carries zero momentum, the value of the SRE is given by eq. (3.9) but when the ground state acquires a finite momentum it increases by a quantity that stays finite even in the thermodynamic limit.

To extend this result to the whole frustrated phase we note that in the thermodynamic limit it is always possible to write the SRE of the ground state of a topologically frustrated spin chain $|g^{TF}\rangle$ as the sum of the SRE of the ground state of the corresponding non-frustrated model $|g^{NF}\rangle$ plus the SRE of a gWs, i.e.

$$\mathcal{M}_2(|g^{TF}\rangle) = \mathcal{M}_2(|g^{NF}\rangle) + \mathcal{M}_2(|W_p\rangle). \quad (3.15)$$

We prove this decomposition numerically. To perform a meaningful finite-size scaling

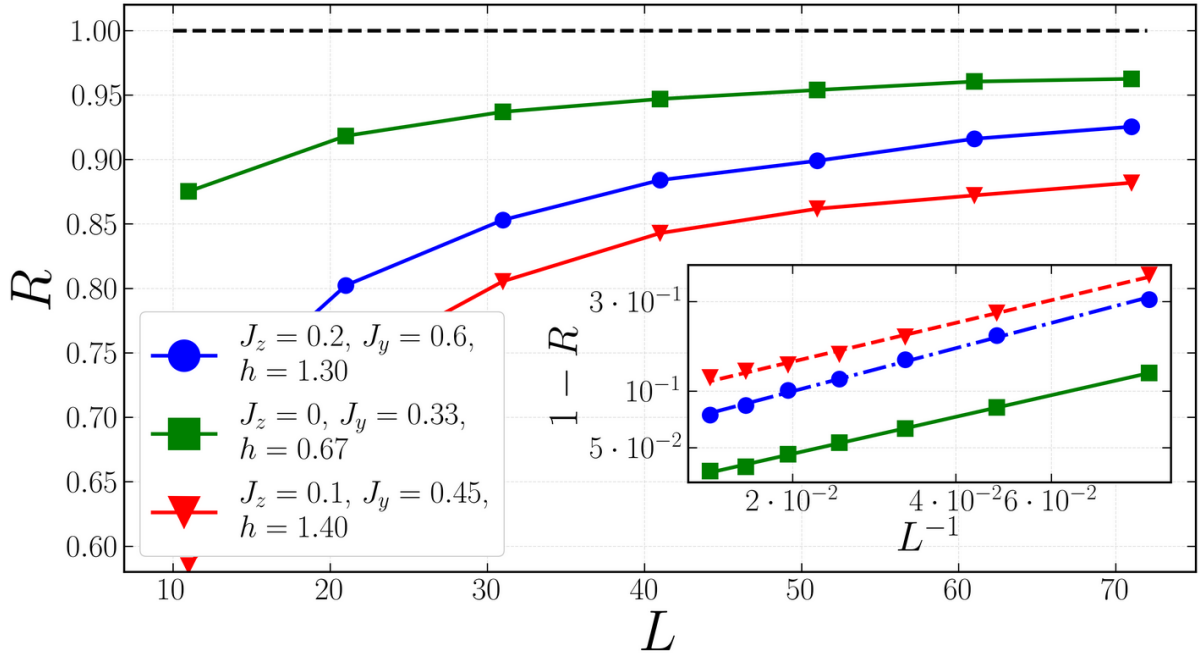


Figure 3.2: The ratio $R(p, L)$ defined in eq. (3.16), as a function of L for different sets of parameters. In both cases, we observe a power-law convergence of $R(p, L) \rightarrow 1$ for $L \rightarrow \infty$, as highlighted in the inset plot, where we plot $1 - R(p, L)$ as a function of L^{-1} in log-log scale.

analysis, we need system sizes that go beyond the capabilities of exact diagonalization techniques. Larger chains typically involve an exponential increment in the number of correlation functions but, recently, several methods have been introduced to estimate SRE using matrix product states (MPS) representations [224, 225, 229]. In our case the most suited approach is the one proposed in [229] since its worse scaling with the MPS bond dimension, compared for instance to [225], is compensated by the possibility of avoiding any statistical sampling on the distribution of Pauli strings. The latter is problematic since it does not converge easily in the frustrated case, due to the emergence of a multi-peaked distribution for the correlation functions. Therefore, we first compute the chain's ground-state chain in the MPS form using a density matrix renormalization group (DMRG) algorithm [232, 233] and then use it to evaluate its SRE. We follow this procedure both to determine the ground state of the topologically frustrated chain $|g^{TF}\rangle$, and the one of the corresponding non-frustrated model $|g^{NF}\rangle$, obtained by inverting the signs of J_x and J_y .

In Fig. 3.2 we plotted the quantity

$$R(p, L) = \frac{\mathcal{M}_2(|\psi^{TF}\rangle)}{\mathcal{M}_2(|\psi^{NF}\rangle) + \mathcal{M}_{2g}(|W_p\rangle)}, \quad (3.16)$$

that clearly approaches unity as $L \rightarrow \infty$ hence proving eq. (3.15).

3.3 The magic transition

The data from the analysis carried out in the previous section would already be sufficient to prove that the phase transition associated with the violation of the mirror symmetry is highlighted by a finite gap of the magic. However, it is also interesting to provide direct verification. Therefore we performed a finite-size scaling analysis of the jump in magic at the transition point h^* for several sets of parameters. To realize this analysis, we fix the values of the anisotropies, determine numerically h^* and plotted the difference in the SRE soon after and soon before this point. In all analyzed cases, the numerical data show a power-law convergence of the amplitude of the discontinuity to the analytically computed value of $\log_2(7/6)$, as shown in Fig. 3.3. On the contrary, the discontinuity in the bipartite entanglement shows a power-law convergence to 0, implying that in the thermodynamic limit, it is unable to highlight the presence of the phase transition. This confirms that the SRE witnesses the quantum phase transition associated to the violation of the mirror symmetry in topologically frustrated spin chains, which could therefore be classified as a *first-order magic (SRE) transition*.

3.4 Conclusion

Summarizing, we introduced a generalization of W -states that promotes a finite momentum. While preserving the value of entanglement of the W -states, they possess a greater degree of complexity as highlighted by the SRE. This generalization of W -

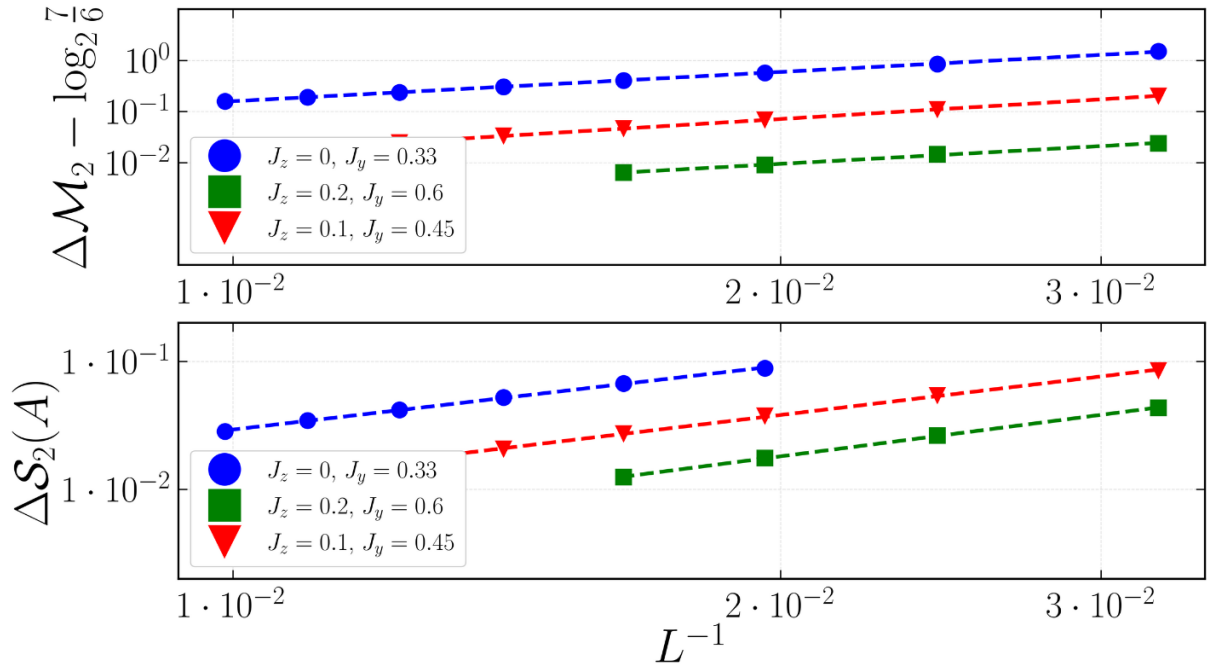


Figure 3.3: Finite-size scaling analysis of the discontinuity in the SRE (top) and in the entanglement (bottom) for different sets of anisotropies ($J_x = 1$ in all analyzed cases). Both the two quantities show a power-law decay to the thermodynamic values that are, respectively $\log_2(7/6)$ and 0. The entanglement is evaluated with the 2-Rényi entropy and the data plotted are associated at the partition $(A|B)$ in which A is a connected subsystem made of $(L - 1)/2$ spins.

states is extremely relevant in topologically frustrated 1D systems since they can be mapped, through a Clifford circuit into the elements of the lowest energy band close to the classical point. Then, we showed that, since the complexity of the ground states of topologically frustrated chains can be decomposed as the sum of a non-frustrated component and that of the gWs, the transition separating the region of zero momentum ground state from that with finite momenta can be characterized by a discontinuity in SRE. While it was already shown in other works that the SRE can detect measurement-induced phase transitions that are not signaled by the entanglement entropy in quantum circuits, to the best of our knowledge, our result constitutes the first instance of a quantum phase transition that can only be witnessed by the SRE in a deterministic system. The reason behind the fact that only the SRE can capture this quantum phase transition is probably related to the fact that the corrections induced by topological frustration on quantities like the correlation functions typically decay at least as L^{-1} , hence vanishing

in the thermodynamic limit. The SRE, however, involves the sum of the expectation values of an exponential number of correlation functions and hence can display a finite jump even in the thermodynamic limit. It is important to stress once more that, while the Clifford mapping does not preserve the bipartite entanglement entropy and thus those of gW s and the spin ground states differ, they do not show discontinuities when a finite momentum appears.

The nature of this transition, being induced by boundary conditions, has remained controversial so far: the results of this work not only show the first instance of a discontinuity in SRE not accompanied by a similar one in the entanglement in a deterministic model, but further establish complexity in condensed matter/statistical physics systems as a detector of unconventional quantum phase transition. Of course, additional instances of such phenomenology are needed to establish whether complexity is just a proxy to detect transitions (like the entanglement entropy) or if it truly captures something fundamental, like topological order parameters.

Chapter 4

Interplay between local and non-local frustration

Moving on from the study of chiral phases in topologically frustrated spin chains, in this chapter we consider the effects of the competition between different sources of frustration in 1D spin chains through the analysis of the paradigmatic ANNNI model, which possesses an extensive amount of frustration of local origin due to the competition between nearest and next-to-nearest neighbor interactions. An additional, non-extensive amount of topological frustration can be added by applying suitable boundary conditions and we show that this seemingly subdominant contribution significantly affects the model. Choosing periodic boundary conditions with an *even* number of sites not divisible by 4 and using the entanglement entropy as a probe, we demonstrate that in one of the model's phases the ground state can be characterized as hosting two (almost) independent excitations. Thus, not only we show an intriguing interplay between different types of frustration, but also manage to propose a non-trivial quasi-particle interpretation for it.

4.1 Introduction

The analysis carried out so far focused on one-dimensional spin chains with just short-range (nearest-neighbor) interactions. These systems, by their nature, could not show any source of local frustration, i.e. generated by different interactions competing on the same sites. Therefore, TF has been the only type of frustration and, being associated with boundary conditions, provides a sub-extensive amount of frustration. In this chapter we extend the analysis to more complex systems, those that present also local sources of frustration due to the interplay between neighboring and non-neighboring spin pairs interactions, and investigate whether TF can influence these systems as well. We consider the ANNNI model, being the simplest one in this respect. It was initially introduced as a theoretical model to understand numerous experimental observations [234, 235], and it is now regaining attention as the right playground to test machine learning algorithms, due to its rich phase diagram and the lack of a general analytical solution [236, 237]. Furthermore, it is amenable to experimental implementation with segmented ion traps [238]. The Hamiltonian of the model for L spins reads

$$H = J_1 \sum_{i=1}^L \sigma_i^x \sigma_{i+1}^x + J_2 \sum_{i=1}^L \sigma_i^x \sigma_{i+2}^x + h \sum_{i=1}^L \sigma_i^z, \quad (4.1)$$

where σ_i^α , with $\alpha = x, y, z$ are the Pauli operators acting on the i -th spin, J_1 and J_2 are respectively the nearest and the next-to-nearest neighbor interactions, and h is a transverse magnetic field. Unless stated otherwise, we assume periodic boundary conditions, i.e. $\sigma_i^\alpha \equiv \sigma_{i+L}^\alpha$.

Indeed, an AFM next-to-nearest neighbors coupling ($J_2 > 0$) induces an extensive frustration of local origin, regardless of the choice of the boundary conditions and of the sign of J_1 and the different interaction terms in eq. (4.1) result into a rich phase diagram (see Fig. 4.1), with four different phases [235, 237], which we will present in the next section.

Here, we add TF, and we will show that this intensive source of frustration affect the

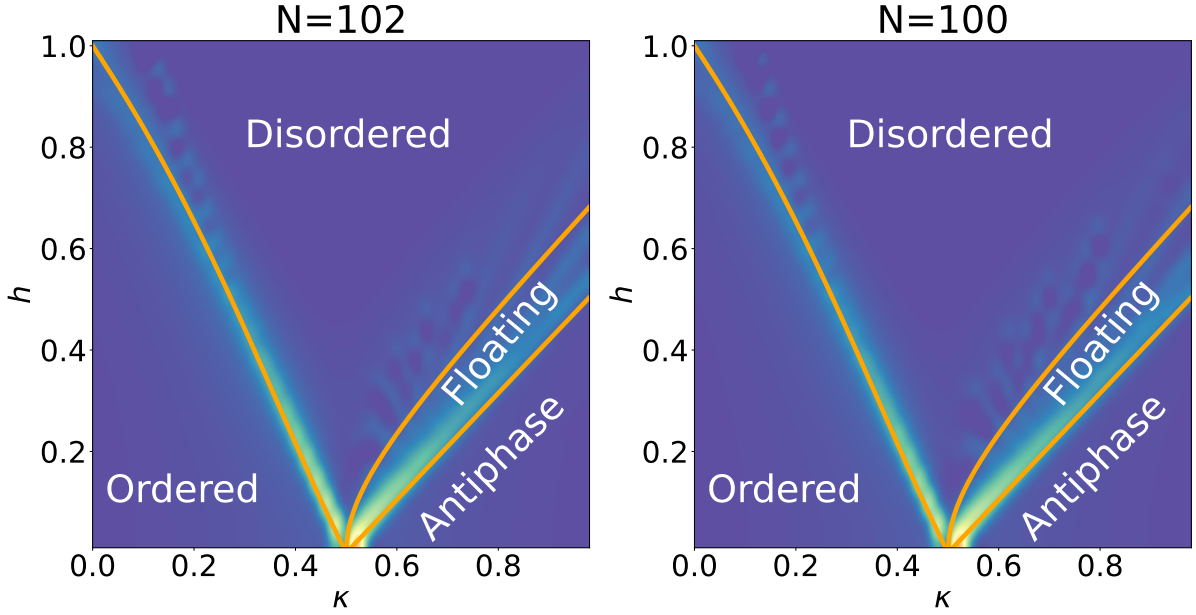


Figure 4.1: Phase diagram of the ANNNI model in the $(h/J_1, \kappa)$ plane in absence ($L = 100$, left panel) and in presence ($L = 102$, right panel) of topological frustration, obtained by analyzing the second derivative of the ground-state energy with respect to h . The solid orange lines represent the quantum phase transitions detected by discontinuities in the energy derivative. While the phase diagram, originally drawn in [235], is unaffected by the different boundary conditions considered, we will show that the antiphase has different properties for $L = 4N$ and $L = 4N + 2$.

model, in particular in the so-called *antiphase* where J_2 is the dominant interaction. To prove such a result, we focus on the bipartite entanglement entropy (EE). In [154, 155] it was shown that in the Ising chain (eq. (4.1) with $J_2 = 0$) TF, induced by FBC, adds an amount of EE corresponding to the presence of a single delocalized excitation. With a finite $J_2 > 0$ we will prove that TF can be induced by choosing a chain with an even number of sites non-divisible by 4 and this results in a contribution to the EE compatible with that of two delocalized excitations, obeying a Pauli principle that prevents them from occupying the same momentum state.

4.2 The Phase Diagram of the ANNNI Model

In Fig. 4.1 we draw the phase diagram of the ANNNI chain, that we obtain by the analysis of the energy discontinuities.

Without the external transverse field ($h = 0$) every term of the Hamiltonian in eq. (4.1)

mutually commute and the model can be considered as classical. Introducing the dimensionless coupling $\kappa \equiv J_2/|J_1|$, in such a limit, we can identify two phases separated by a multicritical point located at $\kappa = \kappa_c = 1/2$. For $\kappa < \kappa_c$ we have a standard ferromagnetic ($J_1 < 0$) or AFM ($J_1 > 0$) ordered phase, while for $\kappa > \kappa_c$ the system endeavors to arrange itself so that each spin has one neighbor spin aligned and one anti-aligned (see also Section 4.3). This order is referred to as the antiphase [235].

Turning back on the magnetic field, three lines of phase transition originate from the multicritical point $(h, \kappa) = (0, 1/2)$. One line extends up to $(|h|, \kappa) = (|J_1|, 0)$, and is a phase transition of the Ising-type between an ordered and a paramagnetic disordered phase [239]. To the right of this line, increasing κ for $h \neq 0$ we encounter two more transition lines. The first marks a Berezinskii–Kosterlitz–Thouless (BKT) transition between the disordered and a floating phase [240, 241]. The latter is a gapless phase described by a Luttinger liquid with algebraic incommensurate correlations [27]. The second line marks a commensurate-to-incommensurate transition between the floating and the antiphase. In this latter region the AFM next-to-nearest interaction J_2 is the dominant one, and we will focus on this antiphase to study the interplay between different kinds of frustration. We will show that, in this phase TF can be induced not only when the system is made of an odd number of spins, but also when the length of the chain is equal to $L = 4N + 2$, for some $N \in \mathbb{N}$.

4.3 Analytical results close to the classical point

Among other properties, the phase transition across the multicritical point $\kappa_c = 0.5$ between the ordered phase and the antiphase at $h = 0$ manifests itself through a change in the dimensionality of the ground state manifold (GSM). For $\kappa < 1/2$, the system shows a two-fold degenerate GSM for any even L , generated by the two orthogonal Néel states. Instead, in the antiphase ($\kappa > 1/2$) two different situations arise, depending on the chain lengths. When $L = 4N$, the system is characterized by a four-fold GSM, composed

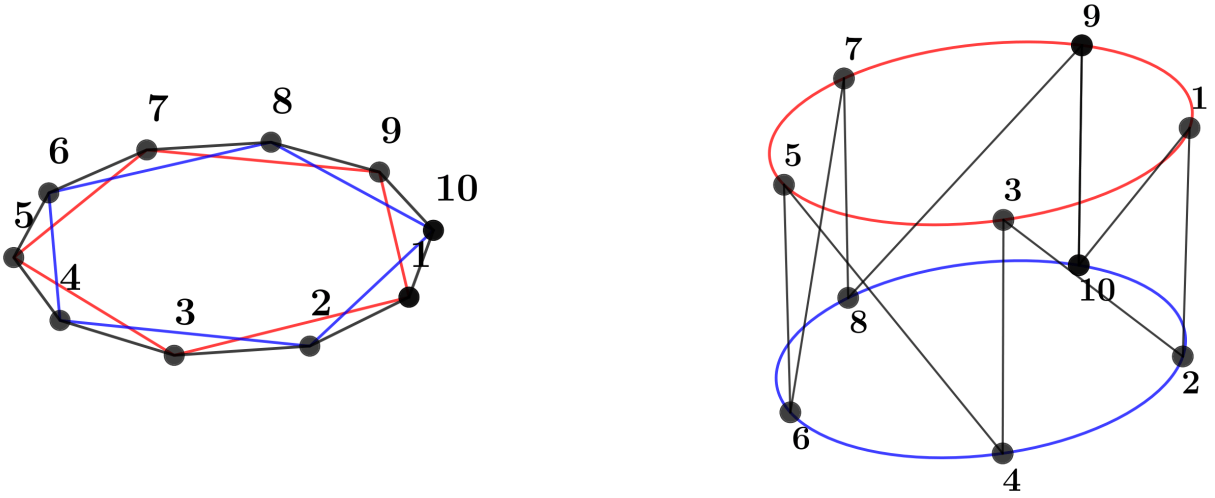


Figure 4.2: ANNNI chain for $L = 10$ lattice sites viewed as two interacting topologically frustrated Ising chains of length $L' = L/2$, composed of the odd and even spins, respectively. When $J_1 = 0$, the two rings are disconnected.

by periodic configurations with 4-sites periodicity ($|\uparrow\uparrow\downarrow\downarrow\uparrow\uparrow\downarrow\downarrow \dots\rangle$). On the contrary, for $L = 4N + 2$, the GSM shows a massive ground state degeneracy in which the number of elements scales quadratically with the system size. To understand it better, let us start by considering the case $J_1 = 0$.

4.3.1 GSM degeneracy for $J_1 = 0$

In this limit the system decomposes exactly into two independent spin rings, respectively made of the odd and the even lattice sites (see Fig. 4.2). Both the two rings are made of an odd number of spins $L' = L/2 = 2N + 1$ and are characterized by PBCs and AFM nearest neighbor interactions. Therefore, both rings are geometrically frustrated and admit $2L' = L$ independent ground states each [150, 155]. These states differ from each other in the position and in the orientation of a single ferromagnetic defect embedded in a Néel AFM state. For each ring, they can be written as

$$|k, \pm\rangle_{o,e} = T_{o,e}^{k-1} \bigotimes_{j=1}^{L'-1} \sigma_{2j}^z |\pm\rangle_{o,e}^{\otimes L'} , \quad (4.2)$$

where k runs from 1 to L' and marks the position of the ferromagnetic bond, $|\pm\rangle_{o,e}$ are the eigenstates of σ_i^x on each odd/even ring, and $T_{o,e}$ is the translational operator acting on each of the two rings. As long as we keep $J_1 = 0$, each state constructed as the direct product of states in Eq. (4.2) is a ground state of the whole system, resulting into a GSM with L^2 independent elements:

$$\mathcal{G}_0 = \{|k, \sigma\rangle_o |p, \sigma'\rangle_e, k, p = 1, \dots, L', \sigma, \sigma' = \pm\}. \quad (4.3)$$

4.3.2 GSM degeneracy for $J_1 > 0$

For finite J_1 , \mathcal{G}_0 splits into two subsets, each containing $L^2/2$ elements. Which of the two has lower energy depends on the sign of J_1 , and thus for definiteness let us focus on the AFM next-neighbor case ($J_1 > 0$). As shown in Fig. 4.3, it is clear that once a ferromagnetic defect is placed in one of the rings, the spin in the other ring lying between the two aligned spins minimizes the J_1 interaction by pointing in the opposite direction, thus halving the lowest energy configurations.

Therefore, for $J_1 > 0$, $h = 0$ and $\kappa > 1/2$ the GSM becomes

$$\begin{aligned} \mathcal{G} &= \{|\psi(k, p)\rangle \equiv |k, (-1)^k\rangle_o |p, (-1)^{p+1}\rangle_e, \\ &k = 1, \dots, L, \quad p = k, \dots, k+L'-1\}, \end{aligned} \quad (4.4)$$

where we exploit the PBCs of each ring, i.e. $k, p \equiv k, p \pmod{L'}$, and with a slight abuse of notation we identify the two eigenstates of σ^x with their eigenvalues, i.e. $\pm = \pm 1$. To make the relationship between the elements of \mathcal{G}_0 and the ones of \mathcal{G} as clear as possible, in Fig. 4.4 we provide a simple pictorial representation for the case $L = 10$.

4.3.3 Ground state near the classical point

A small transverse magnetic field h further breaks the super-extensive degeneracy left in \mathcal{G} , producing a band of closely lying states with a unique ground-state $|g\rangle$, similarly

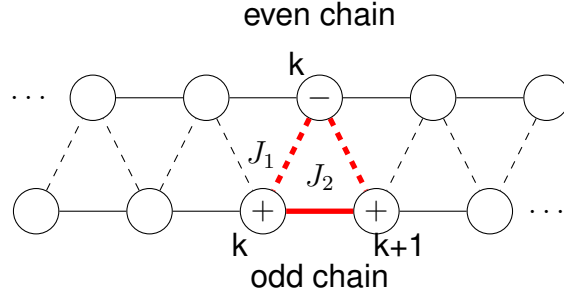


Figure 4.3: Specifying the configuration of the odd chain, namely fixing the ferromagnetic defect position (k in the figure), constrains the site on the even chain coupled to k and $k + 1$ by J_1 to have the opposite orientation to lower the state's energy. The case of a state of type $|k, +\rangle_o$ is illustrated. The overall effect of the J_1 interaction is then to split the degeneracy and reduce the number of low energy states on the even chain from L^2 to $L^2/2$.

to what occurs for 1D chains with only next-neighbor interactions [1, 148, 149]. To extract the ground-state of the system we employed lowest order degenerate perturbation theory. Despite the intricate structure of the perturbation matrix resulting from the interaction between the two TF rings, using graph theory (details for this calculation are presented in Appendix C.1.1), we are able to recover the analytic expression for the ground state in the antiphase with $L = 4n + 2$ sites close to the classical line for $J_1 > 0$.

It reads

$$|g\rangle = A \sum_{k=1}^L \sum_{p=k}^{k+L'-1} \sin \left[\frac{(p - k + 1)L\pi}{L + 2} \right] |\psi(k, p)\rangle, \quad (4.5)$$

where $A = 2/\sqrt{L(L + 2)}$ is the normalization constant.

From Eq. (4.5) we can recover the physical quantities of interest, but we will focus in particular on the bipartite Von Neumann Entanglement Entropy [242, 243].

4.3.4 EE near the classical point

The EE for the ground state $|g\rangle$ in Eq. (4.5) with respect to a bipartition of the chain into a subsystem A made by M contiguous spins and its complement \bar{A} is given by

$$S_M(\rho_A) = \text{Tr} [\rho_A \log \rho_A]. \quad (4.6)$$

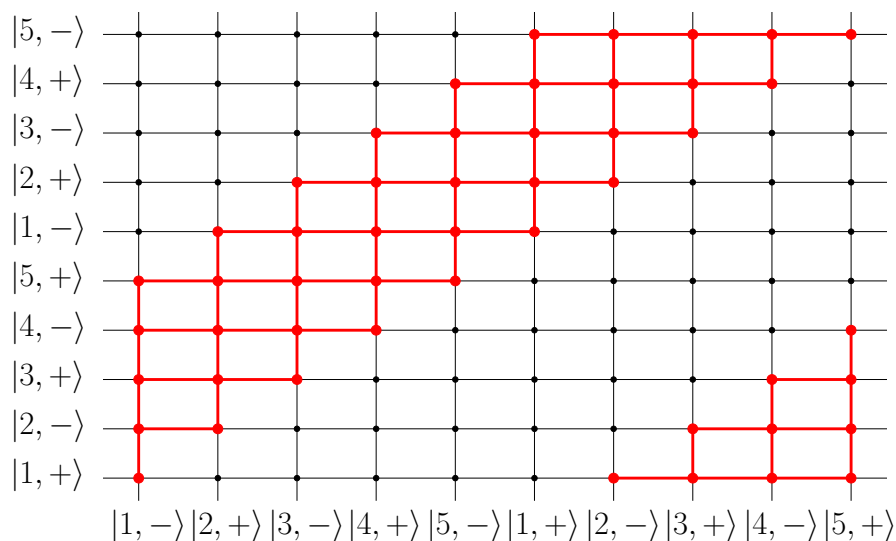


Figure 4.4: Pictorial representation of \mathcal{G}_0 and \mathcal{G} for a system of length $L = 10$. The states of the even and odd rings are represented respectively on the horizontal and vertical axis. Every vertex in the periodic grid is an element of the set \mathcal{G}_0 . The effect of the AFM interaction ($J_1 > 0$) is to select the subset compatible with the constraint in Fig. 4.3, which are represented by the red vertices.

Here ρ_A is the reduced density matrix obtained by tracing out from $|g\rangle$ all degrees of freedom outside A , i.e. $\rho_A = \text{Tr}_{\bar{A}}(|g\rangle\langle g|)$. To evaluate the EE we have to determine the spectrum of ρ_A . Let us sketch of the calculation here, while the details can be found in Appendix C.1.2.

We start noticing that, if both A and \bar{A} are made of more than four sites, only 16 eigenvalues of ρ_A are different from zero (and appear in 4 degenerate multiplets with multiplicity four), while all the others vanish identically. Taking into account the interaction graph showed in Fig. 4.4, it is possible to re-order the basis elements according to the position of the ferromagnetic defects being inside or outside A , such that a block-structure emerges in ρ_A . Although the resulting reduced density matrix is not block-diagonal, it is possible to prove that the off-diagonal block provide only subleading corrections to the matrix eigenvalues and thus in the thermodynamic limit the eigenval-

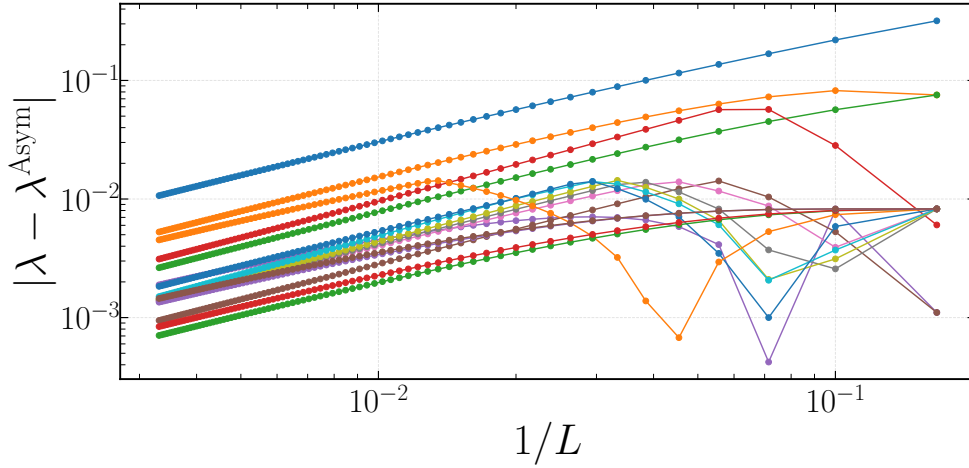


Figure 4.5: Absolute values of the difference of the numerical obtained 16 non-zero eigenvalues of ρ_A and the asymptotic values in Eq. (4.7) as function of the inverse of the chain length L .

ues of ρ_A coincides with those of the diagonal blocks, which are

$$\begin{aligned}
 \lambda_1(x) &= \frac{(1-x)^2}{4} - \frac{\sin^2 \pi x}{4\pi^2}, \\
 \lambda_2(x) &= \frac{x^2}{4} - \frac{\sin^2 \pi x}{4\pi^2}, \\
 \lambda_{3,4}(x) &= \frac{x(1-x)}{4} + \frac{\sin^2 \pi x}{4\pi^2} \pm \frac{\sin \pi x}{4\pi},
 \end{aligned} \tag{4.7}$$

where $x = M/L$ is the relative dimension of the partitions with respect to the chain length. In Fig. 4.5 we can observe for $M = L/2$ how the eigenvalues of ρ_A obtained from numerical diagonalization tend to coincide with the analytically determined values in the thermodynamic limit. Similar results can be obtained for different values of x , hence proving the validity of Eq. (4.7).

From Eq. (4.7) it is possible to recover the expression of the entanglement entropy for diverging L when $J_1 \neq 0$. Remarkably, it can be put in the form

$$\begin{aligned}
 S_M(\rho_A) &= 2 - y \log_2 y - (1-y) \log_2 (1-y) \\
 &\quad - z \log_2 z - (1-z) \log_2 (1-z),
 \end{aligned} \tag{4.8}$$

where

$$y = x - \frac{\sin \pi x}{\pi}, \quad \text{and} \quad z = x + \frac{\sin \pi x}{\pi}. \quad (4.9)$$

The first term on the RHS of Eq. (4.8) stems from the four-fold degeneracy of the eigenvalues and is due to the double \mathcal{Z}_2 symmetry of flipping each spin on each even/odd sub-lattice. The other terms represent the EE of two delocalized particles, each of them having probability y (z) of being in A . The factorization of the entropy contribution for each excitation indicates their independence, however their coefficients do not coincide with the geometrical probabilities $y = z = x = M/L$ (which emerge for $J_1 = 0$): the corrections in eq. (4.9) indicate a correlation between these excitation. Indeed, they are consistent with the result in [244], where the EE was calculated in the case of few excitations over the vacuum of a quadratic theory. In that case, each particle contributes with a probability that displays a correction due to the relative distance in momentum space. Eq. (4.9) fits the results in [244] if the two excitations in the ANNNI chain differ by $\Delta k = \frac{2\pi}{L}$, indicating that they are trying to minimize their kinetic energy under the Pauli-like constraint of occupying different momentum states.

Thus, quite remarkably, we found that the ground state EE of the TF ANNNI is compatible with the existence of two excitations. While the effects of geometrical frustration are commonly interpreted through a single particle description, the existence of multiple proper quasi-particles due to more complex frustration is quite unexpected. Based on previous results [1, 149–151], we expect that the emergence of this quasi-particle picture will have consequences also on other observables of the system. This is the case, for example, for the energy gap, which is expected to close as L^{-2} in a TF system, or for order parameters in the antiphase, which are expected to be destroyed or become incommensurate.

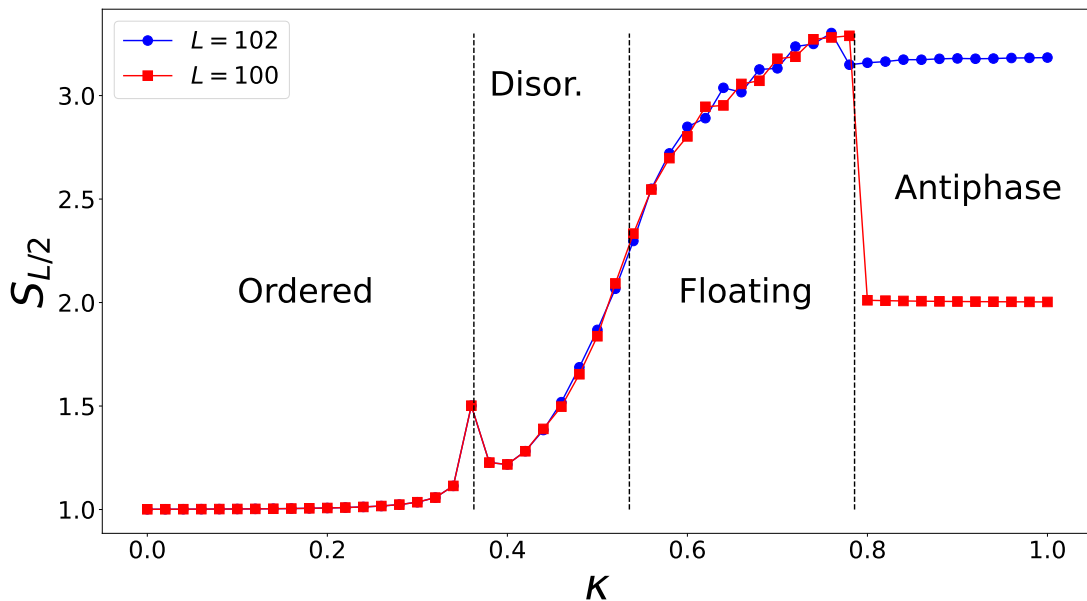


Figure 4.6: Comparison of the EE at half chain as a function of κ for $h/J_1 = 0.3$, between the case with TF ($L = 4N + 2$ blue dots), and without TF ($L = 4N$ red squares). The numerical data are obtained setting $N = 25$.

4.4 Numerical analysis

The ANNNI model Eq. (4.1) is notoriously not analytically solvable: to obtain results beyond the perturbative regime employed so far we use a density matrix renormalization group algorithm (DMRG) based on tensor networks [233, 245–248], in which the ground state is represented through a matrix product state (MPS). In order to avoid ambiguities in the canonization of the MPSs, we implemented the periodic boundary conditions directly in the matrix product operator (MPO) encoding the system’s Hamiltonian [249] rather than using periodic MPSs [250, 251]. Some details about our numerical approach can be found in Appendix C.2. The MPS approximation is known to be efficient for states possessing a finite amount of entanglement, as in the case of the ground-states of one-dimensional systems satisfying the area law [196, 252, 253] and has been already applied successfully for the ANNNI chain [239, 240]. From the results of the previous section, and in analogy with the ones obtained in other systems with TF [154], we expect that the amount of entanglement in the ground state must stay finite inside the antiphase even in presence of TF. Hence, the MPS representation of the ground state

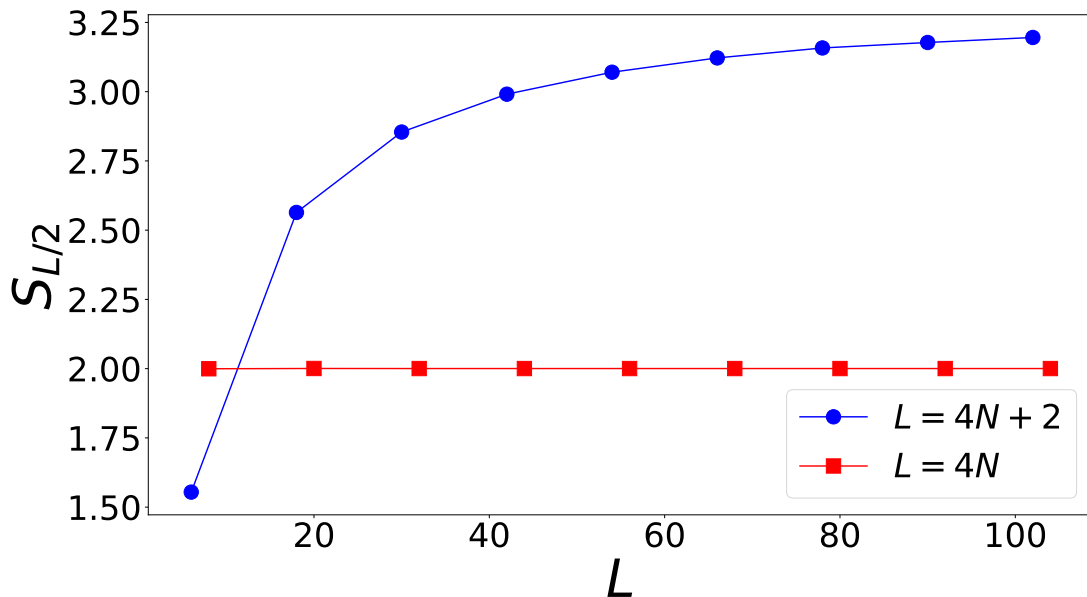


Figure 4.7: Bipartite Entanglement Entropy at half chain as a function of the length of the chain. The data are obtained using our DMRG algorithm for $J_2 = 1$, $h = 0.2$, $J_1 = 1$, for the case with TF ($L = 4N + 2$ blue dots), and without TF ($L = 4N$ red squares).

must be a faithful one. Such a representation of the ground state is particularly useful to evaluate the EE since the extraction of the partition related Schmidt coefficients [243] is straightforward.

Let us start with an overview of the general behavior of the EE across the phase diagram: we set the length of A to a half chain ($M = L/2$) and we evaluate the EE as a function of κ for $h/J_1 = 0.3$. The results obtained both for $L = 4N$ and $L = 4N + 2$ with $N = 25$, are plot in Fig. 4.6. In both the ordered and disordered phases, the EE values are practically indistinguishable from each other. Even in the floating phase, they tend to coincide in the limit of large N , although the convergence is slower and for $N = 25$ the differences can still be observed. This slow convergence is not a surprise, since the floating phase is known to be gapless and well approximated by a conformal field theory and thus the EE at half chain keeps growing logarithmically with the chain length and finite size effect are more prominent [235].

On the contrary, the behavior of the EE becomes different as soon as we enter the antiphase, where the topological frustration drastically affects the behavior of the

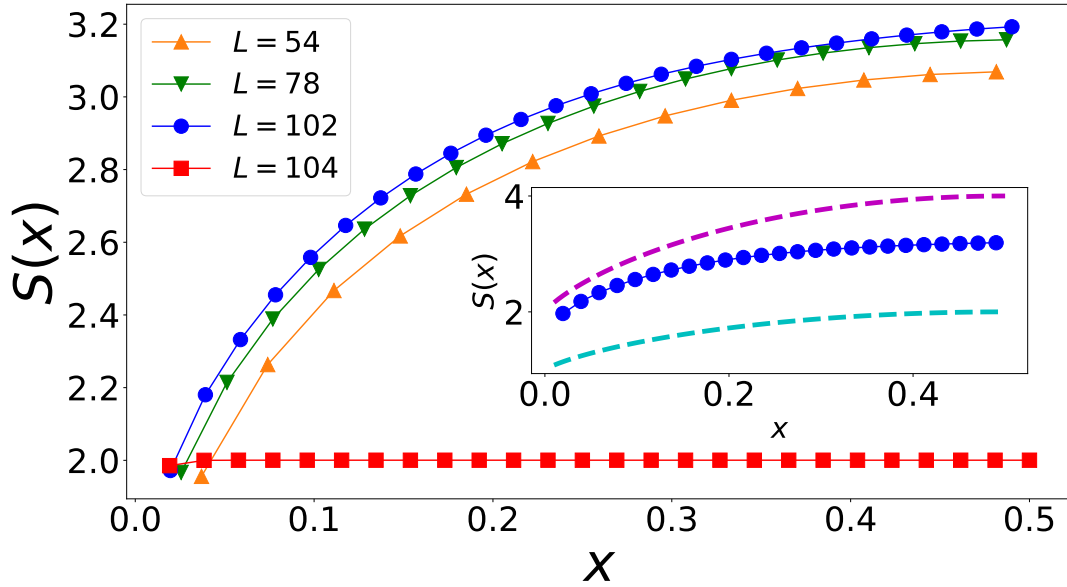


Figure 4.8: Bipartite entanglement entropy as a function of the ratio $x = M/L$ between the subsystem length and the length of the chain. The data is obtained using our DMRG algorithm for $J_2 = 1$, $h = 0.2$, $J_1 = 1$, for the TF (blue dots, green and orange triangles) and locally frustrated (red squares) ANNNI model, with $L = 102, 78, 54$ and $L = 104$ respectively. Inset: EE of the TF chain for $L = 102$ compared to the EE for a state with one (cyan dashed line) and two (purple dashed line) excitations (eq. (4.8) with $y = x, z = 0$ and $y = z = x$ respectively).

entanglement. Such a difference cannot be explained as finite size effects, as evidenced in Fig. 4.7, where the dependence of the EE at half chain is analyzed by varying the chain length for a fixed set of the Hamiltonian parameters inside the antiphase. While for systems whose length is an integer multiple of four the EE is virtually independent from the size, TF induces a dependence on L in the EE that, however, remains finite also in the thermodynamic limit. Fig. 4.8 highlights the different subsystem dependence of the EE in the two cases, with the not TF case quickly saturating to the (constant) area law. The inset further show that in the TF case the growth of the EE with the subsystem size lies in between that expected for a single and two delocalized, independent excitations.

From previous results on other TF models, a noteworthy observation emerged: in the thermodynamic limit, the different contributions to quantum resources decouple in the sum of two terms in which one coincide with the resource of the unfrustrated counterpart and the other is purely due to TF [154, 155]. This naturally leads to the hypothesis that a similar behavior occurs also in the EE of the ANNNI model. However, providing

evidences that support this hypothesis proves to be more delicate than in the previous cases, since for the ANNNI isolating the local contribution is challenging. In models with only nearest neighbor coupling, it is enough to change the interaction sign, thus removing TF. In the ANNNI model, reversing the signs of the interactions eliminates both TF and also the local frustration. Therefore, to remove TF while preserving the other local properties, we evaluate the EE for the same set of the Hamiltonian parameters $\mathcal{J} \equiv (J_1, J_2, h)$ and with the same length L but applying open boundary conditions and considering the subset A in the middle of an open chain, to reduce boundary effects. We compare the EE obtained in this way, which we denote as $S_M^o(\mathcal{J}, L)$, with the EE obtained assuming PBCs, namely $S_M^p(\mathcal{J}, L)$. If the hypothesis stands, the difference of these two quantities must be equal to the topological contribution that is provided by Eq. (4.8). In other words, if the hypothesis is verified the quantity $R(\mathcal{J}, x, L)$, defined as

$$R(\mathcal{J}, x, L) = \frac{S_M^p(\mathcal{J}, L) - S_M^o(\mathcal{J}, L)}{S_M(g)}, \quad (4.10)$$

when $L \rightarrow \infty$, shall tend to $R(\mathcal{J}, x, L) \rightarrow 1$. The data depicted in Fig. 4.9 clearly support this hypothesis. The analysis carried out in the inset indicates a power-law convergence in the thermodynamic limit with $\log(1 - R) = -0.89 \log L + 1.47$.

It is worth mentioning here that, we numerically observe that the local contribution to the EE in addition to the global 2 factor is minimal (approximately 10^{-3}) within the bulk of the antiphase and increases only close to the phase transition. Hence, even at finite h , the total entanglement entropy of the frustrated system can be well approximated by the perturbative formula obtained for $h \ll J_1$.

4.5 Conclusion

In summary, we considered the effects of the interplay between local and non-local sources of frustration in 1D spin chains through the analysis of the entanglement entropy

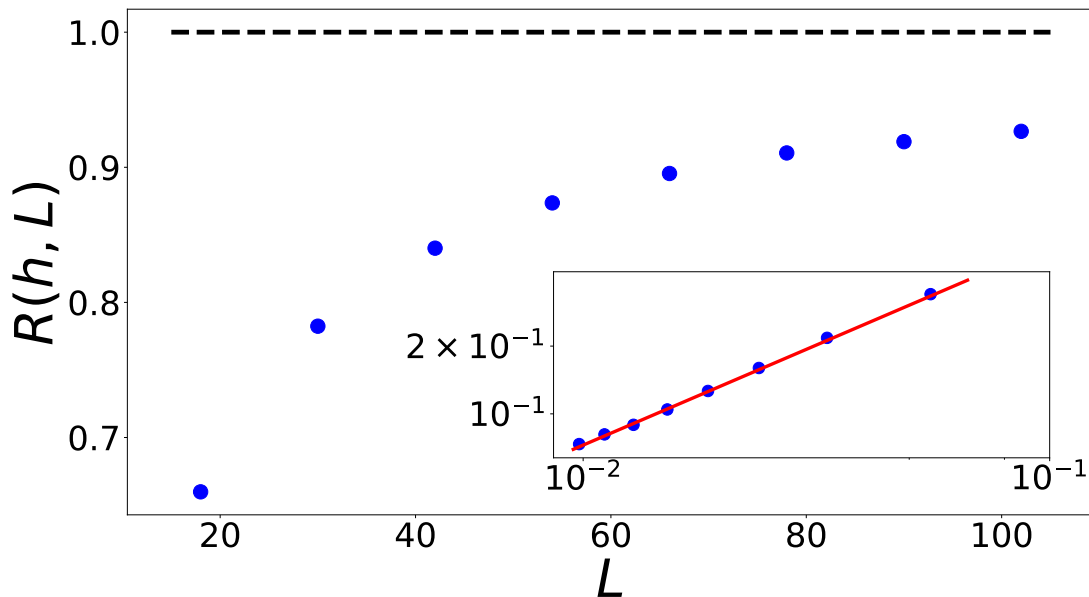


Figure 4.9: $R(h, L)$, defined in Eq. (4.10), as a function of the inverse system's size L^{-1} for $h = 0.2$, $\kappa = 1$. The inset shows a plot in log-log scale of $1 - R$ vs L , together with a linear fit, hinting to a power-law convergence in the thermodynamic limit, describe by the numerical law $\log(1 - R) = -0.89 \log L + 1.47$.

of the ANNNI model. The first type of frustration is due to the interplay between the nearest and next-to nearest neighbor interactions, while the non-local source (TF) is injected by a suitable choice of boundary conditions. In this work our focus centered on the antiphase region, where we revealed the presence of TF even in systems with an even number of spins, when the number of sites is not divisible by four. In this way, we showed that TF can emerge beyond the usual framework of geometrical frustration induced by FBCs (odd number of sites), presenting both usual and novel features.

The emergence of TF with an even number of sites can be traced back to the fact that, in the limit in which the interaction with first neighbors becomes negligible, the system decomposes into two independent topologically frustrated quantum Ising models.

Starting from this consideration, exploiting an analytical, perturbative approach valid close to the classical limit, we managed to obtain an analytical expression of the unique ground state of the model. From it, we were able to obtain the value of the EE for a generic bipartition composed of connected subsets of contiguous spins in the thermodynamic limit. We proved that the EE is decomposed into a contribution present also

without TF and one due to TF that indicates that the ground state hosts two excitations. The latter terms are independent, except for the fact that both particles tend to minimize their momenta, but cannot occupy the same momentum state and in this way they develop a correlation, as often happens in 1D system, where excitations typically acquire a fermionic nature.

To study the EE in the whole phase diagram of the model we employed a tensor network based DMRG code and observed that for $L = 4N + 2$ the effect of TF extends, and is limited, to the entire antiphase. There, we showed that the EE can be decomposed again into a non TF contribution (obtained by applying open boundary conditions to the same Hamiltonian) and that of two excitations, with the same values obtained in the analytical perturbative regime. The importance of this results stems from its consistency with what happens to every quantum resource analyzed so far in models with only nearest-neighbor interaction. It therefore supports the idea that this decomposition of quantum resources is a general characteristic of topologically frustrated systems.

We would like to stress once more that the unveiled quasi-particle description of the TF ANNNI chain is unexpected and required a meticulous effort to be exposed. We expect that similar results may be unveiled also for other frustrated systems.

Chapter 5

Frustrating quantum batteries

We propose to use a quantum spin chain as a device to store and release energy coherently, and we investigate the interplay between its internal correlations and outside decoherence. We employ the quantum Ising chain in a transverse field, and our charging protocol consists of a sudden global quantum quench in the external field to take the system out of equilibrium. Interactions with the environment and decoherence phenomena can dissipate part of the work that the chain can supply after being charged, measured by the ergotropy. We find that the system shows overall remarkably better performances, in terms of resilience, charging time, and energy storage, when topological frustration is introduced. Moreover, we show that in a simple discharging protocol to an external spin, only the frustrated chain can transfer work and not just heat.

5.1 Introduction

As we mentioned in section 1, a lot of effort has been put forward towards the design of quantum energy storage devices, namely quantum batteries (QBs). Inspired by this whole activity, with this work we would like to contribute to this field. However, while in the literature part of the interest around QBs has been directed towards providing energy to macroscopic systems, more recently some efforts have been directed also

towards situations in which quantum fluctuations play a dominant role with respect to thermal fluctuations [91, 115, 254–257]. Following this line, we specialize on devices operating purely in a quantum setting. We present a many-body system that can be charged through a change in the external magnetic field and used to transfer energy on a second target system. Most of all, we consider the effect of certain dephasing to show the resilience of the energy stored in the battery against time. In our investigation, we are driven by the observation that in the future it might be hard to design a universal quantum machine able to withstand any type of decoherence and dephasing and it will be necessary to combine several devices able to perform different tasks, while being optimized for resilience against different external conditions. Thus, we propose a protocol to start the development of such archipelago of devices, starting with the most basic quantum thermodynamic task. We introduce a sort of an activator for a series of quantum devices with which it exchanges energy. Since this device will share most of the properties of a QB, in the following we will refer to it as well as a quantum battery. However, we would like to stress that while QBs based on the Dicke model have already shown some important results in terms of scalability [108], we will defer the investigation of these properties for our device to a subsequent work, since now we are focused on describe the merit of its energy exchange with other quantum devices, not with macroscopic systems.

In particular, we analyze the work extraction from a system made of N interacting spins which, once charged, undergo complete dephasing in the energy eigenbasis of the associated Hamiltonian. More precisely, our analysis is focused on many-body models which exhibit exotic behaviors when proper Frustrated Boundary Conditions (FBCs) are imposed. A typical example is represented by a linear chain of an odd number of spins arranged in a ring geometry (i.e. with periodic boundary conditions): when classically paired with antiferromagnetic (AFM) interactions, such a system cannot realize the perfect Néel ordering [162, 258, 259], hence exhibiting topological frustration due to the presence of a ferromagnetic (FM) kink along the chain. At the quantum level, the

introduction of such frustration radically modifies the structure of both the ground-state manifold [1, 150, 151] and of the low-energy spectrum [149], leading to a whole set of novel behaviors [152–155] which are potentially interesting for technological applications. One important example is that while in non-frustrated models (at least far from critical points) the ground state manifold is separated by a finite energy gap from the rest of the spectrum, for the topologically frustrated systems it belongs to a band (for the ring geometry discussed above the gap closes as N^{-2}).

As a charging mechanism we consider a simple (relatively easy to implement) global quantum quench. Moreover, we show how topological frustration enhances the robustness to decoherence of a quantum battery: while in the non-frustrated case the ergotropy of the battery can be reduced to less than 30% of its initial value by decoherence phenomena, we observe that a frustrated battery manages to retain more than 90% of the original ergotropy in all the parameter ranges analyzed. Finally, we propose a simple discharging protocol that shows how it is possible to transfer energy from a many-body quantum battery charged with our protocol to an ancillary spin. Surprisingly, we observe that only frustrated batteries can transfer work efficiently, in the form of ergotropy, while the non-frustrated battery only manages to heat up the ancillary system.

in Sec. 5.2 we introduce the quantum spin models and the charging protocol that we consider to realize a quantum battery, as well as introducing the role of decoherence in these systems. In Sec. 5.3 we compare the performances of frustrated and non-frustrated batteries under the assumption of *fast charging*, i.e. considering a purely coherent charging protocol. In Sec. 5.4 we drop this assumption and analyze the effect of decoherence during the charging protocol introducing a non-unitary dynamics during the quantum quench. In Sec. 5.5 we present a protocol for energy transfer from a many-body quantum battery to a single ancillary spin. Finally, we discuss our results and possible developments in Sec. 5.6.

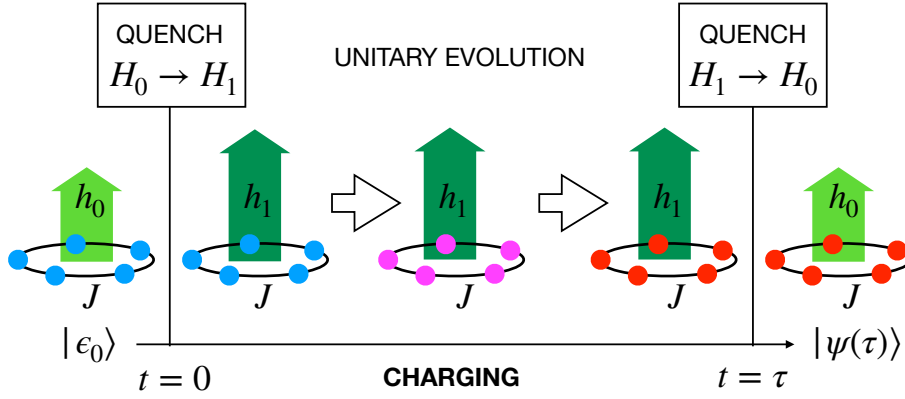


Figure 5.1: Schematic overview of the charging process: the QB is represented by a collection of an odd number N of spin-1/2 particles, initialized in the ground state $|\epsilon_0\rangle$ of the Ising Hamiltonian $H_0 = H(J, h_0)$ with local field $h = h_0$ and coupling J whose modulus is equal to 1. Setting $J = -1$ corresponds to considering a non-frustrated, FM QB model while setting $J = 1$ to a frustrated, AFM QB. Energy is pumped into the system by quenching the local field from h_0 to h_1 at time $t = 0$. The system then evolves during the time interval $[0, \tau]$ via the unitary evolution associated with the Hamiltonian $H_1 = H(J, h_1)$. Finally, the external field is restored to its original value h_0 at $t = \tau$.

5.2 The theoretical framework

5.2.1 The model

While the phenomenology of topological frustration has already been described in detail for more general models like the XYZ chain in Chapters 2 and 3, without losing generality, here we will focus on the simplest case, i.e. a ring of an odd number N of spin-1/2 particles coupled via the quantum Ising chain in a transverse magnetic field. The Hamiltonian of such a model is

$$H(J, h) = J \sum_{l=1}^N \sigma_l^x \sigma_{l+1}^x - h \sum_{l=1}^N \sigma_l^z, \quad (5.1)$$

where σ_l^α ($\alpha = x, y, z$) are Pauli operators acting on the l -th spin, $\sigma_{N+1}^\alpha = \sigma_1^\alpha$ enforces the periodic boundary conditions, and h is the strength of the external field. The constant J governs the nature of the couplings among the spins: its modulus $|J|$ determines the strength of the Ising interactions, while its sign allows us to tune from an AFM frustrated system, for $J > 0$, to a non-frustrated FM one for $J < 0$. In the rest of our analysis we

will fix $|J| = 1$, so that all the energies and times are measure in units of $|J|$ and $1/|J|$ respectively.

Regardless of the sign of J , the model is analytically integrable. Thanks to this, it is possible to observe how while some properties of the system are not affected by the presence or absence of topological frustration, others assume very different behaviors. An example of the latter is the existence of an energy gap between the ground state manifold and the closest set of excited states in the ordered phase $|h| < 1$. If, in the non-frustrated case, in the thermodynamic limit the two-fold ground state manifold is separated from the band of excited states by a finite energy gap equal to $\Delta_{FM} = 1 - |h|$, this disappears completely in presence of frustration. In fact, for $J = 1$, at finite sizes, the ground state is part of a band made of $2N$ states in which the gap between the two lowest energy elements closes according to the law

$$\Delta_{AFM} = \frac{|h|}{2(1 - |h|)} \frac{\pi^2}{N^2} + O(N^{-4}). \quad (5.2)$$

Hence, the frustrated AFM model presents a gap that vanishes quadratically with the system's size in the frustrated phase. While this expression is correct for $|h| < 1$, as we approach the critical points $h_c = \pm 1$ new corrections grow on the RHS of eq. (5.2) and eventually the gap of the frustrated and non-frustrated models tend to coincide and both close as N^{-1} close to criticality.

5.2.2 The charging protocol

To store energy in a spin system as the one described in (5.1), i.e. to use such a system as a QB, we propose a simple protocol based on quenches of the external magnetic field sketched in Fig. 5.1. The starting point is the ground state $|\epsilon_0\rangle$ with associated energy ϵ_0 of the Hamiltonian $H_0 = H(J, h_0)$. Such Hamiltonian admits a set of eigenstates that we denoted as $\{|\epsilon_\ell\rangle\}$, ordered in such a way that the associated eigenvalues ϵ_ℓ satisfy the following condition $\epsilon_\ell \leq \epsilon_{\ell+1}$. At time $t = 0$, we perform a sudden global quench

to the Hamiltonian $H_1 = H(J, h_1)$, whose eigenstates we denote by $\{|\mu_k\rangle\}$, ordered in such a way that $\mu_k \leq \mu_{k+1}$. The system then evolves unitarily under the action of H_1 for a certain time interval τ at which the system Hamiltonian is quenched back to H_0 to close the charging cycle. Note that h_1 can also be greater than $|J| = 1$ crossing the Ising quantum critical point and thus the charging process can also happen in a different phase, before we return to h_0 . In the absence of external interferences, the QB at the end of the charging process is described by the vector $|\psi(\tau)\rangle = e^{-iH_1\tau}|\epsilon_0\rangle$, and the energy stored is given by

$$E_{in} = \langle\psi(\tau)|H_0|\psi(\tau)\rangle - \epsilon_0 = \sum_{\ell} P_{\ell}(\tau)(\epsilon_{\ell} - \epsilon_0), \quad (5.3)$$

where the populations $P_{\ell}(\tau)$ are

$$P_{\ell}(\tau) = \left| \sum_k e^{-i\mu_k\tau} \langle\mu_k|\epsilon_0\rangle \langle\epsilon_{\ell}|\mu_k\rangle \right|^2. \quad (5.4)$$

Thanks to the integrability of the Hamiltonian in (5.1), it is possible to derive analytically the populations $P_{\ell}(\tau)$, see Appendix D.1 for details. In Fig. 5.2 we have plotted the $P_{\ell}(\tau)$ for both the frustrated and non-frustrated case for a specific choice of the system parameters. From the figure, it is possible to observe that, at the level of the populations of the eigenstates of H_0 , there is no clear difference between the two cases. As a consequence, also the amount of energy stored in the system is almost the same with small differences that vanish by increasing the system size.

5.2.3 The role of decoherence

As long as the evolution of the system remains unitary, it is always possible to reverse it, hence completely recovering the stored energy E_{in} . But, in presence of decoherence, the dynamics of a quantum system becomes non-unitary, and hence there is no unitary transformation that can bring the system back to its initial state, thereby reduc-

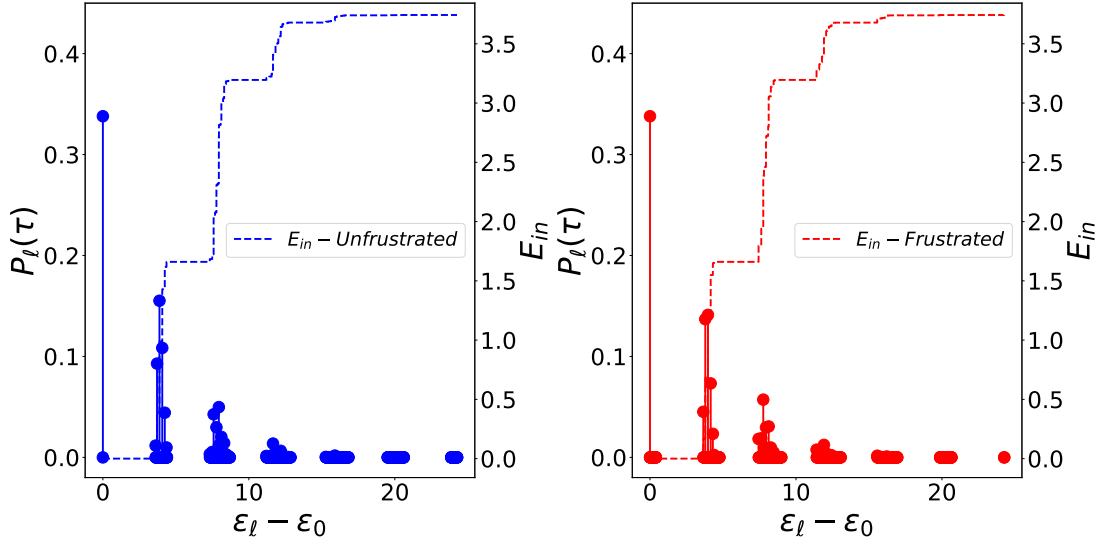


Figure 5.2: Plot of the distribution $P_\ell(\tau)$ of Eq. (5.4) which define the populations of the energy eigenspaces of the QB Hamiltonian $H_0 = H(J, h_0)$ after a cyclic quench from $h_0 = 0.1$ to $h_1 = 0.8$ and back to h_0 , for the frustrated $J = 1$ (right panel) and non-frustrated $J = -1$ (left panel) systems. The dashed lines represent the partial energy contributions to E_{in} , defined in eq. (5.3), due to the occupied states up to that spectral energy. These results are obtained for a chain of $N = 13$ spins setting $\tau = 0.5$.

ing the amount of energy that can be extracted from it [126, 127]. However, one of the main problems in the study of decoherence is that the results obtained are, in general, strongly dependent on the non-unitary dynamics model taken into account which, in turn, depends on the specifics of the experimental apparatus in which the model is tested. To carry out our theoretical analysis, we decided to consider, as a source of decoherence, a purely dephasing dynamics such as the one induced by the master equation proposed by Milburn [260]

$$\dot{\rho}(t) = -i[H(t), \rho(t)] - \frac{1}{2\nu}[H(t), [H(t), \rho(t))]. \quad (5.5)$$

Here $\rho(t)$ and $H(t)$ are the instantaneous system density matrix and Hamiltonian, $\dot{\rho}(t)$ is the derivative of the density matrix and ν parametrizes the characteristic decoherence rate of the model. Notice that the latter could depend, in principle, on the Hamiltonian's parameters and system's size.

Taking into account the charging process that we introduced, and hence the dependence on time of the Hamiltonian, the second term of the r.h.s. of (5.5) implies that the off-diagonal terms of the density matrix in the energy eigenbasis, characterized by finite oscillation frequencies, are exponentially suppressed with a characteristic decoherence time equal to $\tau_{k,l} \approx \frac{2\nu}{\Delta E_{k,l}^2}$, where $\Delta E_{k,l}$ is the energy difference between the states $|\epsilon_k\rangle$ $|\epsilon_l\rangle$ (or $|\mu_k\rangle$ $|\mu_l\rangle$ when we will consider a slow charging process.). While each entry decays at its own rate, it is possible to characterize some general, collective behavior. In order to do so, let us remark that the global quench $H_0 \leftrightarrow H_1$ preserves all the symmetries of the Hamiltonian, most importantly the translational and the parity symmetry along z , with the parity operator defined as $\Pi^z = \prod_{i=1}^N \sigma_i^z$. Therefore, since the initial state $|\epsilon_0\rangle$ is an eigenstate of the momentum operator with zero momentum and fixed parity, the occupied states ϵ_ℓ with $P_\ell(\tau) \neq 0$ are also eigenstates with the same parity as the ground state and vanishing momentum [153] and they are never degenerate, implying that all the relevant $\Delta E_{k,l}$ always differs from zero. As a consequence, after a sufficiently long time, due to the effect of the non-unitary dynamics, the state of the QB will be well approximated by a diagonal density matrix with zero coherence in the eigenbasis of the Hamiltonian (see Appendix D.2 for a formal solution of (5.5)). From Fig. 5.2 we can see that states with a non-vanishing population are distributed across different energy bands and thus their energy difference can be classified as either intra-band or inter-band. The energy difference $\Delta E_{k,l}$ between states belonging to different bands scale as $2(J - h)$ (with only subleading corrections dependent from N): if an off-diagonal term $\rho_{k,l}$ is related to two states coming from different bands, the timescale of its exponential suppression, which we call *fast decoherence time* τ_1 , has a functional dependence of the type $\nu/(J - h)^2$ on the system's parameters, with subleading, finite size N -dependent corrections. On the contrary, if the two states $|\epsilon_k\rangle$ and $|\epsilon_l\rangle$ belong to the same energy band, their energy difference is smaller, dependent on their relative position within the band and also changing with the chain length N . Accordingly, their decoherence timescale will be much larger, resulting into an overall *slow*

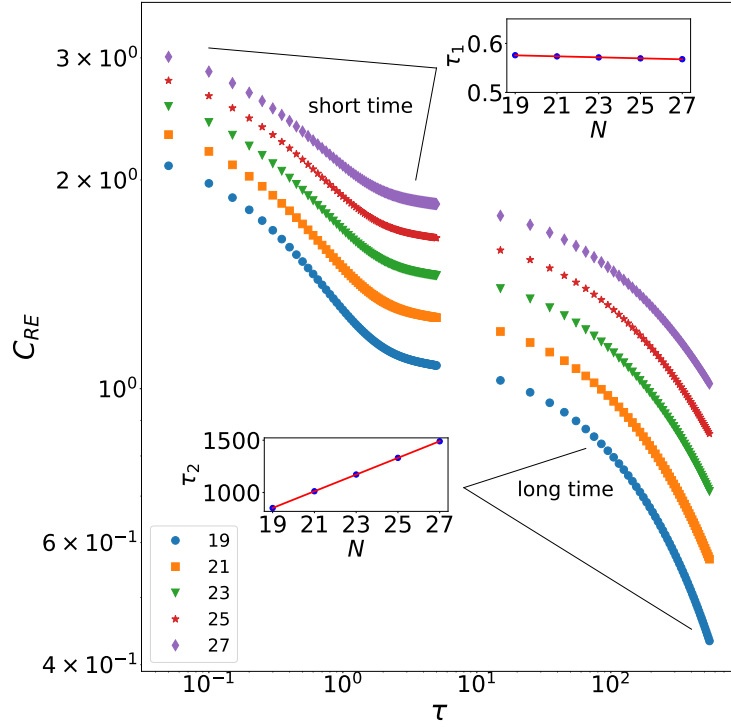


Figure 5.3: Plot of the entropy of coherence in Eq. (5.6) as a function of time under the decoherence dynamics of Eq. (5.5). We observe the emergence of two distinct decoherence time scales. A fast one, characterized by a short time τ_1 , which is weakly dependent on N , and a slower one with characteristic time $\tau_2 \gg \tau_1$, which instead is proportional to N . Data have been obtained for $J = 1$, $h_0 = 0.1$, $\Delta h = 0.5$ and $\nu = 10$. The results are the same for the frustrated and non-frustrated systems. Quantitatively, from a best fit analysis we find that $\tau_1 \approx 0.048 \frac{\nu}{(J-h_0)^2} + 0.001N$, while $\tau_2 \approx 80.8N - 688$.

decoherence time $\tau_2 \gg \tau_1$. The existence of two different timescales in the non-unitary dynamics induced by eq. (5.5) can be appreciated by looking at Fig. 5.3 in which, we have depicted the behavior of the relative entropy of coherence for the state $\rho(t)$, i.e. the $C_{RE}(\rho(t))$ [261], and provided an estimate of $\tau_{1,2}$ for some parameters' choice. The relative entropy of coherence is defined as

$$C_{RE}(\rho(t)) = S(\rho_D(t)) - S(\rho(t)) \quad (5.6)$$

where $S(x) = -\sum_i \lambda_i \log \lambda_i$ is the von Neumann entropy of the density matrix x with eigenvalues $\{\lambda_i\}$ and $\rho_D(t)$ is the diagonal matrix obtained by $\rho(t)$ artificially suppressing all the off-diagonal element in a given basis (the Hamiltonian eigenbasis in our case). From the plot, it is easy to see the existence of two very different time scales. An

heuristic fit on our numerical data show that indeed τ_1 shows a subleading dependence on N , while the linear growth of τ_2 with the system size can be interpreted as arising from the average intraband energy difference, which should go like $1/N$, since each band hosts order of N states in a finite with. Note that these estimates and fits are highly heuristic and valid only for system sizes of the order of those for which we have data, since a straightforward extrapolation to the thermodynamic limit would yield absurd projections. Nonetheless, since we are interested in finite systems, they suffice for our scope.

The estimation of these times allows for identifying different operating regimes for the QB. Since, ideally, a QB should be able to store energy for a long time, we have decided that, in this article, we will focus on the worst-case scenario, i.e. one where you try to extract work after a time $T \gg \tau_2$ has passed since the end of the charging process and we leave a detailed analysis of the time-scales $\tau_{1,2}$ and of the behaviors for intermediate times for further works. In this long-time scenario, the decoherence leads to the complete collapse of the QB density matrix into a diagonal ensemble in the system's energy eigenbasis. On the other hand, regarding the charging process, we will specifically examine two distinct charging regimes. The first of these is the so-called *fast-charging regime*, in which the charging time τ is considered to be much faster than that of any decoherence time $\tau \ll \tau_1$. As a consequence, the charging process can be considered a unitary process. On the other hand, the *slow-charging regime*, in which τ_1 and τ are comparable, a partial dephasing occurs also during the charging process.

5.3 The fast-charging regime

In the fast-charging regime (i.e. for $\tau_1 \gg \tau$) we can neglect the effect of the dephasing during the charging process. Under this hypothesis, the asymptotic state of the QB which emerges from Eq. (5.5) at time $T \gg \tau_2$ corresponds to the completely incoherent

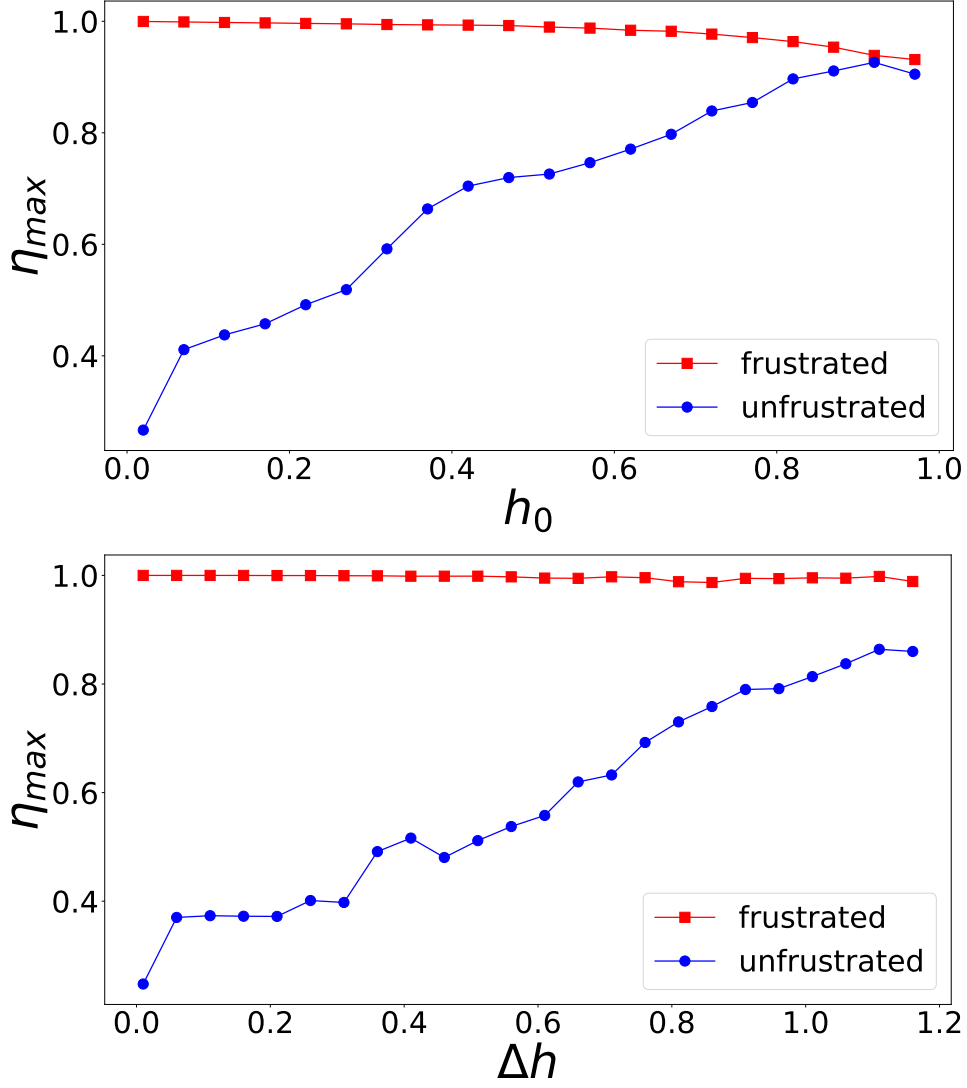


Figure 5.4: Maximum value of η defined in Eq. (5.10), computed as a function of h_0 (upper panel) for $\Delta h = 0.01$, and as a function of Δh (lower panel) for $h_0 = 0.001$. Data are obtained for charging times $\tau \in (0, 50)$, for a chain of $N = 25$ spins. These plots show how, after decoherence, the frustrated chain has retained most of its charge, while the non-frustrated one typically loses the majority of the initial charge.

(in the basis of the eigenstates of H_0) diagonal density matrix state

$$\rho(T) = \sum_{\ell} P_{\ell}(\tau) |\epsilon_{\ell}\rangle \langle \epsilon_{\ell}|, \quad (5.7)$$

where $P_{\ell}(\tau)$ are the populations defined in Eq. (5.4).

Following the prescription of [126, 127] the lowest energy state that can be reached with (reversible) unitary processes acting on the density matrix $\rho(T)$ is its passive coun-

terpart

$$\tilde{\rho}(T) = \sum_{\ell} \tilde{P}_{\ell}(\tau) |\epsilon_{\ell}\rangle \langle \epsilon_{\ell}|, \quad (5.8)$$

where $\tilde{P}_{\ell}(\tau)$ are the eigenvalues of $\rho(T)$ rearranged in decreasing order ($\tilde{P}_{\ell}(\tau) \geq \tilde{P}_{\ell+1}(\tau)$). The energy we can recover from the system via unitary operations can then be computed in terms of the system ergotropy, i.e. the difference between the energy of $\rho(T)$, and the mean energy of $\tilde{\rho}(T)$,

$$\begin{aligned} W &= \text{Tr}(\rho(T)H_0) - \text{Tr}(\tilde{\rho}(T)H_0) \\ &= \sum_{\ell} (P_{\ell}(\tau) - \tilde{P}_{\ell}(\tau))(\epsilon_{\ell} - \epsilon_0) \\ &= E_{in} - \sum_{\ell} \tilde{P}_{\ell}(\tau)(\epsilon_{\ell} - \epsilon_0) = E_{in} - E_{loss}. \end{aligned} \quad (5.9)$$

The quantity $E_{loss} = \sum_{\ell} \tilde{P}_{\ell}(\tau)(\epsilon_{\ell} - \epsilon_0)$ represents the amount of energy that we cannot extract any more from the battery. Since E_{loss} is a positive quantity, we have that, due to the non-unitary dynamics acting after the end of the charge phase, the work W that we can extract from the battery is less than the energy E_{in} stored in it. To quantify how robust the QB is towards decoherence, we compute the ratio between the amount of work we can extract from it at time $T \gg \tau_2$ and the energy initially stored in the QB, i.e.

$$\eta = \frac{W}{E_{in}}. \quad (5.10)$$

The results obtained with a semi-analytical approach, see App. D.1, are shown in Fig. 5.4. The results are obtained by maximizing η throughout the charging time τ in the interval $[0, 50]$ in the unit of $1/|J|$. In the top panel, we depict the behavior of η for a fixed value of $\Delta h = h_1 - h_0$ as a function of h_0 , while in the bottom one, we plot the result obtained keeping h_0 fixed and changing Δh .

As we can see, in the top panel, well below the critical point $h_0 = 1$, the frustrated

AFM battery is very resilient to the decoherence processes and, for a wide range of h_0 , η is close to 1 and well above 0.9. On the contrary, in the same range of parameters, the loss in the work extraction capability for an FM non-frustrated QB can go up to 80%. Moreover, in the bottom panel, the value of η for the frustrated battery is strikingly close to 1 in the whole range, while being considerably smaller for its non-frustrated counterpart.

To understand the difference between the frustrated and non-frustrated systems, we have to consider the different characteristics of their energy spectrum. In the magnetically ordered phase of non-frustrated systems such as the one we are considering, the energy spectrum is characterized by two quasi-degenerate states separated from the first band of excited states by a finite energy gap. Conversely, in frustrated systems, the ground state belongs to a band made of $2N$ states whose width is related to the value of the external field. By comparing these behaviors, taking into account the definition of E_{loss} , it is easy to explain the different behavior. Indeed, in the case of non-topologically frustrated models, already the third term of the summation in the definition of E_{loss} provides a non-negligible contribution to the loss of extractable energy and, likewise, all the others that follow. Conversely, in frustrated systems, the contribution of the first $2N$ terms to E_{loss} , since all states belong to the same band, is small and decreases as $|h_0|$ decreases. This greatly reduces the loss of energy that can be extracted from the battery and, consequently, increases η . However, when $|h_0|$ increases, the bandwidth of the frustrated model increases, reducing the value of W and hence of η while the gap of the ferromagnetic model narrows, resulting in an increment of η . These two different dependences on $|h_0|$ explain why, close to the quantum critical point, the performance of the two systems becomes comparable. Moreover, since the number of states in the first band of the frustrated systems is proportional to the size of the system itself, it is natural to expect that the effect of reduction of the relative weight of E_{loss} increases with N . This expected behavior is confirmed by the results shown in Fig. 5.5. In varying the system size, the value of η of the frustrated system remains approximately constant

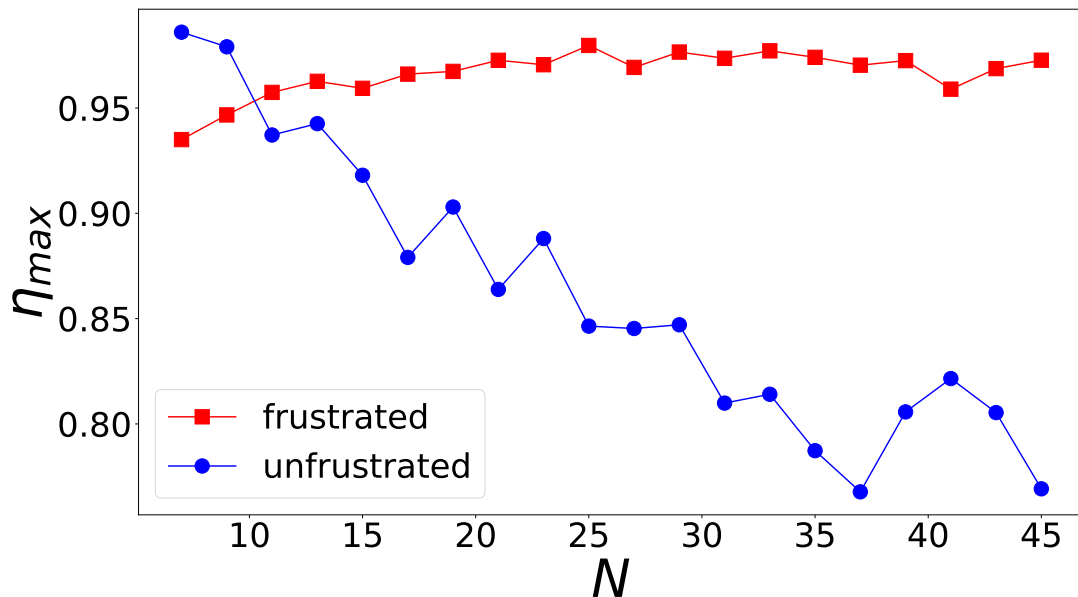


Figure 5.5: Maximum value of η in Eq. (5.10), computed for $\tau \in (0, 50)$, for the frustrated (red squares) and non-frustrated (blue dots) Ising chain. Data are obtained for chains of size $N \in [7, 45]$, for $h_0 = 0.751$ and fixed $h_1 = 0.7$.

while it goes down with the system size for the non-frustrated model.

A further parameter that is useful in characterising the performances of the QB is the time needed to complete the charging process. For our protocol, there is a certain degree in arbitrariness in this choice. We decided to define the *charging time* as the one for which the first local maximum of the E_{in} as a function of time is reached. This choice is motivated by the empirical observation, supported by the plots presented in D, that this time does not seem to scale with the system size and that subsequent maxima do not necessarily bring a significant improvement in energy. Moreover, this choice seems quite natural considering the necessity, inherent in the current status of quantum technologies, of keeping the charging time as short as possible. In Fig. 5.6 we show the results of an analysis of the charging time obtained varying Δh for a fixed value of h_0 . From the figure, we observe that, regardless of the presence or the absence of topological frustration in the system, the charging time generally decreases with increasing Δh while the energy stored in the system increases. This fact gives rise to a virtuous circle in which the time required for this storage decreases as the energy stored by the

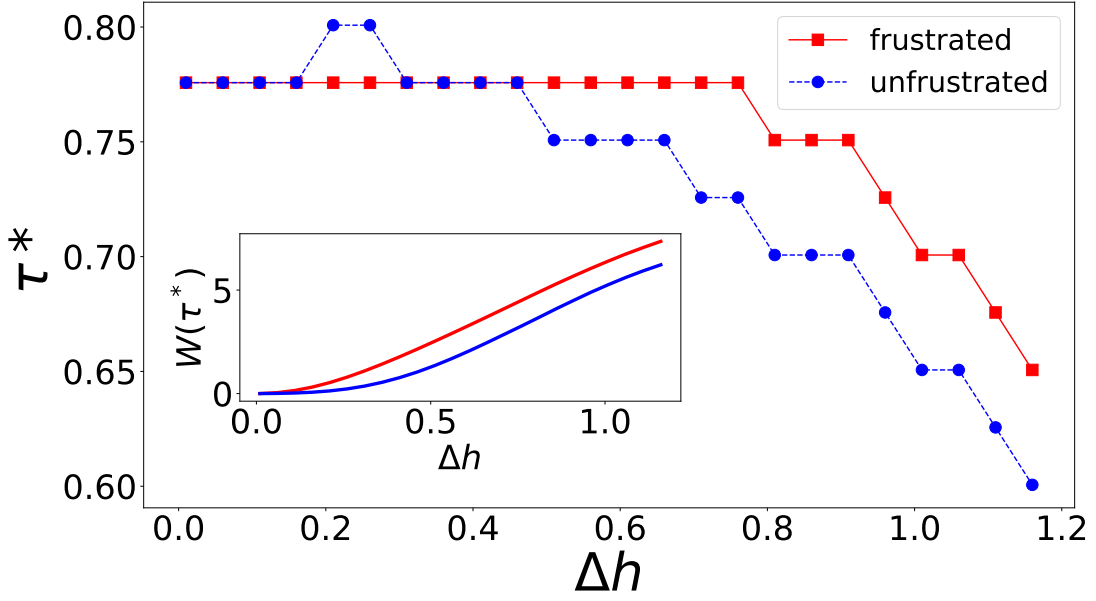


Figure 5.6: Position of the first local time maximum τ^* and the corresponding value of W (inset) for the frustrated (red) and unfrustrated (blue) Ising chain. Data are obtained for a chain of $N = 25$ spins, for $h_0 = 0.001$ and $h_1 - h_0 \in (0.01, 1.2)$.

system increases. Moreover, for frustrated systems, the ratio η always remains greater than 0.8 and significantly higher than the one of the non-frustrated counterparts. This means that by increasing the jump in the external magnetic field it is possible to charge the battery more, faster, and with higher resistance to decoherence. While this behavior is valid for both frustrated and non-frustrated QBs, the data witnesses the fact that the performances of the first are always better than the ones of the second.

5.4 The slow-charging regime

The results presented so far were obtained under the hypothesis that the charging protocol was so fast that we can completely neglect any decoherence effects during it. However, such a hypothesis is quite strong and an analysis of what happens when the charging process is affected by decoherence is mandatory. Therefore, in this section, we study the performance of our QB model in the slow-charging regime where the fast decoherence time τ_1 and the charging time τ are comparable. To this end, we numer-

ically integrate Eq. (5.5) during the charging time up to τ . Even if, in this regime, the analysis is more complex, the basic concepts are the same as in the previous section, and we recover that, after the end of the charging process, waiting for a time $T \gg \tau_2$ the state of the QB reduces to a completely incoherent state of the form

$$\rho(T) \simeq \sum_{\ell} P'_{\ell}(\tau) |\epsilon_{\ell}\rangle \langle \epsilon_{\ell}|, \quad (5.11)$$

where the populations $P'_{\ell}(\tau)$ are

$$\begin{aligned} P'_{\ell}(\tau) &= \sum_{k,k'} \langle \epsilon_{\ell} | \mu_k \rangle \langle \mu_k | \epsilon_0 \rangle \langle \epsilon_0 | \mu_{k'} \rangle \langle \mu_{k'} | \epsilon_{\ell} \rangle \\ &\times \exp \left[-\frac{(\mu_k - \mu_{k'})^2}{2\nu} \tau - i(\mu_k - \mu_{k'}) \tau \right], \end{aligned} \quad (5.12)$$

(see Appendix D.2 for details) that correctly reduces to Eq. (5.4) when all the exponential decays can be neglected. Note that, although the derivation of Eq. (5.5) in [260] is not valid in the $\nu \rightarrow 0$ limit, we can take this limit of fast dephasing by instantaneously removing all off-diagonal contributions.

Similarly to what was done in the previous section, we have compared the performances of the frustrated and non-frustrated QB models using the ratio η and the velocity of charging. We show the outcomes of the analysis in Fig. 5.7. For several values of the decoherence frequency ν , we charged the battery as a function of Δh , maximizing over time the robustness parameter $\eta = W/E_{in}$. As expected, by decreasing the decoherence frequency ν , hence making the decoherence stronger and faster in destroying the coherence of the QB state, η decrease but does not disappear completely even in the limiting case $\nu = 0$ where all the off-diagonal elements of the density matrix are instantaneously suppressed soon after the quench of the external field from $h_0 \rightarrow h_1$. However, once again, the frustrated battery shows a higher robustness with respect to its non-frustrated counterpart. Even in the limiting case of $\nu = 0$ (dashed line), the value of η is above 0.9 for a frustrated battery, while it drops below 0.5 for the non-frustrated

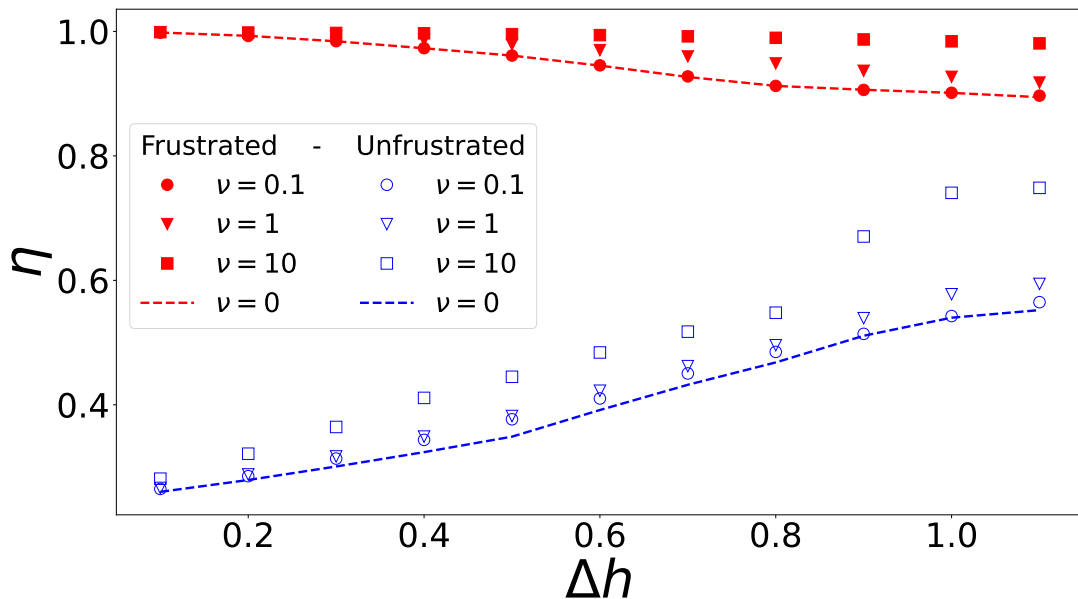


Figure 5.7: Maximum in time of the robustness parameter η for the frustrated (red) and non-frustrated (blue) for a decoherent charging protocol, for different values of the decoherence frequency: $\nu = 10, 1, 0.1, 0$ (squares, triangles, circles, dashed line). $\nu = 0$ corresponds to full decoherence, i.e. instantaneous convergence to the diagonal ensemble. Data are obtained for a chain of $N = 15$ spins, for $h_0 = 0.001$ and $h_1 - h_0 \in (0.02, 1.1)$.

one. These drops in η are more pronounced for larger values of the quench jump Δh . Indeed, for smaller quenches, the most populated state is still the ground state. Hence, at least in principle, one could still try to get as close as possible to the initial state when discharging the battery. However, this becomes more difficult when increasing Δh , as the number of excited states that are macroscopically populated increases, and therefore the loss of quantum coherence has a stronger impact on the value of the ergotropy and hence of η .

The decoherence also affects the charging time, making the charging slower for both the frustrated and the non-frustrated batteries. Therefore, we extend the analysis carried out in the previous section also to the case of the slow charging process. The results in Fig. 5.8 confirm the fact that the charging processes for both frustrated and non-frustrated systems are comparable, but, the virtuous circle that we have seen in the fast charging regime has disappeared. Indeed, while in the fast charging regime by increasing the quench amplitude Δh we would increase the ergotropy of the battery and

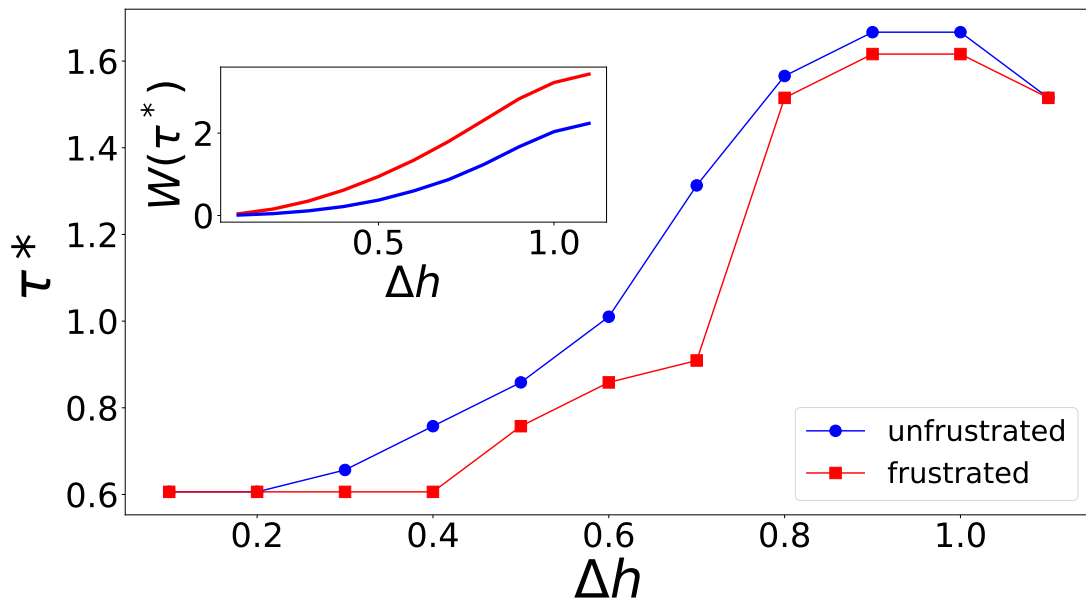


Figure 5.8: Position of the first local time maximum τ^* and the corresponding value of W for the frustrated (red) and unfrustrated (blue) Ising chain. Data are obtained for a chain of $N = 15$ spins, for $h_0 = 0.001$ and $h_1 - h_0 \in (0.01, 1.2)$ and $\nu = 1$.

observe a reduction of the charging time τ , in the slow charging regime it is still true that the ergotropy increases with the quench amplitude, but instead the charging time tends to increase, reducing the performances of the quantum battery.

5.5 Discharging the device

Up to now, we were mainly focused on the ergotropy of the system and how much it could be affected by the presence of an unavoidable non-unitary dynamic that continues to act even after the end of the charging process. However, such a quantity represents an upper bound of energy that can be extracted from a QB, which is hard to approach when this last is represented by a many-body system. Therefore, in this section, we have decided to analyze a more realistic situation in which the battery can act as an activator for a second quantum device. We take into account a situation in which a QB, after ending the charging process and waiting a time $T \gg \tau_2$ such that its state can be considered completely incoherent, is made to interact with an ancillary two-level system.

The Hamiltonian of the total system will therefore read as

$$H_W = J \sum_{k=1}^N \sigma_k^x \sigma_{k+1}^x - h \sum_{k=1}^N \sigma_k^z + \lambda H_{int} + \omega \sigma_S^z, \quad (5.13)$$

where $\{\sigma_k^\alpha\}_{k=1}^N$ and $\{\sigma_S^\alpha\}$ ($\alpha = x, y, z$) are respectively the spin operators of the k -th site of the QB and the ancillary spin, while ω is the characteristic energy of the ancillary spin.

To simulate a realistic condition, we consider that only one of the spins of the battery directly interacts with the ancillary system. Moreover, for the same reason, we do not try to optimize the kind of interaction between the QB and the ancillary system, which can give rise to extremely hard-to-simulate interactions, but we directly take into account a realistic one as the hopping term. Accordingly with these assumptions, H_{int} reads

$$H_{int} = \sigma_1^+ \sigma_S^- + \sigma_1^- \sigma_S^+, \quad (5.14)$$

where $\sigma_1^\pm = \sigma_1^x \pm i\sigma_1^y$ and $\sigma_S^\pm = \sigma_S^x \pm i\sigma_S^y$ and the strength of the interaction is parametrized by λ . Therefore, the ancillary spin is interacting with a single spin in the battery. The interaction that we have chosen breaks both the translational invariance and the parity symmetry of the battery, increasing the number of states accessible during the discharging process. Moreover, it can be experimentally realizable in Rydberg atom systems [262]. Before going further, let us underline that, ideally, one would want an interaction term that commutes with the rest of the combined battery/system Hamiltonian. However, since our battery is a many-body system where the eigenstates are delocalized, this would require an interaction term that interacts with the battery as a whole. However, such interaction, even if theoretically achievable, would be unrealistic from an experimental point of view.

In our simulation, we consider that, at time zero, the battery and the ancillary system are brought into contact by turning on the interaction in the equation. Before this, the two systems have been prepared. As far as the QB is concerned, we have at first charged it with the unitary protocol, stopping at the time of the first peak in η , for $h_0 = 0.018$, $h_1 = 1.5$

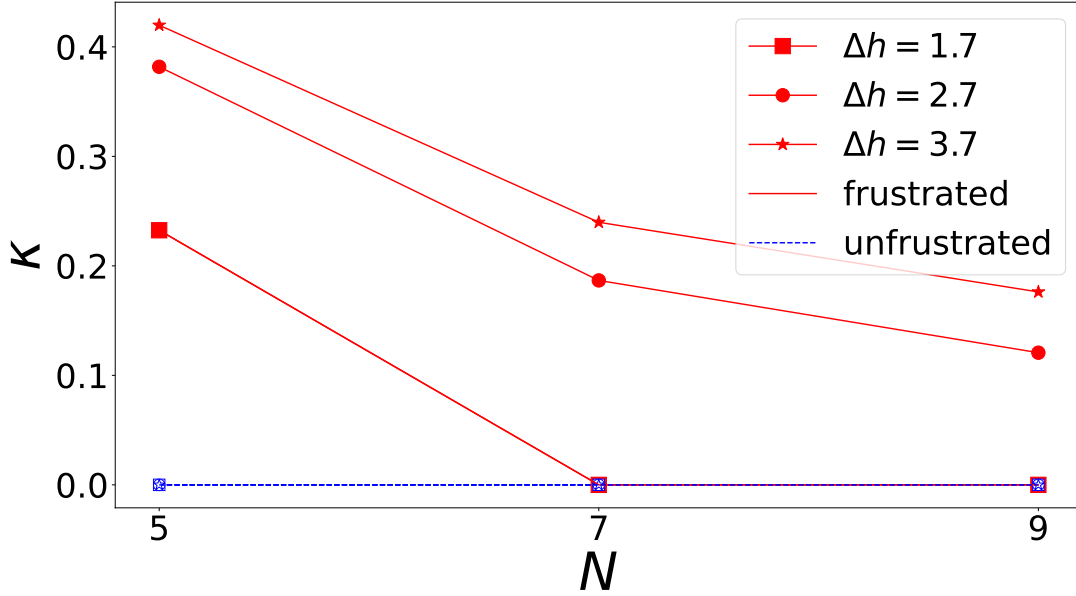


Figure 5.9: Ergotropy charged in the ancillary spin from the frustrated battery (full red) and non-frustrated (empty blue) batteries of $N = 5, 7,$ and 9 spins. The results are obtained for $h_0 = 0.02,$ $\omega = 2,$ $\lambda = 0.02$ and $h_1 = 1.72, 2.72$ and $3.72.$

and then let it relax to the diagonal ensemble. On the contrary, the ancillary system is initialized in its lowest energy state $\rho_S,$ i.e. spin down configuration, for $\omega = 2|J| = 2.$ This value of ω is chosen in such a way as to resonate with the band gaps of the battery spectrum, which for h_0 close to the classical point (i.e. $h_0 = 0$) are proportional to $J.$ The strength of the interaction between the spin and the battery was chosen small enough that the interaction does not carry too much energy into the system, but strong enough to allow for energy transfer. We established numerically that $\lambda = 0.02$ is a good compromise that ensures that no appreciable energy is absorbed or released from the interaction term.

Soon after $t = 0,$ the global system, initialized in the product state $\rho_B \otimes \rho_S,$ is allowed to evolve under the action of global Hamiltonian H_W and the energy starts to flow from the QB to the ancillary system. As for all systems, when some energy is provided to the ancillary spin, a part of it will be stored as work, while the rest will be dissipated as heat. Hence, a crucial question is whether and how much of this energy can be seen as work performed by the QB on the ancillary spin. One way to reply to this question is

to analyze the ratio κ between the ergotropy W_S acquired by the ancillary spin (that is initialized in a zero ergotropy state, i.e. its ground state) and its maximal ergotropy, i.e.

$$\kappa = \frac{W_S}{2\omega}. \quad (5.15)$$

In other words, κ is the amount of energy that can be later used by the ancillary spin to perform some work.

The results obtained through exact diagonalization for κ , for both the frustrated and non-frustrated battery, are shown in Fig. 5.9, for different values of Δh and of the size of the chain. The plot shows that none of the energy transferred from the non-frustrated battery is translated into ergotropy for the ancillary spin. On the contrary, the frustrated battery manages to charge the ancillary spin up to 42% of its maximal ergotropy. This percentage decreases with increasing size of the battery, due to the very local nature of the interaction between the battery and the ancillary spin. Motivated by these impressive results, we analyzed what happens when we change some conditions such as the values of h_0 or ω . The results of this analysis are presented in the Appendix D, and show that in most situations it is possible to find a window of values of λ in which the frustrated QB has good performances and manages to transfer ergotropy to the ancillary spin. This is not the case for the non-frustrated battery, which is never able to charge the ancillary qubit with more than heat. Thus, while a certain fine-tuning of the interaction strength λ is needed to ensure that the energy transferred is not due to the interaction itself, the results presented in Fig. 5.9 seem quite generic. At this stage it is not clear the origin of this striking difference between of the frustrated QB over the unfrustrated one. While the energy resilience against decoherence can be correlated to the battery energy spectrum, with a higher density of state at low energy in the frustrated case, the data we collected, and that we partially report in D indicate that a gapless spectrum is not sufficient to transfer ergotropy during our discharging protocol. We are thus led to speculate that the better performances of the frustrated battery in this respect

are due to the peculiar quantum correlations that are a characteristics of topological frustration [150, 151].

5.6 Conclusion and discussion of results

Quantum batteries are a critical and rapidly advancing technology, holding the promise to revolutionize energy storage. While they show great potential and significant progress has been made in terms of scalability, it is essential to acknowledge that quantum batteries are still in their early stages of research and development. In this context, our goal is to establish the foundation for an alternative approach to QBs that can be used to realize quantum devices that can work as energy activators in quantum technologies, by transferring energy to the quantum devices with which they are interacting. In particular, we propose a quantum battery based on a quantum many-body system, namely the quantum Ising chain, designing a cyclic charging protocol based on a global quench in the external magnetic field to store energy in the battery. We used different figures of merit to characterize the efficiency of such devices. In every case, we observed that the frustrated batteries present a very strong resistance to decoherence effects. This remarkable result is related to the fact that the ground state of the frustrated system belongs to a gapless band, allowing for a more efficient energy extraction with respect to the non-frustrated models, where the presence of a finite gap between the ground state and the rest of the spectrum increases the energy of the final equilibrium state of the battery, therefore reducing the fraction of energy which is possible to extract. Thus, our results show that topologically frustrated systems can represent a much more efficient option for the realization of a quantum battery with respect to their non-frustrated counterparts.

For the ergotropy, we tested the stability of these results by varying the parameters governing the model (N, h_0) and the charging protocol (Δh) . In all the measured ranges we always observe a higher robustness to decoherence for the frustrated model. In the

range of parameters that we considered, the charging time of the frustrated and non-frustrated batteries are comparable, even though for some values of the parameter we have observed shorter charging times for the non-frustrated one. However, even when the non-frustrated battery is charged a bit faster, the frustrated battery still possesses a higher ergotropy and a larger value of η . We expect these results to be valid even after increasing the system size. Moving towards the thermodynamic limit, one might expect that the value of η might decrease since the system will start populating states in higher energy bands (this has to be better investigated). However, at the same time, the density of the states within a band will increase as the gaps tend to close as N^{-2} , and for the frustrated system, the degeneracy will always be larger than for the non-frustrated one. Therefore, also in the thermodynamic limit we expect the frustrated model to be more robust to decoherence than the non-frustrated one.

Moreover, we analyzed what happens in a discharging process in which we connect an ancillary spin to the battery. We defined a protocol that allows energy transfer from the battery to the spin and measured the level of charge acquired by the spin, measured as the fraction of its maximal ergotropy κ . The results show that the energy transferred from the non-frustrated battery is not translated into ergotropy for the ancillary spin, while, within the considered parameters, the frustrated battery charges the spin up to 42% of the maximal ergotropy, which is 2ω . Therefore, topological frustration emerges as a very useful resource to enhance energy transfer from a QB. While the results obtained in Sec. 5.3 and Sec. 5.4 are solely related to the spectral properties induced by topological frustration, it is still unclear to which extent the structure of the internal correlations in topologically frustrated chains also plays a role in the energy transfer to an additional system. We leave this investigation to a future work.

As a final remark, we would like to point out that spin models such as the 1D quantum Ising chain can be experimentally realized with Rydberg atoms. In the currently available experimental platforms, typical values of the couplings are $\tilde{J} \approx \hbar \cdot 672$ MHz, $\tilde{h} \approx \hbar \cdot 25$ MHz, and the system can be stabilized for times of the order of $20 - 70 \mu s$. The

fastest decoherence time scale of the system can be estimated as the time it takes for the oscillating coherences to average out, i.e. $\tau_d \approx \hbar/(\tilde{J}\Delta E)$, where ΔE is the largest dimensionless energy difference between the energy eigenstates populated after the quantum quench for the Ising chain described by the dimensionless Hamiltonian $H(1, \tilde{h}/\tilde{J})$. Since ΔE is of order unity, the typical decoherence time will be of the order of a few tenths of nanoseconds. For the parameters mentioned above, we would have $\tau_d \approx 1.4$ ns. Since this time is considerably smaller than the time for which the system can be stabilized, decoherence effects might become relevant for a quantum battery realized on these platforms. Therefore, topologically frustrated quantum batteries, because of their high robustness to decoherence, might represent a valid alternative for the realization of these quantum devices.

Chapter 6

Exciton transport in two levels systems with long-range interaction

In this chapter we depart from the realm of topologically frustrated spin chains. We analyze the propagation of excitons in a d -dimensional lattice with power-law hopping $\propto 1/r^\alpha$ in the presence of dephasing, described by a generalized Haken-Strobl-Reineker model. We show that in the strong dephasing (quantum Zeno) regime the dynamics is described by a classical master equation for an exclusion process with long jumps. In this limit, we analytically compute the spatial distribution, whose shape changes at a critical value of the decay exponent $\alpha_{\text{cr}} = (d + 2)/2$. The exciton always diffuses anomalously: a superdiffusive motion is associated to a Lévy stable distribution with long-range algebraic tails for $\alpha \leq \alpha_{\text{cr}}$, while for $\alpha > \alpha_{\text{cr}}$ the distribution corresponds to a surprising mixed Gaussian profile with long-range algebraic tails, leading to the coexistence of short-range diffusion and long-range Lévy-flights. In the many-exciton case, we demonstrate that, starting from a domain-wall exciton profile, algebraic tails appear in the distributions for any α , which affects thermalization: the longer the hopping range, the faster equilibrium is reached. Our results are directly relevant to experiments with cold trapped ions, Rydberg atoms and supramolecular dye aggregates. They provide a way to realize an exclusion process with long jumps experimentally.

6.1 Introduction.

Energy transport is of fundamental importance in biological, chemical, and physical systems. In light-harvesting setups, for example, solar energy is converted into excitons that are transported to a reaction center or to the interface between two different semiconductors, which often relies on long-range dipolar couplings between the excitons [263–265]. Transport then results from a competition between coherent hopping that tends to delocalize the wavefunctions and local couplings to vibrational, motional degrees of freedom and disorder potentials, which lead to the localization of carriers [266–269], limiting the conversion efficiency of optoelectronic devices [270]. Theory has mostly focused on short-range couplings among quantum emitters, as they allow simple analytical approaches. For instance, the interplay between short-range hopping and local dephasing, which can be induced by, e.g., thermal noise or vibrational coupling [271], is captured by the Haken–Strobl–Reineker (HSR) model: for large enough dephasing, a transition from ballistic to diffusive motion occurs at time $t \sim 1/\gamma$ [272–274], with γ the local dephasing rate. Diffusion taking place for $t \gg 1/\gamma$ is standard, i.e., an initially localized exciton spreads as a Gaussian distribution $\exp(-r^2/4Dt)$, with a diffusion coefficient $D = 2J^2/\gamma$ (J is the nearest neighbor hopping rate). While the HSR model with nearest-neighbor hopping has been extensively analyzed and even solved exactly [272–276], the interplay of power-law long-range hopping and dephasing is more challenging and has not been analytically treated. Power-law hopping stems from the $\sim 1/r^3$ dipolar coupling in molecular aggregates [263–265] or nanocrystals [277–279], for instance, where large dephasing is naturally present [280–283]. More general power-law-type couplings with arbitrary spatial decay can be engineered in artificial systems such as cold trapped ions [284, 285] or Rydberg gases [286, 287].

Here, we investigate the HSR model with coupling between quantum emitters that decays with distance r as a power-law $\sim 1/r^\alpha$, with variable power α and for a generic dimension d . In the presence of strong dephasing – in the quantum Zeno regime [288]

– we map the system to a classical master equation (CME) that captures the long-time dynamics $t \gg 1/\gamma$, which we solve exactly by analytical and numerical means.

We find that excitons always diffuse anomalously: in the single-exciton limit, the CME is the one of a discrete random walk with long jumps, or discrete Lévy flight [289–291], and for any finite α the exciton density profile always decays algebraically at long distances, in contrast to the standard diffusion obtained from the HSR model with nearest-neighbor hopping. The interaction range α determines whether the variance of the distribution converges or not: based on this, we define the critical exponent $\alpha_{\text{cr}} = (d+2)/2$. For $\alpha \leq \alpha_{\text{cr}}$, the dynamics is superdiffusive and the exciton density at sufficiently long distance is always a Lévy stable distribution [290–293] characterized by a long-range algebraic tail $\sim 1/r^{2\alpha}$. For $\alpha > \alpha_{\text{cr}}$ and small enough time, the exciton density is also solely characterized by an algebraic tail, while at long time it exhibits a surprising mixed profile corresponding to a Gaussian distribution at short distance and an algebraic tail at large distance (Fig. 6.1a). The Gaussian part of the distribution mimics the standard diffusion in the HSR model. However, remarkably, also this Gaussian contribution is non-standard as the diffusion coefficient depends on α and is enhanced by the long range character of the hopping. We show that this finding is relevant to long-range exciton diffusion in light-harvesting systems such as nanocrystal quantum dots, where discrepancies between experimental observations and theory have been reported.

We find that in the case of many excitons our model is equivalent to a long-jump symmetric exclusion process [294–296], with a Markov matrix identical to the Hamiltonian of a long-range ferromagnetic Heisenberg model. Long-range hopping enhances exciton propagation so that equilibrium is reached faster as α is decreased. We capture the equilibration dynamics analytically via a continuous diffusion equation with fractional laplacian that qualitatively reproduces the numerical results for all α .

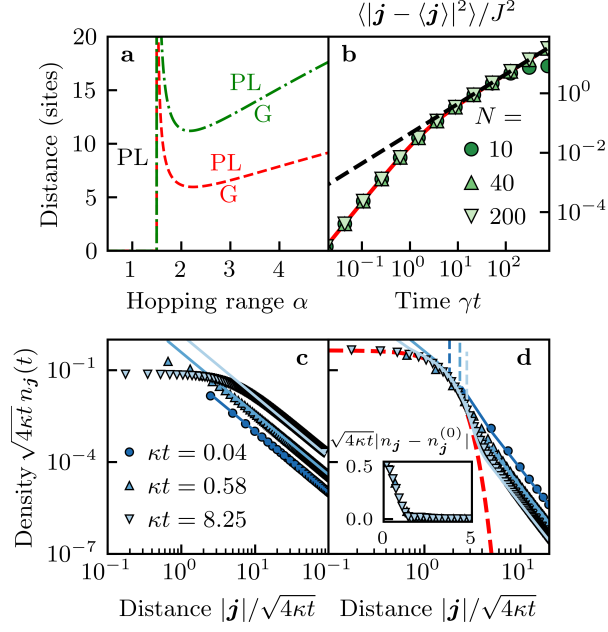


Figure 6.1: Single-exciton regime for $d = 1$: time evolution of an exciton initially located at site 0. The exciton density profile $n_j(t)$ is characterized by a power-law (PL) at long distance and a Gaussian (G) at short distance (a). The boundary between the two regions (red dashed line for $\kappa t = 1$ and green dashed-dotted line for $\kappa t = 3$) corresponds to $\xi_{\alpha,t}$ [see Eqs. (6.10)]. The quantum to classical crossover is illustrated through the time evolution of the exciton variance (b), obtained by numerically solving Eq. (6.1) for $\alpha = 3$ and $\gamma = 10J$. Red solid line: exact solution Eq. (6.3), black dashed line: classical approximation for $\gamma t \gg 1$ [Eq. (6.4)]. A pure power-law density profile for $\alpha = 1 < \alpha_{\text{cr}}$ (c) and mixed Gaussian–power-law for $\alpha = 2 > \alpha_{\text{cr}}$ (d) are obtained by numerically solving Eq. (6.7) for $N = 1000$ and $\gamma = 10J$. Solid lines: approximation Eq. (6.10), thick red dashed line: Gaussian term in Eq. (6.10b), thin dashed lines: $\xi_{\alpha,t}$. The diffusion enhancement with respect to the case $\alpha \rightarrow \infty$ [$n_j^{(0)}(t)$] is shown in the inset.

6.2 The single-exciton case

Excitons are modelled as spin-1/2 operators S . We start with the single-exciton case and study the dynamics in the presence of dephasing governed by the HSR quantum master equation

$$\dot{\rho} = -i[H, \rho] + \gamma \sum_j \left(L_j \rho L_j^\dagger - \frac{1}{2} \{L_j^\dagger L_j, \rho\} \right) = \hat{\mathcal{L}}\rho. \quad (6.1)$$

In our case, the coherent dynamics is described by the power-law hopping Hamiltonian

$$H = \frac{1}{2} \sum_j \sum_{r \neq 0} \frac{J}{r^\alpha} (S_j^+ S_{j+r}^- + S_j^- S_{j+r}^+), \quad (6.2)$$

with ρ the density matrix, $\mathbf{j} \in \mathbb{Z}^d$ the position in a d -dimensional lattice, $r = |\mathbf{r}|$, and $L_{\mathbf{j}} = L_{\mathbf{j}}^\dagger = S_{\mathbf{j}}^z$ the local dephasing operators, in the Lindblad formalism [297, 298]. For $d = 1$ and when a single exciton is initially present on a given site, it is known that the variance of the exciton evolves in time as [272]

$$\langle |\mathbf{j} - \langle \mathbf{j} | \mathbf{j} \rangle|^2 | \mathbf{j} - \langle \mathbf{j} | \mathbf{j} \rangle|^2 \rangle = 2 \sum_{\mathbf{r}} \frac{r^2 H_{\mathbf{r}}^2}{\gamma^2} (\gamma t + e^{-\gamma t} - 1), \quad (6.3)$$

with $H_{\mathbf{r}} = \langle G | S_{\mathbf{j}}^- H S_{\mathbf{j}+\mathbf{r}}^+ | G \rangle$ and $|G\rangle$ the ground state with all the spins down. The short- and long-time approximations of Eq. (6.3) read

$$\langle |\mathbf{j} - \langle \mathbf{j} | \mathbf{j} \rangle|^2 | \mathbf{j} - \langle \mathbf{j} | \mathbf{j} \rangle|^2 \rangle \approx \begin{cases} \sum_{\mathbf{r}} r^2 H_{\mathbf{r}}^2 t^2 & \text{for } \gamma t \ll 1 \\ 2 \sum_{\mathbf{r}} \frac{r^2 H_{\mathbf{r}}^2}{\gamma} t & \text{for } \gamma t \gg 1, \end{cases} \quad (6.4)$$

and reveal a crossover in the dynamics: while a coherent quantum dynamics dominates for short time, a classical diffusive-like behaviour emerges for $t \gg 1/\gamma$. This is illustrated in Fig. 6.1b, where the exciton variance is obtained by numerically solving the quantum master equation (6.1) for different system sizes N , and compared to the analytical solutions Eqs. (6.3) and (6.4). The crossover from ballistic to diffusive regime is clearly visible. Interestingly, the transition to the classical regime always occurs at $t \sim 1/\gamma$, independently of N and α . This is because in Eq. (6.4), the same multiplicative factor $\sum_{\mathbf{r}} r^2 H_{\mathbf{r}}^2$ governs both the short- and late-time behaviors, so the crossover time scale is independent of the details of the Hamiltonian. In Fig. 6.1b we see that for $\gamma t \gtrsim 10$, the quantum dissipative evolution is indistinguishable from the long-time asymptotics in Eq. (6.4).

Importantly, Eq. (6.3) implies that the late-time diffusive-like regime is always reached, for any dephasing strength γ . This can also be seen from the QME (6.1). Indeed, for any dephasing, we observe numerically that for large system size and long time ($t \gg 1/\gamma$) the coherences in the single-particle density matrix, $G_{\mathbf{j},\mathbf{m}} = \text{Tr}[\rho S_{\mathbf{j}}^+ S_{\mathbf{m}}^-]$, with $\mathbf{j} \neq \mathbf{m}$,

become negligible with respect to the population density $n_j = G_{j,j}$. However, in the limit of weak dephasing, this effect cannot simply be explained from perturbation theory in γ , as the long-time dynamics is determined by a non-perturbative branch of eigenmodes of the Liouvillian $\hat{\mathcal{L}}$ [Eq. (6.1)]. An analogous effect has been observed in the case of nearest-neighbors hopping with dephasing [299] and more sophisticated techniques should be used [276] (see Appendix E for some details). Next we turn to the strong dephasing limit, which can be handled analytically more easily.

6.2.1 Strong dephasing: mapping to classical Markov process.

Following Refs. [300, 301], we use a second-order perturbative analysis, deriving an effective Liouvillian $\hat{\mathcal{L}}_{\text{eff}}$ in the limit $\gamma \gg J$ (for similar treatments of the strong dissipative limit, see also [302, 303] for soft-core bosons and nearest-neighbor hopping, or [304, 305] for atom losses instead of dephasing). We split the Liouvillian Eq. (6.1) into two contributions, a term $\hat{\mathcal{L}}_0 \rho = \gamma \sum_j (S_j^z \rho S_j^z - \rho/4)$, and a perturbation $\hat{\mathcal{L}}_1 \rho = -i[H, \rho]$. We find that the effective dynamics $\dot{\rho} = \mathcal{L}_{\text{eff}} \rho$ is governed by a CME for the probability distribution

$$\dot{p}(\boldsymbol{\sigma}) = - \sum_{\boldsymbol{\sigma}'} \langle \boldsymbol{\sigma} | R | \boldsymbol{\sigma}' \rangle p(\boldsymbol{\sigma}'), \quad (6.5)$$

with $|\boldsymbol{\sigma}\rangle$ the eigenstates of the S_j^z operators, and $p(\boldsymbol{\sigma})$ the probability distribution defined by the diagonal entries of the density matrix $\rho = \sum_{\boldsymbol{\sigma}} p(\boldsymbol{\sigma}) |\boldsymbol{\sigma}\rangle \langle \boldsymbol{\sigma}|$. The generator of the CME (6.5) is that of an exclusion process with long jumps, which turns out to be identical to the following Hamiltonian of a long-range ferromagnetic Heisenberg model

$$R = - \sum_{j:r \neq 0} \frac{2J^2}{\gamma r^{2\alpha}} \left[\frac{1}{2} (S_j^+ S_{j+r}^- + S_j^- S_{j+r}^+) + S_j^z S_{j+r}^z - \frac{1}{4} \right]. \quad (6.6)$$

A similar observation was made in Refs. [300, 301] for strictly short-range models, whose strong-dephasing limit corresponds to a ferromagnetic Heisenberg model with

short-range couplings; here we extend this result to long-range hopping. We note that, interestingly, the case $\alpha = d = 1$ in Eq. (6.6) corresponds to the Haldane-Shastry Hamiltonian [306, 307], a famous quantum integrable model. For any exciton number, the associated exclusion process should then be exactly solvable by Bethe Ansatz techniques, which we will investigate in a future work.

6.2.2 Anomalous diffusion of single exciton.

We first focus on the classical dynamics dictated by Eq. (6.5) for the case of a single exciton. Equation (6.6) provides the evolution of the population density

$$\dot{n}_j = \sum_{r \neq 0} \frac{\kappa}{r^{2\alpha}} (n_{j+r} - n_j), \quad (6.7)$$

with the effective Zeno-like rate $\kappa = 2J^2/\gamma$. An alternative derivation of Eq. (6.7) is obtained by adiabatically eliminating the coherences of the single-exciton density matrix $G_{j,m}$ [272, 288]. Notice that Eq. (6.7) is well defined in the thermodynamic limit only if $\alpha > d/2$ so that $\sum_{r \neq 0} r^{-2\alpha}$ is finite. In order to solve Eq. (6.7) for an exciton initially at the origin, $n_j(t=0) = \delta_{j,0}$, we introduce the characteristic function $K(\mathbf{q}, t) = \sum_j n_j(t) e^{i\mathbf{q} \cdot \mathbf{j}}$, where $\mathbf{q} \in \mathbb{R}^d$. Using Eq. (6.7), we find that the characteristic function at time t then reads

$$K(\mathbf{q}, t) = e^{(\mathcal{A}_{2\alpha,d}(\mathbf{q}) - \mathcal{A}_{2\alpha,d}(\mathbf{0}))t}, \quad (6.8)$$

with the initial condition $K(\mathbf{q}, 0) = 1$, and $\mathcal{A}_{2\alpha,d}(\mathbf{q}) = \kappa \sum_{r \neq 0} r^{-2\alpha} e^{-i\mathbf{q} \cdot \mathbf{r}}$. Equation (6.8) provides the time evolution of the mean position $\langle \mathbf{j} \rangle = -i \nabla_{\mathbf{q}} K(\mathbf{0}, t) = \mathbf{0}$ and of the variance $\langle |\mathbf{j}|^2 \rangle = -\Delta_{\mathbf{q}} K(\mathbf{0}, t) = 2D_{\alpha} t$. The diffusion coefficient $D_{\alpha} = \frac{1}{2} \mathcal{A}_{2\alpha-2,d}(\mathbf{0})$ provides a first insight into the character of the dynamics for different α (however, see also discussion below): diffusive-like spreading of excitons takes place when D_{α} converges in the thermodynamic limit, which is ensured when $\alpha > \alpha_{\text{cr}}$. This corresponds to the quantum master equation solution in the regime $\gamma t \gg 1$, shown in Eq. (6.4) and

Fig. 6.1b. On the other hand, for $\alpha \leq \alpha_{\text{cr}}$, D_α diverges and the dynamics is superdiffusive. Equation (6.8) further allows one to determine the exciton density profile $n_j(t)$ for all α and times t . Since the long-distance behavior of $n_j(t)$ is determined by the singularity of $K(\mathbf{q}, t)$ when $q \equiv |\mathbf{q}| \rightarrow 0$, we analyze $\mathcal{A}_{2\alpha, d}(\mathbf{q})$ in that limit. We find $\mathcal{A}_{2\alpha, d}(\mathbf{q}) \approx \mathcal{A}_{2\alpha, d}(\mathbf{0}) - C_\alpha q^{2\alpha-d}$ if $\alpha \leq \alpha_{\text{cr}}$, and $\mathcal{A}_{2\alpha, d}(\mathbf{q}) \approx \mathcal{A}_{2\alpha, d}(\mathbf{0}) - \frac{\mathcal{A}_{2\alpha-2, d}(\mathbf{0})}{2} q^2 - C_\alpha q^{2\alpha-d}$ if $\alpha > \alpha_{\text{cr}}$, with $C_\alpha = -\kappa\pi^{\frac{d}{2}} 2^{d-2\alpha} \Gamma(\frac{d}{2} - \alpha) / \Gamma(\alpha)$. The expression of C_α depends on the boundary conditions: here we have assumed translational invariance. Inserting these expressions into Eq. (6.8), the characteristic function finally reads

$$K(\mathbf{q}, t) \underset{q \rightarrow 0}{\simeq} \begin{cases} e^{-C_\alpha q^{2\alpha-d} t} & \alpha \leq \alpha_{\text{cr}} \\ e^{-D_\alpha q^2 t} e^{-C_\alpha q^{2\alpha-d} t} & \alpha > \alpha_{\text{cr}}. \end{cases} \quad (6.9)$$

For $\alpha \leq \alpha_{\text{cr}}$, this is the characteristic function of a Lévy stable distribution [290–293], which is characterized by a long-range algebraic tail. Such a distribution corresponds to large but infrequent steps, the so-called rare events or big jumps relevant to a large variety of phenomena including motion of cold atoms in laser cooling, transport in turbulent flow, and neural transmission [308]. For $\alpha > \alpha_{\text{cr}}$, instead, the characteristic function has a peculiar mixed nature: it is the product of a Gaussian and of the Lévy flight factor.

From the inverse Fourier transform of $K(\mathbf{q}, t)$ we obtain the population $n_j(t)$. For $\alpha \leq \alpha_{\text{cr}}$ the asymptotic behavior $n_j(t)$ depends on j as

$$n_j(t) \underset{|j| \gg 1}{\simeq} \kappa t / |j|^{2\alpha}, \quad (6.10a)$$

while for $\alpha > \alpha_{\text{cr}}$ we obtain the following mixed Gaussian and power-law behavior with increasing $|j|$

$$n_j(t) \simeq \begin{cases} \frac{\exp(-|\mathbf{j}|^2/4D_\alpha t)}{(4\pi D_\alpha t)^{d/2}} & |\mathbf{j}| \lesssim \xi_{\alpha, t} \\ \kappa t / |\mathbf{j}|^{2\alpha} & |\mathbf{j}| \gg \xi_{\alpha, t}, \end{cases} \quad (6.10b)$$

which is one of the main results of this work. In Eq. (6.10b), $\xi_{\alpha, t}$ is the length scale at which the behavior crosses over from Gaussian to power-law. For large enough time,

$\xi_{\alpha,t}$ is well approximated by $\xi_{\alpha,t} \approx \sqrt{4D_\alpha t \log[4\alpha^\alpha \pi^{-d/2} \kappa^{-1} D_\alpha (4D_\alpha t)^{\alpha-\alpha_{\text{cr}}}]}$. The exact expression of $\xi_{\alpha,t}$ exhibits a minimum as a function of α , and a discontinuity at $\alpha = \alpha_{\text{cr}}$ [Fig. 6.1a]. For large α , $\xi_{\alpha,t}$ increases with α as $\xi_{\alpha,t} \sim \sqrt{4D_\alpha t \alpha \log \alpha}$, and we ultimately recover a standard diffusive (Gaussian) behavior for $\alpha \rightarrow \infty$. For $\alpha \rightarrow \alpha_{\text{cr}}^+$, D_α diverges and therefore $\xi_{\alpha,t}$ does too. For small enough time, the power-law behavior takes over for all α . We emphasize that since $\xi_{\alpha,t}$ grows with time, the Gaussian dynamics ultimately dominates at long times for $\alpha > \alpha_{\text{cr}}$, and thus we expect the algebraic tail to particularly affect transient phenomena.

This behavior is illustrated in Fig. 6.1c,d for $d = 1$, where we show a numerical solution of the CME (6.7) together with the asymptotic behavior Eq. (6.10). For $\alpha < \alpha_{\text{cr}}$, the distribution is only characterized by a power-law decay with amplitude growing linearly with time and independent of the lattice dimension d [Fig. 6.1c]. The scaling with the distance $1/|j|^{2\alpha}$ turns out to be the same as the hopping rate. While the decay of the distribution still goes as $\sim 1/|j|^{2\alpha}$ at long distances for $\alpha > \alpha_{\text{cr}}$, diffusion dominates at short distances showing a Gaussian profile [Fig. 6.1d], but with an enhanced diffusion coefficient D_α as compared to the nearest-neighbor case (inset). In the usual dipolar coupling case $\alpha = d = 3$, for instance, we find that D_α is enhanced by a factor ≈ 2.8 as compared to standard diffusion with nearest-neighbor hopping. Interestingly, we find that those power-law tails have a profound effect on the dynamics in the presence of strong dephasing for all α , which is surprising for $\alpha > \alpha_{\text{cr}}$ where a simple diffusive behavior is expected from short-range models [276]. In the following, we illustrate this effect for the case of many excitons following a quench.

6.3 Many excitons: speedup of relaxation.

We consider the dynamics in the many-exciton sector of Eq. (6.5) on a $d = 1$ lattice, starting from a “domain-wall” initial condition, where the leftmost $N/2$ sites are all occupied, while the other sites are empty, in analogy with a Joule expansion. We analyze the

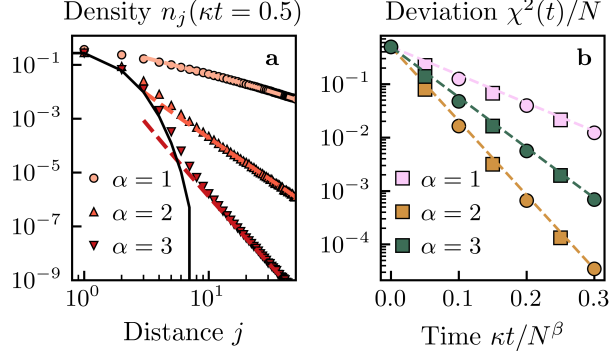


Figure 6.2: Speedup of the relaxation dynamics for $d = 1$. Starting from a domain-wall exciton profile, the occupation profile $n_j(t)$ is computed numerically from Eq. (6.5) for $N = 100$ and $\kappa t = 0.5$ (a), and exhibits power-law tails showing that equilibrium is reached faster as α is decreased. The continuous line corresponds to nearest-neighbour hopping, and the dashed lines to the approximate solution Eq. (6.11). (b) Time evolution of the deviation from equilibrium $\chi^2(t)$ for different α and N . The circles and squares are for $N = 100$ and $N = 1000$, respectively. The dashed lines are the best fit $\propto \exp(-t/\tau)$, with τ given by Eq. (6.12).

occupation profile at time t , i.e. $n_j(t) = \text{Tr}[\rho(t)S_j^+S_j^-]$, where $\rho(t)$ is the density matrix solving Eq. (6.5). Both for $\alpha < \alpha_{\text{cr}}$ and for $\alpha > \alpha_{\text{cr}}$, a flat equilibrium solution is reached at large t , such that $\bar{n} = \lim_{t \rightarrow \infty} n_j(t) = 0.5 \forall j$. Interestingly here, the equilibrium is reached for any hopping range α , which is in contrast to the purely quantum case, where long-range interactions can break ergodicity in the absence of disorder [309–311].

For short time $\kappa t \ll N^{2\alpha}$, the distribution away from the origin is dominated by single exciton hopping events, and we find that the profile has power-law tails

$$n_j(t) \propto \kappa t \int_{-N/2}^0 (j+r)^{-2\alpha} dr \approx \kappa t / j^{2\alpha-1}, \quad (6.11)$$

as shown in Fig. 6.2a. As a consequence, the exciton spreads faster as α is decreased. To quantify how fast the equilibrium profile is reached, we compute the normalized chi-squared $\chi^2(t)/N = \sum_j [n_j(t) - \bar{n}]^2 / (N\bar{n})$ between the profile at time t and the equilibrium one. Figure 6.2b shows that the equilibrium regime is reached exponentially in time for any α , $\chi^2(t)/N \propto \exp(-t/\tau)$. Note that this scaling can be recovered by analyzing the gap of the Liouvillian, Eq. (6.5), which follows from the spinon dispersion of the ferromagnetic Heisenberg model [312]. We observe that the half-time of the exponential

increases with a power of the system size N as

$$\tau = \frac{N^\beta}{2\pi^\beta b_\alpha} \quad \text{with} \quad \beta = \begin{cases} 2\alpha - 1 & \alpha < \alpha_{\text{cr}} \\ 2 & \alpha > \alpha_{\text{cr}} \end{cases}, \quad (6.12)$$

for some constant b_α , while $\tau = \frac{N^2 \log N}{2\pi^2 b_\alpha}$ in the critical case $\alpha = \alpha_{\text{cr}} = 3/2$. Notice that the scaling (6.12) is precisely what is expected from the continuous diffusion equation with (fractional) Laplacian,

$$\frac{\partial n(x, t)}{\partial t} = b_\alpha \Delta^{\beta/2} n(x, t). \quad (6.13)$$

Indeed, the solution to this evolution equation with an initial domain-wall density profile has the Fourier decomposition $n(x, t) = \frac{1}{2} + \sum_{m \in \mathbb{N}} c_m(t) \cos(\pi m x / N)$ with coefficients decaying as $c_m(t) \propto \exp(-b_\alpha (m\pi/N)^\beta t)$, thus $\chi^2(t) \propto N[n(x, t) - 1/2]^2 \propto \exp(-2\pi^\beta b_\alpha t / N^\beta)$.

The fact that the large-scale evolution of our system should be captured by a continuous diffusion equation with fractional Laplacian (6.13) follows from the form of the generator of the CME (6.6), which is $SU(2)$ symmetric. Indeed, exploiting the $SU(2)$ symmetry, one can switch from one ‘magnetization sector’ to another —*i.e.* from one exciton number to another— without changing its spectrum. This suggests that the equation governing the evolution of the density profile for many excitons at large scales should be the same as for a single exciton. In particular, the constant b_α in Eq. (6.12) is expected to match the diffusion constant of a single exciton, *i.e.* $b_\alpha = D_\alpha$ for $\alpha > \alpha_{\text{cr}}$ and $b_\alpha = C_\alpha$ for $\alpha < \alpha_{\text{cr}}$. From the data in Fig. 6.2, we find the numerical values $b_\alpha/\kappa \simeq 1.93, 1.62, 1.1$ for $\alpha = 1, 2, 3$, to be compared with the analytical result $C_1/\kappa = 3.14$, $D_2/\kappa = 1.64$, $D_3/\kappa = 1.08$. The agreement is very good for $\alpha > \alpha_{\text{cr}}$, however the values differ in the long-range case $\alpha < \alpha_{\text{cr}}$: this discrepancy is due to the different boundary conditions between the numerics in Fig. 6.2 (open boundary conditions) and in the analytical derivation of C_α (which assumes translational invariance, *i.e.* periodic boundary conditions). We also emphasize that β decreases with α for $\alpha < \alpha_{\text{cr}}$, which implies that the

equilibrium is reached faster (for large N) as the interaction range increases.

6.4 Conclusion

Our results provide a way to experimentally realize an exclusion process with long jumps [294–296], and are highly relevant to nanocrystal quantum dots that are attracting more and more interest for solar cell applications [282]. In particular, discrepancies between the exciton diffusion length measured experimentally and the values predicted by standard diffusion theory applied to Förster energy transfer ($\alpha = 3$) have been recently reported [277, 313]. We argue in the Appendix E that such discrepancies would typically be reduced by a factor of ~ 2 upon properly including the long range character of the hopping in the diffusion coefficient, which is not the case in standard diffusion models assuming nearest-neighbor hopping [270]. Our model is also relevant to molecular aggregates that play an important role in photosynthetic complexes and optoelectronic devices [314]. Dye monomers interacting via dipole-dipole coupling ($\alpha = 3$) can indeed form highly-ordered assemblies [315]. Supramolecular chemistry offers the possibility to control the mutual arrangement of monomers to achieve a nearest-neighbor hopping $J < 3$ THz, while the typical dephasing rate can exceed 14 THz at room temperature [280, 281]. Our model could also be realized with ions in linear Paul traps, with $J \approx 100 - 1000$ Hz and the possibility to tune the hopping range within $0 < \alpha < 3$ [285, 316, 317]. Controlled dephasing can be realized via detuned lasers that induce time-dependent ac-Stark shifts [318], allowing to reach the large dephasing regime with $\gamma > 10J$ [288]. A similar implementation could also be achieved with Rydberg atoms [319], where the $\gamma \gg J$ regime can be reached for large atom densities.

³See Appendix E including plots of the exciton density profile for $d > 1$, an alternative derivation of the CME Eq. (6.7), and the full derivation of: $\langle \mathbf{j}(t) | \mathbf{j}(t) \rangle$ and $\langle |\mathbf{j}|^2(t) | |\mathbf{j}|^2(t) \rangle$, α_{cr} , $\mathcal{A}_{2\alpha, d}(\mathbf{q})$, $n_{\mathbf{j}}(t)$, $\xi_{\alpha, t}$, Eq. (6.6), and the many-exciton $n_{\mathbf{j}}(t)$. The Appendix E includes Refs. [272, 300, 320].

Chapter 7

Numerically efficient unitary evolution for Hamiltonians beyond nearest-neighbors

Matrix product states (MPSs) and matrix product operators (MPOs) are fundamental tools in the study of quantum many-body systems, particularly in the context of tensor network methods such as Time-Evolving Block Decimation (TEBD). However, constructing compact MPO representations for Hamiltonians with interactions beyond nearest-neighbors, such as those arising in AMO systems or in systems with ring geometry, remains a challenge.

In this paper, we propose a novel approach for the direct construction of compact MPOs tailored specifically for the exponential of spin Hamiltonians. This approach allows for a more efficient time evolution, using TEBD, of spin systems with interactions beyond nearest-neighbors, such as long-range spin-chains, periodic systems and more complex cluster model, with interactions involving more than two spins.

7.1 Introduction

After the triumph of the density-matrix renormalization group (DMRG) [245, 248] in uncovering ground states of one-dimensional (1D) systems, several closely linked techniques have emerged to investigate the dynamic features of short-ranged 1D systems [321]. In their recent formulation, these techniques work in the framework of matrix product states (MPSs) [232, 322–326], an efficient representation of finitely entangled states as the product of rank-3 tensors, and matrix product operators (MPOs) [327], which represent quantum operators as the product of rank-4 tensors. If an Hamiltonian possesses a compact MPO representation for the corresponding time evolution operator $U(t) = e^{-itH}$, meaning that the bond dimension linking the tensors in the MPO is sufficiently small, then the time evolution can be efficiently simulated by repeated application of this MPO to the MPS. This is indeed the case in some simple systems, such as those characterized only by nearest-neighbor interactions or whose Hamiltonian can be written as the sum of commuting terms, in which it is possible to construct compact MPOs with finite error per site. This is the basis behind the highly successful time-evolving block decimation (TEBD) [328–330] and tDMRG [331]. The main variants of TEBD use a second-order (TEBD2) or fourth-order expansion (TEBD4) of the unitary evolution operator in the time-step. Even though TEBD4 gives a smaller error per time-step, typically TEBD2 is preferred since it requires five times less MPO-MPS contractions per time-step than TEBD4. However, these methods do not generalize well to long-range Hamiltonians, since the bond dimension of their MPOs typically scales exponentially with the range of the interaction.

In order to overcome this issue, recently new approaches have been developed that can be applied directly to long-range Hamiltonian [332–337]. The $W^{I,II}$ methods [332] work similarly to TEBD in the sense that they try to approximate the time evolution method for a small time step, with the advantage of producing MPOs which are usually more compact than those produced by TEBD. However, a downside of these methods

is that their dynamics is not strictly unitary. Other techniques, such as the local Krylov method [333, 334] and the time dependent variational principle (TDVP) [335, 336, 338] move from the standard tensor network paradigm of applying an MPO to an MPS, and try to directly approximate the time evolved state without explicitly applying the time evolution MPO to an MPS. One of the advantages of these methods is that they allow to reduce the error per time step, and in its two site variant TDVP has been shown to be the best algorithm in terms of physical accuracy and performance, the latter being comparable to that of TEDB for larger time steps [232]. As a drawback, common to any variational approach, in certain situations TDVP could get stuck in a local minimum, failing to converge to the exact result.

While in many situations TDVP can outperform TEDB techniques, in this manuscript we will focus on the latter. The reason behind this choice is that TEDB is still one of the easiest methods to implement on small scale simulations and, at the same time, it ensures convergence to correct results without getting stuck in local minima, providing a solid algorithm to benchmark TDVP simulations. Within this framework, our goal is to improve the performances of TEDB in the simulation of the time evolution of systems with interactions beyond nearest-neighbors, proposing an alternative approach for the construction of MPOs for the exponentials of non-local spin operators, based on the direct exponentiation of Pauli strings. This provides a very intuitive and natural way of constructing MPOs which contain only tensors acting on a single site. The maximal bond dimension of such MPOs scales as 2^r with the range of the interaction r , as opposite to standard approaches which prescribe the application of swap gates on local two-qubits MPOs to reconstruct the desired long-range nature of the operators [232], where in the typical scenario the bond dimension scales as 2^{4r-3} . Therefore, while unable to cure the exponential growth of the bond dimension with the interaction range, our method still renders the TEDB technique more efficient in terms of MPO's bond dimension to simulate the time evolution of MPSs, at least for systems in which the range of the interaction is not too large. This could be the case, for example, of one dimensional

Rydberg atoms systems in which, because of the R^{-6} decay of the Van der Waals interactions, often only nearest and next-to-nearest neighbors interaction give a significant contribution [339]. Our approach is also relevant to the study of short-range spin chains with periodic boundary conditions, in which a single operator with non-local structure emerges at the boundaries of the system. Indeed, while in Hamiltonians with non-local interactions and open boundary conditions one could try to reduce the overhead introduced by the SWAP operators with special rearrangements [232], in the presence of a single non-local interaction connecting the first and last spin in the chain this is not possible. In this case, our method produces an MPO with constant bond dimension $w = 4$, which is eight times smaller than the bond dimension $w = 32$ achieved with the SWAP gates. This would significantly improve the performance of the simulations of the dynamics of those systems which are very sensitive to the presence of periodic boundary conditions. This is the case, for example, of ring-shaped networks of Rydberg atoms, which exhibit interesting transport properties [2, 340–342], or of topologically frustrated spin chains. Moreover, our technique is easily generalized also to Hamiltonians with more complex cluster interactions [343–347], i.e. interactions involving more than two spins.

7.2 Standard TEBD and its problems for long-range systems

In order to present the general ideas behind TEBD and later, in Sec. 7.3, our novel approach, it is sufficient to start by considering the following family of Hamiltonians describing open spin chains with long-range interactions

$$H_r(J, h) = J \sum_{l=1}^{N-r} \sigma_l^x \sigma_{l+r}^x + h \sum_{l=1}^N \sigma_l^z = JX_{r,N} + hZ_N, \quad (7.1)$$

where $r < N/2$ is the range of the interaction along the \vec{x} direction, J determines its nature and strength, h is a transverse magnetic field along the \vec{z} direction and σ^α for $\alpha = 0, x, y, z$ are the Pauli matrices.

At its heart, TEBD relies on a Trotter-Suzuki decomposition [348] to approximate the time-evolution operator $U(\delta)$. Using the Hamiltonian (7.1) as an example, this decomposition gives

$$U(\delta) = e^{-i\delta H_r} \approx e^{-i\frac{h\delta}{2}Z_N} e^{-iJ\delta X_{r,N}} e^{-i\frac{h\delta}{2}Z_N} + o(\delta^3) = U^{TEBD2}(\delta), \quad (7.2)$$

where every exponential appearing in (7.2) is made up by commuting terms, e.g. $e^{-iJ\delta X_{r,N}} = \prod_{l=1}^{N-r} e^{-iJ\delta\sigma_l^x\sigma_{l+r}^x}$. If we imagine to evolve the system over a time interval T which we divide in T/δ steps, replacing the exact time evolution operator $U(\delta)$ with $U^{TEBD2}(\delta)$ yields an error of order δ^2 after every time interval of length T .

After the decomposition is chosen, the application of tensor network techniques to time evolve an MPS requires the construction of MPOs for the single and two-qubit gates appearing in (7.2). Since the construction of the first ones is trivial and does not produce any overhead in terms of bond dimension, here we will focus only on the construction of the MPO representation of two-qubit gates.

Let $E_{l,l+r} = e^{-iJ\delta\sigma_l^x\sigma_{l+r}^x}$. In presence of short-range interactions, i.e. for $r = 1$, one can start from an MPO of length $N - 1$ containing a tensor with four physical legs at site l and bond dimension $w = 1$ at every link (as indicated above the legs connecting neighbors tensors):

$$E_{l,l+1} = \begin{array}{c} \text{---} \bigcirc \text{---} \bigcirc \text{---} \dots \text{---} \bigcirc \text{---} \bigcirc \text{---} \bigcirc \text{---} \bigcirc \text{---} \text{---} \\ \text{II} \quad \text{II} \quad \quad \quad \text{II} \quad \text{Q} \quad \text{II} \quad \quad \quad \text{II} \\ \text{---} \quad \text{---} \quad \quad \quad \text{---} \quad \text{---} \quad \text{---} \quad \quad \quad \text{---} \quad \text{---} \end{array} \quad (7.3)$$

where $Q = e^{-i\delta J\sigma^x \otimes \sigma^x}$ is the local two-qubit gate of interest and \mathbb{I} is the 2×2 identity matrix. At this point, in order to complete the construction of our MPO we can split the

tensor Q in two tensors, e.g. by SVD, and obtain the desired N -length MPO

$$E_{l,l+1} = \begin{array}{c} \text{---} \bigcirc \text{---} \bigcirc \text{---} \dots \text{---} \bigcirc \text{---} \bigcirc \text{---} \bigcirc \text{---} \bigcirc \text{---} \bigcirc \text{---} \\ \text{II} \quad 1 \quad \text{II} \quad 1 \quad \dots \quad 1 \quad \text{II} \quad 1 \quad \text{II} \quad m \quad \text{II} \quad 1 \quad \text{II} \quad 1 \quad \dots \quad 1 \quad \text{II} \\ \text{---} \end{array} \quad (7.4)$$

which will have bond dimension $w = 1$ at every site but between site l and $l + 1$ where a bond has been created splitting the two-qubit gate and $w = m$. Therefore, it is easy to understand that the full exponential $e^{-iJ\delta X_{1,N}} = \prod_{l=1}^{N-1} E_{l,l+1}$ will be represented by an MPO with constant bond dimension $w = m$ at every site.

For long-range systems, i.e. for $r > 1$, the standard prescription to build an MPO for $E_{l,l+r}$ is to start from the local two-qubit operator $E_{l,l+1}$ and apply swap operators to obtain the desired non-local structure of the operator [232]. Therefore, if we denote by $S_{l,l+1}$ the swap gate between site l and $l + 1$, we have that

$$E_{l,l+r} = S_{l,r} E_{l,l+1} S_{l,r}^\dagger, \quad (7.5)$$

where $S_{l,r} = \prod_{k=l+1}^{l+r-1} S_{k,k+1}$. To understand the resulting MPO structure for $E_{l,l+r}$ we should first take into account the structure of the MPO representing the swap operators.

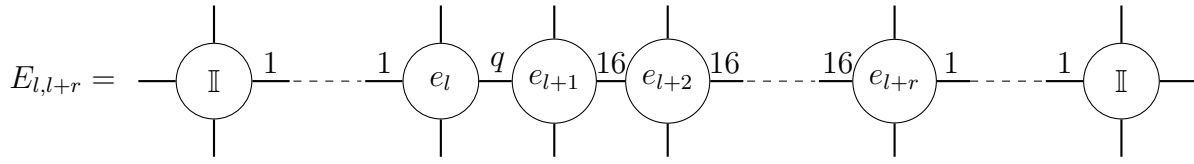
This is given by

$$S_{k,k+1} = \begin{array}{c} \text{---} \bigcirc \text{---} \bigcirc \text{---} \dots \text{---} \bigcirc \text{---} \bigcirc \text{---} \bigcirc \text{---} \bigcirc \text{---} \\ \text{II} \quad 1 \quad \text{II} \quad 1 \quad \dots \quad 1 \quad \text{II} \quad 1 \quad S_k \quad 4 \quad S_{k+1} \quad 1 \quad \text{II} \quad 1 \quad \dots \quad 1 \quad \text{II} \\ \text{---} \end{array} \quad (7.6)$$

where the tensors at site k and $k + 1$ are a row and a column vector, respectively

$$s_k = \left[\mathbb{I}, \sigma^x, \sigma^y, \sigma^z \right], \quad s_{k+1} = \begin{bmatrix} \mathbb{I}/2 \\ \sigma^x/2 \\ \sigma^y/2 \\ \sigma^z/2 \end{bmatrix}. \quad (7.7)$$

Accordingly, the swap strings $\mathcal{S}_{l,r}$ will be represented by an MPO which has bond dimension $w = 4$ at all sites between $l + 1$ and $l + r$. Therefore, the resulting MPO for $E_{l,l+r}$ built using the swap operators will have bond dimension $w = q$ between site l and $l + 1$ and then constant bond dimension $w = 16$ at every site between sites $l + 1$ and $l + r$



$$E_{l,l+r} = \text{---} \circ \text{II} \text{---} \overset{1}{\text{---}} \text{---} \overset{1}{\text{---}} \circ e_l \text{---} \overset{q}{\text{---}} \circ e_{l+1} \text{---} \overset{16}{\text{---}} \circ e_{l+2} \text{---} \overset{16}{\text{---}} \text{---} \overset{16}{\text{---}} \circ e_{l+r} \text{---} \overset{1}{\text{---}} \text{---} \overset{1}{\text{---}} \circ \text{II} \text{---} \text{---} \overset{1}{\text{---}} \text{---} \quad (7.8)$$

Therefore, we can now easily understand that the MPO for the full exponential $e^{-iJ\delta X_{r,N}} = \prod_{l=1}^{N-r} E_{l,l+r}$ will have a maximum bond dimension of $w = m \cdot 16^{r-1} = m \cdot 2^{4r-4}$, producing a minimum scaling which goes like 2^{4r-3} when $m = 2$. This obviously scales quite badly with the range of the interaction, making the TEBD method quite inefficient for long-range systems.

Similarly, it is easy to understand that in the case of an Hamiltonian with nearest-neighbors interactions ($r = 1$) and periodic boundary conditions the total bond dimension would be $w = m \cdot 16$, since the number of swap operators needed to build $E_{1,N}$ is of the order of the system's size.

In the next section we will propose a different approach to the construction of the MPOs for $E_{l,l+r}$, which does not require the application of any SWAP operator.

7.3 Compact MPOs for the exponential of Pauli strings

Let $\sigma = \bigotimes_{i=1}^N \sigma^{\alpha_i}$ be a N -qubit Pauli string, where σ^α for $\alpha = 0, x, y, z$ are Pauli matrices. We are interested in the evaluation of the exponential $e^{-i\delta\sigma}$. This becomes quite straightforward if one considers that $\sigma^2 = \mathbb{I}^{\otimes N}$. Indeed, we have that

$$e^{-i\delta\sigma} = \sum_{n=0}^{\infty} \frac{(-i\delta)^n}{n!} \sigma^n = \sum_{n=0}^{\infty} \frac{(-1)^n \delta^{2n}}{(2n)!} \mathbb{I}^{\otimes N} - i \sum_{n=0}^{\infty} \frac{(-1)^n \delta^{2n+1}}{(2n+1)!} \sigma, \quad (7.9)$$

which yields to

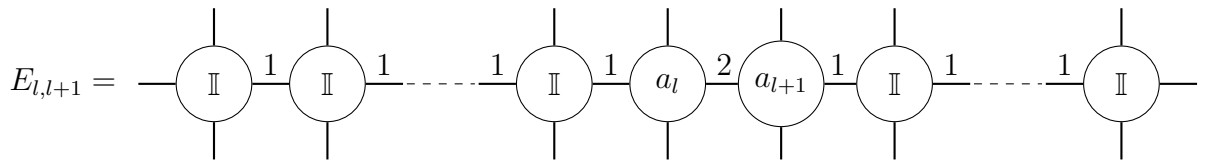
$$e^{-i\delta\sigma} = \cos(\delta) \mathbb{I}^{\otimes N} - i \sin(\delta) \sigma. \quad (7.10)$$

The expression in (7.10) can be easily expressed in tensor networks language as an MPO with constant bond-dimension $w = 2$, where the single qubit operators are given by the rank-4 tensor

$$O_l = \begin{bmatrix} \mathbb{I} & 0 \\ 0 & \sigma^{\alpha_l} \end{bmatrix}, \quad l = 1, \dots, N-1, \quad (7.11)$$

$$O_N = \begin{bmatrix} \cos(\delta) \mathbb{I} & 0 \\ 0 & -i \sin(\delta) \sigma^{\alpha_N} \end{bmatrix}. \quad (7.12)$$

The expression of these MPOs can become even more compact when we are treating two-qubit gates. Using the notation introduced in Sec. 7.2, for local two-qubit gates we indeed have that (7.10) can be expressed as

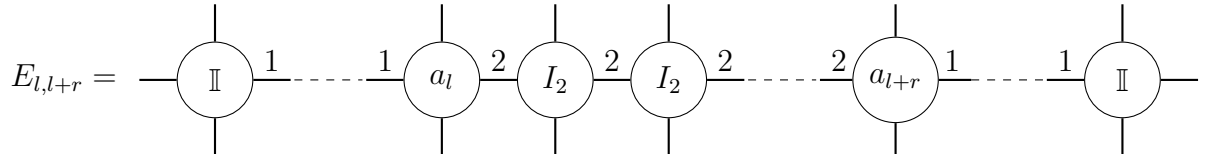


$$E_{l,l+1} = \text{---} \bigcirc \text{---} \bigcirc \text{---} \dots \text{---} \bigcirc \text{---} \bigcirc \text{---} \bigcirc \text{---} \bigcirc \text{---} \dots \text{---} \bigcirc \text{---} \quad (7.13)$$

where

$$a_l = \begin{bmatrix} \mathbb{I} & \sigma^x \end{bmatrix}, \quad a_{l+1} = \begin{bmatrix} \cos(J\delta) \mathbb{I} \\ -i \sin(J\delta) \sigma^x \end{bmatrix}, \quad (7.14)$$

which has bond dimension $w = 1$ at every link but the one connecting the l -th and $(l + 1)$ -th qubit, where $w = 2$. For non-local two qubit gates we instead have



The diagram shows a horizontal chain of qubits represented by circles. From left to right: a circle labeled 'I' with a vertical line above and below it; a dashed line labeled '1' connecting to a circle labeled 'a_l'; a solid line labeled '2' connecting to a circle labeled 'I_2'; another solid line labeled '2' connecting to a second circle labeled 'I_2'; a dashed line labeled '2' connecting to a circle labeled 'a_{l+r}'; and finally a solid line labeled '1' connecting to a circle labeled 'I'. Each circle has a vertical line above and below it. The equation is labeled (7.15) on the right.

where

$$I_2 = \begin{bmatrix} \mathbb{I} & 0 \\ 0 & \mathbb{I} \end{bmatrix}. \quad (7.16)$$

It is immediate to see that the MPO (7.15) constructed using the direct exponentiation of Pauli strings is much more compact than (7.8). Building the full exponential matrix $\prod_{l=1}^{N-r} E_{l,l+r}$ that enters the time evolution operator, using (7.15) we will thus end up with a final MPO whose maximum bond dimension is $w = 2^r$. Unfortunately, this is still scaling exponentially with the range of the interaction, but it still provides a much better scaling than using swap gates.

For systems with $r = 1$ and periodic boundary conditions, we have that $E_{1,N}$ has an MPO representation with constant bond dimension $w = 2$, resulting in a total bond dimension of $w = 4$ when multiplied with the exponentials of the local two-qubit interactions. This is at least 8 times smaller than the one obtained using SWAP gates.

Moreover, we would like to highlight that, thanks to (7.10), also the construction of MPOs for the exponential of Hamiltonians with more complicated cluster interactions could become quite compact and straightforward.

7.4 Some applications

In this section we will use TEBD to simulate the time evolution of some non-integrable spin Hamiltonians after a global quantum quench in the external magnetic field. The

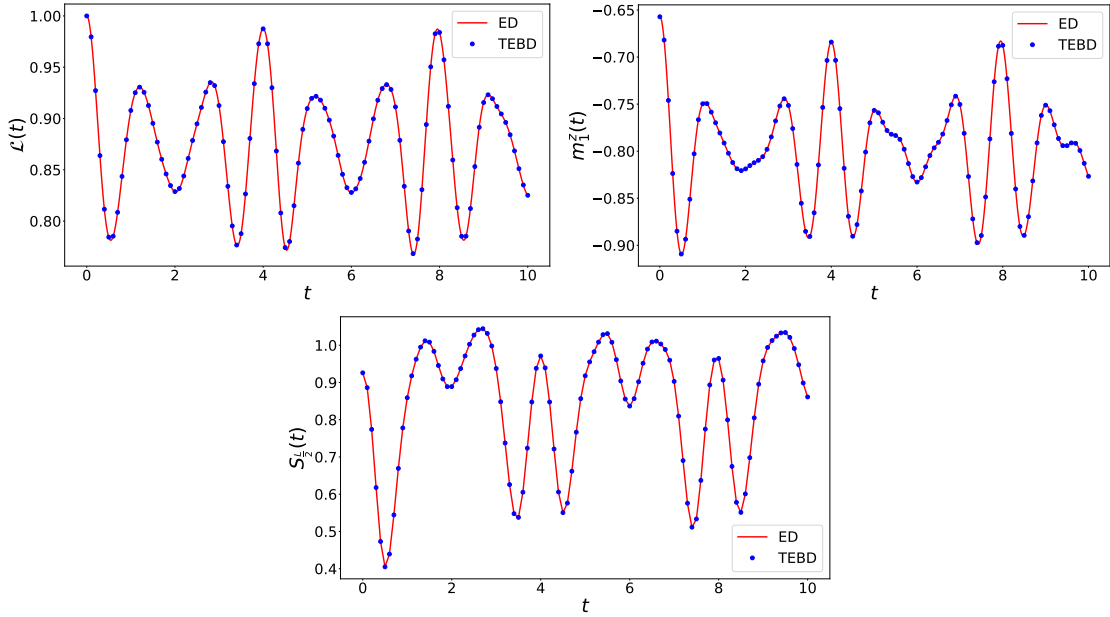


Figure 7.1: Data obtained for a XYZ-ring of $L = 15$ spins for $J_x = 1$, $J_y = -0.3$, $J_z = -0.4$ and $h = 0.5$, with a quench amplitude of $\Delta h = 0.5$. The time step used for the time evolution is $\delta = 0.01$. Blue dots represent data obtained with TEBD while the red line corresponds to exact diagonalization. We plot the Loschmidt echo (top left), local magnetization (top right) and the half-chain entanglement entropy (bottom).

initial state of the dynamics will be the ground-state $|\psi_0\rangle$ of these systems, which we will compute numerically using DMRG. In each case, we will evaluate three quantities, the Loschmidt echo

$$\mathcal{L}(t) = |\langle \psi_0 | \psi(t) \rangle|^2, \quad (7.17)$$

the half-chain bipartite entanglement entropy

$$S_{\frac{L}{2}}(t) = \text{Tr}_A(|\psi(t)\rangle\langle\psi(t)|), \quad (7.18)$$

where A is a subsystem containing half of the spins in the chain, and the local magnetization

$$m_z(t) = \langle \psi(t) | \sigma_1^z | \psi(t) \rangle. \quad (7.19)$$

While our TEBD approach can be used to treat system with sizes of the order of 100 spins, in the following we will limit to $N = 15$ spins in order to compare the results obtained using the MPO construction that we introduced in Sec. 7.3 with those obtained

using exact diagonalization techniques.

7.4.1 Anisotropic XYZ ring

Let us start by considering a short-range model with periodic boundary conditions, namely the anisotropic XYZ chain in a transverse field.

$$H_{XYZ} = \sum_{\alpha=x,y,z} \sum_{l=1}^N J_{\alpha} \sigma_l^{\alpha} \sigma_{l+1}^{\alpha} + h \sum_{i=1}^N \sigma_i^z, \quad (7.20)$$

with periodic boundary conditions, i.e. $\sigma_{l+N}^{\alpha} = \sigma_l^{\alpha}$. As a first step we need to trotterize the time evolution operator. Using the notation introduced in the previous sections, we can write $H_{XYZ} = \tilde{X}_{1,N} + \tilde{Y}_{1,N} + \tilde{Z}_{1,N}$, where this time we are including also the magnetic field term in $\tilde{Z}_{1,N}$ since it obviously commutes with the interaction term along \vec{z} , and the superscript is a reminder that the sums runs from $l = 1$ to $l = N$ because of the periodic boundary conditions. In Sec. 7.3 we have shown that it is possible to design MPO with constant bond dimension $w = 4$ for each of these three terms. Therefore, since all the MPOs after the trotterization will have the same bond dimension, there is no preferred order for the decomposition. The trotterized time evolution operator can thus be written as

$$U^{TEBD2} = e^{-i\frac{\delta}{2}Z_{1,N}} e^{-i\frac{\delta}{2}Y_{1,N}} e^{-i\delta X_{1,N}} e^{-i\frac{\delta}{2}Y_{1,N}} e^{-i\frac{\delta}{2}Z_{1,N}}. \quad (7.21)$$

At this point, we need to construct an MPO for each of the exponentials appearing in (7.21) and apply them sequentially to the MPS that we want to time evolve. We want to stress that, using our method to build the MPOs, the bond dimension is 8 times smaller for each MPO, reducing the number of operations required at every MPO-MPS contraction of 2^6 and reducing the bond-dimension of the resulting time-evolved MPS again by a factor 8 (before subsequent compression).

The results of the time evolution for a chain of $L = 15$ spins are displayed in Fig. 7.1, and they show a very good agreement with those obtained with exact diagonalization

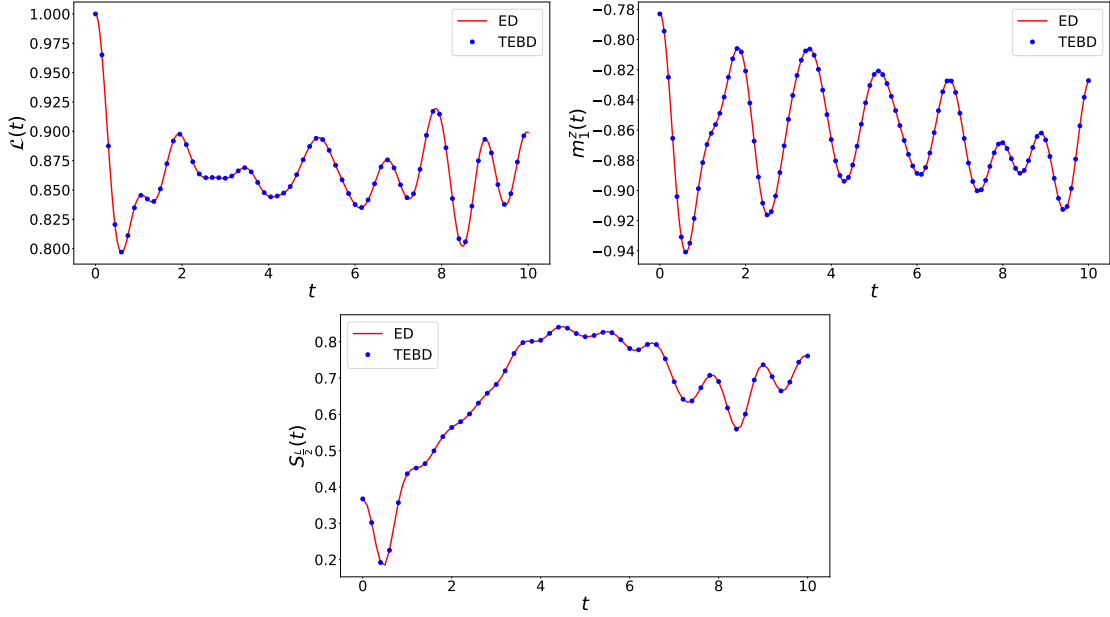


Figure 7.2: Data obtained for an Ising chain of $L = 15$ spins with third neighbors interactions, for $J_1 = 1$, $J_2 = -0.3$, $J_3 = -0.4$ and $h = 0.5$, with a quench amplitude of $\Delta h = 0.5$. The time step used for the time evolution is $\delta = 0.01$. Blue dots represent data obtained with TEBD while the red line corresponds to exact diagonalization. We plot the Loschmidt echo (top left), local magnetization (top right) and the half-chain entanglement entropy (bottom).

for all the measured quantities.

7.4.2 Ising chain with third neighbors interactions

Next we consider an open Ising chain with interactions up to the third nearest neighbors.

The Hamiltonian reads

$$H_{Ising3} = \sum_{r=1}^3 \sum_{l=1}^{N-r} J_r \sigma_l^x \sigma_{l+r}^x + h \sum_{l=1}^N \sigma_l^z = \sum_{r=1}^3 J_r X_r + h Z_N, \quad (7.22)$$

and the trotterized time-evolution operator can be written as

$$U^{TEBD2} = e^{-i\frac{h\delta}{2} Z_N} e^{-iJ_1\delta X_{1,N}} e^{-iJ_2\delta X_{2,N}} e^{-iJ_3\delta X_{3,N}} e^{-i\frac{h\delta}{2} Z_N}. \quad (7.23)$$

The MPO with highest bond dimension is the one corresponding to $e^{-iJ_3\delta X_{3,N}}$. Using our technique, this is equal to $w = 2^3$, which is 2^6 times smaller than the one obtained with a

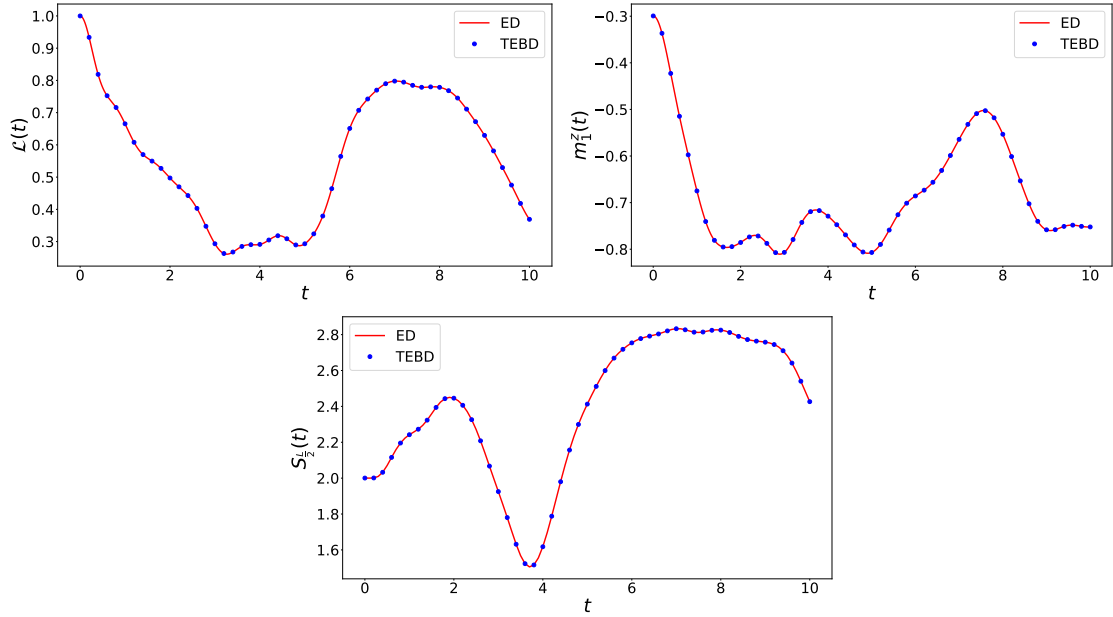


Figure 7.3: Results obtained for the spin chain with cluster interaction with $L = 15$ spins, for $K = 1$ and $h = 0.3$, with a quench amplitude of $\Delta h = 0.5$. The time step used for the time evolution is $\delta = 0.01$. Blue dots represent data obtained with TEBD while the red line corresponds to exact diagonalization. We plot the Loschmidt echo (top left), local magnetization (top right) and the half-chain entanglement entropy (bottom).

naive application of swap gates. Once again, the numerical results obtained with TEBD match accurately those produced with exact diagonalization (see Fig. 7.2)

7.4.3 A non-integrable cluster model

Let us now consider a spin chain with cluster interactions, whose Hamiltonian reads

$$H = K \sum_{l=2}^{N-1} \sigma_{l-1}^x \sigma_l^x \sigma_{l+1}^x + h \sum_{l=1}^N \sigma_l^z. \quad (7.24)$$

After trotterization, the time evolution operator reads

$$U^{TEBD2} = e^{-i\frac{h\delta}{2}Z_N} \prod_{l=1}^N e^{-iK\delta\sigma_{l-1}^x \sigma_l^x \sigma_{l+1}^x} e^{-i\frac{h\delta}{2}Z_N}. \quad (7.25)$$

The largest bond dimension in the MPO representing the exponential of the cluster interaction is again $w = 8$. The results obtained using TEBD are shown in Fig. 7.3, and

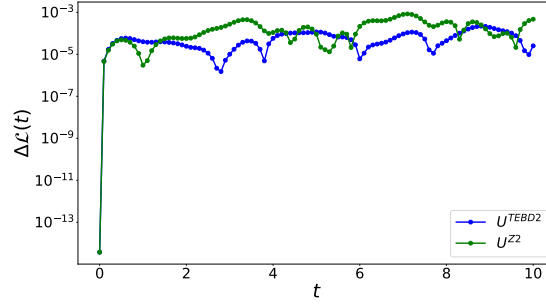


Figure 7.4: Error in the Loschmidt echo using different truncation schemes, measured with respect to exact diagonalization. Data are obtained for Hamiltonian (7.1) with $L = 15$ spins, for $J = 1$ and $h = 0.3$, with a quench amplitude of $\Delta h = 0.5$. The time step used for the time evolution is $\delta = 0.01$. Blue dots represent error obtained with TEBD2 while the green line corresponds to exact that obtained with U^{Z2} .

once again show a very good agreement with exact diagonalization.

7.4.4 Other approximation schemes

Finally, to further highlight the adaptability of our method, we will show that it can be easily applied to truncations of the unitary evolution operator which differ from the Trotter-Suzuki decomposition (7.2). To make a concrete example, let us consider again the Hamiltonian in (7.1)

$$H_r(J, h) = J \sum_{l=1}^{N-r} \sigma_l^x \sigma_{l+r}^x + h \sum_{l=1}^N \sigma_l^z = JX_{r,N} + hZ_N. \quad (7.26)$$

Using the Zassenhaus formula [349, 350] for the exponential of the sum of two operators, we have that

$$e^{-i\delta H_r} = e^{-iJ\delta X_{r,N}} e^{-ih\delta Z_N} e^{\frac{Jh\delta^2}{2}[X_{r,N}, Z_N]} + o(\delta^3) = U^{Z2} + o(\delta^3). \quad (7.27)$$

Therefore, the approximation of the time evolution operator with U^{Z2} yields to a truncation error of the same order as U^{TEBD2} . The commutator appearing in (7.27) is given by

the sum of two-qubit operators

$$[X_{r,N}, Z_N] = -2i \sum_{l=1}^{N-r} (\sigma_l^y \sigma_{l+r}^x + \sigma_l^x \sigma_{l+r}^y), \quad (7.28)$$

whose exponential can be easily evaluated using our method after a first order trotterization, which only yields an error of order δ^4 , leaving unaltered the leading order given by (7.27). In Fig. we show the errors obtained when computing the Lodschmidt echo during the time evolution of the ground-state of (7.1), for $r = 3$, after a global quantum quench in the transverse magnetic field, using both U^{Z2} and U^{TEBD2} . As expected, the errors of the two truncation schemes are of the same order of magnitude.

To reduce the error one could truncate the expansion (7.27) to higher order, which will require the calculation of higher order nested commutators. These, however, will produce other Pauli strings, whose exponential is easily computed within our approach. The main drawback of going to higher orders in the expansion, as in TEBD4, would be that more MPO-MPS contractions and subsequent compressions are required. Nonetheless, we would like to stress that if one is able to think of any truncation scheme which will reduce the error per time step, and this scheme involves the exponentiation of Pauli matrices, our method ensure the construction of compact MPOs for such operators.

7.5 Conclusions

We have proposed an alternative technique for the construction of MPOs for the exponentials of non-local spin operators. This technique is based on the direct exponentiation of Pauli matrices, and finds its natural application in systems with long-range interactions, periodic boundary conditions and cluster interactions. The main advantage of this method is that the maximum bond dimension of the MPOs scales as 2^r if r is the range of the interaction, which despite the exponential scaling provides better performances with respect to the standard approach. This renders the study of the dynamics of quan-

tum many-body systems with TEBD more efficient, in terms of MPO-MPS contraction and MPOs size. Moreover, this technique is highly versatile, and provides a very natural way of exponentiating any spin interaction, producing MPOs containing only single site tensors without needing any additional manipulation. We tested the technique on some non-integrable models, measuring the time evolution of the Loschmidt echo, the local and the half-chain entanglement entropy. In all cases, we found very good agreement with the result obtained using exact diagonalization techniques. Finally, we gave an example of how our approach can be easily adapted to truncation schemes which are different from the Suzuki-Trotter decomposition, therefore it would be interesting to explore the possibility of applying it also to other approximation schemes for the unitary time evolution operator, such as the one recently proposed in [351]. Interestingly, the approach can also be applied to the simulation of the time evolution of realistic Rydberg atoms systems.

Chapter 8

Conclusion

After developing state of the art numerical methods based on tensor networks and combining the latter with analytical techniques, our exploration of topological frustration in quantum spin chains has unveiled intriguing phenomena and potential applications in quantum technology.

As a first result, we uncovered a chiral phase in the fully anisotropic Heisenberg chain (aka XYZ chain), characterized by unique ground-state properties, which resemble those of models with continuous symmetries, whereas the model under study is characterized only by a discrete \mathbb{Z}_2 symmetry. Remarkably, the transition to this phase can be detected only through quantum magic, indicating its importance in capturing elusive properties of novel quantum phases and potentially ushering a new class of quantum phase transitions for Hamiltonian systems. Moreover, the equivalence between the non-stabilizerness of frustrated ground states and W -states suggests avenues for realizing complex quantum states in quantum simulators using, for example, Rydberg atoms, thus establishing the importance of TF also for technological purposes.

We then extended our attention to models which possess different sources of classical frustration. Within this context, we analyzed the interplay between local and topological frustration in the ANNNI model. After showing that TF can be induced even without applying FBCs, we employed degenerate perturbation theory to provide a quasi-particle

description of the entanglement entropy in this system, proving that the properties of TF are resilient also in presence of different sources of frustration. This result paves the way towards the study of more complex TF systems, such as 2D ones, suggesting that the ground-state of such systems might contain a larger number of topological excitations, increasing the resilience of TF features against external noise sources. A thorough analysis of these higher dimensional systems will be produced in future works. However, we would like to highlight that the numerical techniques developed to produce the results discussed in this thesis have already allowed us to obtain some preliminary data and establish an empirical violation of the area law also in a 2D TF Ising chain, realized enforcing FBCs along both spatial directions. Moreover, these preliminary results also motivate a detailed comparison of the performances of matrix product states and tree tensor networks for the simulations of 2D systems, which will also be the object of future studies.

Applications to quantum technologies emerged from our investigations as well, with the design of the first complete protocol (which includes both energy storage and transfer) for the realization of a many-body quantum battery. Using a topologically frustrated Ising chain as a reference model, we first proposed a charging protocol based on a global quantum quench, which brings the battery out of equilibrium and stores some energy in it. Thanks to the spectral properties of TF Hamiltonians, we then showed that our device exhibits remarkable robustness to certain types of decoherence, retaining up to 90% of its initial charge. Finally, we demonstrated that the presence of TF enables also efficient energy transfer, by coupling the quantum battery to an ancillary qubit. All these properties highlight the higher efficiency of TF quantum batteries with respect to their non-frustrated counterparts. While the protocol that we proposed is theoretical, we would like to stress out that such devices could be realized using Rydberg atoms. Indeed, we performed preliminary numerical simulations (not included in this thesis) which showed that also including the long-range interactions typical of these systems, and their specific decoherence mechanisms, it is still possible to observe an advan-

tage in TF batteries with respect to non-frustrated ones. In the future, we will further explore such implementations, with the goal of providing an experimental realization of our device.

While TF has been the main topic of research, as it often happens, curiosity drove us to consider other problems as well, such as the transport properties under the simultaneous effect of long-range interactions and local dissipation, or a more efficient implementation of unitary evolution within TEBD approach applied to a tensor network representation. We have already exploited this numerical technique to simulate the dynamics of Rydberg atoms systems in the Aquila quantum simulator by QuEra, obtaining excellent agreement with experimental data. The results of these simulations, together with the experimental ones, will be published in the next months, and will provide the first experimental observation of the peculiar effects of TF in quantum spin chains.

In conclusion, our findings not only deepen our understanding of topological frustration in quantum systems from a fundamental point of view, with its challenges toward standard classification of phases, but also showed the potential for innovative quantum technologies with near-end implementations and practical implications, positioning us at the forefront of quantum research and applications.

Appendix A

Analytical results for the TF XY chain

A.1 Solution of the topologically frustrated XY chain

The XY chain in equation (2.4) can be diagonalized exactly. For the sake of simplicity, we limit our analysis to the case with $h \geq 0$ and $0 < \gamma \leq 1$, but our results can be easily extended also to the other regions of parameters space. The standard procedure prescribes a mapping of spin operators into fermionic ones, which are defined by the Jordan-Wigner transformation:

$$\sigma_j^- = \prod_{l < j} \sigma_l^z \psi_l^\dagger, \quad \sigma_j^+ = \prod_{l < j} \sigma_l^z \psi_j, \quad \sigma_j^z = 1 - 2\psi_j^\dagger \psi_j, \quad (\text{A.1})$$

where ψ_l (ψ_l^\dagger) are fermionic annihilation (creation) operators. In terms of such operators, taking into account the periodic boundary conditions and discarding constant terms, the Hamiltonian thus becomes

$$H = \sum_{j=1}^{N-1} \left[\psi_{j+1}^\dagger \psi_j + \psi_j^\dagger \psi_{j+1} + \gamma (\psi_j^\dagger \psi_{j+1}^\dagger + \psi_{j+1} \psi_j) \right] + 2h \sum_{j=1}^N \psi_j^\dagger \psi_j + \Pi^z \left[\psi_1^\dagger \psi_N + \psi_N^\dagger \psi_1 + \gamma (\psi_N^\dagger \psi_1^\dagger + \psi_1 \psi_N) \right]. \quad (\text{A.2})$$

The latter expression is not quadratic itself, but reduces to a quadratic form in each of the parity sectors of Π^z . Therefore, it is convenient to write it in the form

$$H = \frac{1 + \Pi^z}{2} H^+ \frac{1 + \Pi^z}{2} + \frac{1 - \Pi^z}{2} H^- \frac{1 - \Pi^z}{2},$$

where both H^\pm are quadratic. Hence we can bring the Hamiltonian into a free fermion form by means of two final steps. First, we perform a Fourier transform

$$\psi_q = \frac{e^{-i\pi/4}}{\sqrt{N}} \sum_{j=1}^N e^{-iqj} \psi_j. \quad (\text{A.3})$$

It is worth noting that, due to the different quantization conditions, H^\pm are defined on two different sets of fermionic modes, respectively $q \in \Gamma^- = \{\frac{2\pi n}{N}\}_{n=0}^{N-1}$ in the odd sector and $q \in \Gamma^+ = \{\frac{2\pi}{N}(n + \frac{1}{2})\}_{n=0}^{N-1}$ in the even one. Finally a Bogoliubov rotation in Fourier space

$$b_q = \cos \theta_q \psi_q + \sin \theta_q \psi_{-q}^\dagger, \quad (\text{A.4})$$

with momentum-dependent Bogoliubov angles

$$\theta_q = \frac{1}{2} \arctan \left(\frac{\gamma \sin q}{h + \cos q} \right) \quad q \neq 0, \pi, \quad \theta_{0,\pi} = 0, \quad (\text{A.5})$$

leads to the Hamiltonians

$$H^- = \sum_{q \in \Gamma^- / \{0\}} \Lambda(q) \left(b_q^\dagger b_q - \frac{1}{2} \right) + \epsilon(0) \left(b_0^\dagger b_0 - \frac{1}{2} \right) \quad (\text{A.6a})$$

$$H^+ = \sum_{q \in \Gamma^+ / \{\pi\}} \Lambda(q) \left(b_q^\dagger b_q - \frac{1}{2} \right) + \epsilon(\pi) \left(b_\pi^\dagger b_\pi - \frac{1}{2} \right), \quad (\text{A.6b})$$

Here b_q (b_q^\dagger) are the Bogoliubov annihilation (creation) fermionic operators. The dispersion relation $\Lambda(q)$ for $q \neq 0, \pi$ obeys

$$\Lambda(q) = \sqrt{(h + \cos q)^2 + \gamma^2 \sin^2 q}, \quad (\text{A.7})$$

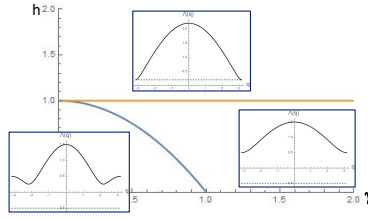


Figure A.1: Phase diagram in the (γ, h) space of the frustrated XY chain: the line at $h = 1$ is the phase transition separating the frustrated phase from a phase where FBC do not affect the behavior of the system. The parabola $h = 1 - \gamma^2$ separates the chiral region from the region with a unique ground state. Instances of the single particle dispersion relation eq. (A.7) are plotted in the various regions together with the energy of the π mode (dashed line), whose occupation lowers the energy of the system for $h < 1$.

while for the two specific modes $q = 0 \in \Gamma^-$ and $q = \pi \in \Gamma^+$ we have

$$\epsilon(0) = h + 1, \quad \epsilon(\pi) = h - 1. \quad (\text{A.8})$$

Having brought the Hamiltonian in the form of a free fermionic system, although with a non-trivial single particle spectrum, we can construct the Hilbert space of the spin chain in terms of the Fock space of the fermionic one, starting from the vacuum states $|\emptyset^\pm\rangle$, defined separately in each parity sector as the states annihilated by all the corresponding destruction operators: $b_q |\emptyset^\pm\rangle = 0, \forall q \in \Gamma^\pm$, and by applying creation operators, always respecting the parity constraint.

It is important to observe that, having assumed $h > 0$, all fermionic modes in the odd sector are associated with a positive energy, while in the even sector there is also a (single) negative contribution to the total energy coming from a fermion with momentum $q = \pi$ if $h < 1$. As depicted in Fig. A.1, we can then partition the phase diagram with $h \geq 0$ and $0 \leq \gamma \leq 1$ into three regions:

- I $h > 1$: In this case, every excited mode brings a positive energy to the system and hence the lowest energy state is the Bogoliubov vacuum state $|\emptyset^+\rangle$ falling in the even parity sector. Such a state is separated from the rest of the spectrum by a finite amount of energy equal to the minimum energy carried by the presence of a single Bogoliubov fermion in the system.

II $1 - \gamma^2 \leq h \leq 1$: In this region, the presence of a fermion in the π -mode, differently from all other modes in the system, is associated with a negative contribution to the total energy. Hence, when populated, the π -mode lowers the energy of the system by a finite amount of energy equal to $|\epsilon(\pi)|$. Therefore, it would be energetically favorable to populate this fermionic mode. However, the π -mode exists only in the even parity sector where the addition of a single excitation is forbidden by the parity constraint. Therefore to obtain a physical state in which the π -mode is populated we have to consider a state with two fermions in which the second lives in a different fermionic mode. But the addition of such a second fermion raises the energy by an amount that is greater than $\epsilon(\pi)$. For this reason, the lowest energy state of the even sector in this region is still its Bogoliubov vacuum $|\emptyset^+\rangle$. In the odd sector, states with a single excitation are allowed, but all fermionic modes hold positive energy and, it is easy to check that each state that can be defined in this sector has an energy greater than the one associated to $|\emptyset^+\rangle$. Despite this, the lowest admissible states in this sector, those with one occupied mode with momentum closest to π (exactly π is not possible because of the quantization rule of this sector) have an energy gap closing as $1/N^2$ compared to $|\emptyset^+\rangle$.

Therefore, the ground state of the whole Hamiltonian is still the Bogoliubov vacuum $|\emptyset^+\rangle$. However, differently from the previous case, the ground state is no longer separated by a finite energy gap. In fact, due to the form of the dispersion relation, one can easily see that the energy gap closes quadratically in the thermodynamic limit and that there is an alternation between states with different parity.

III $h < h^* = 1 - \gamma^2$: Here, the dispersion relation (A.7) develops two symmetric minima at $q = \pm(\tilde{q})$, with

$$\tilde{q} = \arccos\left(\frac{h}{\gamma^2 - 1}\right). \quad (\text{A.9})$$

Note that the threshold parabola $h = 1 - \gamma^2$ differs from the usual circle $h^2 + \gamma^2 = 1$ that encloses the region with oscillatory contributions to the correlation functions

in the non-frustrated XY chain. In general, for finite size systems, \tilde{q} is not an allowed lattice momentum of the system. Therefore let us define \tilde{q}^+ and \tilde{q}^- as the momenta in the even and in the odd sectors closest to \tilde{q} . Since in the odd parity sector, there is no fermionic mode with a negative energy contribution, the lowest energy is associated to the states $|\pm\tilde{q}^-\rangle = b_{\pm\tilde{q}^-}^\dagger |\emptyset^-\rangle$. On the contrary, in the even parity sector, the energy of the $\pm\tilde{q}^+$ modes is smaller than $1 - h$. Thus, because the net contribution of the π and the $\pm\tilde{q}^+$ modes provides an overall negative energy, the two lowest energy states in the even sector are $|\pm\tilde{q}^+\rangle = b_{\pm\tilde{q}^+}^\dagger b_\pi^\dagger |\emptyset^+\rangle$. The four states, i.e. $|\pm\tilde{q}^+\rangle$ and $|\pm\tilde{q}^-\rangle$ have a lattice momentum respectively equal to $\pm(\pi + \tilde{q}^+)$ and $\pm\tilde{q}^-$ [151] and their associated energies are:

$$\begin{aligned} E_e &= \langle \pm\tilde{q}^+ | H | \pm\tilde{q}^+ \rangle \\ &= \Lambda(\tilde{q}^+) + \frac{\epsilon(\pi)}{2} - \frac{1}{2} \sum_{q \in \Gamma^+ / \{\pi\}} \Lambda(q); \end{aligned} \quad (\text{A.10a})$$

$$\begin{aligned} E_o &= \langle \pm\tilde{q}^- | H | \pm\tilde{q}^- \rangle \\ &= \Lambda(\tilde{q}^-) - \frac{\epsilon(0)}{2} - \frac{1}{2} \sum_{q \in \Gamma^- / \{0\}} \Lambda(q). \end{aligned} \quad (\text{A.10b})$$

In each sector, the lowest energy state is separated from the other eigenstates by a gap that closes like $1/N^2$, with the lightest states having finite momenta close to \tilde{q} , as can be easily understood from the dispersion relation in eq. (A.7). Thus, \tilde{q}^\pm act as an effective Fermi momentum and one can think of the states spanning each ground state manifold as resulting from a shell-filling effect that keeps only one of the two Fermi points occupied. To better understand the ground state structure, let us start with the assumption that we choose the parameters of the Hamiltonian such that \tilde{q} coincides with \tilde{q}^+ . Thus, the ground-state manifold is spanned by the states $|\pm\tilde{q}^+\rangle$ and belongs to the even parity sector. A generic change in the parameters h and γ will move \tilde{q} away from \tilde{q}^+ and bring it progressively closer to \tilde{q}^- . At some point E_o becomes smaller than E_e and there will be a crossover between the states $|\pm\tilde{q}^+\rangle$ and $|\pm\tilde{q}^-\rangle$, with the ground-state manifold switching to the odd

parity sector. Further moving the parameters in the same direction, eventually \tilde{q} will come close to a different allowed momentum in the even sector. Hence the system will face a second crossover, and this process will continue until the parameters of the Hamiltonian exit from the chiral region $|h| < h^*$ and settle into the even parity fermionic vacuum as the ground state. Increasing the dimension of the system, the distance between the different momenta becomes progressively smaller and hence the crossing become denser until each point in the region will be characterized by a crossover between two two-fold degenerate manifold belonging to two different parity sectors and having different quantum numbers of the lattice momentum.

In this portrayal, we have assumed that changes in the system parameters always change \tilde{q} . However, from eq. (A.9), we see that we can keep the minimum of the dispersion relation fixed by moving along the parabola $h = c(1 - \gamma^2)$, where c is a constant defined in the interval $[0, 1]$. In chains of finite length, one can identify a strip around each parabola in which the ground state manifold remains constant and this strip becomes narrower as the chain length increases. In this way the system undergoes a foliation of the ground state space that is made of as many manifolds as the number of sites in the system. Let us stress once more that, any time a change of parameters changes \tilde{q}^\pm , hence crossing a strip, even for small systems the fidelity suddenly drops to zero, thus representing an extreme instance of orthogonality catastrophe [163, 164].

To address whether the chiral region represents a different thermodynamic phase or not, we look more closely at the energies. On one side, although the gap between the ground state and the first excited state closes as $1/N^2$ in the whole frustrated phase for $|h| < 1$, for $h^* < h < 1$ the ground state is always represented by the fermionic vacuum state $|\emptyset^+\rangle$, while in the chiral region the ground state manifold keeps changing its parity and momenta. Even increasing the chain length without moving h and γ can switch the ground state parity (see Fig. A.2). Moreover,

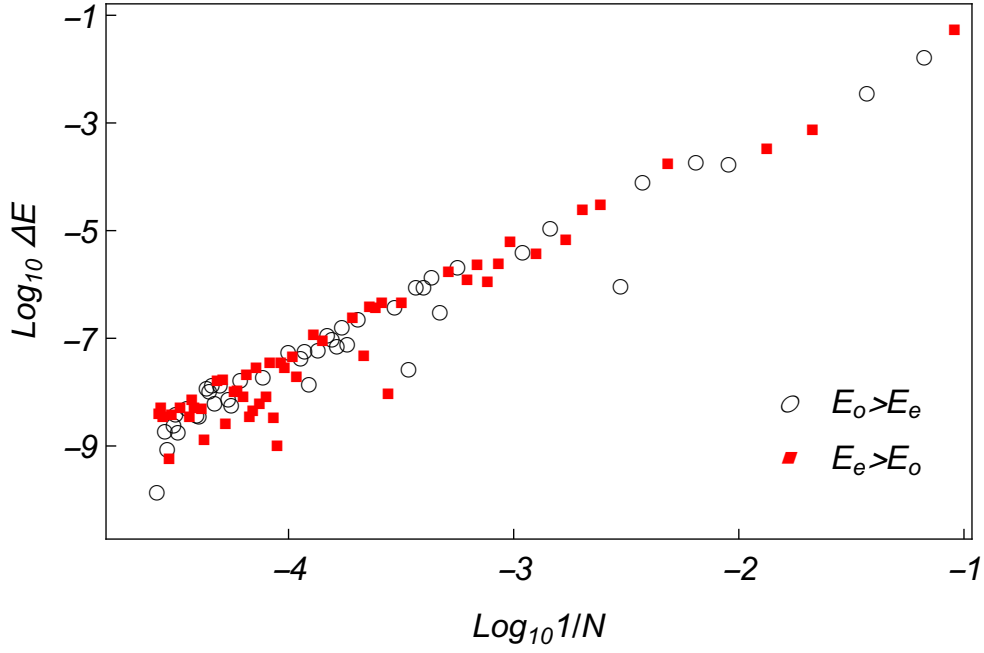


Figure A.2: Behavior of $\Delta E = |E_e - E_o|$, for $h = 0.4$ and $\gamma = 0.6$ as function of the system length N . The red squares represent points in which the states in the even sector have energy greater than the ones in the odd sector, while the black circle signals the presence of a ground state manifold living in the even sector. The parity of the ground state manifold keeps alternating as more sites are added.

as can be appreciated from Fig. A.2, the gap between the alternating ground states closes exponentially with the chain length, which means that in the thermodynamic limit the two manifold become effectively degenerate: crossing the line $h = h^*$ the ground state degeneracy thus grows from 1 to 4, which could indicate a first order quantum phase transition. However, analyzing the free energy derivatives (which at zero temperature coincide with the ground state energy) we cannot detect any discontinuity that remains finite in the thermodynamic limit. For $h > h^*$ the ground state energy associated with the fermionic vacuum $|\emptyset^+\rangle$ is

$$E_{\emptyset} = \langle \emptyset^+ | H | \emptyset^+ \rangle = -\frac{\epsilon(\pi)}{2} - \frac{1}{2} \sum_{q \in \Gamma^+ / \{\pi\}} \Lambda(q). \quad (\text{A.11})$$

Immediately crossing into the chiral region, the ground state energy is the odd state one in eq. (A.10b) with $\tilde{q}^- = \pi (1 - \frac{1}{N})$. Starting from these two expressions for the energy below and above $h = h^*$ it is possible to study the behavior of the

derivatives at any order at the two sides of this line. Selecting a curve in the (h, γ) space, parametrized by a parameter α , which crosses the $h = h^*$ curve at $\alpha = 0$, we compute

$$\Delta(n) = \left. \frac{\partial^n E_o}{\partial \alpha^n} \right|_{\bar{q}^- = \pi(1-1/N)} - \frac{\partial^n E_\emptyset}{\partial \alpha^n}, \quad (\text{A.12})$$

which must be finite, in the thermodynamic limit, to signal a traditional phase transition.

In Fig. 2.6 we show an instance of the dependence of $\Delta(n)$ for n running from 1 to 3 when we cross the line $h = h^*$ keeping γ fixed. As we can see below and above h^* , in the case of finite size systems, all the derivatives show a non-zero $\Delta(n)$, but these differences vanish proportionally to $1/N^2$. This fact implies that in the thermodynamic limit all the derivatives are analytical and hence that if $h = h^*$ represents a quantum phase transition, it has to be one akin to a BKT transition [192–194].

A.2 Global state fidelity and fidelity susceptibility

In order to evaluate the ground state fidelity in eq. (2.3), we observe that all ground-states can be written starting from the vacuum states $|\emptyset^+\rangle$ and $|\emptyset^-\rangle$. In terms of the Bogoliubov angles θ_q , they can be formulated like

$$|\emptyset^+\rangle = |0_\pi\rangle \bigotimes_{q \in \Gamma_2^+} \left(\cos \theta_q |0\rangle_q |0\rangle_{-q} - \sin \theta_q |1\rangle_q |1\rangle_{-q} \right) \quad (\text{A.13a})$$

$$|\emptyset^-\rangle = |0_0\rangle \bigotimes_{q \in \Gamma_2^-} \left(\cos \theta_q |0\rangle_q |0\rangle_{-q} - \sin \theta_q |1\rangle_q |1\rangle_{-q} \right) \quad (\text{A.13b})$$

where Γ_2^+ (Γ_2^-) is the subset of momenta $q \in \Gamma^+$ ($q \in \Gamma^-$) that live in the interval $q \in (0, \pi)$. From these expressions it is easy to obtain that, in the region $h > h^*$ where

the ground state coincide with $|\emptyset^+\rangle$, the ground-state fidelity, becomes

$$\mathcal{F} = \prod_{q \in \Gamma_2^+} \cos(\theta'_q - \theta_q), \quad (\text{A.14})$$

where θ_q (θ'_q) are the Bogoliubov angles associated to the set of parameters $\vec{\lambda} = \{\gamma, h\}$ ($\vec{\lambda} + d\vec{\lambda} = \{\gamma + d\gamma, h + dh\}$).

The situation completely changes entering in the region $|h| < h^*$. In this case, the ground state is no more represented by the vacuum state in the even sector, but by states obtained by populating 1 or 2 fermionic levels, depending on the parity sector in which the ground-state manifold lives. In this situation, we have two different cases. The first is when the two ground states are characterized by having either different numbers of fermions or fermions living in different modes. These occur, in the thermodynamic limit, if the two sets of parameters are not on the same parabola $h = c(1 - \gamma^2)$ where c is a constant obeying to the constraint $|c| \leq 1$. In this case, the overlap between the two states is reduced to the expectation value of either operators like $b_q^\dagger b_{q'}$ with $q \neq q'$, or of single creation (annihilation) operators on the vacuum states. But, from the expression of the vacuum states in eqs. (A.13) it is easy to see that this expectation value is zero, and therefore also the ground-state fidelity vanishes. On the contrary, in the case in which both ground states associated with the two sets of parameters are obtained from the vacuum states by exciting the same fermionic levels, i.e., for large N , if they are both on the same parabola $h = c(1 - \gamma^2)$, the ground-state fidelity does not cancel out identically. Hence, depending on the parity, in the even sector the ground-state fidelity becomes that in eqs. (2.6,2.7).

Differently from all the other paths in the region $|h| < h^*$, along these parabolas it is possible to evaluate also the fidelity susceptibility that, by definition, is equal to the leading order of the expansion of the ground-state fidelity eq. (2.8). The susceptibility χ is expected to be proportional to the system size in the non critical phase. In the case

the ground-states are in the even sector it reads

$$\chi = \sum_{q \in \Gamma^+ / \{\tilde{q}^+\}} \left(\frac{\sin \theta_q (c(1 + \gamma^2) - \cos \theta_q)}{2(\gamma^2 \sin^2 \theta_q + (\cos \theta_q + c(\gamma^2 - 1))^2)} \right)^2 \quad (\text{A.15})$$

while in the odd sector the expression of the terms inside the sum is the same with the sum extending to $q \in \Gamma^- / \{\tilde{q}^-\}$. By introducing the normalized fidelity susceptibility $\tilde{\chi} \equiv \chi/N$, in the thermodynamic limit, we are able to obtain a result independent from the parity sector of the ground-state

$$\tilde{\chi} = \frac{1}{8\pi} \int_0^\pi dx \left[\frac{\sin x (c(1 + \gamma^2) - \cos x)}{[c(\gamma^2 - 1) + \cos x]^2 + \gamma^2 \sin^2 x} \right]^2 \quad (\text{A.16})$$

This integral can be solved analytically using contour integration in the complex plane, upon changing variable to $z = e^{ix}$ obtaining eq. (2.9).

A.3 Majorana Correlation functions

By knowing the ground-states in the different regions of parameter space, it is possible to evaluate the spin correlation functions following the approach described in detail in Ref. [187]. It is based on the introduction of the Majorana fermionic operators A_i and B_i defined as

$$A_i \equiv \psi_i^\dagger + \psi_i; \quad B_i \equiv i(\psi_i - \psi_i^\dagger), \quad (\text{A.17})$$

and the use of Wick's theorem [352]. Indeed, each spin correlation function in which we are interested can be mapped, with the help of the Jordan-Wigner transformation in (A.1) and the definition in (A.17) in a string of Majorana operators on different spins. Then, with the help of Wick's theorem, the expectation value of such a string can be reduced to a Pfaffian in which each single element is the expectation value of a product of two different Majorana operators. Thereby each spin correlation function can be reduced to the evaluation of a particular function of four kind of expectation values i.e. $\langle A_l A_j \rangle$,

$\langle B_l B_j \rangle$, $\langle A_l B_j \rangle$ and $\langle A_j B_l \rangle = -\langle B_l A_j \rangle$ where $\langle \cdot \rangle$ stands for the expectation value on a specific ground-state and the indices l and j run over all sites of the system.

For $h > 1$ the ground state of the system has the form of eq. (A.13) and it is easy to obtain for the Majorana correlation functions $\langle B_l A_j \rangle$

$$\langle B_l A_j \rangle = \frac{i}{N} \sum_{q \in \Gamma^+} [\sin 2\theta_q \sin(qr) + \cos 2\theta_q \cos(qr)] \quad (\text{A.18})$$

where, for brevity, we have defined $r = j-l$, while $\langle A_l A_j \rangle = \langle B_l B_j \rangle = \delta_{l,j}$. For $h^* < h < 1$ the ground state of the system still has the form of eq. (A.13), but Majorana correlation functions change. In fact, moving from values of the local field greater than 1 to less than 1, we have that while in the first case the energy associated with the momentum $q = \pi$ was positive, now it turns negative. Hence, while $\langle A_l A_j \rangle$ and $\langle B_l B_j \rangle$ remain equal to $\delta_{l,j}$, the change in the sign of the energy of the fermionic mode induces a change in the sign of its contribution to the Majorana correlation functions $\langle A_l B_j \rangle$ that become

$$\begin{aligned} \langle B_j A_{j+r} \rangle &= \frac{2i(-1)^r}{N} + \frac{i}{N} \sum_{q \in \Gamma^+} \sin 2\theta_q \sin(qr) \\ &+ \frac{i}{N} \sum_{q \in \Gamma^+} \cos 2\theta_q \cos(qr) \end{aligned} \quad (\text{A.19})$$

For $0 \leq h < h^*$ the situation becomes more complex since not only we have a dense series of crossovers between even and odd states, but also because each single ground-state manifold is two-fold degenerate even for finite N . Let us consider the two cases, i.e. the manifold living in the even or the odd sector, separately. In the latter case, i.e. if the ground-state manifold falls in the odd-parity sector, all its elements can be written as

$$|g^-\rangle = \left(ub_{\tilde{q}^-}^\dagger + vb_{-\tilde{q}^-}^\dagger \right) |\emptyset^-\rangle \quad (\text{A.20})$$

where u and v are complex coefficients obeying the normalization conditions $|u|^2 + |v|^2 = 1$. Due to the presence of the fermions in the modes $\pm \tilde{q}^-$ we obtain that the Majorana correlation functions $\langle A_l A_j \rangle$ and $\langle B_l B_j \rangle$ are no more equal to zero when $l \neq j$, but

become

$$\langle A_j A_{j+r} \rangle = \langle B_j B_{j+r} \rangle = \delta_{0,r} + \frac{2v}{N} (|v|^2 - |u|^2) \sin(r\tilde{q}^-). \quad (\text{A.21})$$

Moreover, also the correlation functions $\langle A_l B_j \rangle$ acquire a state dependent correction and become

$$\begin{aligned} \langle B_j B_{j+r} \rangle &= \frac{v}{N} \sum_{q \in \Gamma^-} [\sin 2\theta_q \sin(qr) + \cos 2\theta_q \cos(qr)] \\ &\quad - \frac{2v}{N} [\sin 2\theta_{\tilde{q}^-} \sin(r\tilde{q}^-) + \cos 2\theta_{\tilde{q}^-} \cos(r\tilde{q}^-)] \\ &\quad + 4|uv^*| \cos(\tilde{q}^-(r+2j) + \alpha) \end{aligned} \quad (\text{A.22})$$

where α is the phase of the complex number uv^* .

On the other hand, in the even sector of the parity the general ground state can be written as

$$|g^+\rangle = b_\pi^\dagger \left(ub_{\tilde{q}^+}^\dagger + vb_{-\tilde{q}^+}^\dagger \right) |\emptyset^+\rangle \quad (\text{A.23})$$

Similarly to the odd case we recover

$$\langle A_j A_{j+r} \rangle = \langle B_j B_{j+r} \rangle = \delta_{0,r} + \frac{2v}{N} (|v|^2 - |u|^2) \sin(r\tilde{q}^+). \quad (\text{A.24})$$

and

$$\begin{aligned} \langle B_j A_{j+r} \rangle &= \frac{v}{N} \sum_{q \in \Gamma^+} [\sin 2\theta_q \sin(qr) + \cos 2\theta_q \cos(qr)] \\ &\quad - \frac{2v}{N} [\sin 2\theta_{\tilde{q}^+} \sin(r\tilde{q}^+) + \cos 2\theta_{\tilde{q}^+} \cos(r\tilde{q}^+)] \\ &\quad + 4|uv^*| \cos(\tilde{q}^+(r+2j) + \alpha) \end{aligned} \quad (\text{A.25})$$

Appendix B

Analytical results for the magic and entanglement of TF spin chains

B.1 Entanglement Entropies of TF ground states close to the classical point

As we have seen in the main text, near the classical point the ground state of a topological frustrated system can be well-approximated by a state ω_p that can be written in the form

$$|\omega_p\rangle = \frac{1}{\sqrt{2L}} \sum_{k=1}^L e^{ipk} (|k\rangle + |k'\rangle), \quad (\text{B.1})$$

Here p is the quantized momentum, i.e. $p = 2\pi\ell/L$, with $\ell = 0, \dots, L-1$ and L being the (odd) length of the chain. The kinks are embedded in Néel order states and are made of the union of two extensive sets of states defined as

$$\begin{aligned} |k^+\rangle &= T^{k-1} \bigotimes_{j=1}^M \sigma_{2j}^z |+\rangle^{\otimes L} \\ |k^-\rangle &= T^{k-1} \bigotimes_{j=1}^M \sigma_{2j}^z |-\rangle^{\otimes L}. \end{aligned} \quad (\text{B.2})$$

In (B.2) $|\pm\rangle$ denote the eigenstates of σ^x associated respectively to the positive/negative eigenvalue in the x -direction, $M = (L - 1)/2$, while T stands for the translation operator that shifts the state of the system by one single site towards the right. For $k = 1$ the ferromagnetic defect is placed between sites 1 and L while with $k > 1$ the translation operator moves it around the whole chain.

Let us now consider a partition of the system $A|B$ in which both A and B are convex sets, i.e. ensembles of contiguous spins. From (B.1) we may recover the reduced density matrix obtained by projecting ω_p into A . In the quite general case $a = \dim(A) \geq 2$, the reduced density matrix can be written as follows.

$$\rho_A = \text{Tr}_B(|\omega_p\rangle\langle\omega_p|) = \frac{1}{2L} \begin{pmatrix} \mathbf{Q}^{(b)} & \mathbf{0}^{(b)} & V^{(b)} & W^{(b)} \\ \mathbf{0}^{(b)} & \mathbf{Q}^{(b)} & W^{(b)} & V^{(b)} \\ (V^{(b)})^\dagger & (W^{(b)})^\dagger & L - b & 2 \cos(\chi p) \\ (W^{(b)})^\dagger & (V^{(b)})^\dagger & 2 \cos(\chi p) & L - b \end{pmatrix} \quad (\text{B.3})$$

In eq. (B.3) ρ_A is a $2a \times 2a$ square matrix, and we defined $b = a - 1$ and $\chi = L - a$. The reduced density matrix ρ_A is not block diagonal but has a block structure and each one of these blocks has a quite regular structure. To begin, the matrices $\mathbf{0}^{(b)}$ and $\mathbf{Q}^{(b)}$ are both $b \times b$ square matrices. All the elements of the first are zeros, i.e. $\mathbf{0}_{m,n}^{(b)} = 0 \forall m, n$, while the elements of $\mathbf{Q}^{(b)}$ obey to the following law $\mathbf{Q}_{m,n}^{(b)} = \exp(-i(m - n)p)$. On the contrary, both $V^{(b)}$ and $W^{(b)}$ are column vectors made of b rows and one single column. The n -th element of $V^{(b)}$ can be written as $V_n^{(b)} = \exp(-i(b + 1 - n)p)$, while for $W^{(b)}$ we have $W_n^{(b)} = \exp(-i(L - n)p)$

Diagonalizing this matrix with the help of Mathematica, and testing the results so obtained with a purely numerical code, we have found that all the eigenvalues are zero except four. These four non-vanishing eigenvalues can be put in the form

$$\lambda_{1,\dots,4} = \frac{1}{4L} \left(L + 2\gamma \cos(p\chi) \pm \sqrt{(L - 2a)^2 + 4L(1 + \gamma \cos(p\chi)) - 4 \sin^2(p\chi)} \right), \quad (\text{B.4})$$

where γ is a dicotomic real parameter of modulus 1, i.e. $\gamma = \pm 1$. The four eigenvalues

are recovered considering all the possible combinations of the \pm sign in front of the square root and the values of γ . From this expression, all the different entropic measures of the entanglement can be easily recovered. A case in which the analytical expression of the entanglement entropy becomes very easy is the 2-Rényi entropy that, after some steps, can be reduced to

$$S_2(a, p) = -\log_2 \left[\frac{L(2 + L) - 2a(L - a) + 2 \cos(p\chi)}{2L^2} \right] \quad (\text{B.5})$$

from which, setting $a = (L - 1)/2$, we can recover the result presented in the main text

B.2 Analytic derivations of Stabilizer Rényi entropy for generalized W states

The main result shown in the main part of the letter is based on the behavior of the SRE on the family of W_P states, which is a family that generalizes the well-known W state. To evaluate the SRE, let us start by recalling its expression for a generic pure state $|\psi\rangle$. It reads

$$\mathcal{M}_2(|\psi\rangle) = -\log_2 \left(\frac{1}{2^L} \sum_{\mathcal{P}} \langle \psi | \mathcal{P} | \psi \rangle^4 \right), \quad (\text{B.6})$$

where the sum runs over all possible Pauli strings \mathcal{P} that can be defined on the system. Taking into account that any $|W_p\rangle$ state can be written as

$$|W_p\rangle = \frac{1}{\sqrt{L}} \sum_{j=1}^L e^{ipj} \sigma_j^z |-\rangle^{\otimes L}, \quad (\text{B.7})$$

we immediately see that to determine the SRE on $|W_p\rangle$, we have to evaluate the terms

$$O(\mathcal{P}) = \sum_{j,k=1}^L \exp[i(j - k)p] \langle - |^{\otimes L} \sigma_k^z \mathcal{P} \sigma_j^z | - \rangle^{\otimes L} \quad (\text{B.8})$$

It is easy to see that in the large majority of cases $O(\mathcal{P}) = 0$, but with two important exceptions. The first exception is when the Pauli string is made only by the identity and σ^x operators, i.e. when \mathcal{P} becomes $\mathcal{P}' = \bigotimes_{k=1}^L \sigma_k^\alpha$, where $\alpha \in \{0, x\}$. In this case, the absolute value of each $O_{j,k}(\mathcal{P}')$ depends on the number $l = 0, \dots, L$ of σ_k^x operators in the string, and it is equal to $\|\frac{L-2l}{L}\|$. Taking into account all the possible combinations of identity and σ^x operators, the contribution of these terms becomes

$$\sum_{\mathcal{P}'} O(\mathcal{P}') = \sum_{l=0}^L \left(\frac{L-2l}{L}\right)^4 \frac{L!}{l!(L-l)!}. \quad (\text{B.9})$$

The second exception is represented by the Pauli strings with only two operators in the set $\{\sigma^y, \sigma^z\}$. Within this hypothesis, the Pauli string can be written as $\mathcal{P}'' = \bigotimes_{k=1, k \neq i, j}^L \sigma_k^\alpha \otimes (\sigma_j^\beta \sigma_k^\gamma)$ where $\alpha = 0, x$ while $\beta, \gamma = y, z$. This contribution comes from the fact that such strings are able to shift the $|+\rangle$ from the site j to the site k and vice versa. When $\beta = \gamma$ both these two terms have the same sign, so giving a contribution proportional to $\cos[(j-k)p]/2L$. On the contrary, when $\beta \neq \gamma$ they show opposite signs, so contributing proportional to $\sin[(j-k)p]/2L$. Naming $r = j - k$ and summing over all possible Pauli strings we have

$$\sum_{\mathcal{P}''} O(\mathcal{P}'') = L \sum_{l=0}^{L-2} \sum_{r=1}^{L-1} \frac{(L-2)!}{l!(L-2-l)!} \left[\left(\frac{2 \cos(pr)}{L}\right)^4 + \left(\frac{2 \sin(pr)}{L}\right)^4 \right]. \quad (\text{B.10})$$

Putting the two non-vanishing contributions together in the definition of the SRE of order 2 we recover, after some steps, the following expression

$$\mathcal{M}_2(W_p) = -\log_2 \left(-\frac{11 - 12L + \frac{\sin((2-4L)p)}{\sin(2p)}}{2L^3} \right). \quad (\text{B.11})$$

Appendix C

Analytical results for the ground state of the ANNNI model

C.1 Perturbation theory close to the classical line

In this appendix we show the details of how to obtain the ground state of the topologically frustrated ANNNI model near the classical line, i.e. in the limit $\hbar \rightarrow 0^+$, resorting to the lowest order perturbation theory and how to use this result to extract its bipartite entanglement entropy.

C.1.1 Determination of the ground state

Let us divide the full Hamiltonian in eq. (4.1) as

$$H = H_0 + \hbar \mathcal{H}^{\text{pert}}, \quad (\text{C.1})$$

with

$$H_0 = J_1 \sum_{i=1}^L \sigma_i^x \sigma_{i+1}^x + J_2 \sum_{i=1}^L \sigma_i^x \sigma_{i+2}^x, \quad (\text{C.2})$$

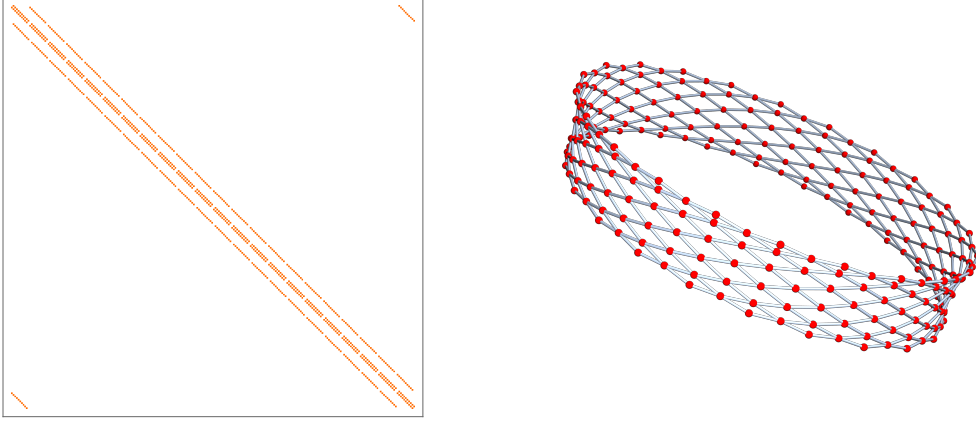


Figure C.1: Left: Matrix representation of the perturbation Eq. (C.3) over the set \mathcal{G} given in Eq. (4.4) for the ANNNI chain of length $L = 14$. Right: Graph representation of the matrix on the left.

and

$$\mathcal{H}^{\text{pert}} = \sum_{j=1}^L \sigma_j^x = \mathcal{H}_o^{\text{pert}} + \mathcal{H}_e^{\text{pert}}, \quad \mathcal{H}_{o/e}^{\text{pert}} = \sum_{j \in \{o/e\}} \sigma_j^x, \quad (\text{C.3})$$

where, keeping the notation introduced in the main text, the e (o) subscript refer to the even (odd) sites subchain.

To find the analytical expression of the ground-state close to $h = 0$ we thus need to diagonalize the matrix $\mathcal{H}^{\text{pert}}$ over the degenerate ground-state manifold \mathcal{G} (Eq. (4.4) in the main text), which reads

$$\begin{aligned} \langle \psi_{(k,p)} | \mathcal{H}^{\text{pert}} | \psi_{(k',p')} \rangle &= f_o(k, p, k', p') + f_e(k, p, k', p'), & (\text{C.4}) \\ f_o(k, p, k', p') &\equiv \left(\delta_{k,k'-1} \delta_{(-1)^k, (-1)^{k'-1}} + \right. \\ &\quad \left. + \delta_{k,k'+1} \delta_{(-1)^k, (-1)^{k'+1}} \right) \times \delta_{p,p'} \delta_{(-1)^p, (-1)^{p'+1}}, \\ f_e(k, p, k', p') &\equiv \delta_{k,k'} \delta_{(-1)^k, (-1)^{k'}} \times \\ &\quad \times \left(\delta_{p,p'+1} \delta_{(-1)^{p+1}, (-1)^{p'+2}} + \delta_{p,p'-1} \delta_{(-1)^{p+1}, (-1)^{p'}} \right), \end{aligned}$$

where periodicity of the indices with respect to L' is intended. The matrix plot and its associated graph are shown in Fig. C.1.

Because of the complex structure of this matrix, its diagonalization is non trivial. Nevertheless, a better insight can be obtained by looking first at the simpler case in

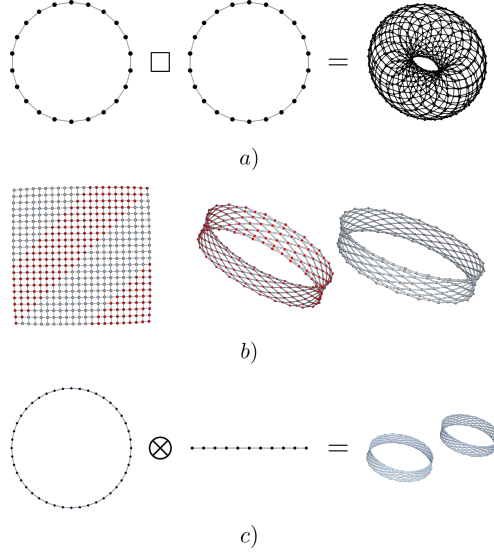


Figure C.2: a) The Torus Grid graph $T_{L,L}$ obtained as the Cartesian product $C_L \square C_L$ for $L = 22$. b) The unfolded Torus with the two subsets corresponding to \mathcal{G} (red vertices) and \mathcal{G}^c (gray vertices) highlighted, and the corresponding disconnected sub-graphs. c) The same sub-graphs can be also obtained as the tensor product of the Cycle graph of cardinality $2L$ and the Path graph of length L' .

which $J_1 = 0$, corresponding to two non-interacting TF Ising rings. In this case, it is easy to check that $\mathcal{H}^{\text{pert}}$ can be written as the cartesian product (box product) of two circulant matrices when evaluated over the manifold \mathcal{G}_0 (see Eq. (4.3) of the main text), namely

$$\mathcal{H}^{\text{pert}} = \mathcal{H}_o^{\text{pert}} \square \mathcal{H}_e^{\text{pert}}. \quad (\text{C.5})$$

While it is known that these matrices can be exactly diagonalized, it is worth noting that all the entries of $\mathcal{H}_{o/e}^{\text{pert}}$ are either zeros or one. Hence, they can be understood as adjacency matrices [353], associated to two identical cycle graphs $C_{\frac{L}{2}}$ [354]. Remembering that for any given two graphs G_1 and G_2 having adjacency matrix $A(G_i)$, $i = 1, 2$ respectively, $A(G_1) \square A(G_1) = A(G_2 \square G_2)$ [355] (Fig, C.2), we can conclude that the resulting graph associated with the full matrix $\mathcal{H}^{\text{pert}}$ is the Torus Grid Graph $T_{\frac{L}{2}, \frac{L}{2}} = C_{\frac{L}{2}} \square C_{\frac{L}{2}}$ [354].

As discussed in the main text, setting $J_1 \neq 0$ acts as a selection rule: its effect being to split the set \mathcal{G}_0 in half according to the orientation of the spin of the second chain that

Graph	A-eigenvalues	A-eigenvectors
G_1	λ_i	X_i
G_2	μ_j	Y_j
$G_1 \square G_2$	$\lambda_i + \mu_j$	$X_i \otimes Y_j$
$G_1 \otimes G_2$	$\lambda_i \mu_j$	$X_i \otimes Y_j$
$G_1 \cup G_2$	λ_i	$\begin{pmatrix} X_i \\ 0 \end{pmatrix}$
	μ_j	$\begin{pmatrix} 0 \\ Y_j \end{pmatrix}$

Table C.1: Properties of the graph operations considered. First column: graphs and graph operations. Second column: eigenvalues of the corresponding adjacency matrix A . Third column: Eigenvector of the corresponding adjacency matrix A .

falls between the two spins of the first ring where the magnetic defect is localized:

$$\mathcal{G}_0 = \mathcal{G} \cup \mathcal{G}^c, \quad (\text{C.6})$$

where \mathcal{G}^c is the complement set of \mathcal{G} . The graphs of the two sets \mathcal{G} and \mathcal{G}^c are respectively the red and gray part of the torus (see Fig. C.2b for its unfolded representation and its decomposition). The red one is also the graph obtained through Eq. (C.4), its ground state being then the required solution. We can now observe that this graph decomposition can be achieved through the Cartesian product of a Cycle graph of length $2L$ and a Path graph of length L' (Fig. C.2c). Specifically, the L kink states of the odd chain couple separately with half of the kink states (L') that are compatible with the condition $J_1 > 0$, and the other half with the condition $J_1 < 0$. The eigenvectors of the adjacency matrix of the desired graph (the red ring in Fig. C.2) can then be obtained directly from the eigenvectors of the graphs involved in the operation (see Tab. C.1) through their tensor product, and finally projecting into the subspace of the desired ring, since the two graphs are disconnected (see Tab. C.1).

The general eigenvector will then be of the form $|b_l\rangle \otimes |a_k\rangle$, that are respectively eigenvectors of the Cycle and Path graphs, with eigenvalue $\lambda_l \mu_k$ (see Tab. C.2). The ground state will correspond to the $\{l, k\}$ values for which the product is minimum. Since

Graph	A-eigenvalues	A-eigenvectors
Cycle	$\lambda_l = \sum_{k=0}^{m-1} c_k \omega^{kj}$ $j = 0, \dots, m-1$	$ b_l\rangle = \sum_{r=0}^{m-1} e^{i\frac{2\pi}{m}lr} r\rangle$
Path	$\mu_k = 2 \cos\left(\frac{k\pi}{m+1}\right)$ $k = 1, 2, \dots, m$	$ a_k\rangle = \sum_{j=1}^m \sin\left(\frac{k\pi}{m+1}j\right) j\rangle$

Table C.2: Eigenvalues and eigenvectors of the adjacency matrix of the Cycle and Path graphs having m vertices. The coefficients c_k is the matrix element on the k -th row of the Circulant matrix associated to the Cycle graph.

the solely effect of the J_1 interaction is to select a sub-set of states, we expected for the odd chain the ground state of the topologically frustrated Ising ring ($l = 0$). As a consequence, the product is minimized for $k = L'$, and the ground states will be of the form $|b_0\rangle \otimes |a_{L'}\rangle$. The ground state will then be of the form

$$|g\rangle = A \sum_{k=1}^L \sum_{r=0}^{L'-1} \sin[\alpha(r+1)] |k, (-1)^k\rangle |k+r, (-1)^{k+r}\rangle, \quad (\text{C.7})$$

where $\alpha = L\pi(r+1)/(L+2)$, and where we disentangle the indexes in Eq. (4.4), writing the general element as $|k, (-1)^k\rangle |k+r, (-1)^{k+r}\rangle$, $k = 1, \dots, L$, $r = 0, \dots, L'-1$. The periodicity of the indices with respect to L' is implicit.

To fix the normalization constant let us first introduce the following quantity

$$f_{d,b}^{m,n}(\alpha) = \sum_{r=m}^n \sin[\alpha(r+d+1)] \sin[\alpha(r+b+1)], \quad (\text{C.8})$$

with $\alpha \in \mathbb{R}$, and we write $f_{b,b}^{m,n}$ instead of $f_{b,b}^{m,n}(\alpha)$. Eq. (C.8) admits a nice representation in terms of the Chebyshev polynomials of first and second type, $T_n(\cos \alpha)$ and $U_n(\cos \alpha)$ respectively, remembering that $\sin[\alpha(n+1)] = \sin \alpha U_n(\cos \alpha)$ and resorting to

the relations [356]

$$T_{a+b}(x) - T_{a-b}(x) = 2(x^2 - 1)U_{a-1}(x)U_{b-1}(x), \quad (\text{C.9})$$

$$T_{2(a-b)}(x) - 1 = 2(x^2 - 1)U_{a-b-1}^2(x), \quad (\text{C.10})$$

$$T_{a+b}(x) + T_{a-b}(x) = 2T_a(x)T_b(x), \quad (\text{C.11})$$

$$T_{2(a-b)}(x) + 1 = 2T_{a-b}^2(x). \quad (\text{C.12})$$

We have

$$\begin{aligned} f_{d,b}^{m,n} &= \frac{1}{2}(n - m + 1)T_{b-d} + \\ &\quad - \frac{1}{4}(U_{-(2m+b+d+2)} + U_{2n+b+d+2}). \end{aligned} \quad (\text{C.13})$$

Furthermore we also need the square of Eq. (C.8)

$$\begin{aligned} (f_{d,b}^{m,n})^2 &= \frac{(n - m + 1)^2}{8}(1 + T_{2(b-d)}) + \\ &\quad + \frac{1}{32 \sin^2(\alpha)}(2 - T_{2(2n+b+d+3)} - T_{2(2m+b+d+1)} + \\ &\quad T_{2(n+m+b+d+2)} - T_{2(n-m+1)}) + \\ &\quad - \frac{n - m + 1}{16}(U_{2(n+b+1)} + U_{2(2n+d+1)} + \\ &\quad + U_{-2(n+d+1)} + U_{-2(n+b+1)}), \end{aligned} \quad (\text{C.14})$$

and we evaluate the asymptotic expression

$$\lim_{\substack{L, M \rightarrow \infty \\ M/L \rightarrow C}} T_{aL+bM+c}(\cos \alpha) = (-1)^{b+c} \cos(2b\pi x), \quad (\text{C.15})$$

with $x = M/L$, $\alpha = L\pi/(L + 2)$, $0 < C < 1$, and $a, b, c \in \mathbb{Z}$, which is valid for even and odd $L, M \in \mathbb{N}$ respectively.

Simplifying the notation as $T_n(\cos \alpha) = T_n$ and $U_n(\cos \alpha) = U_n$, the normalization

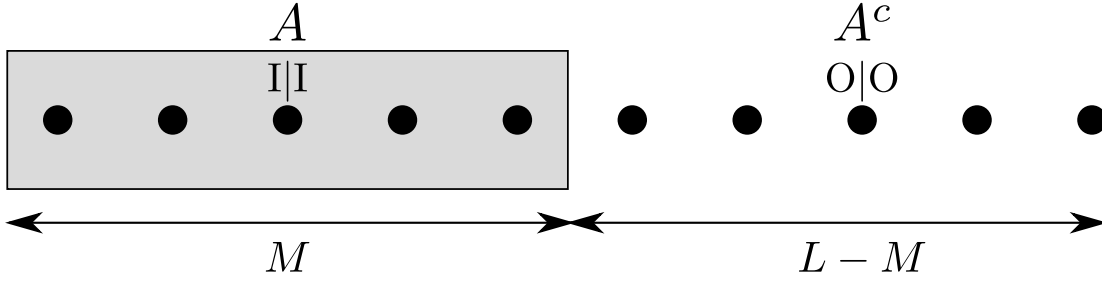


Figure C.3: Partitioning of the ANNNI chain for the computation of the Entanglement Entropy Eq. (4.6) near the classical point. The I (O) notation indicates that the $(k, p) := k|p$ indexes are inside (outside) the partition A .

constant can be then be calculated resulting in

$$\langle g|g \rangle = |A|^2 L f_{0,0}^{0, \frac{L}{2}-1} = |A|^2 \left(\frac{L^2}{4} + \frac{L}{4} - \frac{L}{4} U_L \right) = 1. \quad (\text{C.16})$$

Furthermore, $U_L = -1$ for L even. In fact, remembering that $\sin[\alpha(n+1)] = \sin \alpha U_n(\cos \alpha)$ we can prove equivalently that $\sin[\alpha(L+1)] = -\sin(\alpha)$, $\forall L$ even, condition that it is always satisfied for $L = 4n+2$, $\forall n \in \mathbb{N}$. From Eq. (C.16) it then follows that $A = 2/\sqrt{L(L+2)}$. The translational invariant form Eq. (4.5) is then obtained through the substitution $p \rightarrow k+r$.

C.1.2 Asymptotic expression of the bipartite Entanglement Entropy close to the classical line.

Having determined the expression for the ground state close to the classical line, in this appendix we detail the analytic derivation of its bipartite Entanglement Entropy. Without loss of generality, we consider a system sub-partition A made by an odd number M of consecutive spins. The corresponding spin number inside A for the two sub-chains are then equal to $M_o = (M+1)/2$ and $M_e = (M-1)/2$ respectively (see Fig. C.3).

As discussed in Sec. 4.3, in analogy with the approaches used for the TF Ising chain [156], it is useful to rewrite the state in Eq. (4.5) according to the kink indexes

$(k, p) := k|p$ being internal (I) or external (O) to the subsystem A

$$|g\rangle = |I|I\rangle + |I|O\rangle + |O|I\rangle + |O|O\rangle, \quad (\text{C.17})$$

where the vertical bar ($|$) separates the indexes corresponding to the odd/even chains. We can then express the corresponding reduced density matrix as a 16×16 block matrix. Furthermore, we numerically observe that only four blocks contribute to the spectrum in the thermodynamic limit as shown in Fig. 4.5. We can then consider the following block-diagonal approximated form for the reduced density matrix

$$\rho_A = \begin{pmatrix} \rho^{II|II} & 0 & 0 & 0 \\ 0 & \rho^{IO|IO} & 0 & 0 \\ 0 & 0 & \rho^{OI|OI} & 0 \\ 0 & 0 & 0 & \rho^{OO|OO} \end{pmatrix}. \quad (\text{C.18})$$

Let us now discuss each block matrix and derive their eigenvalues separately.

Asymptotic eigenvalues of the matrices $\rho^{II|II}$ and $\rho^{OO|OO}$

We start considering the matrix $\rho^{OO|OO}$

$$\rho^{OO|OO} = \frac{4}{2L + L^2} \sum_{n=0}^{\frac{L-M-1}{2}-1} f_{0,0}^{0,n} \mathbb{K}_{4 \times 4}, \quad (\text{C.19})$$

where we have used the property $c_r = c_{L/2-r}$. We have then one eigenvalue with multiplicity four

$$\begin{aligned} \lambda_1 &= \frac{4}{2L + L^2} \sum_{n=0}^{\frac{L-M-3}{2}} f_{0,0}^{0,n}(\alpha) = \\ &= \frac{(L - M - 1)(L - M + 3)}{4L(L + 2)} + \\ &- \frac{1}{2L(L + 2) \sin^2 \alpha} (T_2 - T_{L-M+1}). \end{aligned} \quad (\text{C.20})$$

Its asymptotic expression is straightforward resorting to the limit Eq. (C.15)

$$\lambda_1^{\text{Asym}}(x) = \frac{(1-x)^2}{4} - \frac{\sin^2 \pi x}{4\pi^2}. \quad (\text{C.21})$$

The matrix $\rho^{\text{II|II}}$ is a 4×4 diagonal block matrix with identical blocks once resorting to the property $c_r^2 = c_{L/2-r}^2$

$$\rho^{\text{II|II}} = \bigoplus_{k=1}^4 \tilde{\rho}^{\text{II|II}}, \quad (\text{C.22})$$

with the $(M+1)/2 \times (M+1)/2$ matrix $\tilde{\rho}^{\text{II|II}}$ given by

$$\tilde{\rho}^{\text{II|II}} = \left[v_{\frac{M-1}{2}}, v_{\frac{M-3}{2}}, \dots, v_0 \right] \otimes \left[v_{\frac{M-1}{2}}, v_{\frac{M-3}{2}}, \dots, v_0 \right], \quad (\text{C.23})$$

with $v_i = (c_0, c_1, \dots, c_{i-1})$. Despite its complexity this matrix has rank one. From the Cayley-Hamilton theorem then the only non-zero eigenvalue with multiplicity four is given by its trace [357]

$$\begin{aligned} \lambda_2 &= \text{Tr} [\tilde{\rho}^{\text{II|II}}] = \frac{4}{2L+L^2} \sum_{n=0}^{\frac{L-M-1}{2}-1} f_{0,0}^{0,n} = \\ &= \frac{(M-1)(M+3)}{4L(L+2)} + \\ &- \frac{1}{2L(L+2)\sin^2 \alpha} (T_2 - T_{M+1}). \end{aligned} \quad (\text{C.24})$$

Its asymptotic limit is given by

$$\lambda_2^{\text{Asym}}(x) = \frac{x^2}{4} - \frac{\sin^2 \pi x}{4\pi^2}. \quad (\text{C.25})$$

Asymptotic eigenvalues of the matrices $\rho^{\text{IO|IO}}$ and $\rho^{\text{OI|OI}}$

The matrices $\rho^{\text{IO|IO}}$ and $\rho^{\text{OI|OI}}$ are 2×2 block matrices with identical blocks of size respectively $\frac{M+1}{2} \times \frac{M+1}{2}$ and $\frac{M-1}{2} \times \frac{M-1}{2}$

$$\rho^{\text{IO|IO}} = \bigoplus_{k=1}^2 \tilde{\rho}^{\text{IO|IO}}, \quad \rho^{\text{OI|OI}} = \bigoplus_{k=1}^2 \tilde{\rho}^{\text{OI|OI}}, \quad (\text{C.26})$$

with

$$\begin{aligned} (\tilde{\rho}^{\text{IO|IO}})_{i,j} &= f_{\frac{L-M-1}{2}-i, \frac{L-M-1}{2}-j}^{0, \frac{L-M-1}{2}}, \\ (\tilde{\rho}^{\text{OI|OI}})_{i,j} &= f_{i,j}^{1, \frac{L-M-1}{2}}, \end{aligned} \quad (\text{C.27})$$

where we resort again to the property $c_r = c_{L/2-r}$.

The matrices Eqs. (C.27) has rank two. As a consequence, resorting to the Cayley-Hamilton theorem, we can compute the non-zero eigenvalues solving the following quadratic equation [357]

$$\lambda^2 - \text{Tr}A \lambda - \frac{1}{2} [\text{Tr}A^2 - (\text{Tr}A)^2] = 0, \quad (\text{C.28})$$

with $A = \tilde{\rho}^{\text{IO|IO/OI|OI}}$. A straightforward computation thought Eq.s (C.13) and Eq. (C.14) shows that

$$\begin{aligned} \text{Tr} \tilde{\rho}_{\text{IO|IO}} &= \frac{4}{2L+L^2} \sum_{r=0}^{\frac{M-1}{2}} f_{0,0}^{r, \frac{L-M-1}{2}} = \frac{(M+1)(L-M+1)}{2L(L+2)} + \\ &+ \frac{1}{2L(L+2) \sin^2 \alpha} (1 - T_{M+1} - T_{L-M+1} + T_{L+2}). \end{aligned} \quad (\text{C.29})$$

$$\begin{aligned}
\text{Tr}(\tilde{\rho}^{\text{IO|IO}})^2 &= \sum_{b,d=0}^{\frac{M-1}{2}} \left(f_{d,b}^{0, \frac{L-M-1}{2}} \right)^2 = \frac{(L-M+1)^2(M+1)^2}{8L^2(L+2)^2} + \frac{(L-M+1)^2}{4L^2(L+2)^2 \sin^2 \alpha} (1 - T_{M+1}) + \\
&- \frac{(L-M+1)(M+1)}{2L^2(L+2)^2 \sin^2 \alpha} (T_{L-M+1} - T_{L+2} + T_{M+1} - 1) + \frac{(M+1)^2}{4L^2(L+2)^2 \sin^2 \alpha} (1 - T_{L-M+1}) + \\
&+ \frac{1}{4L^2(L+2)^2 \sin^4 \alpha} [2T_{L+2} - T_{L-M+3} - T_{L-M+1} - T_{2L-M+3} + \\
&- T_{M+1} + \frac{1}{2}(T_{2(L-M+1)} + T_{2(L+2)} + T_{2(M+1)})], \tag{C.30}
\end{aligned}$$

$$\begin{aligned}
\text{Tr} \tilde{\rho}^{\text{OI|OI}} &= \frac{4}{2L+L^2} \sum_{r=1}^{\frac{M-1}{2}} f_{0,0}^{r,r+\frac{L-M-3}{2}} = \frac{(M-1)(L-M-1)}{2L(L+2)} + \\
&+ \frac{1}{2L(L+2) \sin^2 \alpha} [T_2 - T_{M+1} - T_{L-M+1} + T_L], \tag{C.31}
\end{aligned}$$

$$\begin{aligned}
\text{Tr}(\tilde{\rho}^{\text{OI|OI}})^2 &= \sum_{b,d=0}^{\frac{M-3}{2}} \left(f_{d,b}^{1, \frac{L-M-1}{2}} \right)^2 = \frac{(L-M-1)^2(M-1)^2}{8L^2(L+2)^2} + \frac{(L-M-1)^2}{4L^2(L+2)^2 \sin^2 \alpha} (1 - T_{L-M+1}) + \\
&- \frac{(L-M-1)(M-1)}{2L^2(L+2)^2 \sin^2 \alpha} (T_{L-M+1} - T_L + T_{M+1} - T_2) + \frac{(M-1)^2}{4L^2(L+2)^2 \sin^2 \alpha} (1 - T_{L-M-1}) + \\
&+ \frac{1}{4L^2(L+2)^2 \sin^4 \alpha} [2T_{L+2} - T_{L-M+3} - T_{L+M+1} - T_{2L-M+1} + \\
&- T_{M+3} + \frac{1}{2}(T_{2(L-M+1)} + T_{2L} + T_{2(M+1)}) + T_4]. \tag{C.32}
\end{aligned}$$

Through the limit Eq. (C.15) we obtain the same asymptotic expression for the eigenvalues of the two matrices, with multiplicity four

$$\lambda_{3,4}^{\text{Asym}}(x) = \frac{x(1-x)}{4} + \frac{\sin^2 \pi x}{4\pi^2} \pm \frac{\sin \pi x}{4\pi}. \tag{C.33}$$

Collecting the reduced density matrix eigenvalues

The asymptotic expression for the entanglement entropy Eq. (4.8) can be obtained through the definition Eq. (4.6) and the asymptotic expression of the eigenvalues Eq. (4.7),

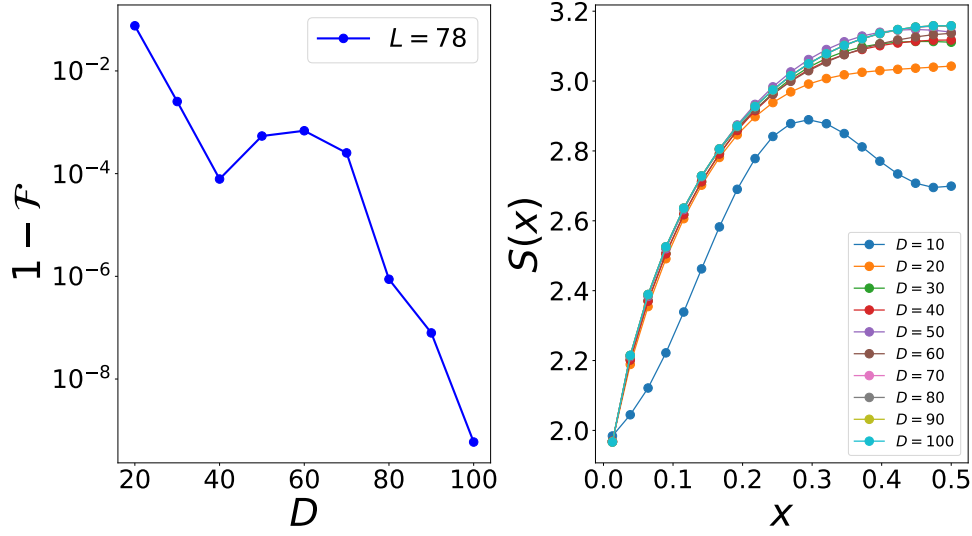


Figure C.4: Left: scaling of the infidelity between ground-states computed with different bond dimension. Right: saturation of the entanglement entropy with increasing bond dimension D .

as well as with Eq.s (C.20), (C.25), and (C.33), noticing that

$$\begin{aligned}
 \lambda_1^{\text{Asym}} &= \frac{1}{4}(1-y)(1-z), & \lambda_2^{\text{Asym}} &= \frac{1}{4}yz, \\
 \lambda_3^{\text{Asym}} &= \frac{1}{4}y(1-z), & \lambda_4^{\text{Asym}} &= \frac{1}{4}(1-y)z,
 \end{aligned} \tag{C.34}$$

with $y = x - \frac{\sin \pi x}{\pi}$ and $z = x + \frac{\sin \pi x}{\pi}$.

C.2 Numerical analysis

We performed a numerical estimation of the ground-state of the Hamiltonian Eq. (4.1) using the density matrix renormalization group (DMRG) technique. In particular, we implemented a DMRG based on tensor networks, following the approach of [248]. Despite the fact that in presence of topological frustration the EE is expected to violate the area law, it is also known from [154] that it will saturate to a finite value for large system's sizes, as opposite to what happens in critical systems where a logarithmic divergence of the EE is expected in thermodynamic limit. Therefore, one could expect that an MPS ansatz can still reproduce the ground-states of topologically frustrated systems in an

efficient way.

In order to benchmark the validity of the MPS ansatz we computed the fidelity between ground-states corresponding to MPS with different bond-dimensions D

$$\mathcal{F} = | \langle GS(D + \Delta D) | GS(D) \rangle |, \quad (\text{C.35})$$

and checked the saturation of the entanglement entropy as a function of the bond dimension. The results are shown in Fig. C.4. We observe that the infidelity, i.e. $1 - \mathcal{F}$, decays with increasing bond-dimension. Moreover, also the EE entropy shows a saturation for increasing bond-dimension, confirming the convergence of the DMRG algorithm for sufficiently large bond-dimension.

Based on the results of Fig. C.4 we decided to use $D = 70$ to collect the data presented in Sec. 4.4.

Appendix D

Analytical results on the Ising chain quantum battery

The analytical results presented in this appendix are a consequence of those presented in Appendix A. The only difference is that, in order to study the quantum Ising chain, we will set the anisotropy parameter γ to 1.

D.1 Projection coefficients after a global quench

In this section we compute analytically the projection coefficients after a global quench from an Hamiltonian $H_0 \equiv H(J, h_0)$ to $H_1 \equiv H(J, h_1)$. Since the fermionic structure of the states is the same, the results hold both for the non-frustrated (FM) and frustrated (AFM) case. The initial state before the quench is considered to be the ground state of H_0 . In the FM ($J = 1$) case this can be given by

$$|G_0^+\rangle = |\emptyset^+\rangle_0, \quad (\text{D.1})$$

or

$$|G_0^-\rangle = b_0^\dagger |\emptyset^-\rangle_0 = |0\rangle_0, \quad (\text{D.2})$$

depending on the parity sector, while in the AFM ($J = -1$) the ground state is always in the even sector and we have

$$|G_0^+\rangle = |\emptyset^+\rangle_0. \quad (\text{D.3})$$

In both situations, since the global quench in the magnetic field preserves the translational invariance and parity of the model, after the quench the initial state will have non-vanishing projection only onto those eigenstates of H_1 with its same parity and momentum, i.e. states with zero momentum. Moreover, since all of the eigenstates are constructed by addition of quasi-particles with a certain quasi-momentum q to a fermionic vacuum, it turns out that the projections will be non-zero only onto those states where excitations are added in couples with opposite momentum, i.e. applying the operator $b_q^\dagger b_{-q}^\dagger$ to the ground-state. Using simple combinatorics, one could hence easily understand that in a system with N spins, starting from the initial states $|\emptyset^+\rangle$ or $|0\rangle$ the number of states with non-zero projections will be

$$M = \sum_{l=0}^{\frac{N-1}{2}} \binom{\frac{N-1}{2}}{l} = 2^{\frac{N-1}{2}}. \quad (\text{D.4})$$

The projections can explicitly be computed by evaluating scalar products between different states. These are easily evaluated when the states are expressed in the fermion basis rather than in the Bogoliubov one as in (A.13), since the fermionic operators are independent of the parameters of the hamiltonian, which will only enter the Bogoliubov angles. Using the notation

$$|\emptyset_k\rangle = \cos \theta_k |0\rangle_k |0\rangle_{-k} - \sin \theta_k |1\rangle_k |1\rangle_{-k}, \quad (\text{D.5})$$

we also have that

$$b_k^\dagger b_{-k}^\dagger |\emptyset_k\rangle = \sin \theta_k |0\rangle_k |0\rangle_{-k} + \cos \theta_k |1\rangle_k |1\rangle_{-k}. \quad (\text{D.6})$$

Therefore, because of the selection rules imposed by the global quench, we have only four possibilities for the scalar products after the quench:

$$\langle \emptyset_k^{(1)} | \emptyset_k^{(0)} \rangle = \cos \Delta_k, \quad (\text{D.7})$$

$$\langle \emptyset_k^{(1)} | b_k^{\dagger(0)} b_{-k}^{\dagger(0)} | \emptyset_k^{(0)} \rangle = -\sin \Delta_k, \quad (\text{D.8})$$

$$\langle \emptyset_k^{(1)} | b_{-k}^{\dagger(1)} b_k^{\dagger(1)} | \emptyset_k^{(0)} \rangle = \sin \Delta_k, \quad (\text{D.9})$$

$$\langle \emptyset_k^{(1)} | b_{-k}^{\dagger(1)} b_k^{\dagger(1)} b_{-k}^{\dagger(0)} b_{-k}^{\dagger(0)} | \emptyset_k^{(0)} \rangle = \cos \Delta_k. \quad (\text{D.10})$$

where $\Delta_k = \theta_k^{(1)} - \theta_k^{(0)}$.

Finally, we can introduce the notation $|P_0\rangle = \prod_{p \in P_0} b_p^\dagger b_{-p}^\dagger |G_0\rangle$, to describe a generic zero-momentum state, P_0 being a subset of $\Gamma^+ \setminus \{\pi\}$ or $\Gamma^- \setminus \{0\}$ depending on the parity sector. With this in mind, the projection coefficient that we are looking for will take the form

$$\langle Q_1 | P_0 \rangle = \prod_{\substack{k_1 \in \Gamma \setminus (Q_1 \cup P_0 \cup \{0, \pi\}), \\ k_2 \in Q_1 \cap P_0, \\ k_3 \in P_0 \setminus Q_1, \\ k_4 \in Q_1 \setminus P_0}} \cos \Delta_{k_1} \cos \Delta_{k_2} (-\sin \Delta_{k_3}) \sin \Delta_{k_4}. \quad (\text{D.11})$$

These coefficients, for opportune choices of the quasi-momenta, will correspond to the $\langle \epsilon_k | \mu_\ell \rangle$ appearing in Eq. (5.12). Therefore, knowing them allows us to compute the populations P_ℓ .

D.2 Formal integration of Eq. (5.5)

In case where the system Hamilton H is time independent, the ME (5.5) admits analytical integration [260]. To see this let us write H as

$$H = \sum_{\epsilon} \Pi_{\epsilon} \epsilon, \quad (\text{D.12})$$

where ϵ are the eigenvalues of such operator, and $\{\Pi_\epsilon\}_\epsilon$ is the set of orthogonal projectors which decompose the the Hilbert space of the system in the associated energy eigenspaces. Exploiting the fact that $\sum_\epsilon \Pi_\epsilon = \mathbb{1}$, $\Pi_\epsilon \Pi_{\epsilon'} = \delta_{\epsilon, \epsilon'} \Pi_\epsilon$, one can then verify that an explicit solution of (5.5) is provided by

$$\rho(t) = \Phi_t^{(H)}[\rho(0)] = \sum_{\epsilon, \epsilon'} \Pi_\epsilon \rho(0) \Pi_{\epsilon'} e^{-\frac{(\epsilon - \epsilon')^2}{2\nu} t - i(\epsilon - \epsilon')t}, \quad (\text{D.13})$$

where $\Phi_t^{(H)}$ is the dynamical superoperator [297]

$$\Phi_t^{(H)}[\dots] = \sum_{\epsilon, \epsilon'} \Pi_\epsilon \dots \Pi_{\epsilon'} e^{-\frac{(\epsilon - \epsilon')^2}{2\nu} t - i(\epsilon - \epsilon')t}. \quad (\text{D.14})$$

Notice that for $t \gg \tau_2$, where τ_2 is the long dephasing time identified in the main text, such evolution induce complete suppression of the off-diagonal terms that involves superpositions associated with energy eigenvectors of different eigenvalues, i.e.

$$\Phi_t^{(H)}[\dots] \Big|_{\nu t \gg 1} \longrightarrow \mathcal{D}^{(H)}[\dots] = \sum_{\epsilon} \Pi_\epsilon \dots \Pi_\epsilon. \quad (\text{D.15})$$

For the model we are considering H is equal to H_1 for $t \in]0, \tau[$ and to H_0 for $t \geq \tau$.

Accordingly we can write

$$\rho(t) = \begin{cases} \Phi_t^{(H_1)}[\rho(0)], & \forall t \in]0, \tau[, \\ \Phi_{t-\tau}^{(H_0)} [\Phi_\tau^{(H_1)}[\rho(0)]], & \forall t \geq \tau, \end{cases} \quad (\text{D.16})$$

which for $t = T \geq \tau$ such that $T \gg \tau_2$, leads to

$$\rho(T) \simeq \mathcal{D}^{(H_0)} [\Phi_\tau^{(H_1)}[\rho(0)]], \quad (\text{D.17})$$

with $\mathcal{D}^{(H_0)}$ the dephasing map (D.15) of H_0 . Equation (5.11) finally follows from (D.17) observing that under the assumption the the initial state of the QB is the ground state

of H_0 , then all the eigenspaces involved in the writing of both of $\Phi_\tau^{(H_1)}$ and $\Phi_{t-\tau}^{(H_0)}$ only involves eigenspaces with zero momentum which turn out to be non-degenerate (i.e. their associated projectors are all rank one).

D.3 The choice of the charging time

In the main text we defined the charging time as the time τ^* after which the energy pumped into the battery through the double-quench protocol $E_{in}(\tau)$ reaches its first local maximum. In order to further justify this choice, in Fig. D.1 we report numerical evidence of the two following results:

- the value of $E_{in}(\tau^*)$ is comparable to the one that $E_{in}(\tau)$ take at the first encountered local maxima;
- τ^* is approximately independent of the system size N .

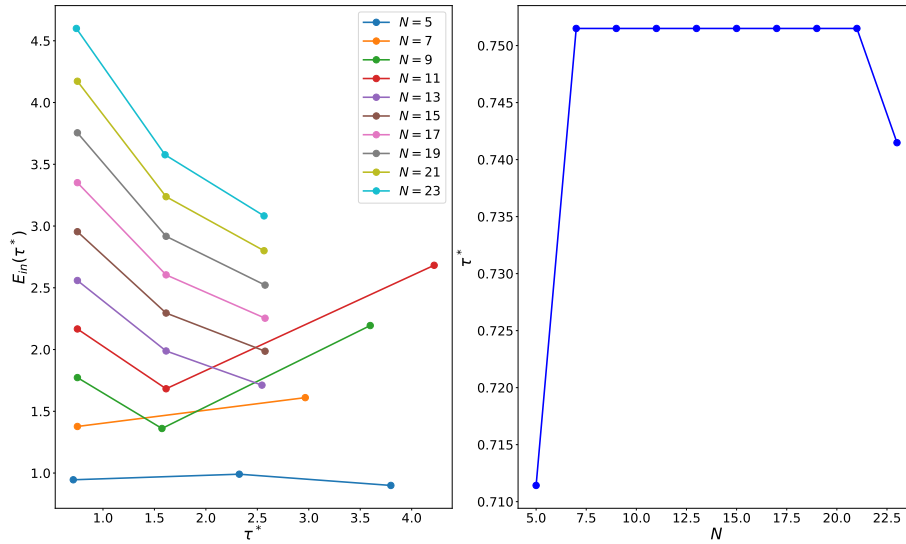


Figure D.1: Left: value of E_{in} at its first three local maxima for different system's sizes. Right: position of the first local maximum τ^* as a function of the system's size N . The data in both plots were obtained for $J = 1$, $h_0 = 0.2$ and $\Delta h = 0.5$. Both energy and time units are expressed in units of J .

These results justify our choice of τ^* since they show how it coincides with the shortest possible time after which the battery contains a relevant amount of energy. For small

system's sizes the next local maxima might have slightly higher energy, but this comes at the expenses of waiting times which are twice or three time longer than τ^* . Waiting for such long charging times might expose the battery to further decoherence effects which would decrease its performances. Moreover, since the position of τ^* is almost independent of N , it seems a reasonable choice in comparing batteries of different system's sizes.

D.4 Analysis of the discharging protocol

In this section we provide the results of different simulations of the energy transfer from the QB to an ancillary spin. As we did in the main text, we take into account a situation in which a QB, after ending the charging process and waiting a time $T \gg \tau_2$ such that its state can be considered completely incoherent, is made to interact with an ancillary two-level system. The Hamiltonian of the total system will therefore read as

$$H_W = J \sum_{k=1}^N \sigma_k^x \sigma_{k+1}^x - h \sum_{k=1}^N \sigma_k^z + \lambda H_{int} + \omega \sigma_S^z, \quad (\text{D.18})$$

where $\{\sigma_k^\alpha\}_{k=1}^N$ and $\{\sigma_S^\alpha\}$ ($\alpha = x, y, z$) are respectively the spin operators of the k -th site of the QB and the ancillary spin, while ω is the characteristic energy of the ancillary spin. Our goal is that of studying the performance of the QB for different values of h or ω . In order to do so, we perform an optimization in terms of the interaction strength λ . The results are shown in Fig. D.2 - D.7. We observe that, in most situations, it is possible to find a value of λ for which the energy transferred by the frustrated QB is converted into ergotropy for the ancillary spin. For example, in Fig. D.2 we see that for $\omega = 1$ and $h = 0.02$, there exist a regime with $\lambda > 1$ in which most of the energy transferred to the ancillary spin comes from the QB ($\Delta E_B < 0, |\Delta E_B| > |\Delta E_i|$) and the ergotropy of the qubit reaches about 80% of its maximum value. We can find something similar in Fig. D.4 and Fig. D.5, in which for $\omega = 2$ and $h = 0.2$ we observe a region around $\lambda \approx 0.2$

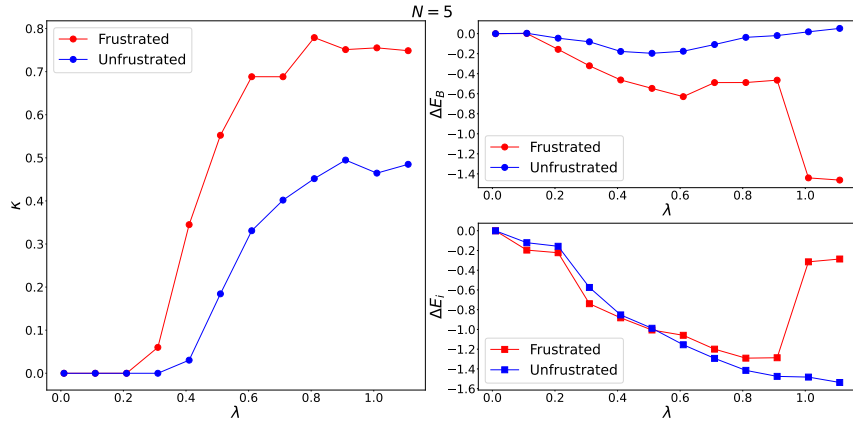


Figure D.2: Values of κ (left), ΔE_B (top right) and ΔE_i (bottom right) as a function of the interaction strength λ . The data are obtained for $\omega = 1$, $h = 0.02$, $J = \pm 1$, $\Delta h = 3.72$ and $N = 5$.

in which the frustrated battery is able to charge the ancillary spin to about 20% – 25% of the maximum level. On the contrary, in all the above mentioned situations the non-frustrated QB is not able to charge the ancillary spin. Indeed, the only situations in which its ergotropy is greater than zero corresponds to regimes in which all the energy is transferred by the interaction term and not by the non-frustrated QB, which in some scenarios is actually absorbing energy from the interaction itself ($\Delta E_B > 0$).

Finally, we checked what happens once we get closer to the critical point at $h = 1$. In particular, we repeated the same analysis for $h = 0.8$ and $\omega = 2$, and in this case both the frustrated and non-frustrated batteries are unable to transfer ergotropy to the ancillary spin.

Therefore, this analysis points towards the fact that the presence of topological frustration can deeply enhance the energy transfer properties of a QB. The exact reason behind this result is still unclear, and in future works we aim at discriminating whether this result is only due to the spectral properties of these systems, or if the peculiar structure of their long-range correlations play also an important role in the energy transfer.

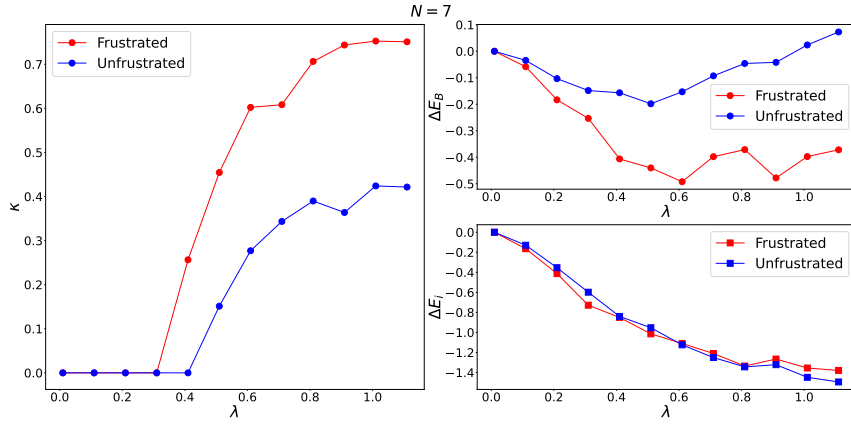


Figure D.3: Values of κ (left), ΔE_B (top right) and ΔE_i (bottom right) as a function of the interaction strength λ . The data are obtained for $\omega = 1$, $h = 0.02$, $J = \pm 1$, $\Delta h = 3.72$ and $N = 7$.

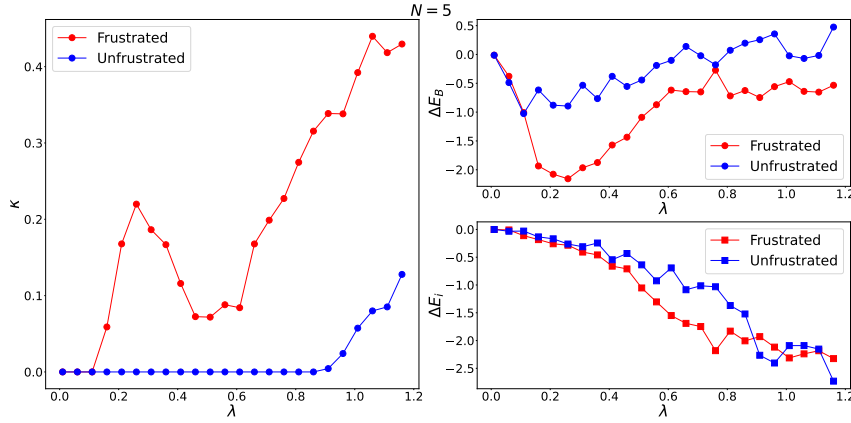


Figure D.4: Values of κ (left), ΔE_B (top right) and ΔE_i (bottom right) as a function of the interaction strength λ . The data are obtained for $\omega = 2$, $h = 0.2$, $J = \pm 1$, $\Delta h = 3.72$ and $N = 5$.

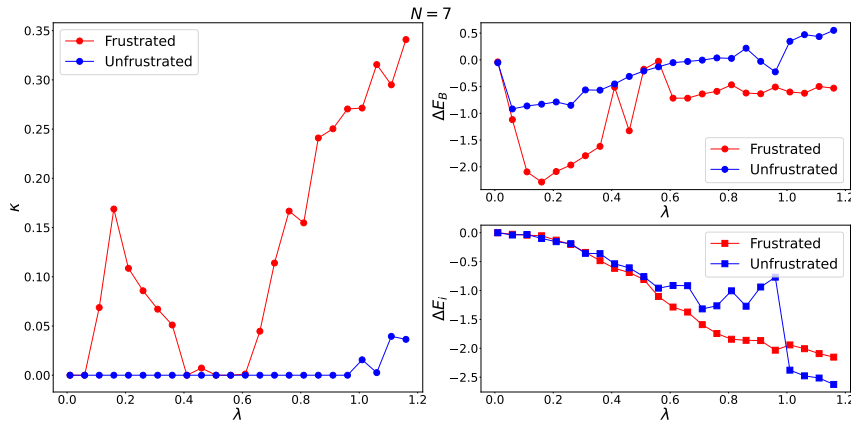


Figure D.5: Values of κ (left), ΔE_B (top right) and ΔE_i (bottom right) as a function of the interaction strength λ . The data are obtained for $\omega = 2$, $h = 0.2$, $J = \pm 1$, $\Delta h = 3.72$ and $N = 7$.

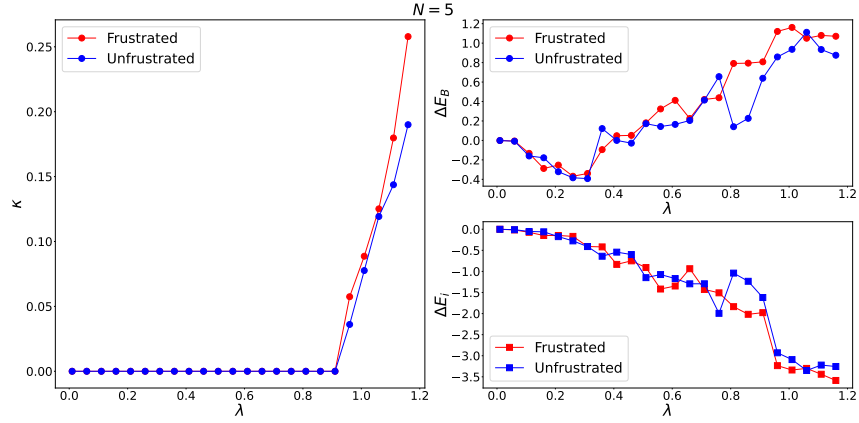


Figure D.6: Values of κ (left), ΔE_B (top right) and ΔE_i (bottom right) as a function of the interaction strength λ . The data are obtained for $\omega = 2$, $h = 0.8$, $J = \pm 1$, $\Delta h = 3.72$ and $N = 5$.

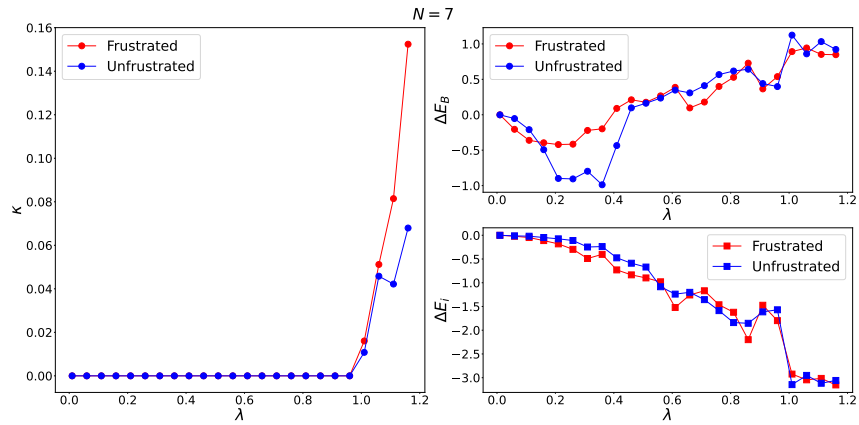


Figure D.7: Values of κ (left), ΔE_B (top right) and ΔE_i (bottom right) as a function of the interaction strength λ . The data are obtained for $\omega = 2$, $h = 0.8$, $J = \pm 1$, $\Delta h = 3.72$ and $N = 7$.

Appendix E

Analytical results for long-range exciton transport in presence of dephasing

In this supplemental material we provide an alternative derivation of the CME Eq. (6.7), and the full derivation of: the moments $\langle j(t)|j(t)\rangle$ and $\langle |j|^2(t)||j|^2(t)\rangle$, the critical exponent α_{cr} , the approximate function $\mathcal{A}_{2\alpha,d}(\mathbf{q})$, the exciton density profile $n_j(t)$, the length scale $\xi_{\alpha,t}$, the effective Liouvillian Eq. (6.6), and the approximate occupation profile $n_j(t)$ in the many-body case.

E.1 The single-particle problem

E.1.1 From the quantum master equation (QME) to the classical master equation (CME): alternative derivation

We consider a long-range spin- $\frac{1}{2}$ model on a d -dimensional hypercubic lattice \mathbb{Z}^d in presence of pure dephasing through the Lindblad QME

$$\dot{\rho} = -i[H, \rho] + \gamma \sum_j \left(L_j^\dagger \rho L_j - \frac{1}{2} \{L_j L_j^\dagger, \rho\} \right), \quad (\text{E.1})$$

with $L_j = S_j^z$, and the Hamiltonian given by

$$H = \frac{J}{2} \sum_j \sum_{r \neq 0} |\mathbf{r}|^{-\alpha} (S_j^+ S_{j+r}^- + h.c.). \quad (\text{E.2})$$

In particular, we study the evolution of the two-point correlation functions $G_{j,m} = \text{Tr}[\rho S_j^+ S_m^-]$. We focus on the single particle subspace, spanned by the states $\{|j\rangle\}$ representing a configuration in which all spins are down but at the lattice site j .

Within this subspace the two-point correlation functions evolve according to

$$\dot{G}_{j,m} = iJ \sum_{r \neq 0} (G_{j+r,m} - G_{j,m+r}) |\mathbf{r}|^{-\alpha} - \gamma G_{j,m}, \quad (\text{E.3})$$

$$\dot{G}_{j,j} = iJ \sum_{r \neq 0} (G_{j+r,j} - G_{j,j+r}) |\mathbf{r}|^{-\alpha}. \quad (\text{E.4})$$

Following the idea of [272], assuming $\dot{G}_{j,m} \ll \gamma G_{j,m}$, i.e. that the phase relations are destroyed very rapidly, we can neglect the time derivative in (E.3). Moreover, considering only time intervals larger than the decay time of the phase, we may also neglect non-diagonal terms w.r.t. to diagonal ones. Then, we obtain an expression for $G_{j,m}$ in

terms of the diagonal elements:

$$G_{j,m} = \frac{iJ}{\gamma} (G_{m,m} - G_{j,j}) |\mathbf{j} - \mathbf{m}|^{-\alpha}. \quad (\text{E.5})$$

We can substitute the latter expression into (E.4), and arrive to the following equation for the diagonal elements

$$\dot{G}_{j,j} = \frac{2J^2}{\gamma} \sum_{r \neq 0} (G_{j+r,j+r} - G_{j,j}) |\mathbf{r}|^{-2\alpha}. \quad (\text{E.6})$$

The latter expression can be recognized as the classical master equation (CME) (6.7) for a random walker in a d -dimensional hypercubic lattice with long-range hopping. In particular, with hopping rate from site \mathbf{j} to site \mathbf{m} given by $\kappa |\mathbf{j} - \mathbf{m}|^{-2\alpha}$, then the CME for the probability $n_j(t)$ of finding the walker at site \mathbf{j} at time t reads

$$\dot{n}_j = \kappa \sum_{r \neq 0} (n_{j+r} - n_j) |\mathbf{r}|^{-2\alpha}, \quad (\text{E.7})$$

where the classical rate κ is related to the parameters entering the quantum master equation by

$$\kappa = \frac{2J^2}{\gamma}. \quad (\text{E.8})$$

The quantum-to-classical transition is illustrated in Fig. 6.1**b** of the main text, where the variance of an initially localized excitation is plotted as a function of time, for $d = 1$ and $\alpha > \alpha_{\text{cr}}$. Here, in Fig. E.1**a,b**, we report the results for $\alpha \leq \alpha_{\text{cr}}$, where we normalize the variance in such a way that the term $\sum_r r^2 H_r^2$ in Eq. (6.3) does not diverge. In Fig. E.1**c** we show an additional case with $\alpha > \alpha_{\text{cr}}$, similar to Fig. 6.1**b** of the main text, where no normalization is required. Interestingly, the transition to the CME happens at $t \sim 1/\gamma$ independently of the hopping range α .

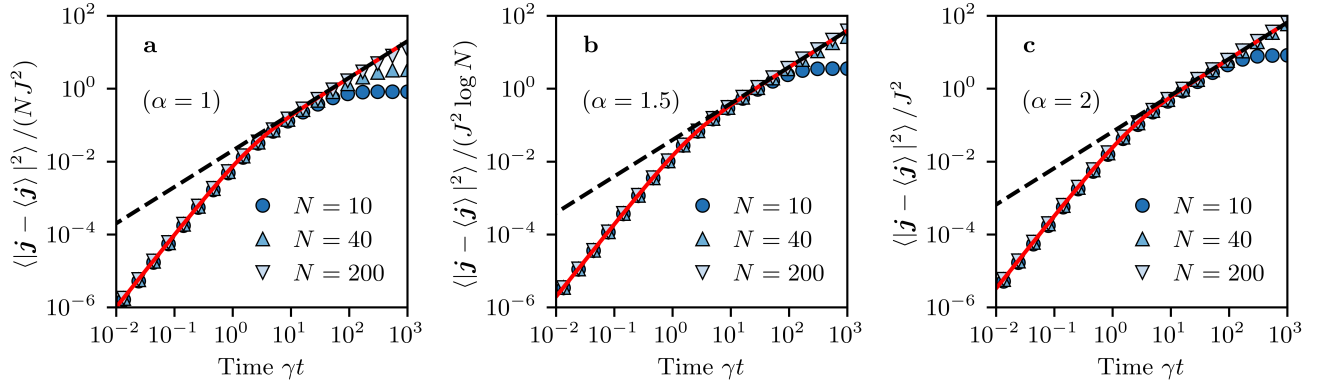


Figure E.1: Variance of the excitation as a function of time, for a $d = 1$ array of N emitters, determined by numerically solving the QME (6.1). In all panels $\gamma = 10J$, the red continuous lines represent Eq. (6.3), while the black dashed lines are the classical approximations, see Eq. (6.4). As discussed in the text, the variance is normalized in **a** ($\alpha = 1 < \alpha_{\text{cr}}$) and **b** ($\alpha = \alpha_{\text{cr}} = 3/2$) in order to avoid its divergence in the $N \rightarrow \infty$ limit.

E.1.2 Moments of the distribution

The moments of the distribution $n_j(t)$ can be obtained from the derivatives of the generating function K . This can be easily understood from its definition

$$K(\mathbf{q}, t) = \sum_j n_j(t) e^{i\mathbf{q} \cdot \mathbf{j}}. \quad (\text{E.9})$$

Indeed, on a lattice of dimension d , we have that

$$\frac{\partial K}{\partial q_\alpha}(\mathbf{0}, t) = i \sum_j j_\alpha n_j(t) = i \langle j_\alpha \rangle, \quad (\alpha = 1, \dots, d) \quad (\text{E.10})$$

$$\frac{\partial^2 K}{\partial q_\alpha \partial q_\beta}(\mathbf{0}, t) = - \sum_j j_\alpha j_\beta n_j(t) = - \langle j_\alpha j_\beta \rangle \quad (\alpha, \beta = 1, \dots, d). \quad (\text{E.11})$$

Therefore, we have that

$$\nabla_{\mathbf{q}} K(\mathbf{0}, t) = i \langle \mathbf{j} \rangle, \quad (\text{E.12})$$

and

$$\Delta_{\mathbf{q}} K(\mathbf{0}, t) = - \langle |\mathbf{j}|^2 \rangle, \quad (\text{E.13})$$

and similarly, considering higher order derivatives we can compute higher order moments.

As an example, let us compute explicitly the first two moments of the distribution. The derivatives of K can be evaluated starting from Eq. (6.8) of the main text, yielding

$$\langle \mathbf{j} \rangle = \mathbf{0}, \quad (\text{E.14})$$

$$\langle |\mathbf{j}|^2 \rangle = \mathcal{A}_{2\alpha-2,d}(\mathbf{0})t = 2D_\alpha t. \quad (\text{E.15})$$

E.1.3 The critical exponent

In (E.15) can we see that the variance of the distribution depends explicitly on the exponent of the power-law hopping α and on the dimensionality d of the lattice through the function \mathcal{A} . In particular, we have that

$$\mathcal{A}_{s,d}(\mathbf{0}) = \kappa \sum_{\mathbf{r} \neq \mathbf{0}} |\mathbf{r}|^{-s}. \quad (\text{E.16})$$

Since the general term appearing in the series in (E.16) is a positive and decreasing function of its argument, then we may study its convergence by studying the convergence of the associated integral. In particular, we would have to check the convergence of

$$\int_1^\infty r^{-s+d-1} dr \propto [r^{-s+d}]_1^\infty, \quad (\text{E.17})$$

which is convergent for $s > d$. Therefore, comparing this result with (E.15), we have that the variance is finite if and only if

$$\alpha > \alpha_{\text{cr}} = \frac{d+2}{2}. \quad (\text{E.18})$$

E.1.4 Analytical properties of $\mathcal{A}_{2\alpha,d}(q)$

As stated in the main text, in order to establish the analytical properties of $n_j(t)$ for different values of α , we have to study the behaviour of the function $\mathcal{A}_{2\alpha,d}$ around $q = 0$.

For $d = 1$ we have that

$$\mathcal{A}_{2\alpha,1}(q) = 2\kappa \operatorname{Re}(\operatorname{Li}_{2\alpha}(e^{iq})), \quad (\text{E.19})$$

where $\operatorname{Li}_\beta(z)$ denotes the polylogarithm function of order β and argument z .

For $\alpha \neq \frac{1}{2}, 1, \frac{3}{2}, 2, \dots$ we can use the expansion about $q = 0$ given in [320]

$$\mathcal{A}_{2\alpha,1}(q) = -C_\alpha |q|^{2\alpha-1} + 2\kappa \sum_{j=0}^{\infty} \zeta_{2\alpha-2j} (-1)^j \frac{q^{2j}}{(2j)!}, \quad (\text{E.20})$$

with $C_\alpha = -2\kappa\Gamma(1 - 2\alpha) \sin(\alpha\pi)$, $\Gamma(z) = \int_0^\infty t^{z-1} e^{-t} dt$ being the gamma function and $\zeta_s = \sum_{k=1}^{\infty} k^{-s}$ the Riemann zeta function.

For all the other values of α , i.e those corresponding to $2\alpha \in \mathbb{N}$, we can derive an expansion about $q = 0$ by exploiting some properties of the polylogarithm functions. In particular, considering that

$$\partial_z \operatorname{Li}_\beta(z) = z^{-1} \operatorname{Li}_{\beta-1}(z), \quad (\text{E.21})$$

and introducing the function $\mathcal{G}_\beta(q) = 2i\kappa \operatorname{Im}(\operatorname{Li}_\beta(e^{iq}))$, we can see that

$$\begin{cases} \partial_q \mathcal{A}_{\beta,1}(q) = i\mathcal{G}_{\beta-1}(q) \\ \partial_q \mathcal{G}_\beta(q) = i\mathcal{A}_{\beta-1,1}(q) \end{cases}, \quad (\text{E.22})$$

$$\Rightarrow \partial_q^2 \mathcal{A}_{\beta,1}(q) = -\mathcal{A}_{\beta-2,1}(q). \quad (\text{E.23})$$

The boundary conditions for these equations are given by the properties of the functions \mathcal{G} and \mathcal{A} at $q = 0$, which can be easily understood by their definition:

$$\mathcal{A}_{\beta,1}(0) = 2\kappa\zeta_\beta, \quad \partial_q \mathcal{A}_{\beta,1}(0) = i\mathcal{G}_{\beta-1}(0) = 0. \quad (\text{E.24})$$

The starting point will be the expression of \mathcal{A} and \mathcal{G} for $\beta = 1$, which are given by

$$\begin{cases} \mathcal{A}_{1,1}(q) = -2\kappa \log 2 - 2\kappa \log \left| \sin \left(\frac{q}{2} \right) \right| \\ \mathcal{G}_1(q) = -i\kappa q + i\pi\kappa\sigma(q) \end{cases}, \quad (\text{E.25})$$

where we denoted the sign function of q by $\sigma(q)$. Let us start our analysis from $\beta = 2\alpha$ with $\alpha \in \mathbb{N}$. The following identities will be useful for our procedure:

$$\int \sigma(q)q^{2j}dq = \frac{|q|^{2j+1}}{2j+1}, \quad \int |q|^{2j-1} = \sigma(q)\frac{q^{2j}}{2j}. \quad (\text{E.26})$$

With them in mind, it is easy to derive $\mathcal{A}_{2,1}$ upon integration of \mathcal{G}_1 :

$$\mathcal{A}_{2,1}(q) = \kappa \left(\frac{q^2}{2} - \pi|q| + 2\zeta_2 \right). \quad (\text{E.27})$$

Similarly, integrating $\mathcal{A}_{2,1}$ twice we get

$$\mathcal{A}_{4,1}(q) = \kappa \left(-\frac{q^4}{4!} + \pi\frac{|q|^3}{3!} - 2\zeta_2\frac{q^2}{2!} + 2\zeta_4 \right).$$

Therefore, it sounds reasonable to assume that we have

$$\mathcal{A}_{2\alpha,1}(q) = (-1)^\alpha \frac{\pi}{(2\alpha-1)!} \kappa |q|^{2\alpha-1} + 2\kappa \sum_{j=0}^{\alpha} (-1)^j \zeta_{2\alpha-2j} \frac{q^{2j}}{(2j)!}, \quad (\text{E.28})$$

$\forall \alpha \in \mathbb{N}$, with $\zeta_0 = -\frac{1}{2}$. This clearly holds for $\alpha = 1$, and as well for $\alpha + 1$, as we can easily check upon substitution of (E.28) in (E.23) and integrating, yielding to

$$\mathcal{A}_{2\alpha+2,1}(q) = (-1)^{\alpha+1} \frac{\pi}{(2\alpha+1)!} \kappa |q|^{2\alpha+1} + 2\kappa \sum_{j=0}^{\alpha+1} (-1)^j \zeta_{2\alpha+2-2j} \frac{q^{2j}}{(2j)!},$$

which proves the validity of (E.28) by induction.

Finally, let us study the $\mathcal{A}_{\beta,1}$ functions with odd integer index, i.e. for $\beta = 2s - 1$, for $s \in \mathbb{N}$. Of course, it would be wonderful to proceed as for the case of even indices, but

this is hard to do since already $\mathcal{A}_{1,1}$ can't be integrated in terms of elementary functions. Therefore, we will limit ourselves to studying the behaviour of these functions close to $q = 0$, where they present a logarithmic non-analyticity. In particular, we can see that

$$\mathcal{A}_{1,1}(q) \approx -\kappa \log q^2. \quad (\text{E.29})$$

Upon integration, we thus get

$$\mathcal{A}_{3,1}(q) \approx \kappa \left(\frac{q^2}{2} \log q^2 + 2\zeta_3 - \frac{3}{2}q^2 \right), \quad (\text{E.30})$$

$$\mathcal{A}_{5,1}(q) \approx \kappa \left(-\frac{q^4}{4!} \log q^2 + 2\zeta_5 - \zeta_3 q^2 \right) + O(q^4), \quad (\text{E.31})$$

and, more in general, we have that

$$\mathcal{A}_{2s+1,1}(q) \approx \kappa \left[(-1)^{s+1} \frac{q^{2s}}{(2s)!} \log q^2 + 2\zeta_{2s+1} - \zeta_{2s-1} q^2 \right] + O(q^4), \quad (\text{E.32})$$

for $s = 2, 3, 4, \dots$. The results in (E.20),(E.28),(E.32) fully characterize the behaviour of \mathcal{A} close to the origin in one dimension, for any value of the exponent α .

Determining the behaviour of $\mathcal{A}_{2\alpha,d}$ for $d > 1$ is a bit more involved. In order to understand its properties, we will introduce a fixed, small but finite, lattice constant λ , and approximate the sum appearing in the definition of \mathcal{A} with an integral, i.e. $\sum_{r \neq 0} \approx \lambda^{2\alpha-d} \int_0^{2\pi} d\theta \left(\prod_{k=1}^{d-2} \int_0^\pi \sin^{d-1-k} \phi_k d\phi_k \right) \int_\lambda^\infty r^{d-1} dr$. In this way, upon further changing variable to $z = \frac{r}{\lambda}$, we obtain that

$$\mathcal{A}_{2\alpha,d} \approx \nu_d \kappa \int_1^\infty dz \int_0^\pi d\phi_1 z^{d-2\alpha-1} \sin^{d-2} \phi_1 e^{-iqz \cos(\phi_1)}, \quad (\text{E.33})$$

where $q = |\mathbf{q}|$ and $\nu_d = 2\pi^{\frac{d-1}{2}} / \Gamma(\frac{d-1}{2})$ is a constant which only depends on the dimension d of the space. The integral in (E.33) has to be computed differently for $d = 2$ and $d > 2$, but after the calculation we are able to write the following expansion about $q = 0$ for \mathcal{A}

$\forall d \geq 2$:

$$\mathcal{A}_{2\alpha,d}(\mathbf{q}) \approx \mathcal{A}_{2\alpha,d}(\mathbf{0}) + \pi^{\frac{d}{2}} 2^{d-2\alpha} \frac{\Gamma(\frac{d}{2} - \alpha)}{\Gamma(\alpha)} \kappa |\mathbf{q}|^{2\alpha-d}, \quad (\text{E.34})$$

for $\alpha \leq \alpha_{\text{cr}}$, and

$$\mathcal{A}_{2\alpha,d}(\mathbf{q}) \approx \mathcal{A}_{2\alpha,d}(\mathbf{0}) - \frac{\mathcal{A}_{2\alpha-2,d}(\mathbf{0})}{2} |\mathbf{q}|^2 + \pi^{\frac{d}{2}} 2^{d-2\alpha} \frac{\Gamma(\frac{d}{2} - \alpha)}{\Gamma(\alpha)} \kappa |\mathbf{q}|^{2\alpha-d}, \quad (\text{E.35})$$

for $\alpha > \alpha_{\text{cr}}$.

E.1.5 Asymptotic properties of $n_j(t)$: $d = 1$

Let us start by considering $\alpha < \alpha_{\text{cr}} = \frac{3}{2}$. In this case, for $\alpha \neq 1$, we can take the inverse Fourier transform of (E.20) obtaining, to leading order in q ,

$$n_j(t) \approx \frac{1}{2\pi} \int_{-\pi}^{\pi} e^{-ijq} e^{-tC_\alpha |q|^{2\alpha-1}} dq.$$

Changing variable to $y = jq$ we thus get

$$n_j(t) \approx \frac{1}{2\pi j} \int_{-j\pi}^{j\pi} e^{-iy} e^{-tC_\alpha |y|^{2\alpha-1}/n^{2\alpha-1}} dy.$$

Expanding the j -dependent exponential in series we therefore have

$$n_j(t) \approx \sum_{l=0}^{\infty} \frac{(-1)^l}{2\pi j^{2\alpha l+1-l}} \frac{(tC_\alpha)^l}{l!} \int_{-j\pi}^{j\pi} |y|^{2\alpha l-l} e^{-iy} dy.$$

For large values of j we can approximate the region of integration with the whole real axis, and to leading order in j we hence obtain that

$$n_j(t) \approx -\frac{t}{j^{2\alpha}} \frac{C_\alpha}{2\pi} \int_{-\infty}^{\infty} |y|^{2\alpha-1} e^{-iy} dy = \frac{\kappa t}{j^{2\alpha}}. \quad (\text{E.36})$$

The case $\alpha = 1$ can be solved exactly since we have an exact expression for $\mathcal{A}_{2,1}$ in (E.27). In this case we have that

$$n_j(t) = \frac{e^{-\kappa t \pi^2/2}}{\pi} \int_0^\pi \cos(jq) e^{\kappa t(q-\pi)^2/2} dq = \frac{e^{-\kappa t \pi^2/2}}{\pi} (-1)^j \int_0^\pi \cos(jy) e^{\kappa t y^2/2} dy,$$

$$\Rightarrow n_j(t) = \frac{1}{\sqrt{2\kappa t \pi^2}} \left[D_F \left(\frac{ij + \pi \kappa t}{\sqrt{2\kappa t}} \right) - D_F \left(\frac{ij - \pi \kappa t}{\sqrt{2\kappa t}} \right) \right], \quad (\text{E.37})$$

where $D_F(z) = e^{-z^2} \int_0^z e^{u^2} du$ is the Dawson integral. One can check that the asymptotic behaviour for large values of j is

$$n_j(t) \approx \frac{\kappa t}{j^2}, \quad (\text{E.38})$$

which agrees with (E.36).

Next, we shall consider the case $\alpha = \frac{3}{2}$, corresponding to the critical point of the model for $d = 1$. In such case we find, using the same logic as above, that to leading order

$$n_j(t) \approx \frac{1}{2\pi} \int_{-\pi}^\pi e^{-ijq} e^{\frac{\kappa t}{2} q^2 \log q^2} dq \approx \frac{\kappa t}{2\pi j^3} \int_{-\infty}^\infty y^2 e^{-iy} \log |y| dy \approx \frac{\kappa t}{j^3}, \quad (\text{E.39})$$

which again agrees with the power-law tail predicted in (E.36).

Above the critical point, when α is neither integer or half-integer, we again take the inverse Fourier transform of (E.20). This time, the leading order in q brings a quadratic Gaussian contribution, while the power with fractional exponent will produce the power-law tail of the distribution:

$$n_j(t) \approx \frac{1}{2\pi} \int_{-\pi}^\pi e^{-ijq} e^{-tC_\alpha |q|^{2\alpha-1} - \kappa t \zeta_{2\alpha-2} q^2} dq.$$

Changing variable to $y = jq$ and expanding the exponential with the faster decaying exponent for large values of n , we get, to leading order, that

$$n_j(t) \approx \frac{1}{2\pi j} \int_{-\infty}^\infty e^{-iy - D_\alpha t y^2 j^{-2}} dy - \frac{tC_\alpha}{2\pi j^{2\alpha}} \int_{-\infty}^\infty |y|^{2\alpha-1} e^{-iy} dy,$$

where $D_\alpha = \kappa \zeta_{2\alpha-2}$. The above steps give the following asymptotic result for n_j :

$$n_j(t) \approx \frac{e^{-\frac{j^2}{4D_\alpha t}}}{\sqrt{4\pi D_\alpha t}} + \frac{\kappa t}{j^{2\alpha}}. \quad (\text{E.40})$$

The case of integer $\alpha \in \mathbb{N}$ is analogous since, as we can see in (E.28), the type of singularity at $q = 0$ is the same as in the case we have just treated. Hence, we would find once again (E.40).

Finally, let us consider the case α half integer. In such case, we find that

$$n_j(t) \approx \frac{1}{2\pi} \int_{-\pi}^{\pi} e^{-ijq} e^{\frac{(-1)^{\alpha+\frac{1}{2}} \kappa t}{(2\alpha-1)!} q^{2\alpha-1} \log q^2 - D_\alpha t q^2} dq.$$

Therefore, we have that to leading order in n

$$n_j(t) \approx \frac{1}{2\pi j} \int_{-\infty}^{\infty} e^{-iy - D_\alpha t y^2 j^{-2}} dy + \frac{(-1)^{\alpha+\frac{1}{2}} \kappa t}{\Gamma(2\alpha) \pi j^{2\alpha}} \int_{-\infty}^{\infty} y^{2\alpha-1} e^{-iy} \log |y| dy,$$

resulting once again in

$$n_j(t) \approx \frac{e^{-\frac{j^2}{4D_\alpha t}}}{\sqrt{4\pi D_\alpha t}} + \frac{\kappa t}{j^{2\alpha}},$$

i.e. again (E.40).

E.1.6 Asymptotic properties of $n_j(t)$: $d > 1$

The procedure for the higher dimensional case is a straightforward generalization of what was done in $d = 1$, using the power-law expansions (E.34),(E.35). The final result is the same behaviour observed in one dimension, i.e.

$$n_j(t) \approx \begin{cases} \frac{\kappa t}{|j|^{2\alpha}} & \alpha \leq \frac{d+2}{2} \\ \frac{e^{-\frac{|j|^2}{4D_\alpha t}}}{(4\pi D_\alpha t)^{d/2}} + \frac{\kappa t}{|j|^{2\alpha}} & \alpha > \frac{d+2}{2}. \end{cases} \quad (\text{E.41})$$

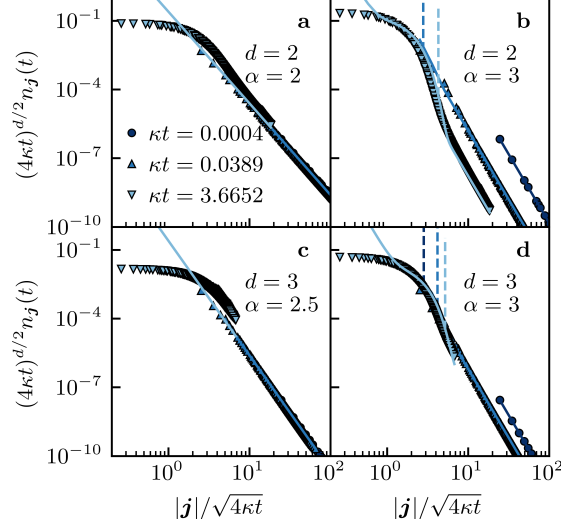


Figure E.2: Re-scaled excitation profile at different times t obtained from the CME (6.7) for arrays of dimension $d = 2$ (**a,b** with $N = 100^2$) and $d = 3$ (**c,d** with $N = 30^3$, respectively). In all panels $\gamma = 10J$ and the continuous lines correspond to Eq. (6.10) of the main text. The vertical dotted lines correspond to the function $\xi_{\alpha,t}$ entering Eq. (6.10b) of the main text. The initial excitation is set on an edge.

E.1.7 Length scale for the crossover between the Gaussian and the power-law profiles

Here we derive, for $\alpha > \alpha_{\text{cr}}$, the length scale $\xi_{\alpha,t}$ beyond which the excitation profile changes from Gaussian to power-law. This length scale is determined by the crossing point between the Gaussian and the power-law profile, i.e.

$$\frac{e^{-\xi_{\alpha,t}^2/4D_{\alpha}t}}{(4\pi D_{\alpha}t)^{d/2}} = \frac{\kappa t}{\xi_{\alpha,t}^{2\alpha}}. \quad (\text{E.42})$$

We define here $x = \xi_{\alpha,t}^2/4D_{\alpha}t$ and $b = (4D_{\alpha}t)^{\alpha_{\text{cr}}-\alpha}\pi^{d/2}\kappa/4D_{\alpha}$ so that we have

$$x^{\alpha}e^{-x} = b, \quad (\text{E.43})$$

which can be solved by means of the Lambert W function. Specifically, our problem is equivalent to $ye^y = -b^{1/\alpha}/\alpha$, where $y = -x/\alpha$. The Lambert W function is defined by its inverse, i.e. $W(ye^y) = y$. In our case, since y is negative, there are two possible solutions (the “0” and the “-1” branch of the W function), corresponding to the two

intersections between a power law and a Gaussian. Since we are interested in the largest length scale, we choose the “−1” branch, so that we have $y = W_{-1}(-b^{1/\alpha}/\alpha)$. Upon substituting the definition of y we have $x = -\alpha W_{-1}(-b^{1/\alpha}/\alpha)$, and recovering the definitions of x and b , we have finally

$$\xi_{\alpha,t} = \sqrt{-4\alpha D_\alpha t W_{-1} \left(-\frac{1}{\alpha} \left(\frac{\pi^{d/2} \kappa}{4D_\alpha} (4D_\alpha t)^{\alpha_{\text{cr}} - \alpha} \right)^{1/\alpha} \right)}. \quad (\text{E.44})$$

Note that $\xi_{\alpha,t}$ exists only within the domain of the W function, that is for

$$t \geq t_{\text{cr}} = \frac{1}{4D_\alpha} \left[\frac{\pi^{d/2} \kappa e^\alpha}{4D_\alpha \alpha^\alpha} \right]^{1/(\alpha - \alpha_{\text{cr}})}. \quad (\text{E.45})$$

Eq. (E.44) is exact, but not very illuminating about the dependence of $\xi_{\alpha,t}$ on α and t . Anyway, for very large t , the argument of the W function tends to 0^- , and it can be approximated as $W_{-1}(y) \approx \log(-y)$. In this way we obtain

$$\xi_{\alpha,t} \approx \sqrt{4D_\alpha t \log \left(\frac{4\alpha^\alpha D_\alpha}{\pi^{d/2} \kappa} (4D_\alpha t)^{\alpha - \alpha_{\text{cr}}} \right)}, \quad (\text{E.46})$$

which is the length scale reported in the main text.

E.1.8 Diffusion-enhancement in the case of Förster energy transfer

The square of the exciton diffusion length (in units of the lattice parameter) corresponds to the variance of the exciton distribution:

$$L_\alpha^2 = \langle |j|^2 \rangle(\tau) = \sum_{r \neq 0} r^2 \kappa(r) \tau, \quad (\text{E.47})$$

with τ the exciton lifetime, and

$$\kappa(r) \propto \sum_{r \neq 0} |H_r|^2 \int d\omega F_D(\omega) \sigma_A(\omega) \quad (\text{E.48})$$

the transfer rate between the sites j (donor) and $j + r$ (acceptor), separated by the distance r . Here, $H_r = \langle G | S_j^- H S_{j+r}^+ | G \rangle$ are the matrix elements of the Hamiltonian Eq. (6.2) connecting the two states involved in the energy transfer, and $|G\rangle$ is the ground state with all spins down. The functions

$$F_D(\omega) = \sigma_A(\omega) = \frac{1}{\pi} \frac{\gamma}{(\omega - \omega_0)^2 + \gamma^2} \quad (\text{E.49})$$

entering the overlap integral denote the normalized donor emission spectrum and acceptor absorption spectrum. Here we assume that all spins have the same energy ω_0 , or equivalently that the energy difference between two sites is negligible compared to the FWHM γ (corresponding to the dephasing rate). One thus finds $L_\alpha^2 \propto \kappa \tau \mathcal{A}_{2\alpha-2,d}(\mathbf{0})/2$, with $\mathcal{A}_{2\alpha,d}(\mathbf{0}) = \sum_{r \neq \mathbf{0}} r^{-2\alpha}$ and $\kappa = 2J^2/\gamma$, as defined in the main text. Our diffusion length L_α including the contribution of the long-range tail can be compared with that of the standard theory of diffusion assuming nearest-neighbor hopping ($\alpha = \infty$). The latter reads $L_\infty^2 \propto \kappa \tau d$ (with d the dimension). For Förster energy transfer ($\alpha = 3$) at play in nanocrystal films, the ratio between the square diffusion lengths in the long-range and nearest-neighbor cases is

$$\frac{L_3^2}{L_\infty^2} \approx \begin{cases} 2.8 & \text{for } d = 3 \\ 1.5 & \text{for } d = 2 \end{cases} \quad (\text{E.50})$$

We emphasize that this factor ~ 2 depending on the dimensionality of the energy transfer (the latter can neither be considered as fully 2D nor fully 3D in Refs. [277, 313]) accounts for part of the discrepancy between the exciton diffusion length measured experimentally and the values predicted by standard (nearest-neighbor) diffusion theory applied to Förster energy transfer [277, 313].

E.2 The many-particle problem

E.2.1 Derivation of the effective Liouvillian

Here we look at the many-body case starting from the long-range Hamiltonian (6.2) and following the idea of [300], which is to study the large-dephasing limit of the model through a second-order perturbative analysis, deriving an effective Liouvillian $\hat{\mathcal{L}}_{\text{eff}}$ in the limit $\gamma \gg J$. Therefore, we split the original Liouvillian, Eq. (6.1), into two contributions, an unperturbed term $\hat{\mathcal{L}}_0 \rho = \gamma \sum_j (S_j^z \rho S_j^z - \rho/4)$, and a perturbation $\hat{\mathcal{L}}_1 \rho = -i[H, \rho]$. The steady states of $\hat{\mathcal{L}}_0$ are given by $|\sigma\rangle \langle\sigma|$ where the $|\sigma\rangle$ are eigenstates of the $\{S_j^z\}$ operators, i.e. $S_j^z |\sigma\rangle = s_j^z |\sigma\rangle$, with $s_j^z = \pm \frac{1}{2}$. Following Ref. [300], the effective Liouvillian projected onto the diagonal subspace generated by the $|\sigma\rangle \langle\sigma|$ reads

$$\hat{\mathcal{L}}_{\text{eff}} = \hat{\mathcal{P}} \hat{\mathcal{L}}_1 \frac{1}{\lambda_0 - \hat{\mathcal{L}}_0} \hat{\mathcal{L}}_1 \hat{\mathcal{P}}, \quad (\text{E.51})$$

where $\hat{\mathcal{P}}$ is the projector onto this subspace.

At this point, we need to evaluate $\hat{\mathcal{L}}_0(\hat{\mathcal{L}}_1 |\sigma\rangle \langle\sigma|)$. Using the notation $h_{jr} = S_j^+ S_{j+r}^- + S_j^- S_{j+r}^+$, we have that

$$\hat{\mathcal{L}}_1 |\sigma\rangle \langle\sigma| = -i \frac{J}{2} \sum_{j;r \neq 0} [h_{jr}, |\sigma\rangle \langle\sigma|] |\mathbf{r}|^{-\alpha}. \quad (\text{E.52})$$

The commutator in (E.52) is given by

$$[h_{jr}, |\sigma\rangle \langle\sigma|] = \delta_{s_{j+r}^z, -s_j^z} (|\sigma', \mathbf{j}\mathbf{r}\rangle \langle\sigma| - h.c.), \quad (\text{E.53})$$

where $|\sigma', \mathbf{j}\mathbf{r}\rangle = |\dots - s_j^z \dots - s_{j+r}^z \dots\rangle$. Substituting into (E.52), we obtain

$$\hat{\mathcal{L}}_1 |\sigma\rangle \langle\sigma| = -i \frac{J}{2} \sum_{j;r \neq 0} \frac{\delta_{s_{j+r}^z, -s_j^z}}{|\mathbf{r}|^\alpha} (|\sigma', \mathbf{j}\mathbf{r}\rangle \langle\sigma| - h.c.). \quad (\text{E.54})$$

Here, if we apply $\hat{\mathcal{L}}_0$ to an element of the sum of (E.54), we obtain

$$\hat{\mathcal{L}}_0 |\sigma', jr\rangle \langle \sigma| = \frac{\gamma}{4} \sum_j (4s_j^z s_j^z - 1) |\sigma', jr\rangle \langle \sigma| = -\gamma |\sigma', jr\rangle \langle \sigma|, \quad (\text{E.55})$$

therefore yielding to

$$\hat{\mathcal{L}}_0(\hat{\mathcal{L}}_1 |\sigma\rangle \langle \sigma|) = -\gamma \hat{\mathcal{L}}_1 |\sigma\rangle \langle \sigma|. \quad (\text{E.56})$$

Now, considering also that $\lambda_0 = 0$ for the steady states, the effective Liouvillian (E.51) is reduced to

$$\begin{aligned} \hat{\mathcal{L}}_{\text{eff}} |\sigma\rangle \langle \sigma| &= \frac{1}{\gamma} \hat{\mathcal{P}} \hat{\mathcal{L}}_1 \hat{\mathcal{L}}_1 |\sigma\rangle \langle \sigma| = -\frac{1}{\gamma} \hat{\mathcal{P}} [H, [H, |\sigma\rangle \langle \sigma|]] \\ &= -\frac{J^2}{4\gamma} \sum_{j;r \neq 0} \sum_{m;r' \neq 0} |r|^{-\alpha} |r'|^{-\alpha} \hat{\mathcal{P}} (h_{jr} h_{mr'} |\sigma\rangle \langle \sigma| + |\sigma\rangle \langle \sigma| h_{jr} h_{mr'} - 2h_{jr} |\sigma\rangle \langle \sigma| h_{mr'}), \end{aligned} \quad (\text{E.57})$$

with $h_{jr} = S_j^+ S_{j+r}^- + S_j^- S_{j+r}^+$. On applying the projector $\hat{\mathcal{P}}$, the only non-vanishing terms have $h_{mr'} = h_{jr}$, and for each h_{jr} we have two such terms: ($m = j; r' = r$) and ($m = j + r; r' = -r$). Therefore we drop the sum over $m; r'$ and multiply by a factor of 2, obtaining

$$\hat{\mathcal{L}}_{\text{eff}} |\sigma\rangle \langle \sigma| = -\frac{J^2}{2\gamma} \sum_{j;r \neq 0} |r|^{-2\alpha} (h_{jr}^2 |\sigma\rangle \langle \sigma| + |\sigma\rangle \langle \sigma| h_{jr}^2 - 2h_{jr} |\sigma\rangle \langle \sigma| h_{jr}). \quad (\text{E.58})$$

Following Ref. [300], we note that $h_{jr}^2 = 2 \left(\frac{1}{4} - S_j^z S_{j+r}^z \right)$. Therefore, we obtain the CME (6.5) with generator (6.6) reported in the main text.

E.2.2 Occupation probability for the 1D symmetric exclusion process with long-jumps

To give some quantitative analysis of the many-particle case we decided to consider the case of a one dimensional lattice of N sites indexed by $\{j\}_{-N/2}^{N/2-1}$, with open boundary

conditions. We take as initial state the configuration where the $N/2$ sites on the left of the origin are all occupied, while the remaining sites are empty. We are interested in understanding how the occupation probability $n_j(t)$ at site j evolves. In particular, considering the flow in and out of each lattice site, we can write the following discrete time evolution for $n_j(t)$:

$$n_j(t + \Delta t) - n_j(t) = [1 - n_j(t)] \sum_{l=-N/2, l \neq j}^{N/2-1} [n_l(t) n_{l-j}^{(sp)}(\Delta t)] - n_j(t) \sum_{l=-N/2, l \neq j}^{N/2-1} [1 - n_l(t)] n_{l-j}^{(sp)}(\Delta t), \quad (\text{E.59})$$

$$\Rightarrow n_j(t + \Delta t) - n_j(t) = \sum_{l=-N/2, l \neq j}^{N/2-1} [n_l(t) - n_j(t)] n_{l-j}^{(sp)}(\Delta t), \quad (\text{E.60})$$

where $n_j^{(sp)}(\Delta t)$ denotes the single-particle hopping probabilities on the lattice. To estimate them, we can look at the short time solution of their master equation, which we derived in the first section of this manuscript

$$\dot{n}_j^{(sp)} = \kappa \sum_{r=-N/2-j, r \neq 0}^{N/2-1-j} (n_{j+r}^{(sp)} - n_j^{(sp)}) |r|^{-2\alpha}, \quad (\text{E.61})$$

with initial condition $n_j^{(sp)}(0) = \delta_{j,0}$. Therefore, for short times and $j \neq 0$ we get

$$n_j^{(sp)}(\Delta t) \approx \frac{\kappa \Delta t}{j^{2\alpha}}. \quad (\text{E.62})$$

Inserting (E.62) in (E.60) we thus obtain

$$\dot{n}_j = \kappa \sum_{l=-N/2, l \neq j}^{N/2-1} (n_l - n_j) |l - j|^{-2\alpha}, \quad (\text{E.63})$$

which we will have to solve with the initial condition $n_j(0) = 1 - \Theta[j]$, where Θ is the discrete Heaviside step function. Since we used a short-time approximation to derive (E.63), it makes sense to solve it in the same approximation. Therefore, for $j \geq 0$ we

would have

$$n_j(\Delta t) \approx \kappa \Delta t \sum_{l=-N/2, l \neq j}^{N/2-1} (1 - \Theta[l]) |l - j|^{-2\alpha}, \quad (\text{E.64})$$

$$\Rightarrow n_j(\Delta t) \approx \kappa \Delta t \sum_{l=-N/2}^{-1} |l - j|^{-2\alpha} = \kappa \Delta t \sum_{r=j+1}^{N/2+j} |r|^{-2\alpha}. \quad (\text{E.65})$$

This has a really simple physical interpretation. Indeed, it amounts to say that the probability that a site $j \gg 0$ is occupied after a short time t corresponds to the independent probabilities that at least one particle has jumped to that site starting from the step-function initial configuration. Similarly, for $j < 0$ we have

$$n_j(\Delta t) \approx 1 - \kappa \Delta t \sum_{l=-N/2, l \neq j}^{N/2-1} \Theta[l] |l - j|^{-2\alpha}, \quad (\text{E.66})$$

$$\Rightarrow n_j(\Delta t) \approx 1 - \kappa \Delta t \sum_{l=0}^{N/2-1} |l - j|^{-2\alpha}, \quad (\text{E.67})$$

and hence

$$\Rightarrow n_j(\Delta t) \approx 1 - \kappa \Delta t \sum_{r=|j|}^{N/2-1+|j|} |r|^{-2\alpha}. \quad (\text{E.68})$$

Again, this has a simple physical explanation, i.e. after a short time t the occupation of a site on the left of the chain is only influenced by the escape probability of the particle that initially was at that position.

Putting (E.65) and (E.68) together we thus get the occupation profile for short time:

$$n_j(t) = \Theta[j] \kappa t \sum_{r=j+1}^{N/2+j} |r|^{-2\alpha} + (1 - \Theta[j]) \left[1 - \kappa t \sum_{r=|j|}^{N/2-1+|j|} |r|^{-2\alpha} \right]. \quad (\text{E.69})$$

To get some insight about the large-time regime we can instead look at the stationary solution of (E.60). In this case we would have

$$\sum_{l=-N/2, l \neq j}^{N/2-1} [n_l - n_j] n_{l-j}^{(sp)} = 0, \quad (\text{E.70})$$

which can be solved by setting $n_j = c \in \mathbb{R} \forall j$. The constant is determined by the normalization condition which implies the conservation of the number of particles, i.e. $\sum_l n_l = \frac{N}{2}$. Therefore, we have that for large t the stationary solution is the flat profile

$$n_j = 1/2 \quad \forall j. \quad (\text{E.71})$$

E.3 The quantum case: weak-dephasing regime

Here we consider the QME [Eq. (6.1) in the main text] in the single-exciton case, for weak dephasing and $d = 1$. We rewrite the Hamiltonian [Eq. (6.2) in the main text] as

$$H = \sum_{1 \leq i < j \leq N} h_{i,j} (S_i^+ S_j^- + h.c.), \quad (\text{E.72})$$

where $h_{i,j} = J[|i - j|^\alpha + (N - |i - j|)^\alpha](1 - \delta_{i,j})$ is the single-particle Hamiltonian with periodic boundary conditions. The evolution of the two-point correlation functions $G_{j,m} = \text{Tr}(\rho S_j^+ S_m^-)$ in the single-particle regime is described by Eqs. (E.3-E.4), that we rewrite in matrix form as

$$\dot{G} = i[h^T, G] - \gamma[G - \text{diag}(G)]. \quad (\text{E.73})$$

In order to solve Eq. (E.73), here we follow the approach of [299]. Thanks to the time-linearity of Eq. (E.73), we can solve it in terms of the eigenvalues and eigenvectors of the time-evolution operator ($E_{q,k}$ and $A^{q,k}$ respectively, with some labels q, k that we characterize below). We substitute $A_{j,m}^{q,k}(t) = A_{j,m}^{q,k} e^{-E_{q,k}t}$ into Eq. (E.73), leaving us with the eigenvalue equation

$$-E_{q,k} A_{j,m}^{q,k} = i \sum_{l=0}^{N-1} [h_{l,j} A_{l,m}^{q,k} - A_{j,l}^{q,k} h_{m,l}] - \gamma(1 - \delta_{j,m}) A_{j,m}^{q,k}. \quad (\text{E.74})$$

At this point we exploit translational invariance to write $A_{j,m}^{q,k} = e^{iqj} A_{0,m-j}^{q,k}$, where $q = \frac{2\pi}{N}j$, $j = 0, \dots, N-1$. Substituting this in Eq. (E.74) we thus have

$$E_{q,k} A_{0,m-j}^{q,k} = -i \sum_{l=0}^{N-1} [h_{l,j} A_{0,m-l}^{q,k} e^{iq(l-j)} - A_{0,l-j}^{q,k} h_{m,l}] + \gamma(1 - \delta_{0,m-j}) A_{0,m-j}^{q,k}. \quad (\text{E.75})$$

This equation can be written in matrix form as

$$(C_q + \gamma X) \vec{A}^{q,k} = E_{q,k} \vec{A}^{q,k}. \quad (\text{E.76})$$

Here, $\vec{A}^{q,k}$ are vectors of size N with components $A_{0,m}^{q,k}$ ($m = 0, \dots, N-1$), while C_q are $N \times N$ circulant matrices with elements

$$(C_q)_{m,j} = i[1 - e^{iq(m-j)}] h_{m,j} \quad (m, j = 0, \dots, N-1) \quad (\text{E.77})$$

and X is a diagonal matrix with elements $X_{m,m} = 1 - \delta_{0,m}$ (where $m = 0, \dots, N-1$). Therefore, we have to solve N independent eigenvalue problems of the type of Eq. (E.76) (one for each value of q), where each provides N eigenvectors and eigenvalues, $\vec{A}^{q,k}$ and $E_{q,k}$, for some labeling index $k = 0, \dots, N-1$. Then, given an initial condition $G(0)$ for the two-point correlation matrix, the time-evolved $G(t)$ is

$$G_{j,m}(t) = \sum_{q,k} \text{Tr}\{[(A^{q,k})^{-1} G(0)]\} A_{j,m}^{q,k} e^{-E_{q,k} t}. \quad (\text{E.78})$$

Since an analytical solution of the eigenvalue problem in Eq. (E.76) for $q \neq 0$ is non-trivial, in the following we focus on the small-dephasing regime, and we treat γX as a perturbation of C_q .

E.3.1 Small dephasing: perturbation theory

For the unperturbed problem ($\gamma = 0$) the normalized eigenstates $(\vec{A}^{q,k})^{(0)}$ and the corresponding eigenvalues $E_{q,k}^{(0)}$ ($k = 0, \frac{2\pi}{N}, \dots, 2\pi\frac{N-1}{N}$) of the circulant matrices C_q are

$$(A_{0,m}^{q,k})^{(0)} = \frac{e^{imk}}{\sqrt{N}}, \quad (\text{E.79})$$

$$E_{q,k}^{(0)} = \sum_{m=0}^{N-1} (C_q)_{0,m} e^{imk}. \quad (\text{E.80})$$

From Eq. (E.77) one can see that C_q are anti-hermitian matrices. Therefore, all the eigenvalues in (E.80) are purely imaginary conjugated pairs, except one which is equal to zero¹. In order to use standard perturbation theory formulas for the eigenvalues of hermitian operators we multiply both sides of Eq. (E.76) by the imaginary unit, so that, up to correction of order γ^4 , we have

$$E_{q,k} = E_{q,k}^{(0)} + \gamma\delta_{q,k}^{(1)} - i\gamma^2\delta_{q,k}^{(2)} + \gamma^3\delta_{q,k}^{(3)} + o(\gamma^4), \quad (\text{E.81})$$

with the following real coefficients:

$$\delta_{q,k}^{(1)} = \frac{N-1}{N}, \quad (\text{E.82})$$

$$\delta_{q,k}^{(2)} = \frac{i}{N^2} \sum_{p \neq k} \frac{1}{E_{q,p}^{(0)} - E_{q,k}^{(0)}}, \quad (\text{E.83})$$

$$\delta_{q,k}^{(3)} = \frac{1}{N^3} \sum_{p \neq k} \sum_{s \neq k,p} \frac{1}{(E_{q,k}^{(0)} - E_{q,p}^{(0)})(E_{q,k}^{(0)} - E_{q,s}^{(0)})}. \quad (\text{E.84})$$

The first order of the perturbation series gives a constant contribution to the real part of the eigenvalues, whose fluctuations are captured by the third-order term. The second-order term captures the fluctuations of the imaginary part of the eigenvalues. These fluctuations are small, as one can see from Fig. E.3: for large system sizes the smallest

¹For even values of N exact degeneracies appear in the unperturbed spectrum, therefore the results obtained here assume an odd number of sites in the lattice.

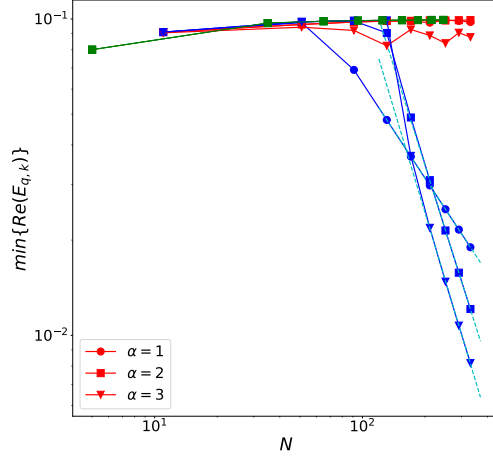


Figure E.3: Scaling of the smallest real part for complex Liouvillian eigenvalues (red) and real ones (blue) with the system size. The green symbols show the results obtained for the real eigenvalues using perturbation theory, while the cyan dashed lines are power-law fits ($\sim 1/N$ for $\alpha = 1$ and $\sim 1/N^2$ for $\alpha = 2, 3$). Data are taken for $\alpha = 1, 2, 3$, $J = 1$ and $\gamma = 0.1$.

real part of the eigenvalues predicted by (E.81) (green symbols) converges to γ , and the convergence does not depend on the value of the hopping rate α . This means that the correction obtained from the first-order perturbation theory is effectively dominant. Therefore, for weak dephasing, we can keep just the leading order corrections for the eigenvectors,

$$A_{0,m}^{q,k} = (A_{0,m}^{q,k})^{(0)} - \frac{\gamma}{N} \sum_{p \neq k} \frac{(A_{0,m}^{q,p})^{(0)}}{E_{q,k}^{(0)} - E_{q,p}^{(0)}}, \quad (\text{E.85})$$

and eigenvalues,

$$E_{q,k} = E_{q,k}^{(0)} + \gamma \frac{N-1}{N}, \quad (\text{E.86})$$

which, when plugged into (E.78), would imply that $G_{j,m}$ relaxes to its stationary state with a fixed rate $\sim \gamma$.

E.3.2 Exact diagonalization

An exact diagonalization approach reveals that the real part of the vast majority of the eigenvalues are indeed $\sim \gamma$, independent of α (see red symbols in Fig. E.3). However,

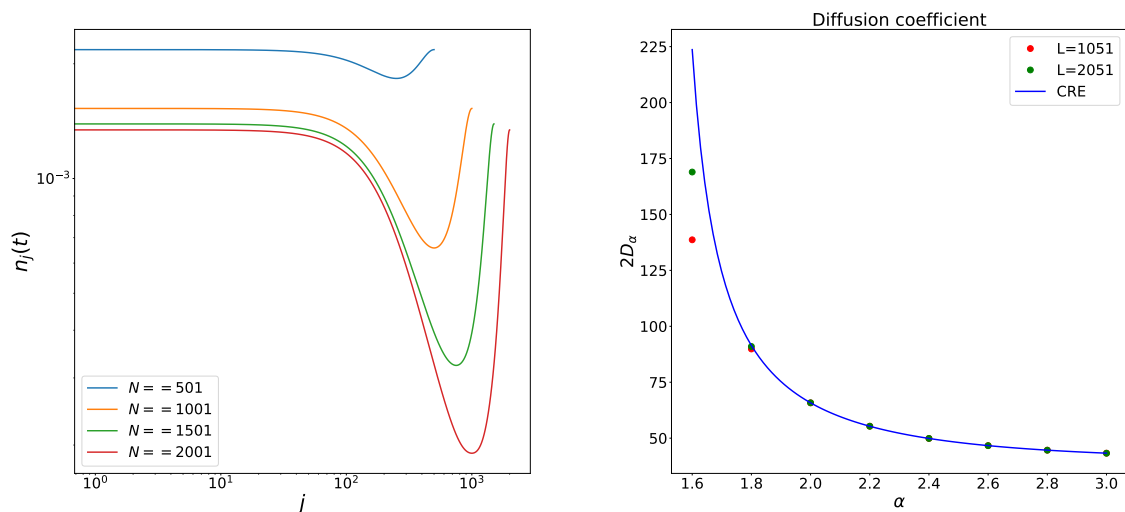


Figure E.4: Left: exciton density profile for $\alpha = J = 1$, $\gamma = 0.1$ and $t = 250$ for different system sizes N . Right: diffusion constant determined by fitting the variance of the exciton density vs. time, $\langle |j|^2 ||j|^2 \rangle = 2D_\alpha t$, for $J = 1$, $\gamma = 0.1$.

we find also that there are $N - 1$ real eigenvalues which, for large system sizes, acquire a decay rate smaller than γ (see blue symbols in Fig. E.3). This is not captured by the perturbation theory, and thus the long-time dynamic, which is dominated by these small eigenvalues, is non-perturbative. Therefore, in the long-time limit we can restrict our analysis to these slow-decaying terms. The results obtained with exact numerics are shown in Fig. E.4 (left panel). The logarithmic plot shows the emergence of a power-law tail in the exciton density profile $n_j = G_{j,j}$ before reaching a minimum at $j = N/2$. There, the profile bends and the density increases because of the periodic boundary conditions that we have employed. Comparing the amplitudes of the populations and coherences obtained in the long-time limit we found that the populations are at least one order of magnitude larger than the coherences. Therefore, this justifies an adiabatic elimination of the coherences in Eq. (E.73) similarly to the large dephasing regime (see Sec. E.1.1) which would lead us to the classical master equation (E.7). Indeed, as one can see in the right panel in Fig. E.4, the diffusion constant obtained numerically in the weak-dephasing regime (symbols) agrees quite well with that predicted by the CME (continuous line), and the agreement improves as we increase the system size.

Bibliography

- [1] A. G. Catalano, D. Brtan, F. Franchini, and S. M. Giampaolo, Phys. Rev. B **106**, 125145 (2022).
- [2] A. G. Catalano, F. Mattiotti, J. Dubail, D. Hagenmüller, T. Prosen, F. Franchini, and G. Pupillo, PRL **131**, 053401 (2023), arXiv:2212.07744 [quant-ph] .
- [3] A. Catalano, S. Giampaolo, O. Morsch, V. Giovannetti, and F. Franchini, PRX Quantum **5**, 10.1103/prxquantum.5.030319 (2024).
- [4] D. Sacco Shaikh, A. G. Catalano, F. Cavaliere, F. Franchini, M. Sasseti, and N. Traverso Ziani, arXiv e-prints , arXiv:2312.06291 (2023), arXiv:2312.06291 [cond-mat.stat-mech] .
- [5] A. G. Catalano, Numerically efficient unitary evolution for hamiltonians beyond nearest-neighbors (2024).
- [6] G. Torre, A. G. Catalano, S. B. Kožić, F. Franchini, and S. M. Giampaolo, Interplay between local and non-local frustration in the 1d annni chain i – the even case (2024), arXiv:2406.19449 [cond-mat.str-el] .
- [7] A. G. Catalano, J. Odavić, G. Torre, A. Hamma, F. Franchini, and S. M. Giampaolo, Magic phase transition and non-local complexity in generalized w state (2024), arXiv:2406.19457 [quant-ph] .
- [8] H. Nishimori and G. Ortiz, *Elements of Phase Transitions and Critical Phenomena* (Oxford University PressOxford, 2010).

- [9] G. Mussardo, *Statistical Field Theory: An Introduction to Exactly Solved Models in Statistical Physics*, Oxford Graduate Texts (Oxford University Press, 2020).
- [10] E. Ising, *Zeitschrift für Physik* **31**, 253–258 (1925).
- [11] L. Onsager, *Phys. Rev.* **65**, 117 (1944).
- [12] W. Heisenberg, *Zeitschrift für Physik* **49**, 619–636 (1928).
- [13] R. B. Potts, *Mathematical Proceedings of the Cambridge Philosophical Society* **48**, 106–109 (1952).
- [14] K. G. Wilson, *Phys. Rev. B* **4**, 3174 (1971).
- [15] K. G. Wilson, *Phys. Rev. B* **4**, 3184 (1971).
- [16] M. E. Fisher, *Rev. Mod. Phys.* **46**, 597 (1974).
- [17] in *Collected Papers of L.D. Landau* (Elsevier, 1965) p. 193–216.
- [18] A. Einstein, B. Podolsky, and N. Rosen, *Phys. Rev.* **47**, 777 (1935).
- [19] J. S. Bell, *Physics Physique Fizika* **1**, 195 (1964).
- [20] A. Aspect, J. Dalibard, and G. Roger, *Phys. Rev. Lett.* **49**, 1804 (1982).
- [21] B. Hensen, H. Bernien, A. E. Dréau, A. Reiserer, N. Kalb, M. S. Blok, J. Ruitenberg, R. F. L. Vermeulen, R. N. Schouten, C. Abellán, W. Amaya, V. Pruneri, M. W. Mitchell, M. Markham, D. J. Twitchen, D. Elkouss, S. Wehner, T. H. Taminiau, and R. Hanson, *Nature* **526**, 682–686 (2015).
- [22] N. Defenu, A. Leroze, and S. Pappalardi, arXiv e-prints , arXiv:2307.04802 (2023), arXiv:2307.04802 [cond-mat.quant-gas] .
- [23] N. Defenu, T. Donner, T. Macrì, G. Pagano, S. Ruffo, and A. Trombettoni, *Reviews of Modern Physics* **95**, 035002 (2023), arXiv:2109.01063 [cond-mat.quant-gas] .

- [24] S. Sachdev, *Quantum Phase Transitions* (Cambridge University Press, 2011).
- [25] F. D. M. Haldane, Phys. Rev. Lett. **60**, 635 (1988).
- [26] B. S. Shastry, Phys. Rev. Lett. **60**, 639 (1988).
- [27] T. Giamarchi, *Quantum Physics in One Dimension*, International Series of Monographs on Physics (Clarendon Press, 2004).
- [28] C. K. Majumdar and D. K. Ghosh, Journal of Mathematical Physics **10**, 1388–1398 (1969).
- [29] C. K. Majumdar and D. K. Ghosh, Journal of Mathematical Physics **10**, 1399–1402 (1969).
- [30] X. G. Wen and Q. Niu, Phys. Rev. B **41**, 9377 (1990).
- [31] X. G. WEN, International Journal of Modern Physics B **04**, 239–271 (1990).
- [32] B. Zeng, X. Chen, D. Zhou, and X. Wen, *Quantum Information Meets Quantum Matter: From Quantum Entanglement to Topological Phases of Many-Body Systems*, Quantum Science and Technology (Springer New York, 2019).
- [33] R. Moessner and J. E. Moore, *Topological Phases of Matter* (Cambridge University Press, 2021).
- [34] X.-G. Wen, Physics Letters A **300**, 175–181 (2002).
- [35] X. Chen, Z.-C. Gu, and X.-G. Wen, Phys. Rev. B **82**, 155138 (2010).
- [36] A. Hamma, R. Ionicioiu, and P. Zanardi, Physical Review A **71**, 10.1103/physreva.71.022315 (2005).
- [37] X.-G. Wen, ISRN Condensed Matter Physics **2013**, 1–20 (2013).
- [38] X.-G. Wen, Reviews of Modern Physics **89**, 10.1103/revmodphys.89.041004 (2017).

- [39] X.-G. Wen, *Science* **363**, 10.1126/science.aal3099 (2019).
- [40] A. Acín, I. Bloch, H. Buhrman, T. Calarco, C. Eichler, J. Eisert, D. Esteve, N. Gisin, S. J. Glaser, F. Jelezko, S. Kuhr, M. Lewenstein, M. F. Riedel, P. O. Schmidt, R. Thew, A. Wallraff, I. Walmsley, and F. K. Wilhelm, *New Journal of Physics* **20**, 080201 (2018).
- [41] M. F. Riedel, D. Binosi, R. Thew, and T. Calarco, *Quantum Science and Technology* **2**, 030501 (2017).
- [42] P. Shor, in *Proceedings 35th Annual Symposium on Foundations of Computer Science*, SFCS-94 (IEEE Comput. Soc. Press, 1994).
- [43] P. W. Shor, *SIAM Journal on Computing* **26**, 1484–1509 (1997).
- [44] L. K. Grover, in *Proceedings of the twenty-eighth annual ACM symposium on Theory of computing - STOC '96*, STOC '96 (ACM Press, 1996).
- [45] A. Somoroff, Q. Ficheux, R. A. Mencia, H. Xiong, R. Kuzmin, and V. E. Manucharyan, *Phys. Rev. Lett.* **130**, 267001 (2023).
- [46] I. Cong, H. Levine, A. Keesling, D. Bluvstein, S.-T. Wang, and M. D. Lukin, *Phys. Rev. X* **12**, 021049 (2022).
- [47] J. W. Britton, B. C. Sawyer, A. C. Keith, C. C. J. Wang, J. K. Freericks, H. Uys, M. J. Biercuk, and J. J. Bollinger, *Nature* **484**, 489 (2012), arXiv:1204.5789 [quant-ph] .
- [48] P. Scholl, M. Schuler, H. J. Williams, A. A. Eberharter, D. Barredo, K.-N. Schymik, V. Lienhard, L.-P. Henry, T. C. Lang, T. Lahaye, A. M. Läuchli, and A. Browaeys, *Nature* **595**, 233 (2021), arXiv:2012.12268 [quant-ph] .
- [49] C. Monroe, W. C. Campbell, L. M. Duan, Z. X. Gong, A. V. Gorshkov, P. W. Hess, R. Islam, K. Kim, N. M. Linke, G. Pagano, P. Richerme, C. Senko, and N. Y. Yao, *Reviews of Modern Physics* **93**, 025001 (2021), arXiv:1912.07845 [quant-ph] .

- [50] A. Keesling, A. Omran, H. Levine, H. Bernien, H. Pichler, S. Choi, R. Samajdar, S. Schwartz, P. Silvi, S. Sachdev, P. Zoller, M. Endres, M. Greiner, Vuletić, V. , and M. D. Lukin, *Nature* **568**, 207 (2019), arXiv:1809.05540 [quant-ph] .
- [51] J.-R. Li, K. Matsuda, C. Miller, A. N. Carroll, W. G. Tobias, J. S. Higgins, and J. Ye, *Nature* **614**, 70 (2023), arXiv:2208.02216 [cond-mat.quant-gas] .
- [52] K. Kim, in *APS Division of Atomic, Molecular and Optical Physics Meeting Abstracts*, APS Meeting Abstracts, Vol. 55 (2010) p. OPL.30.
- [53] G. Jotzu, M. Messer, R. Desbuquois, M. Lebrat, T. Uehlinger, D. Greif, and T. Esslinger, *Nature* **515**, 237–240 (2014).
- [54] M. Greiner, O. Mandel, T. Esslinger, T. W. Hänsch, and I. Bloch, *Nature* **415**, 39–44 (2002).
- [55] J. Zhang, P. W. Hess, A. Kyprianidis, P. Becker, A. Lee, J. Smith, G. Pagano, I.-D. Potirniche, A. C. Potter, A. Vishwanath, N. Y. Yao, and C. Monroe, *Nature* **543**, 217–220 (2017).
- [56] C. H. Bennett, G. Brassard, C. Crépeau, R. Jozsa, A. Peres, and W. K. Wootters, *Phys. Rev. Lett.* **70**, 1895 (1993).
- [57] D. Bouwmeester, J.-W. Pan, K. Mattle, M. Eibl, H. Weinfurter, and A. Zeilinger, *Nature* **390**, 575–579 (1997).
- [58] S. Liu, Y. Lv, X. Wang, J. Wang, Y. Lou, and J. Jing, *Phys. Rev. Lett.* **132**, 100801 (2024).
- [59] X.-M. Hu, Y. Guo, B.-H. Liu, C.-F. Li, and G.-C. Guo, *Nature Reviews Physics* **5**, 339–353 (2023).
- [60] S. Shen, C. Yuan, Z. Zhang, H. Yu, R. Zhang, C. Yang, H. Li, Z. Wang, Y. Wang, G. Deng, H. Song, L. You, Y. Fan, G. Guo, and Q. Zhou, *Light: Science amp; Applications* **12**, 10.1038/s41377-023-01158-7 (2023).

- [61] N. Gisin, G. Ribordy, W. Tittel, and H. Zbinden, *Reviews of Modern Physics* **74**, 145–195 (2002).
- [62] C. H. Bennett and G. Brassard, *Theoretical Computer Science* **560**, 7–11 (2014).
- [63] C. L. Degen, F. Reinhard, and P. Cappellaro, *Rev. Mod. Phys.* **89**, 035002 (2017).
- [64] J. Borregaard and A. S. Sørensen, *Phys. Rev. Lett.* **111**, 090802 (2013).
- [65] B. C. Nichol, R. Srinivas, D. P. Nadlinger, P. Drmota, D. Main, G. Araneda, C. J. Ballance, and D. M. Lucas, *Nature* **609**, 689–694 (2022).
- [66] D. Schöffner, T. Schreiber, F. Lenz, M. Schlosser, and G. Birkel, *PRX Quantum* **5**, 10.1103/prxquantum.5.010311 (2024).
- [67] D. DeMille, N. R. Hutzler, A. M. Rey, and T. Zelevinsky, *Nature Physics* **20**, 741–749 (2024).
- [68] R. Kosloff, *Entropy* **15**, 2100–2128 (2013).
- [69] J. P. Peterson, T. B. Batalhão, M. Herrera, A. M. Souza, R. S. Sarthour, I. S. Oliveira, and R. M. Serra, *Physical Review Letters* **123**, 10.1103/physrevlett.123.240601 (2019).
- [70] N. Linden, S. Popescu, and P. Skrzypczyk, *Physical Review Letters* **105**, 10.1103/physrevlett.105.130401 (2010).
- [71] G. Piccitto, M. Campisi, and D. Rossini, *New Journal of Physics* **24**, 103023 (2022).
- [72] B. Karimi and J. P. Pekola, *Physical Review B* **94**, 10.1103/physrevb.94.184503 (2016).
- [73] V. R. Arezzo, D. Rossini, and G. Piccitto, *Physical Review B* **109**, 10.1103/physrevb.109.224309 (2024).

- [74] A. Solfanelli, G. Giachetti, M. Campisi, S. Ruffo, and N. Defenu, *New Journal of Physics* **25**, 033030 (2023).
- [75] R. Alicki and M. Fannes, *Phys. Rev. E* **87**, 042123 (2013).
- [76] F. C. Binder, S. Vinjanampathy, K. Modi, and J. Goold, *New Journal of Physics* **17**, 075015 (2015).
- [77] F. Campaioli, F. A. Pollock, F. C. Binder, L. Céleri, J. Goold, S. Vinjanampathy, and K. Modi, *Phys. Rev. Lett.* **118**, 150601 (2017).
- [78] D. Ferraro, M. Campisi, G. M. Andolina, V. Pellegrini, and M. Polini, *Phys. Rev. Lett.* **120**, 117702 (2018).
- [79] G. M. Andolina, D. Farina, A. Mari, V. Pellegrini, V. Giovannetti, and M. Polini, *Phys. Rev. B* **98**, 205423 (2018).
- [80] G. M. Andolina, M. Keck, A. Mari, M. Campisi, V. Giovannetti, and M. Polini, *Phys. Rev. Lett.* **122**, 047702 (2019).
- [81] D. Farina, G. M. Andolina, A. Mari, M. Polini, and V. Giovannetti, *Phys. Rev. B* **99**, 035421 (2019).
- [82] K. V. Hovhannisyan, M. Perarnau-Llobet, M. Huber, and A. Acín, *Phys. Rev. Lett.* **111**, 240401 (2013).
- [83] X. Yang, Y.-H. Yang, M. Alimuddin, R. Salvia, S.-M. Fei, L.-M. Zhao, S. Nimmrichter, and M.-X. Luo, *Phys. Rev. Lett.* **131**, 030402 (2023).
- [84] S. Gherardini, F. Campaioli, F. Caruso, and F. C. Binder, *Phys. Rev. Res.* **2**, 013095 (2020).
- [85] D. Rosa, D. Rossini, G. M. Andolina, M. Polini, and M. Carrega, *Journal of High Energy Physics* **2020**, 10.1007/jhep11(2020)067 (2020).
- [86] S. Tirone, R. Salvia, and V. Giovannetti, *Phys. Rev. Lett.* **127**, 210601 (2021).

- [87] S. Tirone, R. Salvia, S. Chessa, and V. Giovannetti, Quantum work capacitances: ultimate limits for energy extraction on noisy quantum batteries (2022).
- [88] S. Tirone, R. Salvia, S. Chessa, and V. Giovannetti, Phys. Rev. Lett. **131**, 060402 (2023).
- [89] S. Tirone, R. Salvia, S. Chessa, and V. Giovannetti, Quantum work extraction efficiency for noisy quantum batteries: the role of coherence (2023).
- [90] R. R. Rodríguez, B. Ahmadi, G. Suárez, P. Mazurek, S. Barzanjeh, and P. Horodecki, New Journal of Physics **26**, 043004 (2024).
- [91] F. Pirmoradian and K. Mølmer, Phys. Rev. A **100**, 043833 (2019).
- [92] F. Mazzoncini, V. Cavina, G. M. Andolina, P. A. Erdman, and V. Giovannetti, Phys. Rev. A **107**, 032218 (2023).
- [93] P. A. Erdman, G. M. Andolina, V. Giovannetti, and F. Noé, Reinforcement learning optimization of the charging of a dicke quantum battery (2022).
- [94] G. M. Andolina, M. Keck, A. Mari, V. Giovannetti, and M. Polini, Phys. Rev. B **99**, 205437 (2019).
- [95] Z. Wang, H. Li, W. Feng, X. Song, C. Song, W. Liu, Q. Guo, X. Zhang, H. Dong, D. Zheng, H. Wang, and D.-W. Wang, Phys. Rev. Lett. **124**, 013601 (2020).
- [96] A. Stockklauser, P. Scarlino, J. V. Koski, S. Gasparinetti, C. K. Andersen, C. Reichl, W. Wegscheider, T. Ihn, K. Ensslin, and A. Wallraff, Phys. Rev. X **7**, 011030 (2017).
- [97] N. Samkharadze, G. Zheng, N. Kalhor, D. Brousse, A. Sammak, U. C. Mendes, A. Blais, G. Scappucci, and L. M. K. Vandersypen, Science **359**, 1123–1127 (2018).
- [98] S. Haroche, Rev. Mod. Phys. **85**, 1083 (2013).
- [99] Y.-Y. Zhang, T.-R. Yang, L. Fu, and X. Wang, Phys. Rev. E **99**, 052106 (2019).

- [100] A. Crescente, M. Carrega, M. Sassetti, and D. Ferraro, *New Journal of Physics* **22**, 063057 (2020).
- [101] A. Crescente, M. Carrega, M. Sassetti, and D. Ferraro, *Phys. Rev. B* **102**, 245407 (2020).
- [102] A. Crescente, D. Ferraro, M. Carrega, and M. Sassetti, *Phys. Rev. Res.* **4**, 033216 (2022).
- [103] F.-Q. Dou, Y.-Q. Lu, Y.-J. Wang, and J.-A. Sun, *Phys. Rev. B* **105**, 115405 (2022).
- [104] F.-Q. Dou, H. Zhou, and J.-A. Sun, *Phys. Rev. A* **106**, 032212 (2022).
- [105] F. Zhao, F.-Q. Dou, and Q. Zhao, *Phys. Rev. Res.* **4**, 013172 (2022).
- [106] D. Rossini, G. M. Andolina, and M. Polini, *Phys. Rev. B* **100**, 115142 (2019).
- [107] D. Rossini, G. M. Andolina, D. Rosa, M. Carrega, and M. Polini, *Phys. Rev. Lett.* **125**, 236402 (2020).
- [108] J. Q. Quach, K. E. McGhee, L. Ganzer, D. M. Rouse, B. W. Lovett, E. M. Gauger, J. Keeling, G. Cerullo, D. G. Lidzey, and T. Virgili, *Science Advances* **8**, 10.1126/sciadv.abk3160 (2022).
- [109] J. Monsel, M. Fellous-Asiani, B. Huard, and A. Auffèves, *Phys. Rev. Lett.* **124**, 130601 (2020).
- [110] M. Maffei, P. A. Camati, and A. Auffèves, *Phys. Rev. Res.* **3**, L032073 (2021).
- [111] J. Oppenheim, M. Horodecki, P. Horodecki, and R. Horodecki, *Phys. Rev. Lett.* **89**, 180402 (2002).
- [112] M. Carrega, A. Crescente, D. Ferraro, and M. Sassetti, *New Journal of Physics* **22**, 083085 (2020).
- [113] S.-Y. Bai and J.-H. An, *Phys. Rev. A* **102**, 060201 (2020).

- [114] F. T. Tabesh, F. H. Kamin, and S. Salimi, *Phys. Rev. A* **102**, 052223 (2020).
- [115] S. Ghosh, T. Chanda, S. Mal, and A. Sen(De), *Phys. Rev. A* **104**, 032207 (2021).
- [116] A. C. Santos, *Phys. Rev. E* **103**, 042118 (2021).
- [117] S. Zakavati, F. T. Tabesh, and S. Salimi, *Phys. Rev. E* **104**, 054117 (2021).
- [118] G. T. Landi, *Entropy* **23**, 1627 (2021).
- [119] D. Morrone, M. A. C. Rossi, A. Smirne, and M. G. Genoni, *Quantum Science and Technology* **8**, 035007 (2023).
- [120] K. Sen and U. Sen, *Noisy quantum batteries* (2023).
- [121] A. C. Santos, B. i. e. i. f. m. c. Çakmak, S. Campbell, and N. T. Zinner, *Phys. Rev. E* **100**, 032107 (2019).
- [122] A. C. Santos, A. Saguia, and M. S. Sarandy, *Phys. Rev. E* **101**, 062114 (2020).
- [123] J. Q. Quach and W. J. Munro, *Phys. Rev. Appl.* **14**, 024092 (2020).
- [124] J. Liu and D. Segal, *Boosting quantum battery performance by structure engineering* (2021).
- [125] M. B. Arjmandi, H. Mohammadi, and A. C. Santos, *Phys. Rev. E* **105**, 054115 (2022).
- [126] A. E. Allahverdyan, R. Balian, and T. M. Nieuwenhuizen, *Europhysics Letters (EPL)* **67**, 565–571 (2004).
- [127] W. Niedenzu, M. Huber, and E. Boukobza, *Quantum* **3**, 195 (2019).
- [128] G. H. Wannier, *Phys. Rev.* **79**, 357 (1950).
- [129] J. Stephenson, *Journal of Mathematical Physics* **11**, 413–419 (1970).
- [130] L. Balents, *Nature* **464**, 199–208 (2010).

- [131] R. Moessner and J. T. Chalker, Phys. Rev. Lett. **80**, 2929 (1998).
- [132] R. Moessner and J. T. Chalker, Phys. Rev. B **58**, 12049 (1998).
- [133] C. L. Henley, Phys. Rev. B **71**, 014424 (2005).
- [134] R. M. F. Houtappel, Physica **16**, 425 (1950).
- [135] J. Villain, R. Bidaux, J.-P. Carton, and R. Conte, Journal de Physique **41**, 1263–1272 (1980).
- [136] R. Movassagh and P. W. Shor, Proceedings of the National Academy of Sciences **113**, 13278–13282 (2016).
- [137] B. Tong, O. Salberger, K. Hao, and V. Korepin, Journal of Physics A: Mathematical and Theoretical **54**, 394002 (2021).
- [138] S. M. Giampaolo, G. Adesso, and F. Illuminati, Phys. Rev. Lett. **100**, 197201 (2008).
- [139] S. M. Giampaolo, G. Adesso, and F. Illuminati, Phys. Rev. B **79**, 224434 (2009).
- [140] S. M. Giampaolo, G. Adesso, and F. Illuminati, Phys. Rev. Lett. **104**, 207202 (2010).
- [141] M. M. WOLF, F. VERSTRAETE, and J. IGNACIO CIRAC, International Journal of Quantum Information **01**, 465–477 (2003).
- [142] S. M. Giampaolo, G. Gualdi, A. Monras, and F. Illuminati, Phys. Rev. Lett. **107**, 260602 (2011).
- [143] U. Marzolino, S. M. Giampaolo, and F. Illuminati, Phys. Rev. A **88**, 020301 (2013).
- [144] S. M. Giampaolo, B. C. Hiesmayr, and F. Illuminati, Phys. Rev. B **92**, 144406 (2015).

- [145] G. Toulouse, in *SPIN GLASS THEORY AND BEYOND: AN INTRODUCTION TO THE REPLICA METHOD AND ITS APPLICATIONS*. Edited by MEZARD M ET AL. Published by World Scientific Press (1987) pp. 99–103.
- [146] J. Vannimenus and G. Toulouse, *Journal of Physics C: Solid State Physics* **10**, L537 (1977).
- [147] J.-J. Dong, P. Li, and Q.-H. Chen, *Journal of Statistical Mechanics: Theory and Experiment* **2016**, 113102 (2016).
- [148] A. Sen(De), U. Sen, J. Dziarmaga, A. Sanpera, and M. Lewenstein, *Phys. Rev. Lett.* **101**, 187202 (2008).
- [149] V. Marić, S. M. Giampaolo, and F. Franchini, *Phys. Rev. B* **105**, 064408 (2022).
- [150] V. Marić, S. M. Giampaolo, D. Kuić, and F. Franchini, *New Journal of Physics* **22**, 083024 (2020).
- [151] V. Marić, S. M. Giampaolo, and F. Franchini, *Communications Physics* **3**, 10.1038/s42005-020-00486-z (2020).
- [152] V. Marić, G. Torre, F. Franchini, and S. M. Giampaolo, *SciPost Physics* **12**, 10.21468/scipostphys.12.2.075 (2022).
- [153] G. Torre, V. Marić, D. Kuić, F. Franchini, and S. M. Giampaolo, *Phys. Rev. B* **105**, 184424 (2022).
- [154] S. M. Giampaolo, F. B. Ramos, and F. Franchini, *Journal of Physics Communications* **3**, 081001 (2019).
- [155] J. Odavić, T. Haug, G. Torre, A. Hama, F. Franchini, and S. M. Giampaolo, *SciPost Physics* **15**, 10.21468/scipostphys.15.4.131 (2023).
- [156] G. Torre, J. Odavić, P. Fromholz, S. M. Giampaolo, and F. Franchini, arXiv e-prints , arXiv:2310.16091 (2023), arXiv:2310.16091 [cond-mat.str-el] .

- [157] P. Fromholz, G. Magnifico, V. Vitale, T. Mendes-Santos, and M. Dalmonte, *Phys. Rev. B* **101**, 085136 (2020).
- [158] T. Micallo, V. Vitale, M. Dalmonte, and P. Fromholz, *SciPost Physics Core* **3**, 10.21468/scipostphyscore.3.2.012 (2020).
- [159] J. Goldstone, A. Salam, and S. Weinberg, *Phys. Rev.* **127**, 965 (1962).
- [160] W. F. Wreszinski, *Journal of Mathematical Physics* **17**, 109 (1976), https://pubs.aip.org/aip/jmp/article-pdf/17/1/109/19046475/109_1_online.pdf.
- [161] N. D. Mermin and H. Wagner, *Phys. Rev. Lett.* **17**, 1133 (1966).
- [162] F. Franchini, *An Introduction to Integrable Techniques for One-Dimensional Quantum Systems* (Springer International Publishing, 2017).
- [163] P. W. Anderson, *Phys. Rev.* **164**, 352 (1967).
- [164] P. W. Anderson, *Phys. Rev. Lett.* **18**, 1049 (1967).
- [165] H.-M. Kwok, C.-S. Ho, and S.-J. Gu, *Phys. Rev. A* **78**, 062302 (2008).
- [166] G. Toulouse, Theory of the frustration effect in spin glasses: I, in *Spin Glass Theory and Beyond* (WORLD SCIENTIFIC, 1986) p. 99–103.
- [167] J. Sadoc and R. Mosseri, *Geometrical Frustration*, Aléa-Saclay (Cambridge University Press, 1999).
- [168] H. T. Diep, *Frustrated Spin Systems* (WORLD SCIENTIFIC, 2012).
- [169] O. Cador, D. Gatteschi, R. Sessoli, F. K. Larsen, J. Overgaard, A. Barra, S. J. Teat, G. A. Timco, and R. E. P. Winpenny, *Angewandte Chemie International Edition* **43**, 5196–5200 (2004).
- [170] C. R. Laumann, R. Moessner, A. Scardicchio, and S. L. Sondhi, *Phys. Rev. Lett.* **109**, 030502 (2012).

- [171] V. Subrahmanyam, Phys. Rev. B **50**, 6468 (1994).
- [172] V. Subrahmanyam, Phys. Rev. B **52**, 1133 (1995).
- [173] D. Poilblanc, Phys. Rev. B **96**, 121118 (2017).
- [174] P. Zanardi and N. Paunković, Phys. Rev. E **74**, 031123 (2006).
- [175] P. Zanardi, M. Cozzini, and P. Giorda, Journal of Statistical Mechanics: Theory and Experiment **2007**, L02002–L02002 (2007).
- [176] L. Campos Venuti and P. Zanardi, Phys. Rev. Lett. **99**, 095701 (2007).
- [177] P. Zanardi, P. Giorda, and M. Cozzini, Phys. Rev. Lett. **99**, 100603 (2007).
- [178] W.-L. You and W.-L. Lu, Physics Letters A **373**, 1444–1448 (2009).
- [179] M. Kolodrubetz, V. Gritsev, and A. Polkovnikov, Phys. Rev. B **88**, 064304 (2013).
- [180] U. Bhattacharya, S. Dasgupta, and A. Dutta, Phys. Rev. E **90**, 022920 (2014).
- [181] C. Lanczos, J. Res. Natl. Bur. Stand. B **45**, 255 (1950).
- [182] I. U. OJALVO and M. NEWMAN, AIAA Journal **8**, 1234–1239 (1970).
- [183] A. Vourdas, Reports on Progress in Physics **67**, 267–320 (2004).
- [184] K. Bärwinkel, P. Hage, H.-J. Schmidt, and J. Schnack, Phys. Rev. B **68**, 054422 (2003).
- [185] X. G. Wen, F. Wilczek, and A. Zee, Phys. Rev. B **39**, 11413 (1989).
- [186] E. Lieb, T. Schultz, and D. Mattis, Annals of Physics **16**, 407–466 (1961).
- [187] E. Barouch and B. M. McCoy, Phys. Rev. A **3**, 786 (1971).
- [188] A. Y. Kitaev, Physics-Uspekhi **44**, 131–136 (2001).
- [189] S.-J. GU, International Journal of Modern Physics B **24**, 4371–4458 (2010).

- [190] J. Ma, L. Xu, H.-N. Xiong, and X. Wang, *Phys. Rev. E* **78**, 051126 (2008).
- [191] T. J. Osborne and M. A. Nielsen, *Phys. Rev. A* **66**, 032110 (2002).
- [192] V. L. Berezinsky, *Sov. Phys. JETP* **32**, 493 (1971).
- [193] V. L. Berezinsky, *Sov. Phys. JETP* **34**, 610 (1972).
- [194] J. M. Kosterlitz and D. J. Thouless, *Journal of Physics C: Solid State Physics* **6**, 1181–1203 (1973).
- [195] L. Amico, R. Fazio, A. Osterloh, and V. Vedral, *Reviews of Modern Physics* **80**, 517–576 (2008).
- [196] J. Eisert, M. Cramer, and M. B. Plenio, *Reviews of Modern Physics* **82**, 277–306 (2010).
- [197] L. Susskind, *Entanglement is not enough* (2014).
- [198] C. Chamon, A. Hama, and E. R. Mucciolo, *Physical Review Letters* **112**, 10.1103/physrevlett.112.240501 (2014).
- [199] A. W. Harrow and A. Montanaro, *Nature* **549**, 203–209 (2017).
- [200] D. Gottesman, *Physical Review A* **57**, 127–137 (1998).
- [201] S. Aaronson and D. Gottesman, *Physical Review A* **70**, 10.1103/physreva.70.052328 (2004).
- [202] S. Bravyi and A. Kitaev, *Physical Review A* **71**, 10.1103/physreva.71.022316 (2005).
- [203] V. Veitch, S. A. Hamed Mousavian, D. Gottesman, and J. Emerson, *New Journal of Physics* **16**, 013009 (2014).
- [204] Z.-W. Liu and A. Winter, *PRX Quantum* **3**, 10.1103/prxquantum.3.020333 (2022).

- [205] T. Haug and M. Kim, PRX Quantum **4**, 10.1103/prxquantum.4.010301 (2023).
- [206] S. Bravyi, D. Browne, P. Calpin, E. Campbell, D. Gosset, and M. Howard, Quantum **3**, 181 (2019).
- [207] H. Pashayan, J. J. Wallman, and S. D. Bartlett, Physical Review Letters **115**, 10.1103/physrevlett.115.070501 (2015).
- [208] L. Leone, S. F. Oliviero, and A. Hamma, Physical Review Letters **128**, 10.1103/physrevlett.128.050402 (2022).
- [209] S. F. E. Oliviero, L. Leone, A. Hamma, and S. Lloyd, npj Quantum Information **8**, 10.1038/s41534-022-00666-5 (2022).
- [210] E. Tirrito, P. S. Tarabunga, G. Lami, T. Chanda, L. Leone, S. F. E. Oliviero, M. Dalmonte, M. Collura, and A. Hamma, Physical Review A **109**, 10.1103/physreva.109.1040401 (2024).
- [211] P. Niroula, C. D. White, Q. Wang, S. Johri, D. Zhu, C. Monroe, C. Noel, and M. J. Gullans, Phase transition in magic with random quantum circuits (2023).
- [212] D. Rattacaso, L. Leone, S. F. E. Oliviero, and A. Hamma, Physical Review A **108**, 10.1103/physreva.108.042407 (2023).
- [213] S. F. E. Oliviero, L. Leone, and A. Hamma, Physical Review A **106**, 10.1103/physreva.106.042426 (2022).
- [214] L. Leone, S. F. E. Oliviero, G. Esposito, and A. Hamma, Physical Review A **109**, 10.1103/physreva.109.032403 (2024).
- [215] G. E. Fux, E. Tirrito, M. Dalmonte, and R. Fazio, Entanglement-magic separation in hybrid quantum circuits (2023).
- [216] M. Bejan, C. McLauchlan, and B. Béri, Dynamical magic transitions in monitored clifford+t circuits (2023).

- [217] W. Dür, G. Vidal, and J. I. Cirac, *Physical Review A* **62**, 10.1103/physreva.62.062314 (2000).
- [218] V. Coffman, J. Kundu, and W. K. Wootters, *Physical Review A* **61**, 10.1103/physreva.61.052306 (2000).
- [219] L. Yeh, in *Companion Proceedings of the 7th International Conference on the Art, Science, and Engineering of Programming*, <Programming> '23 Companion (ACM, 2023).
- [220] L. Gioia and R. Thorngren, *w* state is not the unique ground state of any local hamiltonian (2023).
- [221] V. Lipinska, G. Murta, and S. Wehner, *Physical Review A* **98**, 10.1103/physreva.98.052320 (2018).
- [222] C.-W. Tsai and T. Hwang, *Science China Physics, Mechanics and Astronomy* **56**, 1903–1908 (2013).
- [223] M. K. Vijayan, A. P. Lund, and P. P. Rohde, *Quantum* **4**, 303 (2020).
- [224] T. Haug and L. Piroli, *Physical Review B* **107**, 10.1103/physrevb.107.035148 (2023).
- [225] G. Lami and M. Collura, Quantum magic via perfect pauli sampling of matrix product states (2023).
- [226] T. Haug and L. Piroli, *Quantum* **7**, 1092 (2023).
- [227] G. Lami, T. Haug, and J. De Nardis, Quantum state designs with clifford enhanced matrix product states (2024).
- [228] M. Frau, P. S. Tarabunga, M. Collura, M. Dalmonte, and E. Tirrito, Non-stabilizerness versus entanglement in matrix product states (2024).

- [229] P. S. Tarabunga, E. Tirrito, M. C. Bañuls, and M. Dalmonte, Nonstabilizerness via matrix product states in the pauli basis (2024).
- [230] B. Sutherland, *Beautiful Models: 70 Years of Exactly Solved Quantum Many-body Problems*, G - Reference, Information and Interdisciplinary Subjects Series (World Scientific, 2004).
- [231] J. Odavić, G. Torre, N. Mijić, D. Davidović, F. Franchini, and S. M. Giampaolo, *Quantum* **7**, 1115 (2023).
- [232] U. Schollwöck, *Annals of Physics* **326**, 96 (2011), arXiv:1008.3477 [cond-mat.str-el] .
- [233] R. Orús, *Annals of Physics* **349**, 117–158 (2014).
- [234] W. Selke, *Physics Reports* **170**, 213–264 (1988).
- [235] S. Suzuki, J.-i. Inoue, and B. K. Chakrabarti, *Quantum Ising Phases and Transitions in Transverse Ising Models* (Springer Berlin Heidelberg, 2013).
- [236] S. Monaco, O. Kiss, A. Mandarino, S. Vallecorsa, and M. Grossi, *Physical Review B* **107**, 10.1103/physrevb.107.1081105 (2023).
- [237] A. Canabarro, F. F. Fanchini, A. L. Malvezzi, R. Pereira, and R. Chaves, *Physical Review B* **100**, 10.1103/physrevb.100.045129 (2019).
- [238] S. Zippilli, M. Johanning, S. M. Giampaolo, C. Wunderlich, and F. Illuminati, *Phys. Rev. A* **89**, 042308 (2014).
- [239] M. Beccaria, M. Campostrini, and A. Feo, *Physical Review B* **73**, 10.1103/physrevb.73.052402 (2006).
- [240] M. Beccaria, M. Campostrini, and A. Feo, *Physical Review B* **76**, 10.1103/physrevb.76.094410 (2007).
- [241] P. Bak, *Reports on Progress in Physics* **45**, 587–629 (1982).

- [242] I. Bengtsson and K. Zyczkowski, *Geometry of Quantum States: An Introduction to Quantum Entanglement* (Cambridge University Press, 2006).
- [243] M. A. Nielsen and I. L. Chuang, *Quantum Computation and Quantum Information: 10th Anniversary Edition* (Cambridge University Press, 2012).
- [244] R. Berkovits, *Physical Review B* **87**, 10.1103/physrevb.87.075141 (2013).
- [245] S. R. White, *Phys. Rev. Lett.* **69**, 2863 (1992).
- [246] R. Orús, *Nature Reviews Physics* **1**, 538–550 (2019).
- [247] J. Biamonte, *Lectures on quantum tensor networks* (2019).
- [248] G. Catarina and B. Murta, *European Physical Journal B* **96**, 111 (2023), arXiv:2304.13395 [cond-mat.str-el] .
- [249] M. Weyrauch and M. Rakov, *Ukrainian Journal of Physics* **58**, 657–665 (2013).
- [250] F. Verstraete, D. Porras, and J. I. Cirac, *Physical Review Letters* **93**, 10.1103/physrevlett.93.227205 (2004).
- [251] P. Pippin, S. R. White, and H. G. Evertz, *Physical Review B* **81**, 10.1103/physrevb.81.081103 (2010).
- [252] G. Vidal, J. I. Latorre, E. Rico, and A. Kitaev, *Physical Review Letters* **90**, 10.1103/physrevlett.90.227902 (2003).
- [253] J. Latorre, E. Rico, and G. Vidal, *Quantum Information and Computation* **4**, 48–92 (2004).
- [254] M. B. Arjmandi, H. Mohammadi, A. Saguia, M. S. Sarandy, and A. C. Santos, *Phys. Rev. E* **108**, 064106 (2023).
- [255] T. P. Le, J. Levinsen, K. Modi, M. M. Parish, and F. A. Pollock, *Phys. Rev. A* **97**, 022106 (2018).

- [256] H.-L. Shi, S. Ding, Q.-K. Wan, X.-H. Wang, and W.-L. Yang, *Phys. Rev. Lett.* **129**, 130602 (2022).
- [257] R. Shastri, C. Jiang, G.-H. Xu, B. P. Venkatesh, and G. Watanabe, Dephasing enabled fast charging of quantum batteries (2024).
- [258] M. L. Néel, *Annales de Physique* **12**, 137–198 (1948).
- [259] U. Schollwöck, J. Richter, D. J. J. Farnell, and R. F. Bishop, *Quantum Magnetism* (Springer Berlin Heidelberg, 2004).
- [260] G. J. Milburn, *Phys. Rev. A* **44**, 5401 (1991).
- [261] T. Baumgratz, M. Cramer, and M. B. Plenio, *Phys. Rev. Lett.* **113**, 140401 (2014).
- [262] D. Barredo, H. Labuhn, S. Ravets, T. Lahaye, A. Browaeys, and C. S. Adams, *Phys. Rev. Lett.* **114**, 113002 (2015).
- [263] G. D. Scholes, *Annu. Rev. Phys. Chem.* **54**, 57 (2003).
- [264] K. Feron, W. J. Belcher, C. J. Fell, and P. C. Dastoor, *Int. J. Mol. Sci.* **13**, 17019 (2012).
- [265] S. M. Menke and R. J. Holmes, *Energy Environ. Sci.* **7**, 499 (2014).
- [266] F. Fassioli, R. Dinshaw, P. C. Arpin, and G. D. Scholes, *J. R. Soc. Interface* **11**, 20130901 (2014).
- [267] P. W. Anderson, *Phys. Rev.* **109**, 1492 (1958).
- [268] B. Kramer and A. MacKinnon, *Rep. Prog. Phys.* **56**, 1469 (1993).
- [269] F. Evers and A. D. Mirlin, *Rev. Mod. Phys.* **80**, 1355 (2008).
- [270] O. V. Mikhnenko, P. W. M. Blom, and T.-Q. Nguyen, *Energy Environ. Sci.* **8**, 1867 (2015).

- [271] S. Mukamel, *Chemical Physics* **31**, 327 (1978).
- [272] V. M. Kenkre and P. Reineker, *Exciton Dynamics in Molecular Crystals and Aggregates*, Springer Tracts in Modern Physics (Springer-Verlag, Berlin Heidelberg, 1982).
- [273] H. Haken and G. Strobl, *Z. Phys. A-Hadron Nucl.* **262**, 135 (1973).
- [274] A. Madhukar and W. Post, *Phys. Rev. Lett.* **40**, 70 (1978).
- [275] J. M. Moix, M. Khasin, and J. Cao, *New J. Phys.* **15**, 085010 (2013).
- [276] M. V. Medvedyeva, F. H. Essler, and T. Prosen, *Phys. Rev. Lett.* **117**, 137202 (2016).
- [277] A. J. Mork, M. C. Weidman, F. Prins, and W. A. Tisdale, *The Journal of Physical Chemistry C* **118**, 13920 (2014).
- [278] K. F. Chou and A. M. Dennis, *Sensors* **15**, 13288 (2015).
- [279] E. Penzo, A. Loiudice, E. S. Barnard, N. J. Borys, M. J. Jurow, M. Lorenzon, I. Rajzbaum, E. K. Wong, Y. Liu, A. M. Schwartzberg, S. Cabrini, S. Whitelam, R. Buonsanti, and A. Weber-Bargioni, *ACS Nano* **14**, 6999 (2020).
- [280] A. G. Dijkstra, H.-G. Duan, J. Knoester, K. A. Nelson, and J. Cao, *J. Chem. Phys* **144**, 134310 (2016).
- [281] T. Brixner, R. Hildner, J. Köhler, C. Lambert, and F. Würthner, *Adv. Energy Mater.* **7**, 1700236 (2017).
- [282] M. A. Becker, L. Scarpelli, G. Nedelcu, G. Rainò, F. Masia, P. Borri, T. Stöferle, M. V. Kovalenko, W. Langbein, and R. F. Mahrt, *Nano Letters* **18**, 7546 (2018).
- [283] S. Davidson, F. A. Pollock, and E. Gauger, *PRX Quantum* **3**, 020354 (2022).

- [284] P. Richerme, Z.-X. Gong, A. Lee, C. Senko, J. Smith, M. Foss-Feig, S. Michalakis, A. V. Gorshkov, and C. Monroe, *Nature* **511**, 198 (2014).
- [285] P. Jurcevic, B. P. Lanyon, P. Hauke, C. Hempel, P. Zoller, R. Blatt, and C. F. Roos, *Nature* **511**, 202 (2014).
- [286] J. Zeiher, J.-y. Choi, A. Rubio-Abadal, T. Pohl, R. van Bijnen, I. Bloch, and C. Gross, *Phys. Rev. X* **7**, 041063 (2017).
- [287] S. de Léséleuc, V. Lienhard, P. Scholl, D. Barredo, S. Weber, N. Lang, H. P. Büchler, T. Lahaye, and A. Browaeys, *Science* **365**, 775 (2019).
- [288] C. Maier, T. Brydges, P. Jurcevic, N. Trautmann, C. Hempel, B. P. Lanyon, P. Hauke, R. Blatt, and C. F. Roos, *Phys. Rev. Lett.* **122**, 050501 (2019).
- [289] E. Valdinoci, arXiv:0901.3261 (2009).
- [290] A. A. Dubkov, B. Spagnolo, and V. V. Uchaikin, *Int. J. Bifurc. Chaos* **18**, 2649 (2008).
- [291] R. Metzler, A. V. Chechkin, V. Y. Gonchar, and J. Klafter, *Chaos Solit. Fractals* **34**, 129 (2007).
- [292] V. Zolotarev, V. Uchaikin, and V. Saenko, *JETP* **88**, 780 (1999).
- [293] S. Janson, arXiv:1112.0220 (2011).
- [294] M. D. Jara, arXiv:0707.4491 (2007).
- [295] M. Jara, arXiv:0805.1326 (2008).
- [296] C. Bernardin, P. Cardoso, P. Goncalves, and S. Scotta, arXiv:2007.01621 (2020).
- [297] H.-P. Breuer, F. Petruccione, *et al.*, *The theory of open quantum systems* (Oxford University Press on Demand, 2002).
- [298] H. Pichler, A. Daley, and P. Zoller, *Physical Review A* **82**, 063605 (2010).

- [299] V. Eisler, *Journal of Statistical Mechanics: Theory and Experiment* **2011**, P06007 (2011).
- [300] Z. Cai and T. Barthel, *Phys. Rev. Lett.* **111**, 150403 (2013).
- [301] D. Bernard, T. Jin, and O. Shpielberg, *EPL* **121**, 60006 (2018).
- [302] J.-S. Bernier, P. Barmettler, D. Poletti, and C. Kollath, *Physical Review A* **87**, 063608 (2013).
- [303] D. Poletti, P. Barmettler, A. Georges, and C. Kollath, *Physical Review Letters* **111**, 195301 (2013).
- [304] J. J. García-Ripoll, S. Dürr, N. Syassen, D. M. Bauer, M. Lettner, G. Rempe, and J. I. Cirac, *New J. Phys.* **11**, 013053 (2009).
- [305] D. Rossini, A. Ghermaoui, M. B. Aguilera, R. Vatré, R. Bouganne, J. Beugnon, F. Gerbier, and L. Mazza, *Physical Review A* **103**, L060201 (2021).
- [306] F. D. M. Haldane, *Phys. Rev. Lett.* **60**, 635 (1988).
- [307] B. S. Shastry, *Phys. Rev. Lett.* **60**, 639 (1988).
- [308] A. Vezzani, E. Barkai, and R. Burioni, *Sci. Rep.* **10**, 2732 (2020).
- [309] H. Korbmacher, P. Sierant, W. Li, X. Deng, J. Zakrzewski, and L. Santos, *arXiv:2207.06186* (2022).
- [310] W.-H. Li, X. Deng, and L. Santos, *Phys. Rev. Lett.* **127**, 260601 (2021).
- [311] E. Khatami, G. Pupillo, M. Srednicki, and M. Rigol, *Phys. Rev. Lett.* **111**, 050403 (2013).
- [312] H. Nakano and M. Takahashi, *Phys. Rev. B* **50**, 10331 (1994).
- [313] D. Giovanni, M. Righetto, Q. Zhang, J. W. M. Lim, S. Ramesh, and T. C. Sum, *Light: Science & Applications* **10**, 2 (2021).

- [314] F. Würthner, T. E. Kaiser, and C. R. Saha-Möller, *Angew. Chem. Int. Ed.* **50**, 3376 (2011).
- [315] N. J. Hestand and F. C. Spano, *Chem. Rev.* **118**, 7069 (2018).
- [316] C. Monroe, W. C. Campbell, L.-M. Duan, Z.-X. Gong, A. V. Gorshkov, P. W. Hess, R. Islam, K. Kim, N. M. Linke, G. Pagano, P. Richerme, C. Senko, and N. Y. Yao, *Rev. Mod. Phys.* **93**, 025001 (2021).
- [317] I. Pogorelov, T. Feldker, C. D. Marciniak, L. Postler, G. Jacob, O. Kriegelsteiner, V. Podlesnic, M. Meth, V. Negnevitsky, M. Stadler, B. Höfer, C. Wächter, K. Lakhmanskii, R. Blatt, P. Schindler, and T. Monz, *PRX Quantum* **2**, 020343 (2021).
- [318] N. Trautmann and P. Hauke, *Phys. Rev. A* **97**, 023606 (2018).
- [319] H. Schempp, G. Günter, S. Wüster, M. Weidemüller, and S. Whitlock, *Phys. Rev. Lett.* **115**, 093002 (2015).
- [320] F. Olver, D. Lozier, R. Boisvert, and C. Clark, *The NIST Handbook of Mathematical Functions* (Cambridge University Press, New York, NY, 2010).
- [321] S. Paeckel, T. Köhler, A. Swoboda, S. R. Manmana, U. Schollwöck, and C. Hubig, *Annals of Physics* **411**, 167998 (2019), arXiv:1901.05824 [cond-mat.str-el] .
- [322] M. Fannes, B. Nachtergaele, and R. F. Werner, *Communications in Mathematical Physics* **144**, 443 (1992).
- [323] S. Östlund and S. Rommer, *PRL* **75**, 3537 (1995), arXiv:cond-mat/9503107 [cond-mat] .
- [324] P. Silvi, F. Tschirsich, M. Gerster, J. Jünemann, D. Jaschke, M. Rizzi, and S. Montangero, *SciPost Physics Lecture Notes* 10.21468/scipostphyslectnotes.8 (2019).

- [325] S. Montangero, *Introduction to Tensor Network Methods: Numerical simulations of low-dimensional many-body quantum systems* (2018).
- [326] D. Jaschke, S. Montangero, and L. D. Carr, *Quantum Science and Technology* **4**, 013001 (2019), arXiv:1804.09796 [cond-mat.quant-gas] .
- [327] B. Pirvu, V. Murg, J. I. Cirac, and F. Verstraete, *New Journal of Physics* **12**, 025012 (2010), arXiv:0804.3976 [quant-ph] .
- [328] G. Vidal, *Phys. Rev. Lett.* **93**, 040502 (2004).
- [329] F. Verstraete, J. J. García-Ripoll, and J. I. Cirac, *Phys. Rev. Lett.* **93**, 207204 (2004).
- [330] S. R. White and A. E. Feiguin, *Phys. Rev. Lett.* **93**, 076401 (2004).
- [331] A. J. Daley, C. Kollath, U. Schollwöck, and G. Vidal, *Journal of Statistical Mechanics: Theory and Experiment* **2004**, 04005 (2004), arXiv:cond-mat/0403313 [cond-mat.str-el] .
- [332] M. P. Zaletel, R. S. K. Mong, C. Karrasch, J. E. Moore, and F. Pollmann, *Phys. Rev. B* **91**, 165112 (2015).
- [333] A. E. Feiguin and S. R. White, *Phys. Rev. B* **72**, 020404 (2005).
- [334] E. Ronca, Z. Li, C. A. Jimenez-Hoyos, and G. Kin-Lic Chan, *arXiv e-prints* , arXiv:1706.09537 (2017), arXiv:1706.09537 [physics.chem-ph] .
- [335] P. Hauke and L. Tagliacozzo, *Phys. Rev. Lett.* **111**, 207202 (2013).
- [336] J. Haegeman, J. I. Cirac, T. J. Osborne, I. Pižorn, H. Verschelde, and F. Verstraete, *Phys. Rev. Lett.* **107**, 070601 (2011).
- [337] P. Seitz, I. Medina, E. Cruz, Q. Huang, and C. B. Mendl, *Quantum* **7**, 964 (2023), arXiv:2206.01000 [quant-ph] .

- [338] P. Secular, N. Gourianov, M. Lubasch, S. Dolgov, S. R. Clark, and D. Jaksch, Phys. Rev. B **101**, 235123 (2020).
- [339] P. Schauss, Quantum Science and Technology **3**, 023001 (2018).
- [340] F. Perciavalle, O. Morsch, D. Rossini, and L. Amico, arXiv e-prints , arXiv:2310.17967 (2023), arXiv:2310.17967 [cond-mat.quant-gas] .
- [341] F. Perciavalle, D. Rossini, T. Haug, O. Morsch, and L. Amico, PRA **108**, 023305 (2023), arXiv:2212.12490 [cond-mat.quant-gas] .
- [342] J. Polo, P. Naldesi, A. Minguzzi, and L. Amico, PRA **101**, 043418 (2020), arXiv:1911.07159 [cond-mat.quant-gas] .
- [343] P. Smacchia, L. Amico, P. Facchi, R. Fazio, G. Florio, S. Pascazio, and V. Vedral, Phys. Rev. A **84**, 022304 (2011).
- [344] S. M. Giampaolo and B. C. Hiesmayr, New Journal of Physics **16**, 093033 (2014), arXiv:1403.7184 [cond-mat.stat-mech] .
- [345] G. Zonzo and S. M. Giampaolo, Journal of Statistical Mechanics: Theory and Experiment **6**, 063103 (2018), arXiv:1709.06147 [quant-ph] .
- [346] J. H. H. Perk, arXiv e-prints , arXiv:1710.03384 (2017), arXiv:1710.03384 [cond-mat.stat-mech] .
- [347] C. Ding, PRE **100**, 042131 (2019).
- [348] M. Suzuki, Communications in Mathematical Physics **51**, 183 (1976).
- [349] W. Magnus, Communications on Pure and Applied Mathematics **7**, 649 (1954), <https://onlinelibrary.wiley.com/doi/pdf/10.1002/cpa.3160070404> .
- [350] H. Kleinert, *Path Integrals in Quantum Mechanics, Statistics, Polymer Physics, and Financial Markets*, 3rd ed. (WORLD SCIENTIFIC, 2004) <https://www.worldscientific.com/doi/pdf/10.1142/5057> .

[351] M. Schilling, F. Preti, M. M. Müller, T. Calarco, and F. Motzoi, arXiv e-prints , arXiv:2402.01498 (2024), arXiv:2402.01498 [quant-ph] .

[352] G. C. Wick, Phys. Rev. **80**, 268 (1950).

[353] S.-L. Lee and Y.-N. Yeh, Journal of Mathematical Chemistry **12**, 121–135 (1993).

[354] K. Clancy, M. Haythorpe, and A. Newcombe, Australas. J Comb. **78**, 209 (2019).

[355] S. Barik, D. Kalita, S. Pati, and G. Sahoo, Special Matrices **6**, 323–342 (2018).

[356] E. Kılıç, S. Kopalal, and N. Ömür, Iranian Journal of Science and Technology, Transactions A: Science **44**, 425–435 (2020).

[357] G. H. Weiss, Science **131**, 1216 (1960).